IDENTIFYING THE DOMINANT PHYSICAL PROCESSES FOR MIXING IN FULL-SCALE RACEWAY TANKS

BY

ANDREW S. LEMAN

THESIS

Submitted in partial fulfillment of the requirements
for the degree of Master of Science in Civil Engineering
in the Graduate College of the
University of Illinois at Urbana-Champaign, 2018

Urbana, Illinois

Adviser:

Assistant Professor Rafael O. Tinoco

Abstract

Biodiesels from microalgae are a promising alternative to fossil fuels with a number of unique benefits over other alternative fuel sources. However, to date, their viability in the fuels market remains infeasible due in part to a number of inefficiencies in the cultivation process. This has led to a growing interest in the hydrodynamics of open raceway tank (RWT) reactors, and cultivating conditions that are favorable to algae growth. In particular, two impediments require attention: the lack of vertical mixing in the straight portions of the reactor, and the need for efficient introduction of atmospheric carbon into the growth medium. It is proposed that the promotion of cellular, secondary currents by introduction of longitudinal ridges along the bed of the reactor can both promote vertical mixing and enhance gas transfer across the free surface of the growth medium. Experiments are performed in a full-scale open RWT at the University of Illinois, Urbana-Champaign, Ecohydraulics and Ecomorphodynamics Laboratory (EEL), in which the bed of the RWT is modified with longitudinal ridges of two different sizes, triangular and semi-circular cross-sections, and variable spacing. The 3-dimensional velocity components are monitored at significant locations in the reactor by means of acoustic doppler velocimetry (ADV) and surface particle image velocimetry (sPIV), and the gas transfer across the free-surface is measured by re-aeration curves of dissolved oxygen (DO). It is found that the cellular, secondary cells can be visualized in the velocity data after the introduction of longitudinal ridges. However, the impacts at the free surface are limited and consequently so is the gas transfer. A range of flow structures are observed that impact the relative significance of these cellular currents, including: vortex shedding from bend vanes, secondary currents of Prandtl's first kind induced by the bends, paddlewheel pulsation, and boundary layer development. These structures are found to overwhelm the presence of the cellular currents, and indicate that flows in the straight portions of the RWT reactor are a complex composite of boundary layer flow, secondary currents, resonance structures, energy input conditions, and shear flows. If cellular, secondary currents are to be used to promote the ideal algae growth conditions, further developments on this method will be required to overwhelm or work cooperatively with the dominant bend-induced dynamics.

To Jarah.

"Let knowledge grow from more to more,
But more of reverence in us dwell;
That mind and soul, according well,
May make one music as before..."

Alfred Lord Tennyson (In Memoriam, A.H.H.)

Acknowledgements

This work would not have been possible without the technical, personal, and practical support of a host of people. Foremost acknowledgment belongs to my adviser, Prof. Rafael Tinoco, who not only directed me into this field of research and gave me an excitement for a study that crosses the departmental divide, but who also suffered with me through the lack of air-conditioning, the long commutes, and the equally long-winded drafts of this document. His technical understanding, experimental dexterity, and investment in the work have been indispensable to my graduate studies and the completion of this research.

From the laboratory, I would like to thank Melanie Holland for her support in the experimentation and long-suffering with the acoustic doppler velocimeters. I am very grateful to Andy Waratuke for his help in developing the measurement apparatus and his seasoned, practical advice. Jorge San Juan, from the very start of my graduate studies, has been an incredibly patient officemate and sounding board. Many thanks to him and the other ecohydraulics and ecomorphodynamics group members, Pallav Ranjan, Chien-Yung Tseng, Andrés Prada, and Jieyu Qin for being such good friends and coworkers over the past two years.

I would also like to gratefully acknowledge the Civil and Environmental Engineering Department at the University of Illinois, Urbana-Champaign, for their financial support in the completion of this study.

I am indebted to my family in more ways than I even know, and I am very grateful to them for their support at a distance. I have certainly felt them behind me through these studies. Most of all, thanks to my wife, Jarah, who has been by my side, graciously bearing the load of this work with me. She has undoubtedly heard her fill of fluid mechanics, and I can't thank her enough for her unconditional support.

Table of Contents

List of Symbols

C	Concentration
C_a	Concentration in air
C_w	Concentration in water
$C_{a,sat}$	Saturation concentration in air
$C_{w,sat}$	Saturation concentration in water
δ_a	Gaseous diffusive boundary layer thickness
δ_w	Aqueous diffusive boundary layer thickness
$\theta_{s,small}$	Small eddy renewal time
$\theta_{s,large}$	Large eddy renewal time
z	Vertical coordinate
$\mathbf{F}_{w,z}$	Vertical flux into water
$\overline{\mathbf{F}}_{w,z}$	Time-averaged vertical flux into water
D_z	Vertical diffusivity
$\overline{k}$	Time-averaged gas transfer velocity
α	Equilibrium solubility coefficient
t	Time
θ_s	Renewal time
s	Rate of surface renewal
$\overline{u}$	Average streamwise velocity
h	Flow depth

L	Bulk integral length scale/Characteristic length scale
$\langle u' \rangle_{rms}$	Root-mean-square streamwise velocity fluctuation
ν	Kinematic viscosity
ε	Turbulence dissipation rate
$\mathbf{Sc}$	Schmidt number
u_η	Kolmogorov velocity microscale
$\mathbf{Re}_t$	Turbulent Reynolds number
x	Streamwise coordinate
y	Lateral coordinate
u'	Streamwise velocity fluctuation
v'	Lateral velocity fluctuation
c	Empirical coefficient
$\langle \beta \rangle_{rms}$	Root-mean-square surface divergence
β'	Surface divergence fluctuation
S	Bed slope
U_s	Time-averaged surface streamwise velocity
k_s	Surface turbulence kinetic energy
u_i/u_j	Velocity vector
x_i/x_j	Cartesian coordinates
ρ	Fluid density
p	Pressure
f_i	Body force vector
δ_{ij}	Kronecker delta
$\overline{S}_{ij}$	Strain rate tensor
τ_w	Wall shear stress
δ	Boundary layer thickness
u_*	Shear velocity

z_*	Wall vertical coordinate
u^+	Inner non-dimensional velocity
z^+	Inner non-dimensional length scale
η	Outer non-dimensional length scale
P	Production term of turbulence kinetic energy
Re_*	Inner Reynolds number
κ	Von Kármán constant
C^+	Law of the wall constant
C	Empirical coefficient
Π	Coles wake constant
$\mathbf{Re}_x$	Reynolds number based on streamwise coordinate
$\mathbf{Re}/\mathbf{Re}_b$	Bulk Reynolds number
$\mathbf{Fr}$	Froude number
$\mathbf{\Omega}$	Vorticity vector
Ω_x	Streamwise vorticity
Ω_y	Lateral vorticity
Ω_z	Vertical vorticity
$\overline{w}$	Average vertical velocity
∇^2	Laplace operator
w'	Vertical velocity fluctuation
L/W	Length-to-width ratio
θ	Twist angle
u_{corr}	Corrected streamwise velocity
v_{corr}	Corrected lateral velocity
S	Power spectral density function
ω	Frequency space coordinate
T	Sampling time

τ	Secondary time variable
$\hat{\Phi}(u')$	Fast Fourier Transform of velocity signal
f_s	Sampling frequency
N	Number of samples
DO_{sat}	Saturation concentration of dissolved oxygen
DO_{total}	Total mass of dissolved oxygen
V	Volume of water
A	Interfacial area
$v'w'$	Reynolds stress in the secondary plane
v'_{rms}	Root-mean-square lateral velocity fluctuations
w'_{rms}	Root-mean-square vertical velocity fluctuations
f	Frequency
f_u	Frequency of the streamwise velocity signal
f_v	Frequency of the lateral velocity signal
f_w	Frequency of the vertical velocity signal
S_{uu}	Power spectral density function in streamwise velocity
S_{vv}	Power spectral density function in lateral velocity
S_{ww}	Power spectral density function in vertical velocity
V_{bars}	Time-averaged lateral velocity with bed modifications
V_0	Time-averaged lateral velocity of empty bed condition
U	Nominal velocity
$f_{inverter}$	Inverter frequency
$f_{paddlewheel}$	Frequency of paddlewheel rotations
$\mathbf{St}$	Strouhal number
f_{flume}	Natural frequency of the flume
g	Gravitational constant
n	Resonance mode

B	Width of the cross-section
t_B	Bursting period
U_{max}	Maximum streamwise velocity

Chapter 1

Introduction

With the general scientific consensus on the certainty and gravity of anthropogenic climate change (Oreskes, 2004), one of the major research challenges of the 21st Century has been in managing the growing levels of greenhouse gas (GHG) emissions worldwide. The International Panel on Climate Change (IPCC) has reported that global GHG emissions have increased by 70% between 1970 and 2004, and foremost among them is carbon dioxide, which has increased by 80% over the same period (Greenwell et al., 2009). One method of mitigating these anthropogenic sources is by adoption of alternative fuels like biodiesels. From its earliest days, the diesel engine has been demonstrably capable of operating on renewable, organic material such as plant and animal oils (Demirbas, 2008), which could present a carbon-neutral alternative to petroleum-based products. Despite significant initiatives over the past 50 years (Van Gerpen, 2005; Demirbas, 2008), however, biofuels remain only 5% of the transportation fuel market in the United States (U.S. Energy Information Administration, 2017), and that while consuming approximately 40% of the U.S. corn grains (Guo et al., 2015).

This has signaled the introduction of several new generations of biodiesel feedstock to increase the cost-effectiveness and thereby competition with petroleum-based products. Most recently, biodiesel from microalgae (deemed the “third-generation” biofuel feedstock) has received much attention, because of its favorable attributes compared with competing terrestrial crops. Microalgae has a particularly high oil-content, typically ranging from 20% to 50% (Demirbas, 2010; Chisti, 2007; Stephens et al., 2010; Arenas et al., 2016), which has been found to be 10-23 times the yield of the highest oil producing terrestrial crop

(Nagarajan et al., 2013). Table 1.1 provides a comparison of the oil yields by crop, as well the land requirements to meet half of the U.S. transportation fuel demands.

Table 1.1: Oil yield and land requirement by crop. Table data reproduced from Chisti, 2007.

Crop	Oil Yield (L/ha)	Land Area Required (Mha)
Corn	172	1540
Soybean	446	594
Canola	1,190	223
Jatropha	1,892	140
Coconut	2,689	99
Oil Palm	5,950	45
Microalgae	136,900	2

In addition to its high oil yield, microalgae has the added benefits of not requiring arable land (Wijffels & Barbosa, 2010), productivity in otherwise agriculturally ineffective climates (Kumar et al., 2015; Chisti, 2013), growth rates 100 times that of terrestrial crops (Arenas et al., 2016), inexpensive growth media (Chisti, 2007), concurrent treatment of wastewater (Demirbas, 2010), and numerous other advantages identified by researchers that promote microalgae as the future of the biodiesel industry, and a possible path forward to decreasing dependence on fossil fuels.

The major hindrance, however, remains becoming cost-effective in markets with petroleum diesel. It is widely agreed upon that, to be competitive, the production of microalgae for biofuel feedstock needs to happen on a much larger scale at a lower cost (Chisti, 2013; Wijffels & Barbosa, 2010; Stephens et al., 2010; Kumar et al., 2015; Sheehan et al., 1998). This can be alleviated, to a degree, through concurrent treatment of wastewater (Sutherland et al., 2014) and the production of other "high value products" (HVPs) from microalgae (e.g. animal feedstock, nutritional supplements, natural dyes, etc.), but these small, easily-saturated markets will not be able to sustain the microalgae industry for long (Stephens et al., 2010; Spolaore et al., 2006). The cost of cultivation will need to be reduced.

One of the most significant cost drivers for algae biodiesel is the cost of biomass cultivation. Kumar et al. (2015) estimate the cost of cultivation around one-third of the total cost of biofuel production. Microalgae is cultivated in two typical methods, (1) open raceway tanks/ponds (RWTs), and (2) tubular photobioreactors (PBRs). A lively discussion exists in the literature about the relative merits of these two methods, but practically RWTs represent the major share (95%) of current algal biomass production (Kumar et al., 2015; Mendoza et al., 2013), and it is predicted that going forward RWTs will be the cultivation method of choice for their simplicity, ease of cleaning, ability to scale, and low costs (Sheehan et al., 1998; Demirbas, 2010; Kumar et al., 2015; Hreiz et al., 2014). Kumar et al. (2015) also point out that, on the basis of production cost, lipid production in open ponds (12.73 USD per gallon) is much more cost-effective than PBRs (31.61 USD per gallon).

Open RWTs are typically a closed loop consisting of straight sections with 180^o bends. Solution is guided around bends by use of baffles (Chisti, 2016). Flow depths range from 15-40 cm in order to provide optimal exposure to sunlight in the water column (Hreiz et al., 2014; Hadiyanto et al., 2013; Kumar et al., 2015). Flows in the raceway pond are typically generated by use of a paddlewheel, which provides the additional benefit of mixing the solution (Hreiz et al., 2014; Chisti, 2007).

For their simplicity, however, these facilities contain a number of hydrodynamic impediments to algal growth, which represents one possible area of optimization that could aid in making algal biodiesel cost-competitive. This is evidenced by the growing number of physical and numerical studies into the hydrodynamics of these facilities (see e.g., Hadiyanto et al., 2013; Mendoza et al., 2013; Liffman et al., 2013; Prussi et al., 2014; Hreiz et al., 2014; Ali et al., 2014).

One major impediment is that the straight portions of the flume tend to undergo minimal vertical mixing. This results in algal cells near the free surface receiving continuous overexposure to sunlight, and undergoing photoinhibition, a decrease in specific growth rate from elevated light intensity (Chisti, 2007; Nagarajan et al., 2013). In the meantime, at sufficient density, the cells at the surface can block the light from reaching the lower strata, where algal cells receive insufficient sunlight for photosynthetic reactions and subsequent growth. Effective methods of mixing the straight portions of the flume while minimally impacting the power input from the paddlewheel are needed to increase biomass productivity.

A second impediment to algal growth is the concentration of both dissolved oxygen (O_2) and carbon dioxide (CO_2) in the growth medium. Microalgal biomass is approximately 50% carbon on a dry weight basis (Mirón et al., 2003), and therefore efficient methods of introducing carbon into the medium are critical to biomass production. Typically this is performed by pumping carbon dioxide from a nearby power plant or chemical plant (Chisti, 2007; Kadam, 1997), however this significantly restricts the locations of these ponds and can amount to significant supply costs (Kumar et al., 2015; Kadam, 1997). Alternative methods of introducing atmospheric carbon would both save cost, and could enhance the growth rates (Hanagata et al., 1992) without such restrictions on location. Likewise, oxygen is produced as a byproduct in photosynthetic reactions which can supersaturate the medium and reduce growth rates. Miron et al. (1999) have shown in studies of *Chlorella Vulgaris* that this can lead to a 35% decrease in photosynthetic efficiency. Thus, processes are required to catalyze mass transfer both into (CO_2) and out of (O_2) the growth medium.

The focus of this study will be on improving the hydrodynamics of these facilities with respect to the optimal algae growth conditions. Two questions, in particular, will be considered. First, "can passive structures be used to enhance mixing in RWT?" It has been theorized that the structure of the turbulence in the straight portions of the open RWT reactors can be enhanced with respect to the algae by introduction of cellular, secondary currents (further discussed later in this chapter) to both increase the vertical mixing and in turn accelerate the gas transfer at the free surface (see Citerone, 2016). This has been examined experimentally in a straight flume at shallow depths, but has not yet been applied to an industrial application in a full-scale RWT. Experiments are here performed that test this hypothesis in a full-scale open RWT reactor. Longitudinal bars of varying shapes and sizes are used to modify the bed of the reactor such that secondary currents are enhanced. A suite of measurement techniques, including: (1) acoustic doppler velocimetry (ADV), (2) surface particle image velocimetry (sPIV), and (3) dissolved oxygen (DO) measurements are used to characterize both the flow structures in the reactor, and the mass transfer across the air-water interface. Experimental data is then queried for mean velocity, turbulence statistics, and re-aeration rates to determine whether the introduction of these longitudinal bars is effective.

Second, "what are the primary structures involved in mixing in a RWT reactor?" Measurements addressing the first question are supplemented with additional ADV sampling. Velocity signals are then considered in spectral space and compared with features of known open-channel flow structures in the published literature to determine what the most likely candidates are for driving mixing in open RWTs.

This chapter will provide some brief theoretical background and literature survey of the biological, chemical, and physical processes at work in open RWT reactors. First, some features of microalgae are considered generally to establish some of the operational boundaries of this, primarily hydrodynamic, study. Then, a brief history of gas transfer theory and existing models are outlined. This will be important for understanding the interactions between the turbulence generated near the bed of the RWT and the process at the free-surface. Recent studies are considered that establish this pairing and seek to define significant parameters to the gas transfer. Finally, theoretical background in the field of open-channel turbulence is provided that will be indispensable both to the design of these experiments and to the analysis of the measurements. General theory behind boundary layer flows and secondary currents are provided that then give way to recent studies in the particular application of open RWT reactors.

Chapter 2 describes in detail the experimental design, including facilities, experimental conditions, and descriptions of the measurement techniques. Chapter 3 discusses the turbulence measurement results, and provides a detailed discussion of observations relating to the cellular, secondary currents. Here questions are answered as to whether these secondary currents can be enhanced and what are the dominant processes for mixing. Chapter 4 discusses the gas transfer measurement results, and the impacts of the enhanced turbulence on transfer velocities is examined. Finally, Chapter 5 provides some concluding discussion and recommendations for future work.

1.1 Biological Processes: Microalgae

Microalgae is a broad term that is fairly inclusive, and thereby it can represent a wide variety of cells and properties. It can be used to refer to eukaryotic cells (dinoflagellates, diatoms) and prokaryotic cells (cyanobacteria), that can be autotrophic, mixotrophic, or in some cases entirely heterotrophic (Scott et al., 2010), and can grow in saline or freshwater conditions (Sheehan et al., 1998). Thus, speaking generally about microalgae cultivation represents somewhat of a challenge. That said, there are a few characteristics of microalgae that are widely applicable, especially to those strains under consideration for biodiesel feedstock, and have been widely discussed in the literature.

1.1.1 Photosynthesis and Lipid Biosynthesis

First, it is valuable to consider the compounds most salient to biodiesel generation. Triacylglycerides (TAGs) are lipids that are extracted from algal oil bodies, and are used in the process of transesterification to create biodiesel. An overview of the pathways to TAG synthesis is given in Figure 1.1 as originally presented in Scott et al. (2010). In very brief overview, requisite fatty acids are produced in the chloroplast of individual microalgal cells from carbon either fixed during photosynthesis or from exogenous supplies of organic carbon. Fatty acids then pass through the cytosol to the endoplasmic reticulum where they are further processed into TAGs and bud off into oil bodies within the cytosol (Scott et al., 2010; Hu et al., 2008).

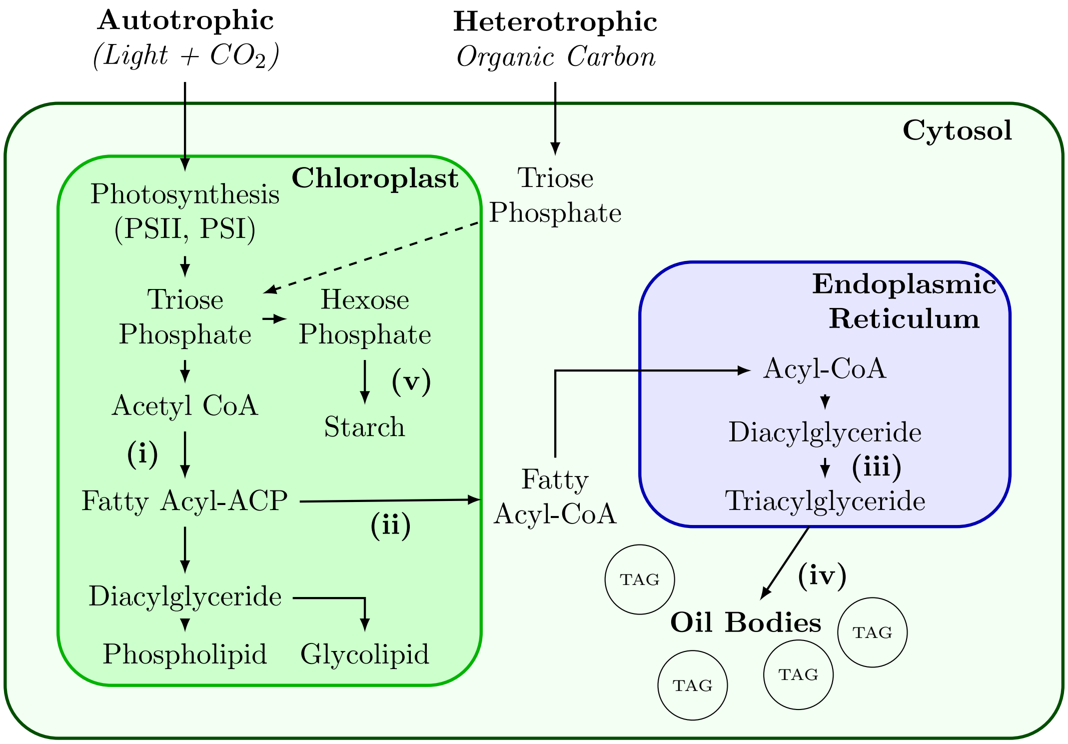

Figure 1.1: Lipid biosynthesis schematic. Reproduced from Scott et al. (2010). Schematic includes only major steps. Key: (i) = acetyl-CoA carbosylase (ACCase) and fatty acid synthase (FAS); (ii) = fatty acid thioesterases and acyl-CoA synthetases; (iii) = TAG biosynthesis enzymes, including acyl-CoA:diacylglycerol acyltransferase (DGAT); (iv) = oil body formation; and (v) = ADP-glucose pyrophosphorylase and starch synthase.

It can be seen that for autotrophic cells, light and carbon dioxide are the two primary exogenous inputs that drive the process of lipid production (other nutrients are required, though not shown in this broad overview). These will be discussed in the following sections.

1.1.2 Light

Borowitzka (2016) has noted that “the quantity and quality of light available to the algae are recognised as the single main factors limiting the productivity of algal mass cultures outdoors.” However, increasing photosynthetic efficiency is not so simple as merely exposing the cells to more light. Algal cells reach a “light saturation” point at which the relative merit of light intensity to specific growth rate begins to decrease. This tends to be significantly lower than midday sunlight levels. Additionally, at some point the cells reach a maximum specific growth rate, after which increasing light intensity reduces the biomass growth rate, a phenomenon known as "photoinhibition" (see Figure 1.2, Chisti, 2007; Nagarajan et al., 2013).

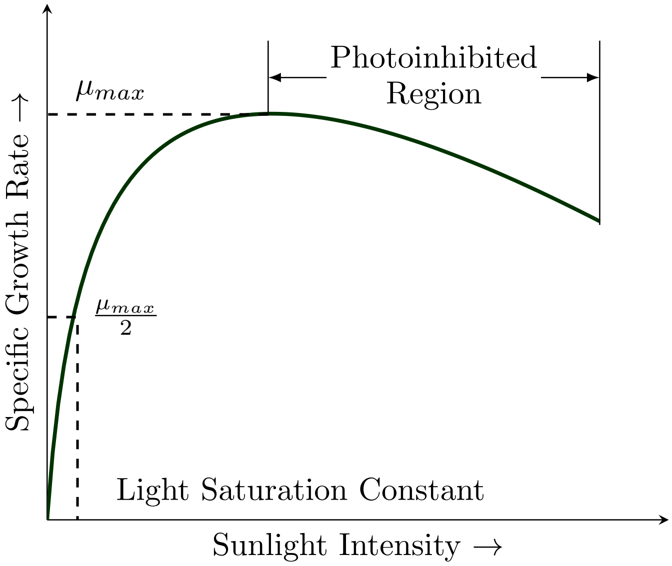

Figure 1.2: Conceptual relationship of algal specific growth rate to sunlight intensity. Reproduced from Chisti (2007).

It has been observed, therefore, that the optimal conditions for algae growth follow what is called the "flashing-light effect." This was observed experimentally by Kok (1953), though the idea preceded his work by several decades. A short burst of light can excite available reaction centers in the photosynthetic apparatus in the cell's chlorophyl, but overexposure can cause saturation of the reaction centers and the excitation energy is lost to fluorescence and heat. If the burst of light is followed by a dark cycle, the non-photochemical reactions can take place and free up the reaction centers for another excitation. Thus, due to the combination of photochemical and non-photochemical reactions in the cell, the ideal light exposure of algal cells is a short period of light (i.e. a "flash") followed by a period of darkness. This process has demonstrated increased productivity in algal cells (see Borowitzka, 2016, and references therein).

It has already been discussed how conditions in typical open RWT reactors tend to stratify with respect to light, and therefore there has been several attempts to generate these conditions in RWTs (e.g. Laws et al., 1983; Voleti, 2012, among others). Recent studies will be discussed further in Section 1.3.3.

1.1.3 Carbon Dioxide

The significance of available carbon dioxide to biomass production has already been noted. However, like light, simplistic solutions of merely pumping in high concentrations of carbon dioxide will not suffice. Hanagata et al. (1992) have performed studies on several strains of green algae and blue-green algae in which increasing concentrations of carbon dioxide were bubbled into the growth medium, and specific growth rates of the algae were measured. It was found that while increasing the gas flow rate yielded faster doubling times, elevated levels of concentration actually inhibited the growth of the algae. Thus, it could be surmised that atmospheric air, even with its low concentrations of carbon dioxide (0.039%, see Chisti, 2013), could increase the efficiency of the algae growth, if efficiently introduced into the culture medium. It is proposed that sufficient mixing of the culture medium would aid in the process of efficiently introducing carbon dioxide.

1.1.4 Shear

While the benefits of mixing on both light-exposure and on carbon availability have been demonstrated, there are physical limits on the amount of mixing that is beneficial to algal cells. With increasing levels of turbulence the smallest scales of turbulent activity approach the scales of the microalgae cells. As these scales become commensurate with each other, the algae cells are subject to mechanical damage or behavioral change from shear stress generated by the fluid which ultimately leads to reduced growth rates (Hadiyanto et al., 2013). Grobbelaar (1994) demonstrated in *Chlorella vulgaris* that increased turbulence resulted in increased productivity up to a Reynold's number of approximately 5,000, after which the photosynthetic rates decreased. This threshold, however, is highly dependent on the algal strain (Sullivan & Swift, 2003).

In summary, there are numerous benefits of mixing on the algae growth, both for light exposure and gas transfer. However, this is moderated by the response of algae cells to shear stresses, which provide natural limits on the levels of mixing.

1.2 Chemical Processes: Gas Transfer

It follows from the preceding discussion that gas transfer across the air-water interface is of particular importance in open RWTs, because of the significance of O_2 and CO_2 to the mechanisms of cellular respiration and photosynthesis. There is a long history to this field of study, and much work has been done in recent years with particular application to atmospheric carbon capture in oceans. The history provided here follows the excellent summaries of Liao and Wang (2013) as well as Turney and Banerjee (2013), and the reader is directed there for a more comprehensive survey of the field.

1.2.1 Theoretical Background

Gas transfer at the air-water interface is a fairly complex process, because it is influenced by a number of physical mechanisms (e.g. wave breaking, wind shear, turbulence renewal, etc.), and as such, the field has seen a number of different models that even now are continuing to develop. The most basic foundation of these models conceptualizes the air-water interface as a stagnant surface being bounded by gaseous and aqueous diffusive boundary layers (DBLs) through which molecules pass by molecular diffusion (see Figure 1.3). In the case of gas transfer into water, it is assumed that the gas in question is readily available in the atmosphere, and therefore it is the aqueous DBL that is of interest. It is within this DBL that the concentration gradient extends from the bulk concentration in the water to the saturation concentration at the interface, and the thickness of this DBL (δ_w) is determined by the turbulence in the water near the interface.

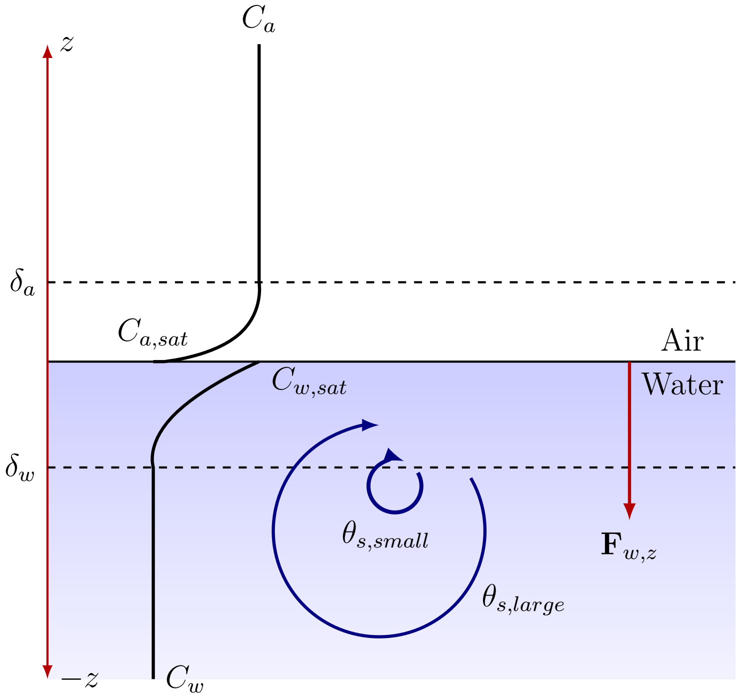

Figure 1.3: Schematic of the air-water interface for gas transfer models. Adapted from Socolofsky and Jirka (2005). C_w and C_a represent aqueous and gaseous concentrations, respectively, reaching saturation values at the interface. $\mathbf{F}_{w,z}$ represents the flux into the water, δ_w and δ_a represent the aqueous and gaseous DBL thicknesses, and $\theta_{s,small}$ and $\theta_{s,large}$ represent the small and large eddy renewal times.

Fick's first law gives the flux across the interface for the case of pure diffusion as:

$$\mathbf{F}_{w,z} = -D_z \frac{\partial C}{\partial z}\bigg|_{z=0} \tag{1.1}$$

where D_z represents a vertical diffusion coefficient. This can then be expressed as a function of the bulk concentrations in air and water by defining an average gas transfer velocity, $\overline{k}$, such that:

$$\overline{\mathbf{F}}_{w,z} = \overline{k}(C_{w,sat} - C_w) = \overline{k}(\alpha C_a - C_w) \tag{1.2}$$

where $C_{w,sat}$ is the saturation concentration of the gas in water, C_w is the bulk concentration in the water, C_a is the bulk concentration in air, α is the equilibrium solubility coefficient, and the overbar designates a time average. This gas transfer velocity, then, serves as the foundational parameter for measuring the rate at which gas is entrained in the liquid, and it will capture many of the physical mechanisms in one lumped parameter.

1.2.2 Legacy Models

The simplest model available, then, is attributed to Nernst (1904), and was developed into what was known as the Lewis-Whitman model (Lewis & Whitman, 1924) or Thin Film model. This model makes no modification on the initial assumptions of a stagnant surface, and assumes strictly laminar flow with a DBL of constant thickness. Returning to Fick's first law, the average transfer velocity by equations 1.1 and 1.2 is equal to:

$$\overline{k} = \frac{D_z}{\delta_w} \tag{1.3}$$

While this model is simple and gives a foundational look into the mechanics at the surface, the direct proportionality of $\overline{k}$ to D_z is not supported by experimental results (Turney & Banerjee, 2013). In reality, the aqueous DBL is poorly modeled by a constant thickness because turbulent eddies disrupt this layer, and higher concentration fluid is replaced or "renewed" by fluids from the bulk mass below the DBL. Therefore, further developments to this model were required.

The Thin Film model then gave way to the Penetration model first proposed by Higbie (1935). This model recognizes that turbulent eddies will disrupt the aqueous DBL, and models them with a constant renewal time, θ_s. In this case, the governing 1D transport equation (neglecting advection) can be used to find the concentration:

$$\frac{\partial C}{\partial t} = D_z \frac{\partial^2 C}{\partial z^2} \tag{1.4a}$$

$$C(-\infty, t) = C_0 \tag{1.4b}$$

$$C(0, t) = C_{sat} \tag{1.4c}$$

$$C(z, 0) = C_0 \tag{1.4d}$$

where C_0 is the initial concentration in the bulk flow, and C_{sat} is the concentration at the interface. The solution to this partial differential equation is:

$$\frac{C_{(z,t)} - C_0}{C_{sat} - C_0} = \text{erfc}\Big\{\frac{-z}{\sqrt{4D_z t}}\Big\} \tag{1.5}$$

Consequently, the concentration gradient can be calculated by taking the derivative, which yields:

$$\frac{\partial C}{\partial z} = -(C_{sat} - C_0)\Big(\frac{2}{\sqrt{\pi}}\Big)e^{-\frac{z^2}{4D_z t}}\Big(-\frac{1}{\sqrt{4D_z t}}\Big) \tag{1.6}$$

The local gradient at the interface ($z = 0$) is then:

$$\frac{\partial C}{\partial z}\Big|_{z=0} = (C_{sat} - C_0)\frac{1}{\sqrt{\pi D_z t}} \tag{1.7}$$

When this is plugged back into Fick's first law (Equation 1.1) for the flux into the water, the following relationship is attained:

$$\mathbf{F}_{w,z} = -(C_{sat} - C_0)\sqrt{\frac{D_z}{\pi t}} \tag{1.8}$$

When this is integrated over one renewal period, the resulting cycle-averaged flux is:

$$\overline{\mathbf{F}}_{w,z} = \frac{1}{\theta_s}\int_0^{\theta_s} -(C_{sat} - C_0)\sqrt{\frac{D_z}{\pi t}}dt = -(C_{sat} - C_0)\sqrt{\frac{4D_z}{\pi \theta_s}} \tag{1.9}$$

Thus making the average transfer velocity for the Penetration model:

$$\overline{k} = \sqrt{\frac{4D_z}{\pi\theta_s}} \tag{1.10}$$

It may be observed that the transfer velocity is no longer proportional to the diffusion coefficient, D_z, but rather $\overline{k} \sim D_z^{1/2}$. This has been supported by laboratory experiments, and provides a significant improvement on the Thin Film model, however it introduces a new parameter that needs to be estimated: the renewal time, θ_s.

A variation on this Penetration model, the Surface Renewal model, was given by Danckwertz (1951) whereby the turbulence near the surface was modeled stochastically using a Poisson probability density distribution to determine the age of a "parcel" of fluid at the interface:

$$\overline{k} = \int_0^{\theta_s} se^{-st}\sqrt{\frac{D_z}{\pi t}}dt = \sqrt{D_z s}\ \mathrm{erf}\{\sqrt{s\theta_s}\} \approx \sqrt{D_z s} \tag{1.11}$$

where s is the rate of surface renewal, $s = 1/\theta_s$. This makes the gas transfer velocity equal to:

$$\overline{k} = \sqrt{\frac{D_z}{\theta_s}} \tag{1.12}$$

This retains the relationship of $\overline{k} \sim D_z^{1/2}$, however, the model is still dependent on a mean surface renewal time (θ_s), which has generated several subsequent methods of estimating this parameter.

O'Connor and Dobbins (1958) were the first to relate the mean renewal time to bulk flow parameters. They estimated:

$$\theta_s = \frac{h}{\overline{u}} \tag{1.13}$$

where h is the flow depth, and $\overline{u}$ is the temporal- and spatial-average of the streamwise velocity. This, however, gave way to models that were based on characteristic scales of the turbulence. Fortescue and Pearson (1967) developed what is known as the "Large Eddy Surface Renewal model," which bases the mean renewal time on the bulk integral length scale, L, and the turbulence intensity, expressed as the root-mean-square of the velocity fluctuations in the bulk fluid, $\langle u' \rangle_{rms}$:

$$\theta_s = \frac{L}{\langle u' \rangle_{rms}} \tag{1.14}$$

Alternatively, Banerjee et al. (1968) and Lamont and Scott (1970) proposed the "Small Eddy Surface Renewal model," in which the mean renewal time was related to the smallest scales of turbulence, also known as the Kolmogorov micro-timescale:

$$\theta_s = (\nu/\varepsilon)^{1/2} \tag{1.15}$$

where ν is the kinematic viscosity of the fluid, and ε is the turbulence dissipation rate. This makes the transfer velocity equal to:

$$\overline{k} \sim \mathbf{Sc}^{-1/2}(\nu\varepsilon)^{1/4} = \mathbf{Sc}^{-1/2}u_\eta \tag{1.16}$$

where $\mathbf{Sc}$ is the Schmidt number ($\mathbf{Sc} \equiv \nu/D_z$), and u_η is the Kolmogorov velocity microscale.

Both of these models make assumptions about the scales at which surface renewal occurs, however Theofanous et al. (1976) followed on this work and found that a "two regime model" better fit experimental results. They found that for low turbulent Reynolds numbers ($\mathbf{Re}_t < 500$) large scale eddies dominated, and that for high turbulent Reynolds numbers ($\mathbf{Re}_t > 500$) small scale eddies were more characteristic, where the turbulent Reynolds number is defined as:

$$\mathbf{Re}_t = \frac{\langle u' \rangle_{rms} L}{\nu} \tag{1.17}$$

This led to their two-regime gas transfer velocity coefficients:

$$\overline{k} = 0.73\mathbf{Sc}^{-1/2}u'\mathbf{Re}_t^{-1/2} \quad ; \quad \mathbf{Re}_t < 500 \tag{1.18a}$$

$$\overline{k} = 0.25\mathbf{Sc}^{-1/2}u'\mathbf{Re}_t^{-1/4} \quad ; \quad \mathbf{Re}_t > 500 \tag{1.18b}$$

Ultimately, the renewal time remains a difficult parameter to experimentally determine, and the development of models that could accurately express these phenomena without relying on θ_s is still an open field of research.

1.2.3 Surface Divergence Model

This necessity set the stage for the Surface Divergence model, which was put forward by McCready et al. (1986) and developed into a gas transfer velocity relationship by Banerjee (1990). This model recognizes divergence at the interface as a signature of local upwelling bringing renewed fluid from the bulk mass up to the surface (Banerjee et al., 2004). This is represented in the gas transfer velocity relationship:

$$\overline{k} \approx \mathbf{Sc}^{-1/2}\langle u'\rangle_{rms}\mathbf{Re}_t^{-1/2}\left[\left\langle \frac{\partial u'}{\partial x} + \frac{\partial v'}{\partial y}\right\rangle^2\right]^{1/4}_{interface} \tag{1.19}$$

where the term in the square brackets is the square of the surface divergence (based on the fluctuating velocities in the free surface plane). This model eliminates the need for estimating renewal time and replaces it with a physically-meaningful term easily measurable using techniques like sPIV. This can alternatively be expressed in terms of an empirically determined coefficient, c:

$$\overline{k} \approx c\sqrt{D\langle\beta\rangle_{rms}} \tag{1.20}$$

where $\langle\beta\rangle_{rms}$ is the bulk root mean square of the divergence fluctuations:

$$\langle\beta\rangle_{rms} = \sqrt{(\beta')^2} = \sqrt{\left\langle \frac{\partial u'}{\partial x} + \frac{\partial v'}{\partial y} \right\rangle^2} \tag{1.21}$$

Following this approach, Turney and Banerjee (2013) tabulated experimental results for various conditions, given in Table 1.2.

Table 1.2: Experimentally derived coefficients for gas transfer (as per Equation 1.20). Original table found in Turney and Banerjee (2013).

Publication	**Flow Condition**	**Transfer Velocity, $\overline{\mathbf{k}}$**
McCready et al. (1986)	counter-current wind shear	$\overline{k} \sim 0.71\sqrt{D\langle\beta\rangle_{rms}}$
Law and Khoo (2002)	grid-stirred tank and wind waves	$\overline{k} \sim 0.22\sqrt{D\langle\beta\rangle_{rms}}$
Tamburrino and Gulliver (2002)	open-channel flow	$\overline{k} \sim 0.24\sqrt{DS_{\beta_{max}}/u_{*cb}}$
McKenna and McGillis (2004)	grid-stirred tank	$\overline{k} \sim 0.50\sqrt{D\langle\beta\rangle_{rms}}$
Banerjee and MacIntyre (2004)	low wind flow	$\overline{k} \sim 0.35\sqrt{D\langle\beta\rangle_{rms}}$
Turney et al. (2005)	low and moderate wind flow	$\overline{k} \sim 0.50\sqrt{D\langle\beta\rangle_{rms}}$
Magnaudet and Calmet (2006)	LES of channel flow; single condition	$\overline{k} \sim 0.60\sqrt{D\langle\beta\rangle_{rms}}$
Z. Xu et al. (2006)	grid-stirred tank and wind waves	$\overline{k} \sim 0.20\sqrt{D\langle\beta\rangle_{rms}}$
Herlina and Jirka (2008)	grid-stirred tank	$\overline{k} \sim 0.33\sqrt{D\langle\beta\rangle_{rms}}$

Most recently, Sanjou et al. (2016, 2017) have found, that the functional form of the Surface Divergence model holds experimentally. However, given the variability in the empirical coefficient, c, of the transfer velocity relationship (demonstrated above) they have observed that there is an additional dependency on the flow depth, due to turbulence generated at the bed. They propose two possible modifications to the standard Surface Divergence model to correct for this. The first is based on the time-averaged streamwise velocity at the free surface, U_s:

$$\overline{k} = c\sqrt{D\langle\beta\rangle_{rms}\frac{h\langle\beta\rangle_{rms}}{U_s}} \tag{1.22}$$

where c is measured to be 0.691. This was found to be inaccurate in cases where the bed was modified by vegetation, thus the modification was altered to be dependent, instead, on the surface turbulence kinetic energy, k_s:

$$\overline{k} = c\sqrt{D\langle\beta\rangle_{rms}\frac{h\langle\beta\rangle_{rms}}{k_s^{1/2}}} \tag{1.23}$$

where c is measured to be 0.146. Experimental results were found to converge on this relationship very well.

It is significant to the present study that (1) the functional form of the Surface Divergence model was upheld, and (2) that the turbulence generated near the bed had a significant effect on the divergence at the free surface and consequently on the re-aeration rates. The present study will build on this understanding by modifying the bed and monitoring the surface divergence and transfer velocities.

1.3 Physical Processes: Open Channel Turbulence

Of principal importance to this study are the hydrodynamics of the algae growth medium. Hydrodynamics influence gas transfer across the air-water interface, light exposure, cellular shear stress, nutrient uptake, and numerous other factors. The purpose of this study, therefore, is to manipulate the flow structures in typical RWT configurations to best approximate optimal growth conditions for microalgae.

The governing equations for fluid motion of the medium, derived from Newton's second law and mass conservation, are the Navier-Stokes equations for incompressible flow, expressed below in Einstein notation:

$$\frac{\partial u_i}{\partial t} + u_j \frac{\partial u_i}{\partial x_j} = -\frac{1}{\rho}\frac{\partial p}{\partial x_i} + \nu \frac{\partial^2 u_i}{\partial x_j \partial x_j} + f_i \tag{1.24a}$$

$$\frac{\partial u_i}{\partial x_i} = 0 \tag{1.24b}$$

where u_i, u_j are the velocity vector, ρ is the density of the fluid, p is the local pressure, and f_i is the body force vector. When flow is turbulent, as is the case for most open-channel flows, it is meaningful to further decompose the velocity signal into a time-averaged component, $\overline{u}_i$, and a fluctuation about that mean, u_i', such that the instantaneous velocity signal can be expressed as:

$$u_i = \overline{u}_i + u_i' \tag{1.25}$$

When this decomposition is applied to the governing Navier-Stokes equations, and the equations themselves are likewise averaged in time, the resultant equations are the well-known Reynolds-Averaged Navier-Stokes (RANS) equations:

$$\frac{\partial \overline{u}_i}{\partial t} + \overline{u}_j \frac{\partial \overline{u}_i}{\partial x_j} = \overline{f_i} + \frac{\partial}{\partial x_j}\left[-\frac{\overline{p}}{\rho}\delta_{ij} + 2\nu \overline{S}_{ij} - \overline{u_i' u_j'} \right] \tag{1.26a}$$

$$\text{where: } \overline{S}_{ij} = \frac{1}{2}\left(\frac{\partial \overline{u}_i}{\partial x_j} + \frac{\partial \overline{u}_j}{\partial x_i} \right)$$

$$\frac{\partial \overline{u}_i}{\partial x_i} = 0 \tag{1.26b}$$

Notably, the fluctuating components are mostly lost in the time-averaging of these equations, with the exception of the final term $\partial/\partial x_j(-\overline{u_i' u_j'})$, which represents the spatial derivative of the Reynolds stresses for a fluid of constant density. This term will play a significant role in the discussion of secondary currents.

These equations form the foundation for a wide variety of fluid flows. Flows in open RWTs, like many other open-channel flows, are typically classified as boundary layer flows over a boundary of zero incidence. Given the narrow aspect ratio of the channels, however, as well as the centrifugal forces introduced by the 180^o bends and paddlewheel mixing, there are a number of complexities and three-dimensional features in these flows that are not adequately accounted for in typical boundary layer theory. This is evidenced by the growing volume of experimental and numerical studies exploring the three-dimensional idiosyncrasies of these facilities (see e.g. Hadiyanto et al., 2013; Mendoza et al., 2013; Hreiz et al., 2014; Prussi et al., 2014). In particular, this study will focus on secondary currents in the plane perpendicular to the streamwise flow.

What follows will first explore some of the foundational theory in turbulent boundary layers that will form the basis of these flows. Next, secondary flows will be introduced both in theory and in a number of recent experimental and field studies that demonstrate the current understanding of these flow structures. Finally, recent experimental and numerical studies in RWT applications will be presented. Studies in RWTs have been broad and far-reaching, thus focus will be given to studies that explore low-cost modifications to typical RWT structure seeking to enhance vertical mixing and gas transfer at the free surface.

1.3.1 Turbulent Boundary Layer Theory

Turbulent boundary layer theory has a long history and has been written about extensively by many. Most reference volumes on boundary layer theory or turbulence theory will provide full derivations of the governing equations (e.g. Schlichting et al., 1955; Tennekes & Lumley, 1972; Pope, 2001). Here some general concepts of turbulent boundary layers are outlined in brief, and the reader is directed to the foregoing references for an exhaustive treatment of the subject.

The foundations of boundary layer theory began with the pioneering observation of Prandtl (1904), that wall-bounded flows can be separated into two distinct regions with respect to the viscous effects of the fluid. There exists an inviscid “outer layer” of the flow where viscosity can be neglected, and a thin “inner layer” where viscosity is significant. In the turbulent regime, this inner layer can be further subdivided into an overlying layer where turbulence is active but damped by viscosity, and an even smaller “viscous sublayer” in which viscosity is dominant and turbulence is suppressed. Figure 1.4 represents this discretization along with a summary of the distinct regions of applicability.

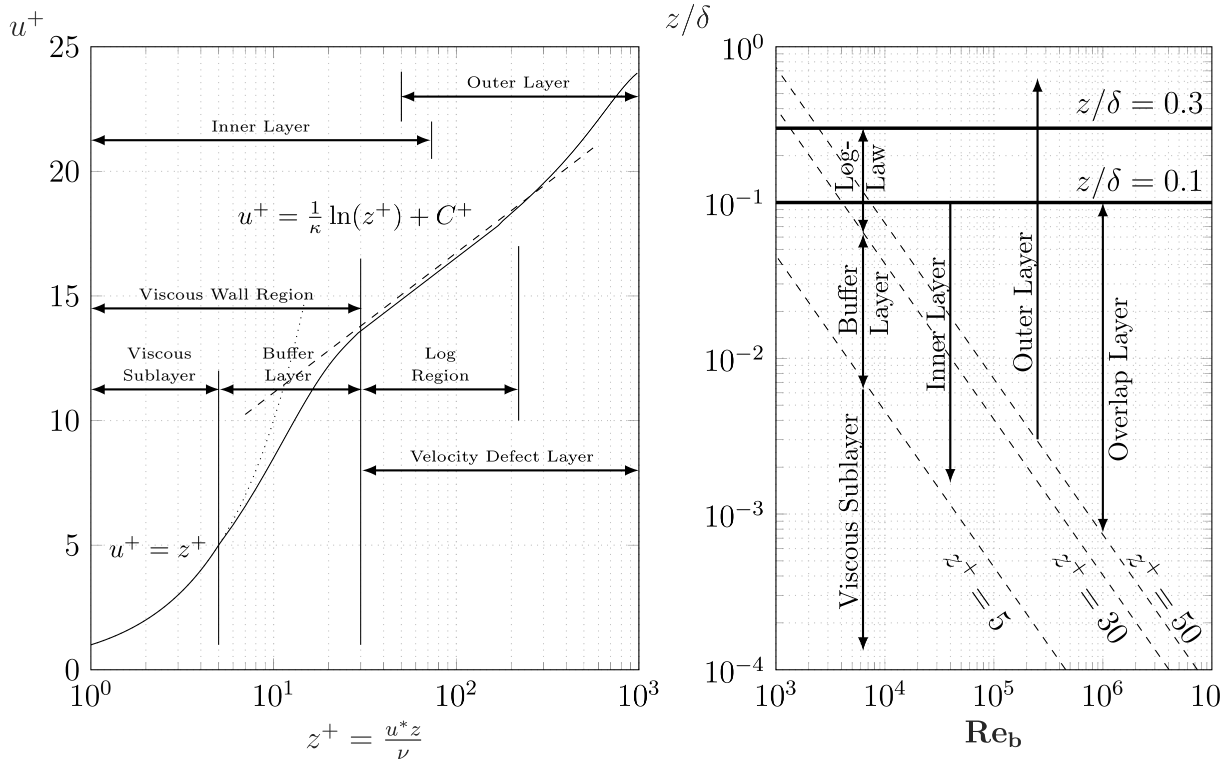

Figure 1.4: Boundary layer discretization. Chart on the right reproduced from Pope (2001).

These discrete regions can be further understood by dimensional analysis. It is evident that the velocity is dependent on the density of the fluid, the kinematic viscosity, the shear stress at the wall, the distance from the wall, and the boundary layer thickness:

$$\overline{u} = \Phi(\rho, \nu, \tau_w, z, \delta) \tag{1.27}$$

For convenience, a velocity scale and a length scale can be defined commensurate with the viscous effects of the flow. These are the shear velocity and inner length scale, respectively:

$$u_* = \sqrt{\frac{\tau_w}{\rho}} \qquad \textit{and} \qquad z_* = \frac{\nu}{u_*} \tag{1.28}$$

These, in turn, can be used to create three dimensionless parameters:

$$u^+ = \frac{\overline{u}}{u_*}, \qquad z^+ = \frac{z}{z_*}, \qquad \eta = \frac{z}{\delta} \tag{1.29}$$

where u^+ designates the non-dimensional velocity, z^+ designates an inner length scale based on viscous effects, and η designates an outer length scale based the thickness of the boundary layer. Therefore, it can be surmised that the non-dimensional velocity is strictly a function of the inner length scale, and near the edge of the boundary layer it is strictly a function of the outer length scale.

Near the wall, further definition can be given by taking the Taylor expansion of the non-dimensional velocity about $z^+ = 0$:

$$u^+ = u^+\Big|_{z^+=0} + \frac{\partial u^+}{\partial z^+}\Big|_{z^+=0} z^+ + \frac{1}{2}\frac{\partial^2 u^+}{(\partial z^+)^2}\Big|_{z^+=0} (z^+)^2 + ... \tag{1.30}$$

For a Newtonian fluid, however, the equation for shear stress at the wall yields:

$$\tau_w = \rho\nu \frac{\partial \overline{u}}{\partial z}\Big|_{z=0} \quad \Rightarrow \quad \tau_w = \rho\nu u_* \frac{u_*}{\nu}\frac{\partial u^+}{\partial z^+}\Big|_{z^+=0} \quad \Rightarrow \quad \frac{\partial u^+}{\partial z^+}\Big|_{z^+=0} = 1 \tag{1.31}$$

Therefore, imposing a no-slip condition at the wall, and neglecting second-order terms and higher, the velocity relationship near the wall is given by:

$$u^+ = z^+ \tag{1.32}$$

This is valid only within the viscous sublayer, $z^+ \leq 5$, where the viscosity dominates. The production term of turbulence kinetic energy is given by, $P = -\overline{u_i' u_j'}\ \partial \overline{u}/\partial z$, and therefore because this is the region of maximum velocity gradient, this becomes particularly important to the production of turbulence.

At the opposite extreme, flow is inviscid and the viscous scales no longer play a role in the velocity function. Thus, the velocity at the upper extreme of the boundary layer can be cast in relation to the non-dimensional free stream velocity, u_∞^+, as:

$$u_\infty^+ - u^+ = \Phi(\eta) \tag{1.33}$$

Little else can be said about this function at this point. However, at some point in between these two extremes it is assumed that there is a region of overlap, where the inner and outer solutions match. Solving these two equations for $\overline{u}$, and setting them equal yields:

$$u_* \Phi_1(z^+) = \overline{u}_\infty - u_* \Phi_2(\eta) \tag{1.34}$$

Taking the derivative with respect to the vertical coordinate, z, and multiplying by z yields:

$$\frac{z u_*^2}{\nu} \Phi_1'(z^+) = -\frac{z u_*}{\delta} \Phi_2'(\eta) \quad \Rightarrow \quad z^+ \Phi_1'(z^+) = -\eta \Phi_2'(\eta) \tag{1.35}$$

z^+ and η are proportional by an inner Reynolds number ($Re_* = u_* \delta / \nu$), however, Equation 1.35 holds true over a wide range of Re_*, and therefore these two coordinates are functionally independent. As a result, it can be seen that Equation 1.35 must be equal to a constant. Experimentally, this was determined to be $1/\kappa$, where κ is the von Kármán constant, 0.41. The equation, written from the inner coordinates perspective, then becomes:

$$z^+ \frac{du^+}{dz^+} = \frac{1}{\kappa} \tag{1.36}$$

Which can be integrated to yield the celebrated logarithmic law of the wall:

$$u^+ = \frac{1}{\kappa} \ln(z^+) + C^+ \tag{1.37}$$

The constant of integration will vary with the roughness of the wall, but it has been determined experimentally for the smooth wall case to be approximately 5.2. This relationship holds on the range between $30 < z^+$ and $\eta < 0.3$. Between $z^+ = 5$ and $z^+ = 30$ is what is called the "buffer zone," where the velocity profile transitions from being linear in depth to logarithmic.

Subsequently, it was desirable to find a composite form of this equation that fit experimental data, particularly in the outer "velocity defect region" where the logarithmic law does not perform very well. Coles (1956) developed a composite inner-outer form of the law with good experimental agreement, given by:

$$u^+ = \frac{1}{\kappa}\ln(z^+) + C + \frac{2\Pi}{\kappa}\omega(\eta) \tag{1.38}$$

where Π is "Coles wake constant," which is determined by the geometry and pressure gradient of the flow, and $\omega(\eta)$ is an empirical function given by:

$$\omega(\eta) = \sin^2\left(\frac{\pi\eta}{2}\right) \tag{1.39}$$

This velocity distribution is summarized in Figure 1.4.

Boundary Layer Development

The foregoing discussion is based on an assumption that the flow has "fully developed" ($\partial/\partial x \approx 0$), however at the leading edge of a boundary layer flow there will always be a region where the flow is still developing. In open channel flows, it is valuable to define the boundary layer thickness in this region as it will not extend all the way to the free surface. This has significant effects, especially when studying the near surface region, because turbulence is generated near the wall and scales with the boundary layer thickness.

Using Prandtl's 1/7th power law for the velocity distribution within the boundary layer and an empirical formula for the friction, the turbulent boundary layer thickness can be derived (Schlichting et al., 1955):

$$\frac{\delta}{x} = 0.37\mathbf{Re_x}^{-1/5}, \qquad \mathbf{Re_x} = \frac{\overline{u}_\infty x}{\nu} \tag{1.40}$$

where all values are as previously defined. This in turn can be used to determine the length required for the boundary layer thickness to reach the free surface. Alternatively, others have sought to determine the development length empirically, as in the relationship of Kirkgöz and Ardiçlioğlu (1997):

$$\frac{L}{h} = 76 - 0.0001\frac{\mathbf{Re}}{\mathbf{Fr}} \tag{1.41}$$

where L is the development length, h is the open-channel flow depth, **Re** is the bulk Reynolds number, and **Fr** is the Froude number. This was found to have good agreement with experiments over the approximate range of Reynolds numbers $10^4 < \mathbf{Re} < 10^5$.

1.3.2 Secondary Currents

Fully developed boundary layer flow is one-dimensional in nature ($\partial/\partial x = \partial/\partial y = 0$). Given the shape and aspect ratios of open RWTs, however, it is evident that there will be non-trivial gradients in the plane perpendicular to the principal direction of flow. Flows in this plane are termed "secondary currents," and represent a more recent field of study than boundary layer flows. They have been notably surveyed in recent years by Nezu (2005), and the reader is directed to that work for a more comprehensive survey of recent research.

Streamwise Vorticity Equation

Secondary currents are governed by the transport equation for streamwise vorticity, Ω_x. The vorticity vector is defined as:

$$\boldsymbol{\Omega} = (\Omega_x, \Omega_y, \Omega_z) = \left(\left[\frac{\partial \overline{w}}{\partial y} - \frac{\partial \overline{v}}{\partial z} \right], \left[\frac{\partial \overline{w}}{\partial x} - \frac{\partial \overline{u}}{\partial z} \right], \left[\frac{\partial \overline{v}}{\partial x} - \frac{\partial \overline{u}}{\partial y} \right] \right) \tag{1.42}$$

The streamwise vorticity equation can be calculated by taking the first term of the curl of the RANS momentum equation. Performing the curl operation on the left hand side of this equation yields:

$$\frac{\partial}{\partial y}\left[\frac{\partial \overline{w}}{\partial t} + \overline{u}\frac{\partial \overline{w}}{\partial x} + \overline{v}\frac{\partial \overline{w}}{\partial y} + \overline{w}\frac{\partial \overline{w}}{\partial z} \right] - \frac{\partial}{\partial z}\left[\frac{\partial \overline{v}}{\partial t} + \overline{u}\frac{\partial \overline{v}}{\partial x} + \overline{v}\frac{\partial \overline{v}}{\partial y} + \overline{w}\frac{\partial \overline{v}}{\partial z} \right] \tag{1.43}$$

This can be further decomposed using the product rule, to define some of the component parts in terms of the vorticity. Two terms (in gray) have been added to the below equation summing to zero, in order to simplify the expression:

$$\begin{aligned}
&\underbrace{\frac{\partial}{\partial t}\left[\frac{\partial \overline{w}}{\partial y} - \frac{\partial \overline{v}}{\partial z} \right]}_{\frac{\partial}{\partial t}\Omega_x} + \underbrace{\left[\frac{\partial \overline{u}}{\partial y}\frac{\partial \overline{w}}{\partial x} - \frac{\partial^2 \overline{u}}{\partial y \partial z} \right]}_{-\Omega_y \frac{\partial \overline{u}}{\partial y}} + \underbrace{\left[- \frac{\partial \overline{u}}{\partial z}\frac{\partial \overline{v}}{\partial x} + \frac{\partial^2 \overline{u}}{\partial z \partial y} \right]}_{-\Omega_z \frac{\partial \overline{u}}{\partial z}} + \\
&\quad \underbrace{\left[\overline{u}\frac{\partial^2 \overline{w}}{\partial x \partial y} - \overline{u}\frac{\partial^2 \overline{v}}{\partial x \partial z} \right]}_{\overline{u}\frac{\partial \Omega_x}{\partial x}} + \underbrace{\left[\overline{v}\frac{\partial^2 \overline{w}}{\partial y^2} - \overline{v}\frac{\partial^2 \overline{v}}{\partial y \partial z} \right]}_{\overline{v}\frac{\partial \Omega_x}{\partial y}} + \underbrace{\left[\overline{w}\frac{\partial^2 \overline{w}}{\partial y \partial z} - \overline{w}\frac{\partial^2 \overline{v}}{\partial z^2} \right]}_{\overline{w}\frac{\partial \Omega_x}{\partial z}} + \\
&\quad \underbrace{\left[\frac{\partial \overline{v}}{\partial y}\frac{\partial \overline{w}}{\partial y} - \frac{\partial \overline{v}}{\partial z}\frac{\partial \overline{v}}{\partial y} + \frac{\partial \overline{w}}{\partial y}\frac{\partial \overline{w}}{\partial z} - \frac{\partial \overline{w}}{\partial z}\frac{\partial \overline{v}}{\partial z} \right]}_{\left(\frac{\partial \overline{v}}{\partial y} + \frac{\partial \overline{w}}{\partial z}\right)\left(\frac{\partial \overline{w}}{\partial y} - \frac{\partial \overline{v}}{\partial z}\right) = -\Omega_x \frac{\partial \overline{u}}{\partial x}}
\end{aligned} \tag{1.44}$$

The final term was further simplified using the continuity equation:

$$\frac{\partial \overline{v}}{\partial y} + \frac{\partial \overline{w}}{\partial z} = -\frac{\partial \overline{u}}{\partial x} \tag{1.45}$$

The left hand side, then, finally reduces to:

$$\frac{\partial \Omega_x}{\partial t} + \overline{u}\frac{\partial \Omega_x}{\partial x} + \overline{v}\frac{\partial \Omega_x}{\partial y} + \overline{w}\frac{\partial \Omega_x}{\partial z} - \Omega_x \frac{\partial \overline{u}}{\partial x} - \Omega_y \frac{\partial \overline{u}}{\partial y} - \Omega_z \frac{\partial \overline{u}}{\partial z} \tag{1.46}$$

The right hand side of the streamwise vorticity equation can likewise be expressed as the curl of the RANS equation:

$$\begin{aligned} &\frac{\partial}{\partial y}\left[-\frac{1}{\rho}\frac{\partial \overline{p}}{\partial z} + \nu\left(\frac{\partial^2 \overline{w}}{\partial x^2} + \frac{\partial^2 \overline{w}}{\partial y^2} + \frac{\partial^2 \overline{w}}{\partial z^2}\right) - \frac{\partial \overline{w'u'}}{\partial x} - \frac{\partial \overline{w'v'}}{\partial y} - \frac{\partial \overline{w'^2}}{\partial z}\right] \\ &\quad - \frac{\partial}{\partial z}\left[-\frac{1}{\rho}\frac{\partial \overline{p}}{\partial y} + \nu\left(\frac{\partial^2 \overline{v}}{\partial x^2} + \frac{\partial^2 \overline{v}}{\partial y^2} + \frac{\partial^2 \overline{v}}{\partial z^2}\right) - \frac{\partial \overline{v'u'}}{\partial x} - \frac{\partial \overline{v'^2}}{\partial y} - \frac{\partial \overline{v'w'}}{\partial z}\right] \end{aligned} \tag{1.47}$$

Assuming flow is incompressible and barotropic in the spanwise direction, the pressure terms are lost, and the remaining right hand side of the equation can be expressed as:

$$\nu\frac{\partial^2 \Omega_x}{\partial x_j \partial x_j} + \frac{\partial^2}{\partial y \partial z}\left(\overline{v'^2} - \overline{w'^2}\right) + \left(\frac{\partial^2}{\partial y^2} - \frac{\partial^2}{\partial z^2}\right)(-\overline{v'w'}) + \frac{\partial}{\partial x}\left[\frac{\partial}{\partial y}(-\overline{u'w'}) - \frac{\partial}{\partial z}(-\overline{u'v'})\right] \tag{1.48}$$

Altogether, then, the streamwise vorticity equation becomes:

$$\begin{aligned}
\frac{D\Omega_x}{Dt} = \frac{\partial\Omega_x}{\partial t} + \underbrace{\left[\overline{u}\frac{\partial\Omega_x}{\partial x} + \overline{v}\frac{\partial\Omega_x}{\partial y} + \overline{w}\frac{\partial\Omega_x}{\partial z}\right]}_{V1} = \\
\underbrace{\nu\frac{\partial^2\Omega_x}{\partial x_j \partial x_j}}_{V2} + \underbrace{\left[\frac{\partial\overline{u}}{\partial x}\Omega_x + \frac{\partial\overline{u}}{\partial y}\Omega_y + \frac{\partial\overline{u}}{\partial z}\Omega_z\right]}_{V3} + \\
\underbrace{\frac{\partial^2}{\partial y \partial z}\left(\overline{v'^2} - \overline{w'^2}\right)}_{V4} + \underbrace{\left(\frac{\partial^2}{\partial y^2} - \frac{\partial^2}{\partial z^2}\right)(-\overline{v'w'})}_{V5} + \underbrace{\frac{\partial}{\partial x}\left[\frac{\partial}{\partial y}(-\overline{u'w'}) - \frac{\partial}{\partial z}(-\overline{u'v'})\right]}_{V6}
\end{aligned} \tag{1.49}$$

Because this equation is a linear superposition of several terms, each term can be understood in its own right. The terms can be interpreted in the following way:

V_1: Advection of Ω_x

V_2: Viscous diffusion of Ω_x

V_3: Amplification of Ω_x by vortex stretching

V_4: Turbulent stresses generating Ω_x

V_5: Turbulent stresses suppressing Ω_x

V_6: Primary turbulent stress term with minimal effects on Ω_x (Perkins, 1970; Nezu, 2005)

This equation sheds some light on the nature of these currents. Traditionally, secondary currents have been classified into one of two categories. Secondary currents of Prandtl's first kind are those currents that arise from curved section of channel, and do not require turbulence for formation. These are governed by term V_3, which is strictly a function of the mean velocities and mean vorticity components. Alternatively, secondary currents of

Prandtl's second kind can form in straight channel and are generally the results of anisotropy in the Reynolds stresses and the channel geometry (terms V_4 through V_6).

Both of these secondary currents are expected in an open RWT application, however, it is expected that there will be differing regions of dominance. In the vicinity of the bend exits it is expected that secondary currents of Prandtl's first kind will dominate from the overturning, however, just how far this vorticity will be advected before becoming negligible due to diffusion is unknown. Conversely, in the straight sections of the reactor it is expected that secondary currents of Prandtl's second kind will form, especially if enhanced with modifications along the bed. In the straight regions, assuming the V_6 term is negligible for a boundary layer flow, the streamwise vorticity equation reduces to:

$$\frac{D\Omega_x}{Dt} = \overline{v}\frac{\partial \Omega_x}{\partial y} + \overline{w}\frac{\partial \Omega_x}{\partial z} = \nu \nabla^2 \Omega_x + \frac{\partial^2}{\partial y \partial z}\left(\overline{v'^2} - \overline{w'^2}\right) + \left(\frac{\partial^2}{\partial y^2} - \frac{\partial^2}{\partial z^2}\right)\left(-\overline{v'w'}\right) \tag{1.50}$$

Nezu and Nakagawa (1984) found in their studies of straight conduit that the V_4 and V_5 terms were dominant, and of opposite signs. They conclude that the V_4 term represents a production of streamwise vorticity and the V_5 term represents a suppression of streamwise vorticity. These terms will be useful in characterizing different regions of the flow in the experimental results.

Experimental & Field Studies

Studies in secondary open-channel flows have largely been motivated by observations in nature. Kinoshita (1967) found from aerial survey of rivers in flood that lines of high-sediment concentration formed regularly at a spacing of twice the flow depth. This was further confirmed by the report of sand ribbons in the longitudinal direction after flooding subsided (Culbertson, 1967; Karcz, 1973). It was suggested by Kinoshita that these sediment "boils" were caused by counter-rotating secondary vortices with a diameter equal to the flow depth (see Figure 1.5; Nezu & Nakagawa, 1984). However, the mechanism for initiation of these currents was unknown.

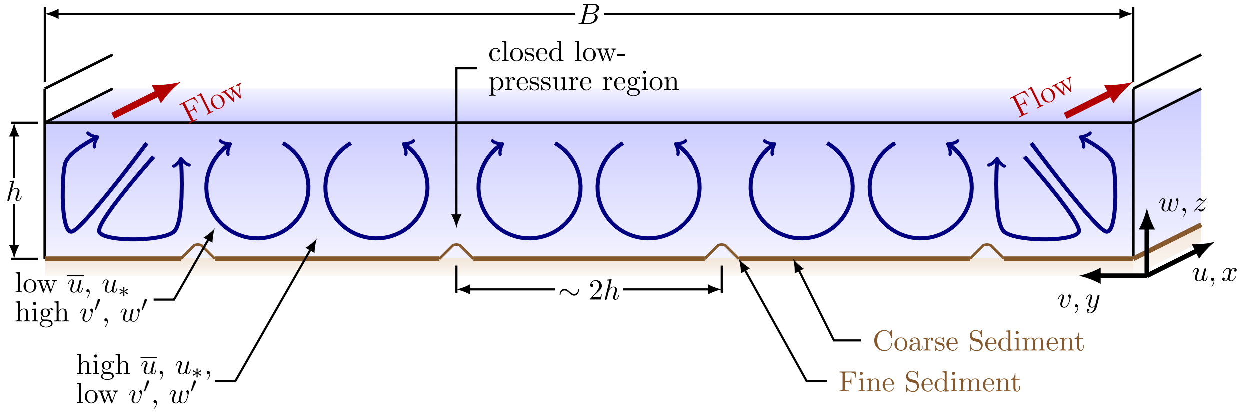

Figure 1.5: Naturally-occurring secondary currents schematic, after Nezu (2005).

Nezu and Nakagawa (1984) then performed comparative studies of open-channel flow and air-duct flow with longitudinal ridges, and found that in open channels the initiation of these currents was caused by spanwise gradients in the Reynolds stresses, and not by the free-surface or the corners as was previously hypothesized. A number of experimental and numerical studies have since been performed that further confirm this conceptual understanding of secondary flow formation (see Nezu, 2005, and references therein). Secondary currents in this study are induced, much like the experiments of Nezu & Nakagawa.

1.3.3 Open RWTs and Existing Studies

Moving on to flows specifically in open RWT reactors, the large number of experimental and numerical studies in these reactors has already been alluded to. However, the nature of these studies has varied wildly from modifying the reactor shape (Liffman et al., 2013), to inserting obstructions into the flow (e.g. Voleti, 2012), to entirely re-imagining what constitutes an RWT (B. Xu et al., 2014). Furthermore, the scale of these studies can vary from experimental studies of 2 m^2 to large numerical studies of 500 m^2, and all with different

Table 1.3: Recent, existing experimental and numerical studies on open RWT reactors (not comprehensive). Studies vary widely in modifications to conventional RWT design, in parameters of interest, and in methods of quantifying efficiency. Scales are reported based on typical reactor configuration with the width (W) being the width of one leg, and length (L) being the length of straight channel. B. Xu et al. (2014) is an exception given the deviation from standard RWT design, but similar dimensions are reported for sense of scale. For Utah State University Raceway Group, see Voleti (2012); Godfrey (2012); Lance (2012); Vaughan (2013); Blakely (2014).

Description	**Author**	**Study Type**	**Scale (W×L)**	**Efficiency Evaluation**
Inserted delta wing vortex generators	USU Raceway Group*	Numerical/ Experimental	0.4m × 5.2m	Vertical mixing index & power consumption
Varied L/W ratio and bend configurations	Hadiyanto et al. (2013)	Numerical	0.7m × (3.5m to 10.5m)	Dead zone percentage
Varied bend geometries	Liffman et al. (2013)	Numerical	5.0m × 96.0m	Power Consumption
Sump baffle, varied bend deflectors and flow depths	Mendoza et al. (2013)	Experimental	0.9m × 48.0m	Power consumption, residence times, and dispersion coefficients
Outdoors subject to seasonal variability, with CO_2 supplied, and algal growth	Sutherland et al. (2014)	Experimental	1.0m × 2.2m	Photosynthetic parameters
Model validated by experimental facility and scaled up to industrial scale	Prussi et al. (2014)	Numerical/ Experimental	1.0m × 8.0m (500 m^2 CFD)	Particle tracking statistics
Varied paddlewheel configurations	Hreiz et al. (2014)	Numerical/ Experimental	1.9m × 10.2m	Mixing time & power consumption
Novel configuration with slope and propeller pump	B. Xu et al. (2014)	Numerical/ Experimental	0.7m × 1.4m	Conceptual flow pathlines
Comparison of paddlewheel pulsating velocity to flat velocity profile	Ali et al. (2014)	Numerical	2.3m × 23.0m	Power consumption, vorticity magnitude, and dead zone volumes
Bed modifications in a straight flume	Citerone (2016)	Experimental	2.0m × 15.0m	Surface divergence & transfer velocity

measures of efficiency and performance. Table 1.3 provides a summary of some of the recent studies performed on these facilities.

Narrowing the focus, somewhat, there have been several recent studies that focus on vertical mixing and enhanced gas transfer by means of low-cost modifications to the typical reactor configuration. The Raceway Hydraulics Group of Utah State University (Voleti, 2012; Godfrey, 2012; Lance, 2012; Vaughan, 2013; Blakely, 2014) has focused on inserting arrays of delta wing vortex generators (DWVGs) to a small-scale laboratory RWT, with success in generating quantifiable vertical mixing. This does, however, come at the expense of energy input. Vaughan (2013) found an increase of 1.5 W from the paddlewheel for the addition of a single DWVG, and in reality an array of DWVGs would be required to achieve sufficient mixing. Additionally, it was observed by Godfrey (2012) that turbulence levels exceeded critical values for many algal strains, resulting in damage to the algal cells. This leaves open the necessity for less intrusive methods of generating vertical mixing.

Citerone (2016) used PVC half-pipe ridges on the bed of a shallow, straight flume to generate cellular, secondary currents after the fashion of Nezu and Nakagawa (1984). It was found that the gas transfer velocity did increase 9-15% with the addition of the PVC ridges. This modification, however, was performed in a straight, shallow flume, and needs to be understood in the context of a full-scale open RWT flow.

The current study seeks to build on the findings of Citerone (2016), by incorporating the longitudinal bed modifications and cellular, secondary current generation into a full-scale flume. Additionally, variations in the shape and size of the longitudinal ridges may provide some insight into optimal geometric conditions for generating vertical mixing.

Chapter 2

Experimental Methods and Materials

The present chapter will discuss the experimental facilities, conditions, and measurement techniques employed in examining the mixing and gas transfer in open RWTs. In brief, the aim of this experimental program is to expand the existing knowledge base of open RWT hydrodynamics by inducing cellular, secondary currents in the straight portion of the reactor and monitoring the resultant mean velocities, turbulence statistics, and mass transfer at the air-water interface.

Longitudinal bars of various shapes and sizes are placed along the bed, which has been observed in straight flumes and ducts to enhance the formation of cellular, secondary currents. Three-dimensional velocities are then monitored in the bulk flow using acoustic doppler velocimetry (ADV). Likewise, the two-dimensional velocity field at the free surface is monitored using surface particle image velocimetry (sPIV). Concurrent use of these methods to determine mean velocity fields and turbulence statistics can then be used to compare the modified bed case with the base case of an unpopulated bed. It is anticipated that the presence of secondary currents induced by the longitudinal bars would leave a measurable footprint on the mean and turbulent velocity fields.

The gas transfer at the interface is monitored under the same conditions through the surrogate, dissolved oxygen (DO). DO is depleted by chemical methods from the reactor, and allowed to re-aerate under observation. The resulting re-aeration curves and derivative transfer velocities are likewise compared between the modified and unpopulated bed cases to determine the impact of these presumed secondary currents on the gas transfer processes. Detailed descriptions of these methods follow.

2.1 Facilities

Experiments were performed at the University of Illinois, Urbana-Champaign (UIUC) Ecohydraulics and Ecomorphodynamics Laboratory (EEL) in a full-scale, open RWT reactor flume (see Figure 2.1). The flume is 11.2 m in total length, with a single-leg width of 77 cm, and a depth of 60 cm. Flume geometry followed typical raceway pond construction guidance (see Chisti, 2016), with the exception of the length-to-width (L/W) ratio. For this facility the L/W ratio was approximately 12.4, which is lower than the recommended value of 20 (note definitions of L/W in Figure 2.1). The effects of this deviation are discussed in Chapter 3.

Bends were modified with three vanes (or baffles) to minimize overturning currents and consequent energy losses, as is a common industry practice (Hadiyanto et al., 2013; Liffman et al., 2013). Additionally, these vanes induce more uniform flows in the straight portions flume. The flume is of all-acrylic construction, with the exception of lateral aluminum stabilizing bars provided at intervals outside of the flow area.

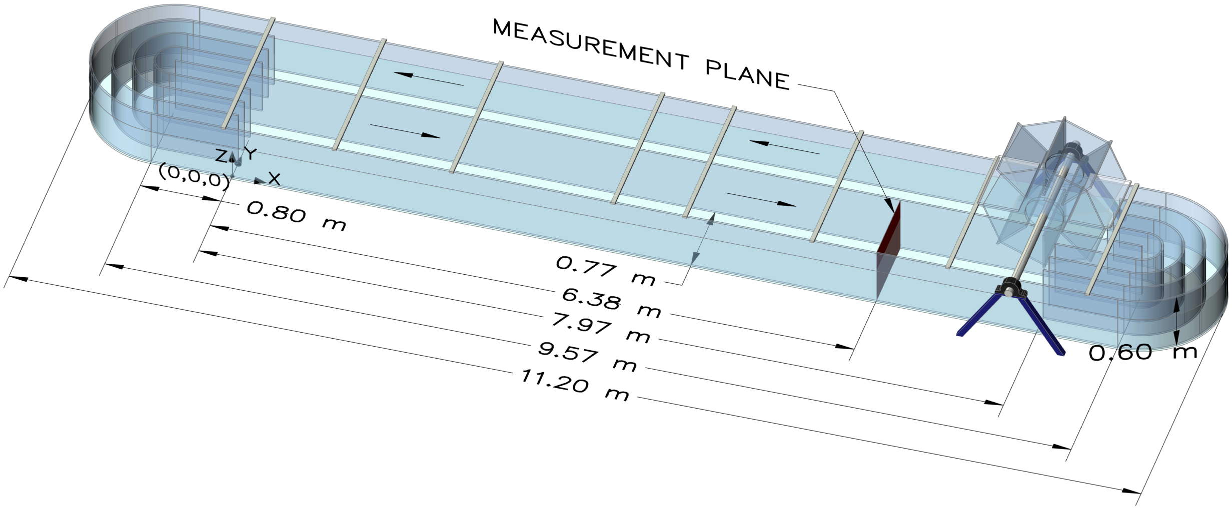

Figure 2.1: UIUC EEL Open RWT flume rendering. The L/W ratio of this facility is 12.4, and is defined as the length of straight flume (9.57 m) over the width of a single leg (0.77 m). Coordinate system is defined as shown, with the origin at the outer wall of the bend vane exit. A measurement plane is defined 6.38 m "downstream" of the first bend, where the majority of experimental measurements take place.

Flows are generated by an acrylic 8-blade paddlewheel with a NORDBLOC.1 gear drive (`https://www.nord.com/cms/us/product_catalogue/geared_motors/helical_inline_geared_motors/pdp_helical_inline_geared_motors_1542.jsp`) and Altivar 212 AC Drive (henceforth “inverter,” `http://www.schneider-electric.us/en/product-range/60162-altivar-212-drive`). The flume was operated indoors at room temperature, and no effects of wind shear were anticipated.

Figure 2.2: UIUC EEL Open RWT flume photographs. Operating conditions with ADV sampling and longitudinal bars in place pictured on the right.

Measurements were primarily performed in the leg of the flume opposite the paddlewheel (henceforth “measurement leg”), and a “measurement section” was defined 6.38 m downstream of the bend vanes (see Figure 2.1) where the primary measurements would be taken. This section was located at a sufficient distance from the “downstream” bend such that paddlewheel back effects would not influence the measurements. Conversely, the section was located sufficiently far from the “upstream” bend so that boundary layer flows in the straight portion of the flume would have maximal length over which to develop.

2.1.1 Calibration

Prior to the experimental runs, it was important to determine the nominal operating conditions of the flume. Several calibration runs were performed to determine 1) the relationships between the inverter and both the paddlewheel blades and the nominal velocities at the measurement section, 2) the longitudinal boundary layer development in the measurement leg of the flume, and 3) the evolution of the lateral velocity profile along the measurement leg of the flume.

Paddlewheel

First, the frequency of the AC Drive was related to the paddlewheel frequency and the nominal velocity at the measurement section for four flow depths. For the 38 cm depth, the AC Drive was operated at frequencies ranging from 0.0 to 16.0 Hz. Three-dimensional velocity measurements were taken for a duration of 5 minutes using a Nortek Vectrino at the lateral center of the measurement section 31 cm above the bed, and paddlewheel revolutions were counted. The corresponding time-averaged velocities and paddlewheel revolutions were then related to the inverter frequency. A similar process was then repeated for the 19 cm depth and 9.5 cm depth cases, with velocity measurements being taken as near to the free surface as possible without the sampling being interrupted by surface waves. The paddlewheel revolutions were assumed to be mechanically driven and therefore were not counted for these cases.

The velocity for the 6.4 cm depth was unable to be measured using the Vectrino, due to instrument limitations. Therefore, the velocity along the measurement leg of the flume was measured using a passive surface tracer and a stopwatch for inverter frequencies ranging from 1.0 Hz to 12.0 Hz. This was then confirmed by extrapolating trendline slopes from the inverter relationships at other depths and comparing with the surface tracer measurements. The two methods were found to agree well ($R^2 = 0.99$). It is further noted that these velocity relationships served only to determine nominal velocities for experimental runs. Actual measurements were derived from ADV or sPIV data as appropriate to the experimental conditions.

Figures 2.3 and 2.4 report the relationships of the inverter frequency to paddlewheel revolutions and nominal velocity at the measurement section, respectively.

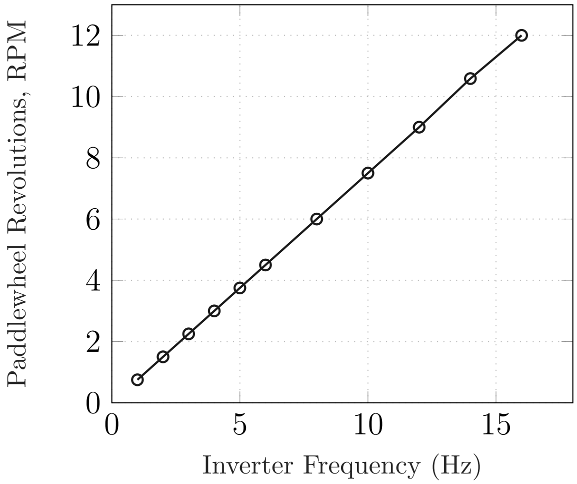

Figure 2.3: Paddlewheel revolution relationship to the inverter frequency as measured from the 38 cm depth revolution count. As the inverter relationship to the paddlewheel is purely mechanical, the two frequencies are linearly related.

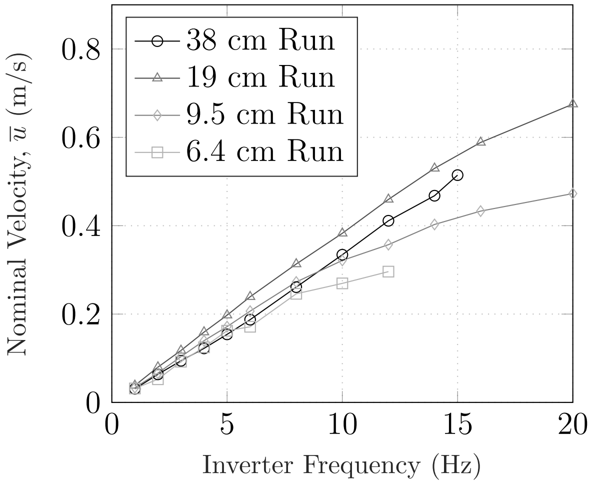

Figure 2.4: Nominal velocity calibrations for 4 flow depths of interest. The area of paddlewheel submerged and the inertial resistance to the paddlewheel motions vary with the flow depth yielding a maximum velocity relationship at the 19 cm depth. The velocity relationships to the inverter frequencies are approximately linear over the frequencies of interest: 1.0 Hz to 8.0 Hz.

It can be seen that the paddlewheel revolutions are strictly linear with the inverter frequency, as is to be expected from the mechanical connection between the two. The nominal velocity likewise follows a linear relationship to the inverter frequency, but only up to a frequency of approximately 8.0 Hz. Operating conditions for the experimental runs were all within this linear range, and therefore inverter frequencies for the experimental conditions were calculated by linear interpolation based on the nominal velocity of interest.

Vertical Profiles

Next, ADV measurements were taken of vertical profiles at intervals along the measurement leg of the flume to examine the boundary layer development in the streamwise direction. Measurements were taken for the maximum water depth case of 38 cm, and sampled for inverter frequencies of 1.0 Hz (nominal velocity, $\overline{u} = 3$ cm/s) and 6.3 Hz (nominal velocity, $\overline{u} = 20$ cm/s). Sample durations were 164 seconds, and were sufficient for convergence of the mean streamwise velocity component (see below at Section 2.3). Time-averaged streamwise velocity profiles for the two frequencies are provided in Figure 2.5 below.

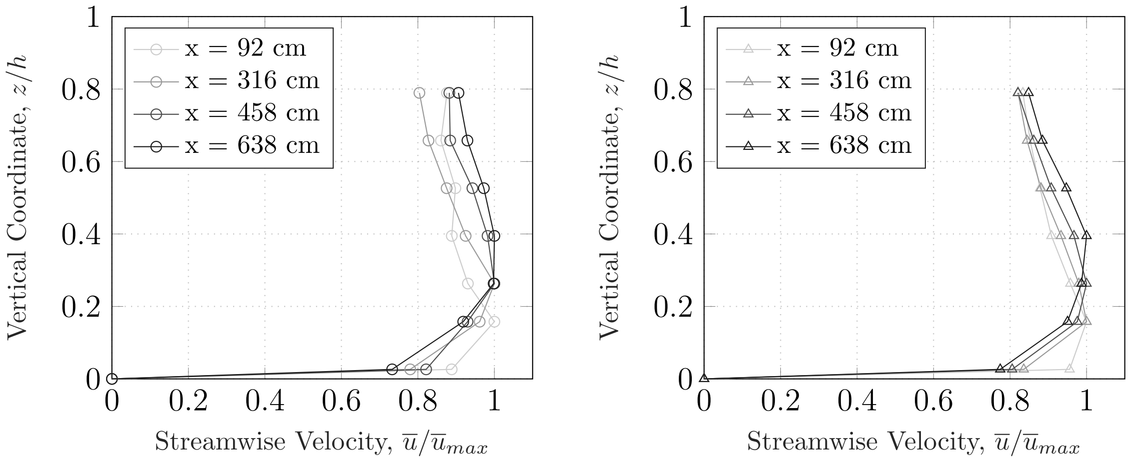

(a) $f_{inv} = 1.0$ Hz, $\overline{u} = 3$ cm s^{-1} (b) $f_{inv} = 6.3$ Hz, $\overline{u} = 20$ cm s^{-1}

Figure 2.5: Boundary layer development along measurement leg. Both sets of profiles show significant attenuation as the free surface is approached. Additionally, the profile in both cases continues to develop between the last two streamwise coordinates, indicating that the flow may not be fully developed at the measurement section.

For both frequencies the velocity distributions develop into a logarithmic profile in the overlap region, however in the velocity defect region there appears to be significant attenuation. Thus, the resulting peak velocities are found at $z/h = 0.4$. It can additionally be observed that between downstream coordinates 4.58 m and 6.38 m, the profile is still developing near the bed and it may be that the boundary layer has not yet fully developed over this range. This will be further explored in Chapter 3.

Lateral Profiles

Finally, ADV measurements were sampled laterally near the middle of the 38 cm flow depth at two downstream locations to determine if bend effects from "upstream" persist to the measurement section. Lateral profiles were sampled 38 cm downstream of the bend vanes and 638 cm downstream (measurement section). Samples were taken for a duration of 164 seconds and an inverter frequency of 6.3 Hz (nominal velocity, $\overline{u} = 20$ cm/s). Data was then time-averaged, and the lateral velocity profiles are presented in Figure 2.6.

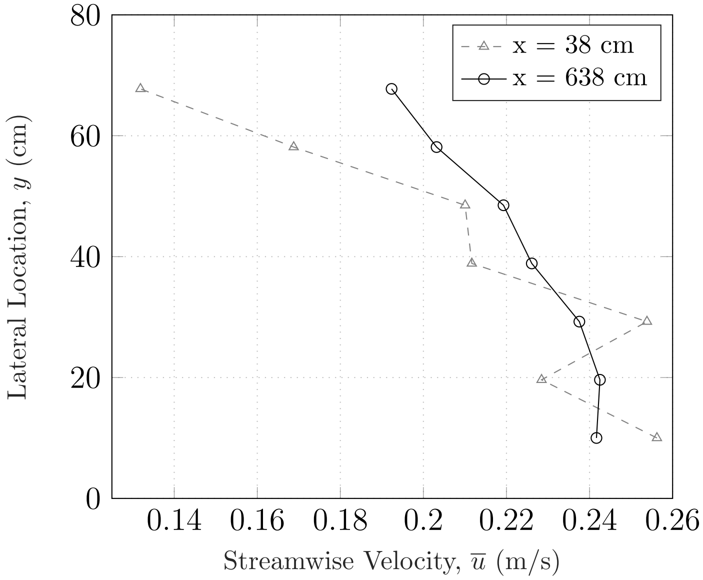

Figure 2.6: Measurement leg evolution of lateral velocity profiles. Immediately following the bend there is a large disparity between the velocity at the outer and inner wall. This is subdued, but still present, at the measurement section.

The dashed line indicates that immediately after the bend there is a significant lateral gradient in streamwise mean velocity, with faster flows favoring the outside of the bend and slower flows generated near the inner wall. Perhaps more interestingly, however, the solid line indicates that by the time the measurement section is reached this gradient persists, though to a lesser degree. The anticipated result is that a net positive lateral current will form, which will be significant for the experimental measurements. This will also be explored in Chapter 3.

2.2 Experimental Conditions

Experimental conditions were determined from the geometric constraints given by naturally-occurring cellular, secondary currents, and by iterating the variables of interest, including: bar shape, bar size, flow velocity, and flow depth.

2.2.1 Lining Materials (Longitudinal Bars)

In order to induce and attempt to enhance these secondary currents, the flume bed was modified with longitudinal bars that extended along the length of the measurement leg of the flume to within 1.0 m of the bend vanes. Five alternatives were considered:

1. An empty bed case with no modifications;
2. A small aluminum 90^o angle approximately 9 mm in height;
3. A large aluminum 90^o angle approximately 18 mm in height;
4. A small PVC half-pipe approximately 11 mm in height; and
5. A large PVC half-pipe approximately 21 mm in height.

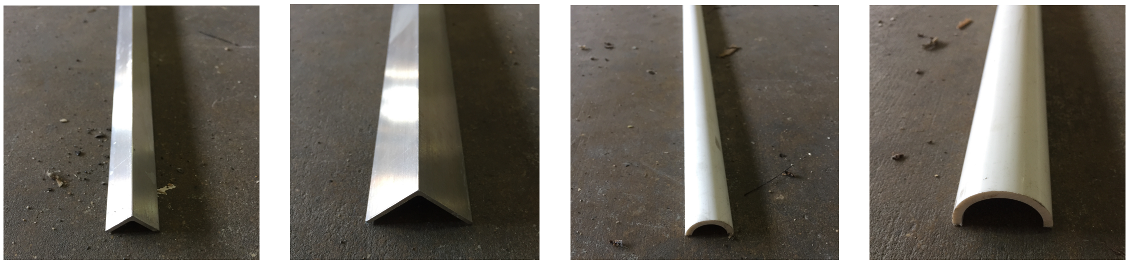

(a) Small Angle (b) Large Angle (c) Small Pipe (d) Large Pipe

Figure 2.7: Longitudinal bars for lining the bed

Bed modifications were kept in place by self-weight, and were monitored throughout the experimentation to ensure that they did not deviate from their original placement.

2.2.2 Lining Configuration/Depths

The number and spacing of the bars was determined by the desired configuration of counter-rotating cells. It has previously been observed that sets of naturally-occurring, counter-rotating cells are typically found at a spacing of two times the flow depth (Nezu & Nakagawa, 1984; Kinoshita, 1967), and therefore bed modifications were placed to enhance this phenomenon. Flow depths were consequently selected based on the number of counter-rotating cells desired and the fixed width of the flume. Four cases were desired:

1. Corner induced currents only (1 bar);
2. 1 set of counter-rotating cells (2 bars);
3. 3 sets of counter-rotating cells (4 bars); and
4. 5 sets of counter-rotating cells (6 bars).

This corresponded to four flow depth conditions: 38 cm, 19 cm, 9.5 cm, and 6.4 cm. These cases are summarized in Figure 2.8.

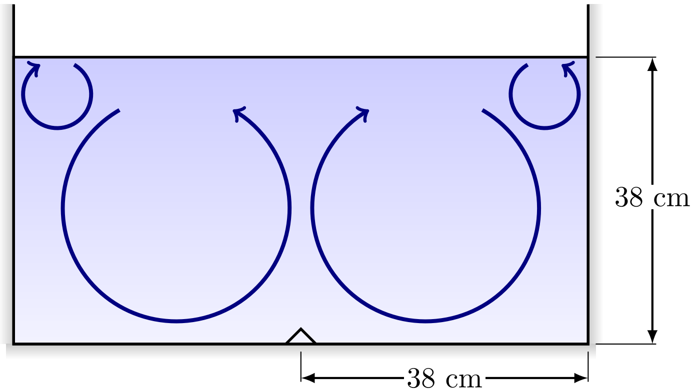

(a) 38 cm Depth

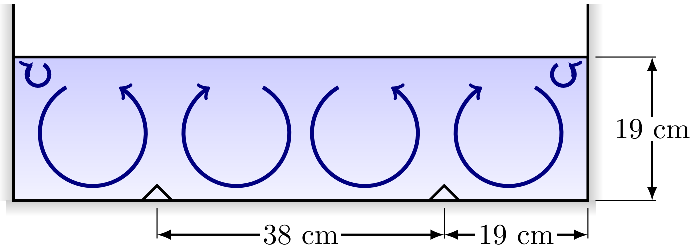

(b) 19 cm Depth

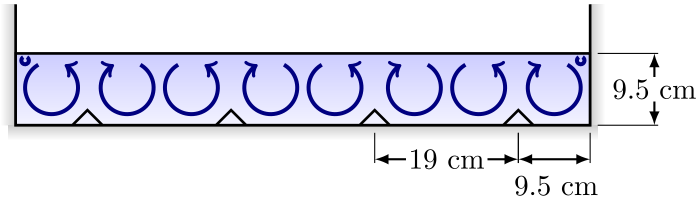

(c) 9.5 cm Depth

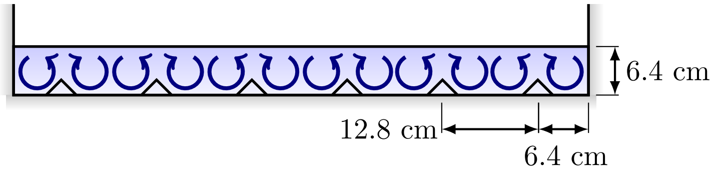

(d) 6.4 cm Depth

Figure 2.8: Lining cases and anticipated secondary currents' cells. At the walls, corner induced currents form in the upper strata of the flow in addition to those locked into place by the longitudinal bars.

2.2.3 Measurement Techniques

In order to monitor the secondary currents and their impact on the interfacial gas transfer, it was necessary to measure the mean velocities and turbulent statistics within the bulk flow, the surface flow conditions (in particular, surface divergence), and the entrained gaseous material within the flow. A testing regimen consisting of three experimental methods was employed to understand these conditions at the measurement section. Each will be discussed in detail in Sections 2.3 through 2.5, but will be briefly outlined here.

Acoustic Doppler Velocimetry (ADV) was used to sample a cross-section of the flume to determine turbulence characteristics in the bulk flow, and to visualize the secondary currents. Due to the limitations of the ADV methodology, however, surface sampling cannot be attained through this method. Surface Particle Image Velocimetry (sPIV) was, therefore, used to determine the flow conditions at the free surface. Finally, to measure the interfacial gas transfer, a technique was used in which the dissolved oxygen (DO) was depleted from the water, and measurements were taken of the subsequent re-aeration under different conditions.

2.2.4 Summary of Experimental Cases

A summary of the resulting experimental cases is provided in Table 2.1. All lining conditions were included in the 19.0 cm depth cases. It was subsequently determined that the “Large Angle” produced the largest signature of secondary currents, and this was used to represent the lined bed case for other flow depths. For ADV measurements, only the nominal velocity of 20.0 $cm\ s^{-1}$ was used as this represented a typical operating condition (Kumar et al., 2015). This was then varied from 5 $cm\ s^{-1}$ to 40 $cm\ s^{-1}$ in the sPIV and DO measurements to subsequently consider any effects of the velocity magnitude.

Table 2.1: List of experimental runs. Bar spacing is strictly defined as the distance between two bars center-to-center. Distances from the outside bars to the flume wall are precisely half of the bar spacing. In the case of 38.0 cm depth, the singular bar is located at the center of the flume.

Case I.D.	**Depth (cm)**	**Lining**	**Number of Bars**	**Bar Spacing (cm)**	**Nominal Velocity ($\mathbf{cm\ s^{-1}}$)**	**Method**
A1	9.5	Empty	-	-	20.0	ADV
A2	9.5	Large Angle	4	19.25	20.0	ADV
A3	19.0	Empty	-	-	20.0	ADV
A4	19.0	Small Angle	2	38.5	20.0	ADV
A5	19.0	Large Angle	2	38.5	20.0	ADV
A6	19.0	Small Pipe	2	38.5	20.0	ADV
A7	19.0	Large Pipe	2	38.5	20.0	ADV
A8	38.0	Empty	-	-	20.0	ADV
A9	38.0	Large Angle	1	-	20.0	ADV
S1	6.4	Empty	-	-	20.0	sPIV
S2	6.4	Large Angle	6	12.83	20.0	sPIV
S3	9.5	Empty	-	-	20.0	sPIV
S4	9.5	Large Angle	4	19.25	20.0	sPIV
S5	19.0	Empty	-	-	20.0	sPIV
S6	19.0	Empty	-	-	10.0	sPIV
S7	19.0	Empty	-	-	5.0	sPIV
S8	19.0	Small Angle	2	38.5	20.0	sPIV
S9	19.0	Large Angle	2	38.5	20.0	sPIV
S10	19.0	Large Angle	2	38.5	10.0	sPIV
S11	19.0	Large Angle	2	38.5	5.0	sPIV
S12	19.0	Small Pipe	2	38.5	20.0	sPIV
S13	19.0	Large Pipe	2	38.5	20.0	sPIV
S14	38.0	Empty	-	-	20.0	sPIV
S15	38.0	Large Angle	1	-	20.0	sPIV
D1	9.5	Empty	-	-	10.0	DO
D2	9.5	Large Angle	4	19.25	10.0	DO
D3	9.5	Empty	-	-	20.0	DO
D4	9.5	Large Angle	4	19.25	20.0	DO
D5	9.5	Empty	-	-	40.0	DO
D6	9.5	Large Angle	4	19.25	40.0	DO
D7	19.0	Empty	-	-	10.0	DO
D8	19.0	Large Angle	2	38.5	10.0	DO
D9	19.0	Empty	-	-	20.0	DO
D10	19.0	Small Angle	2	38.5	20.0	DO
D11	19.0	Large Angle	2	38.5	20.0	DO
D12	19.0	Small Pipe	2	38.5	20.0	DO

Table 2.1 Continued: List of experimental runs.

Case I.D.	**Depth (cm)**	**Lining**	**Number of Bars**	**Bar Spacing (cm)**	**Nominal Velocity ($\mathbf{cm\ s^{-1}}$)**	**Method**
D13	19.0	Large Pipe	2	38.5	20.0	DO
D14	19.0	Empty	-	-	40.0	DO
D15	19.0	Large Angle	2	38.5	40.0	DO
D16	38.0	Empty	-	-	10.0	DO
D17	38.0	Large Angle	1	-	10.0	DO
D18	38.0	Empty	-	-	20.0	DO
D19	38.0	Large Angle	1	-	20.0	DO

In addition to the above experimental regimen, bend measurements were performed to better understand the dominant processes at work in the flume as a whole. ADV measurements were performed along nine transects about the "upstream" bend (see Figure 2.9), for the 19 cm flow depth and 20 $cm\ s^{-1}$ nominal velocity. Measurement listings are tabulated in Table 2.2.

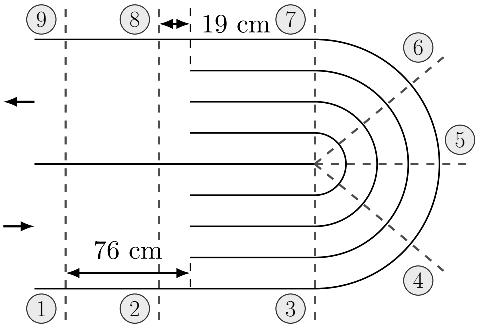

Figure 2.9: Bend measurement transects. Two transects were selected upstream and downstream of the bend vanes, a distance equal to the channel width and a distance equal to the flow depth. The channel bend itself was divided into five equally spaced transects, each 45^o apart.

Table 2.2: List of bend measurements

Case I.D.	**Depth (cm)**	**Transect**	**Nominal Velocity ($\mathbf{cm\ s^{-1}}$)**	**Method**
B1	19.0	1	20.0	ADV
B2	19.0	2	20.0	ADV
B3	19.0	3	20.0	ADV
B4	19.0	4	20.0	ADV
B5	19.0	5	20.0	ADV
B6	19.0	6	20.0	ADV
B7	19.0	7	20.0	ADV
B8	19.0	8	20.0	ADV
B9	19.0	9	20.0	ADV

2.3 Acoustic Doppler Velocimetry

Acoustic Doppler Velocimetry is a technology that utilizes a pair of acoustic pulses of known time lag and the phase shift from the Doppler effect to measure the three-dimensional velocities in the flow (e.g., Rusello, 2009). The instrument's probe consists of an acoustic pulse emitter and 3-4 receivers which collect signals scattered from particles within the measurement volume, 5 cm below the probe. In turn, signal processing techniques are employed to calculate velocity components in a Cartesian coordinate system.

In the current application, a single Nortek Vectrino (`http://www.nortek-as.com/en/products/velocimeters/vectrino`) was mounted on a Velmex BiSlide (`http://www.velmex.com/Products/BiSlide/index.html`) biaxial stepper system above the measurement section of the flume (see Figure 2.1 for measurement section, Figure 2.10 for measurement apparatus). The Vectrino and BiSlide system were then operated from a computer where both ADV data and the flume itself could be visually monitored.

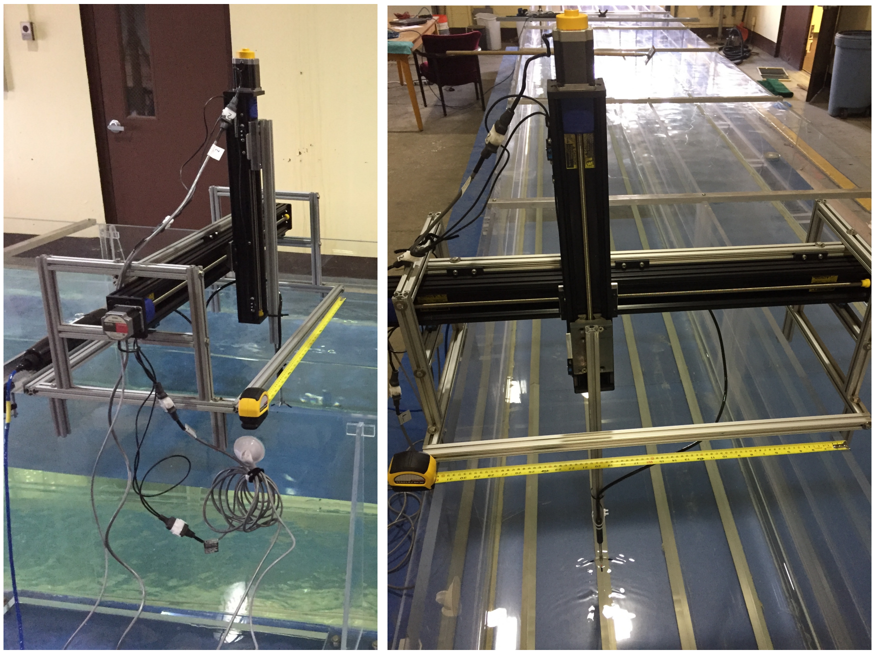

Figure 2.10: ADV measurement apparatus

In order to attain suitable signal diagnostics (signal-to-noise ratio, SNR, and correlation), the flow was seeded with neutrally buoyant, ∼10 μm, hollow glass spheres for scattering of the acoustic signal. Seeding was added until SNR was in the acceptable range (> 15 dB), which was in quantities insufficient to significantly impact the flow.

2.3.1 Sampling Regimen

The sampling locations were adapted for each experimental run to the anticipated secondary current cells such that higher resolution was afforded to anticipated upflows and downflows and lower resolution to the intervening regions. For each run, measurements were performed for three transects: a near-bed transect, a transect immediately above the bed modifications (or corresponding location for the empty cases), and a near surface transect. Figure 2.11 presents the sampling locations performed at the measurement section, and exact sampling locations are provided in Appendix A. It can be noted that there was no sampling regimen for the 6.4 cm depth case. This is due to the fact that the probe head must be submerged, and can only measure 5 cm below the pulse emitters, yielding only minimal and relatively insignificant volume that was able to be sampled.

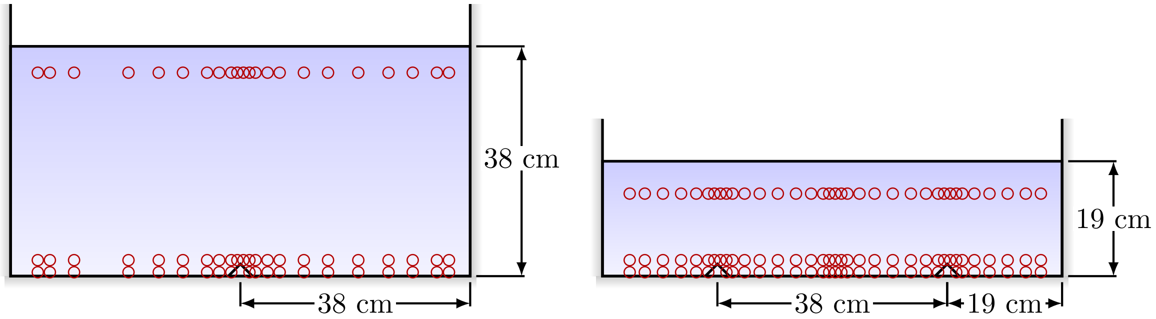

(a) 38 cm Depth

(b) 19 cm Depth

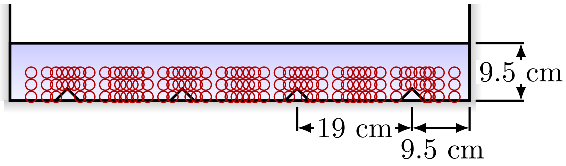

(c) 9.5 cm Depth

Figure 2.11: Measurement section ADV sampling locations

For the bend measurements, a 4×4 grid of sampling locations was used such that the lateral centers between the bend vanes and walls were sampled at 4 equidistant elevations ($z = \{1, 5, 9, 13\}\ cm$). At transect 8 (I.D. B8) greater resolution was desirable to elucidate what the flow structure was leaving the bend, and therefore additional lateral and vertical locations were sampled. These sampling locations are shown in Figure 2.12, and exact sampling locations are provided in Appendix A.

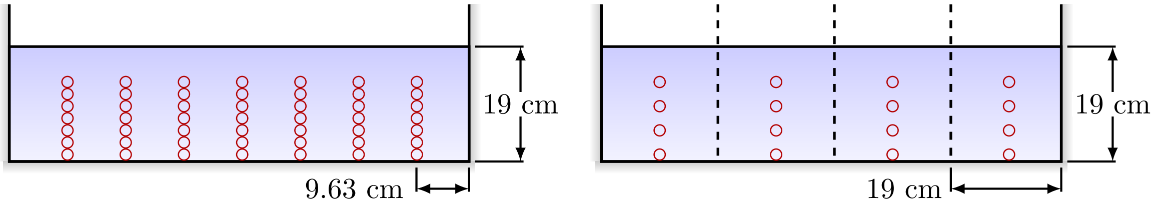

(a) Transect 8

(b) All Other Transects

Figure 2.12: Bend transects ADV sampling locations

Where possible, all of the above sampling locations were maintained, however "weak spots," or areas of echo off of the boundaries, resulted in non-physical measurements at some locations. In such cases, the locations were either perturbed slightly until physical readings could be attained, or where this was not achievable the location was skipped altogether.

2.3.2 Sampling Parameters

At each location, 16,384 samples (2^{14}) were taken at a sampling frequency of 100 Hz, or the equivalent of approximately 164 seconds. Five minute runs were collected during the flume calibration, and it was found that for typical operating inverter frequencies between 4.0 Hz and 8.0 Hz the 164 second sample record was sufficient for both the mean velocity and root-mean-square velocity fluctuations to converge to within 5% of the long run values (see Figure 2.13).

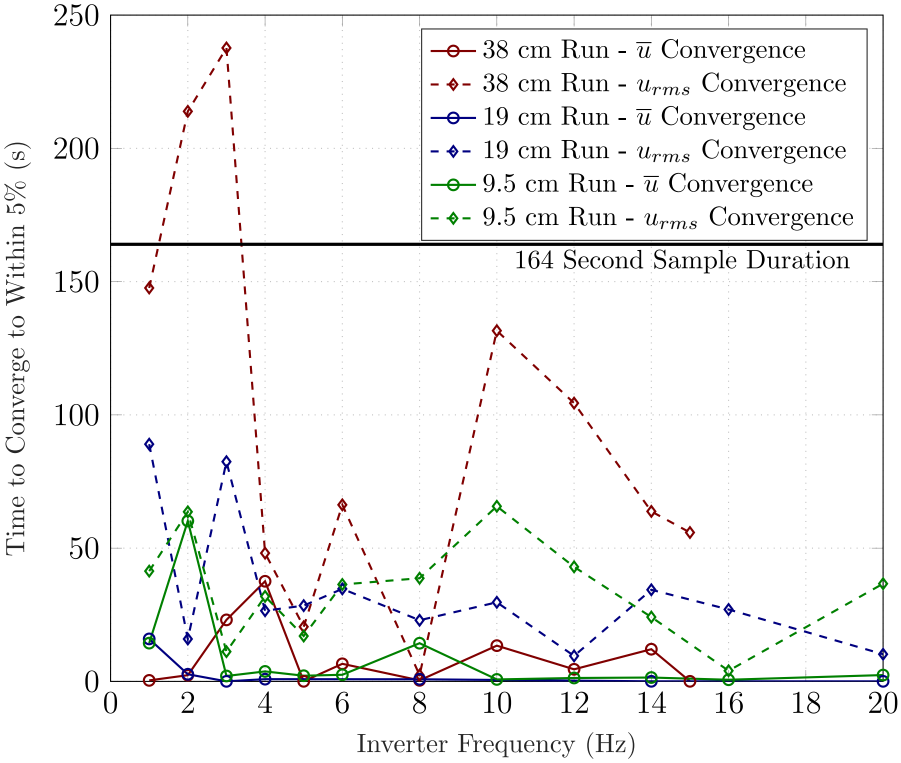

Figure 2.13: Mean velocity and turbulence statistics convergence. In the frequencies of interest, 4.0 - 8.0 Hz, both the mean velocity and the turbulence statistics converge to within 5% of the long run values in well under the 164 second threshold.

The sampling frequency of 100 Hz was selected under the assumption that frequencies higher than 50 Hz, the Nyquist frequency for this sampling rate, were well outside the range of interest for secondary currents and would likely be found in the inertial subrange region of the velocity spectra. Additional ADV settings are summarized in Table 2.3.

Table 2.3: ADV sampling settings

Sampling Rate	100 Hz
Nominal Velocity Range	Varied By Location
Transmit Length	1.8 mm
Sampling Volume	7.0 mm
Power Level	High
Coordinate System	XYZ

2.3.3 Data Filtering & Processing

One disadvantage of ADV measurements is that Doppler noise, phase wrapping, and boundary reflections can occasionally pollute the turbulent data set (Rusello, 2009; Goring & Nikora, 2002). As such, following acquisition, data was filtered and processed to ensure errant readings would not impact time-averaged values or turbulence parameters.

The Vectrino software outputs two primary means of evaluating the quality of data being collected. The first is the SNR, which, as mentioned previously, was maintained at or above approximately 15 dB with sufficient seeding of the flow. The second is the correlation, which is a measure of similarity of the pulse emitted to the pulse received. Generally, the manufacturer recommends 70% correlation or higher (Rusello, 2009), with lower values being discarded. While the 70% threshold is somewhat arbitrary, it was determined from the time series data that it provided a good distinction between results that appeared physical and those that clearly were not, and therefore was adopted. Below this level points were replaced by cubic interpolation.

Even with the correlation and SNR diagnostics, there are some data samples that meet these criteria that are clearly non-physical. For these, a phase-space thresholding method

(Goring & Nikora, 2002) was employed to remove non-physical spikes in the data, and they were replaced using a cubic interpolation of the surrounding data points.

Once the data had been filtered, a final correction was applied to one case (Case I.D. A3; h = 19 cm, Empty) where the probe had twisted slightly out of alignment with the experimental coordinate system. Streamwise and lateral time-averaged velocity components were adjusted for an angle of rotation, θ, that ranged from -45^o to 45^o. The value of θ that produced the maximum time-averaged streamwise component in the overwhelming majority of the sampling locations was selected as the representative twist of the probe. Given that the streamwise component of velocity was significantly stronger than the lateral component, it was assumed that the maximal value would be oriented along the streamwise axis. Correction of the lateral and streamwise components was applied using this twist angle, θ, and the clockwise rotation vector such that:

$$u_{corr} = u\cos\theta + v\sin\theta \tag{2.1a}$$

$$v_{corr} = -u\sin\theta + v\cos\theta \tag{2.1b}$$

2.3.4 Data Analysis

Finally, the filtered, corrected data was then decomposed into mean and fluctuating components. The fluid flow was assumed to be an ergodic process, and therefore ensemble averaging of the samples was used. Turbulent properties including turbulence kinetic energy, Reynolds stresses, autocorrelation coefficients, and turbulence intensities were calculated in addition to mean velocity fields. These were then compared to visualize the presence and strength of secondary currents at the measurement section. It was anticipated that traces of the intensified secondary currents would appear in comparisons of the empty case to the modified bed for both the mean velocity fields and the turbulence characteristics.

Additionally, the data was considered in spectral space by calculating the power spectral density function, $S(\omega)$:

$$S(\omega) = \frac{1}{T}\int_0^T \int_0^T \langle u'^*(t)u'(t+\tau)\rangle e^{-i\omega\tau} dt d\tau \tag{2.2}$$

where sampling is taken over a finite interval T, u' denotes the fluctuating component of the velocity signal, and ω denotes the frequency space coordinate. The time series of velocity was subdivided into 8 groups, Fast Fourier transforms (FFT) were used to calculate the spectra, and they were ensemble averaged to minimize uncertainty. This is summarized in the following equation where $\hat{\Phi}(u')$ is the FFT of the velocity signal, angle brackets denote an ensemble average of the 8 groups, and the star indicates a complex conjugate:

$$S(\omega) = \left\langle \frac{1}{f_s N}\hat{\Phi}(u')\hat{\Phi}(u'^*) \right\rangle \tag{2.3}$$

Here f_s denotes the sampling frequency, and N denotes the number of samples. It was anticipated that the power spectra would follow a typical -5/3 power law within the inertial subrange. Additionally, a low frequency spike roughly corresponding to the paddlewheel revolutions was expected, and an additional spike corresponding to the large eddies induced by the bed modifications.

2.4 Surface Particle Image Velocimetry

Surface particle image velocimetry utilizes a camera with a fixed frame rate to collect a series of images capturing the motion of buoyant tracer particles on the surface of the flow. Cross-correlation statistical techniques are then implemented to trace the particles through a series of interrogation areas (i.e. "subwindows"), and velocity vectors are derived from image pairs given the known frame rate of the camera (e.g., Turney & Banerjee, 2013;

Sanjou et al., 2016). This can be converted into meaningful units given the relationship between pixels and surface distances derived from calibration images.

2.4.1 Image Capture

A JAI GO-5000-USB 5-Megapixel CCD Camera (`http://www.jai.com/en/products/go-5000-usb`) with Navitar 25-mm focal length, 1” Format, 6-Megapixel lens (`http://www.mengelengineering.dk/PDF/KW/LM25SC.pdf`) was attached to the measurement frame used in the ADV analysis and centered over the measurement section of the flume. The aperture and focal length were manually adjusted such that the free surface of the flow was in focus and well-illuminated. A 7,000-lumen, twin-head, LED floodlight was situated next to the flume to provide as much illumination to the free surface as possible (see Figure 2.14). The flow was then seeded with Pliolite particles (SG = 1.03) to sufficient density that particles were uniformly distributed in preliminary image captures. The cases specified in Table 2.1 were run, and 10-bit grayscale images were captured for a duration of 2 minutes. A sampling frequency (frame rate) of 30 Hz was used as dictated by the camera and computer storage capabilities. This resulted in a total of 3600 images per run. Camera exposure time was 5 ms in order to provide adequate illumination for the images, while allowing minimal movement and distortion within the individual image captures.

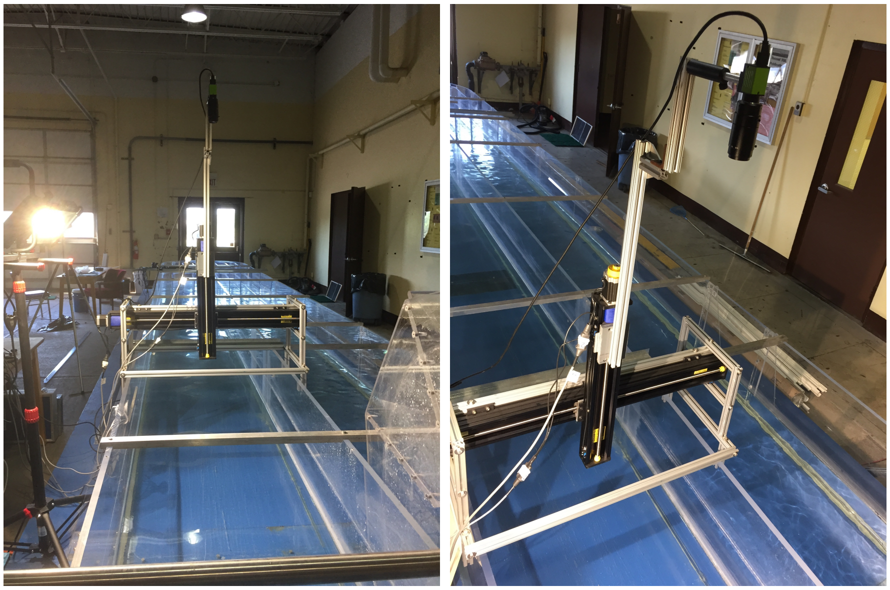

Figure 2.14: sPIV measurement apparatus. LED floodlights are pictured on the left, just outside of the flume. The camera was centered over the measurement section of the flume, and aligned such that image coordinates would be consistent with experimental coordinates.

2.4.2 Image Processing

Images were then processed in PIVlab (Thielicke & Stamhuis, 2014a, 2014b; Thielicke, 2014) in three steps. First, images were preprocessed such that surface points would be easily identifiable to the program's algorithms. A high-pass filter was applied to the images to remove low frequency background light and clumps of particles larger than 10-20 pixels. Likewise, a Wiener Method adaptive filter was applied to smooth out areas of low local variance, which for these images eliminated any subsurface particles that were out of focus.

Next, preprocessed images were fed to the cross-correlation algorithm using FFT to produce vector fields for each of the image pairs. Interrogation windows were sized based on the nominal streamwise velocity such that maximum particle displacement in each image pair was less than half of the interrogation window size. The windows were then subject to 50% overlap, which yielded the vector resolutions summarized in Table 2.4.

Table 2.4: sPIV vector resolutions by nominal velocity

Velocity, ms^{-1}	Resolution, cm × cm
0.20	0.72×0.72
0.10	0.36×0.36
0.05	0.18×0.18

These vector fields then underwent validation for which velocities outside the physical range were removed and replaced with interpolated values. Figure 2.15 demonstrates characteristic fields at each stage of this process.

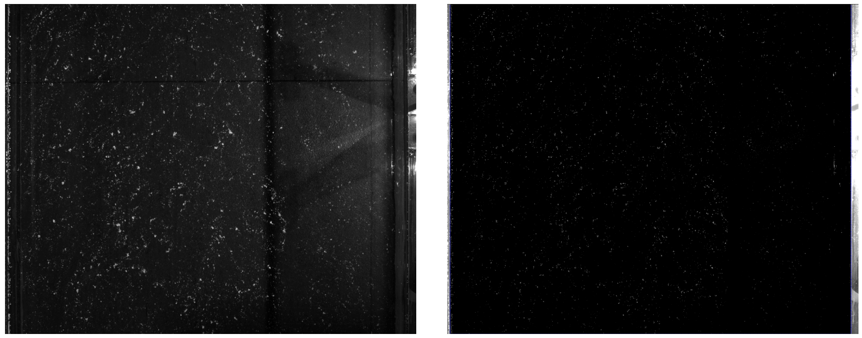

(a) Raw Image (b) Preprocessed Image

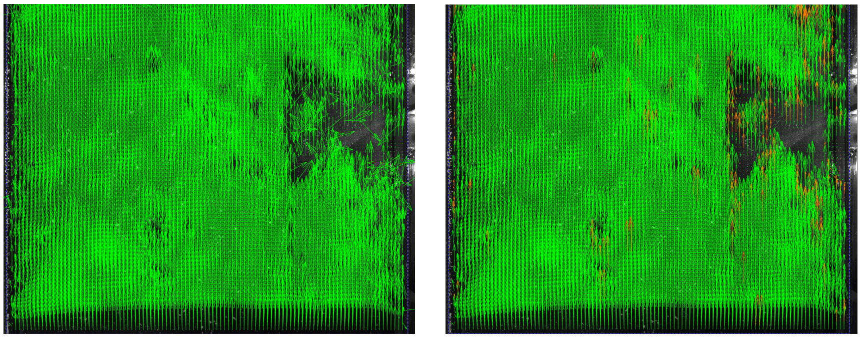

(c) Vector Field (d) Validated Vectors

Figure 2.15: sPIV image processing. Raw photographs (a) are preprocessed for PIVlab algorithms to find tracers (b). Image pairs are then fed to cross-correlation algorithms to create a vector field (c), which then undergoes data validation (d).

As seen in Figure 2.15, the images contained areas of either low local seeding density or low contrast with background light causing gaps in the vector fields. These gaps, or any errant data associated with them, were removed from the record, and subsequent ensemble averaging at these locations was performed with the available data. Any effects this had on the results will be discussed in Chapter 3.

Finally, calibration images of a ruler at the free surface were acquired for each flow depth. These calibration images were then used in Matlab to determine the number of pixels per centimeter such that velocity vectors could be converted into a meaningful unit system.

2.4.3 Data Analysis

Vector fields were subsequently decomposed into mean and fluctuating velocity components, and fields of mean velocity and turbulence parameters were calculated, as with the ADV data. Local power spectral density functions were likewise calculated to the Nyquist frequency of 15 Hz. Velocity direction and magnitude were then compared with the upper strata of the ADV data for validation, and were found to have good agreement. Finally, surface divergence fields were calculated for the fluctuating velocity components.

All of these parameters were then queried in relation to the modified bed case and the empty case, to determine if the bars were having an influence at the free surface. It was anticipated that the secondary currents enhanced by the presence of the bed modifications would reach the free surface causing a diverging velocity field along the bars, signaling local upwelling, and a converging velocity field in between, signaling local downwelling.

2.5 Dissolved Oxygen Measurements

Gas transfer velocity measurements were made by first depleting the water in the RWT of dissolved oxygen (DO) by chemical processes, and then a DO meter was used to monitor the recovery rate under various flow and bed modification conditions.

The *American Society of Civil Engineers* (ASCE) provides guidelines for this method in published work by Stenstrom (2007). First a catalyst, Cobalt Chloride Hexahydrate ($CoCl_2 \cdot 6\,H_2O$), was added to the flow in the amount of 0.2 mg/L, twice the amount required per ASCE guidelines. Sodium Sulfite (Na_2SO_3) was then introduced as an oxygen scavenging agent which reacts with dissolved oxygen according to the following reaction:

$$2\,Na_2SO_3 + O_2 \longrightarrow 2\,Na_2SO_4$$

The stoichiometric amount of Na_2SO_3 required was 7.88 mg/L per concentration of 1.0 mg/L of DO. A preliminary measurement of DO, temperature, and pressure was made using a YSI optical dissolved oxygen (ODO) meter, and adjusted to the saturated condition using the equations of Benson and Krause (1980, 1984). This was multiplied by the 7.88 mg/L and increased by a factor of 30% to determine the actual required amount of Sodium Sulfite. Table 2.5 summarizes these calculations.

Table 2.5: Required deoxygenation chemical quantities

Flow Depth (cm)	Volume (m^3)	$[DO]_{sat}$ (mg/L)	DO_{total} (g)	Na_2SO_{3req} (g)	130% Na_2SO_3 (g)
9.5	1.65	8.25	13.61	107.28	139.46
19.0	3.30	8.33	27.49	216.64	281.63
38.0	6.60	8.42	55.57	437.91	569.28
Flow Depth (cm)	Volume (m^3)	[Co] (mg/L)	Co (g)	$CoCl_2 \cdot 6\,H_2O$ (g)	200% $CoCl_2 \cdot 6\,H_2O$ (g)
9.5	1.65	0.1	0.17	0.67	1.33
19.0	3.30	0.1	0.33	1.33	2.67
38.0	6.60	0.1	0.66	2.67	5.33

Once the oxygen levels were depleted in the RWT, the dissolved oxygen levels were recorded using a YSI ODO Meter (`https://www.ysi.com/proODO`, see Figure 2.16) at mid-depth of the measurement section. The ODO meter emits a blue light at a certain wavelength that causes dye in the sensing element to luminesce. Presence of DO in the sample diffuses through the dye impacting the luminescence of the sensing element, which can then be compared against calibrated values to determine the amount of DO in the sample. The meter was calibrated beforehand using a one-point calibration in water-saturated air, and mounted on the apparatus used for ADV and sPIV measurements. Measurements of DO, barometric pressure, and water temperature were taken at a 30 second sampling frequency until the dissolved oxygen time series approached a steady-state value.

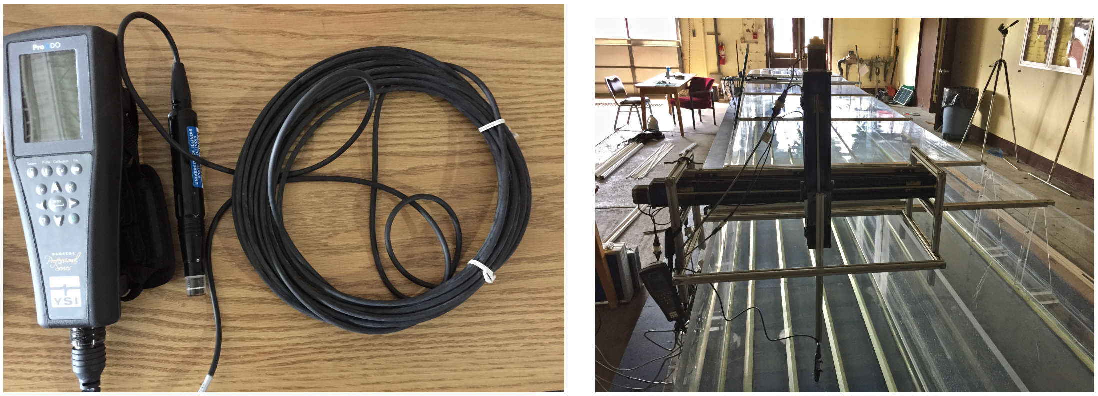

(a) YSI ODO Meter

(b) DO Measurement Apparatus

Figure 2.16: Optical DO meter and experimental apparatus

2.5.1 Data Analysis

The transfer velocity was determined from the time series of dissolved oxygen concentration. It was observed in Chapter 1 that the flux across the air-water interface can be expressed in terms of a transfer velocity according to Equation 1.2. Likewise, the flux can be expressed from an Eulerian perspective as:

$$\mathbf{F_{w,z}} = \frac{V}{A}\frac{\partial C}{\partial t} \tag{2.4}$$

where A represents the interfacial area over which the flux is passing, V represents the control volume, and C represents the concentration in the control volume. Combining these two definitions, yields the first order differential equation:

$$\frac{\partial C}{\partial t} + \frac{A}{V}\overline{k}C_w - \frac{A}{V}\overline{k}\alpha C_a = 0 \tag{2.5}$$

Because αC_a is equal to the saturation concentration in the water by Henry's Law, then this can be solved yielding the following:

$$C_{DO} = C_{DO,sat}\Big[1 - \exp\Big\{-\frac{A}{V}\overline{k}t\Big\}\Big] \tag{2.6}$$

where C_{DO} is the concentration of dissolved oxygen, $C_{DO,sat}$ is the saturation concentration, and $\overline{k}$ is the average transfer velocity. This solution was fit to the experimental data using a least-squares regression, yielding results for the saturation concentration and the average transfer velocity, for a given interfacial area ($\sim$16.6 m^2) and volume. Time series data was subsequently normalized to the saturation concentration, and expressed as a percent saturation.

Transfer velocities and re-aeration curves were then compared between the empty bed cases and the modified bed cases to determine if the enhanced secondary currents improved the transfer velocity at the free surface. It was expected that the cases with the longitudinal bars would see higher transfer velocities yielding steeper re-aeration curves.

Chapter 3

Results and Discussion: Secondary Currents

The aim of this study, with respect to secondary currents, was to answer two primary questions: (1) can cellular, secondary currents be replicated in a full-scale RWT reactor by introduction of longitudinal ridges along the bed, and (2) what are the dominant physical mechanisms at work in the reactor. This chapter explores the results of the ADV and sPIV measurements described in Chapter 2, in answer to these two questions.

3.1 ADV Results

ADV measurements can be parsed out into three distinct methods of evaluation: mean velocities, turbulence statistics, and power spectral density functions (power spectra). These three approaches are presented and discussed hereafter.

3.1.1 Mean Velocities

Two preliminary observations may be made that influenced the analysis of the mean velocity fields. First, as seen in the lateral velocity "calibration" of Chapter 2, a significant bias in streamwise velocity was found toward the outer wall. Higher velocities favored the outer wall with a negative gradient in streamwise velocity in the positive y-direction ($\partial\overline{u}/\partial y < 0$), consistent with other studies that found a considerable recirculation zone at the inside of the 180^o bends, resulting in non-uniform distributions of streamwise velocity in and after the bends.

Secondly, this gave way to a mean lateral velocity component in the positive y-direction (toward the inner wall) that was evident in all of the sample locations at the measurement section. It is presumed that this is caused by the low pressures at and behind the inside of the bend that draws fluid from the high velocity region creating a positive lateral current. Consequently, cellular lateral currents induced by the Reynolds stress mechanism (secondary flows of Prandtl's second kind, see Chapter 1.3) were overwhelmed by these currents and difficult to visualize.

In response, lateral mean velocities from the ADV measurements were modified by subtracting out a spatial- and time-average of the lateral velocity component such that the lateral velocities as presented would be a delta about the spatial mean. This allows for visualization of the lateral currents' spatial distribution. The resulting mean velocity distributions are given below for the 9.5 *cm* depth case (Figure 3.1), the 19 *cm* depth case (Figure 3.2), and the 38 *cm* depth case (Figure 3.3).

It will be noticed that something resembling the structure of cellular, secondary currents is easily recognizable in the mean velocity plots with the longitudinal bed modifications, particularly for the case of the 9.5 *cm* depth. Downflows are clearly visible between the longitudinal bars with local, mean upflow at the bars. Likewise, in the lower two swaths of measurements, there tends to be a divide between bars splitting positive and negative lateral velocities. These are characteristic of cellular, secondary currents, however a few nuances may be further derived from these plots.

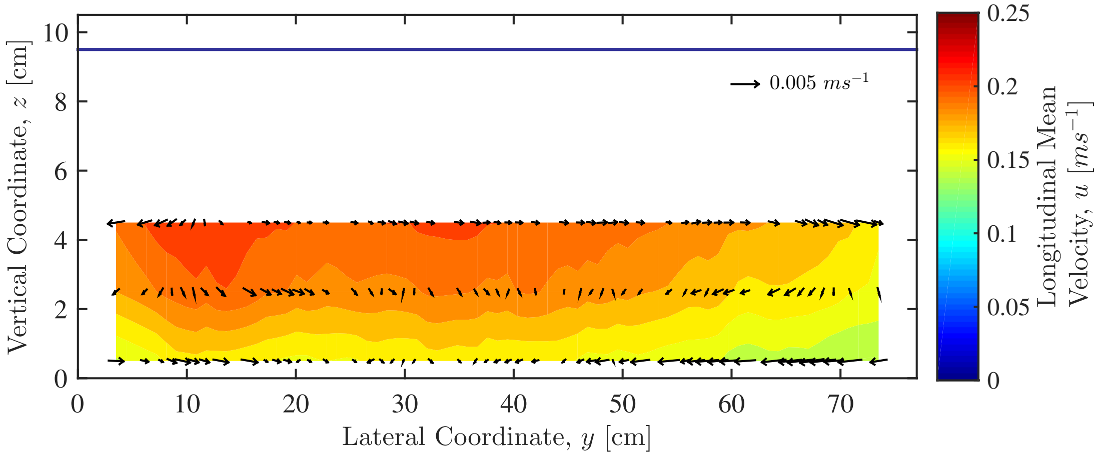

(a) Empty Bed

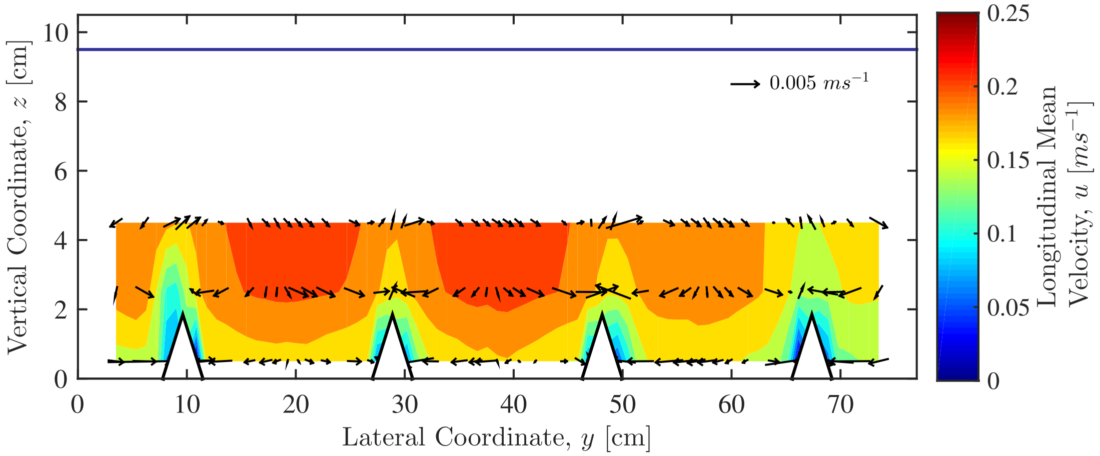

(b) Large Angle

Figure 3.1: Mean velocities from ADV data at 9.5 *cm* depth. Colormap indicates the streamwise (longitudinal) velocity, and arrows indicate secondary flows. Arrows additionally indicate measurement locations. Colormap is interpolated between these points.

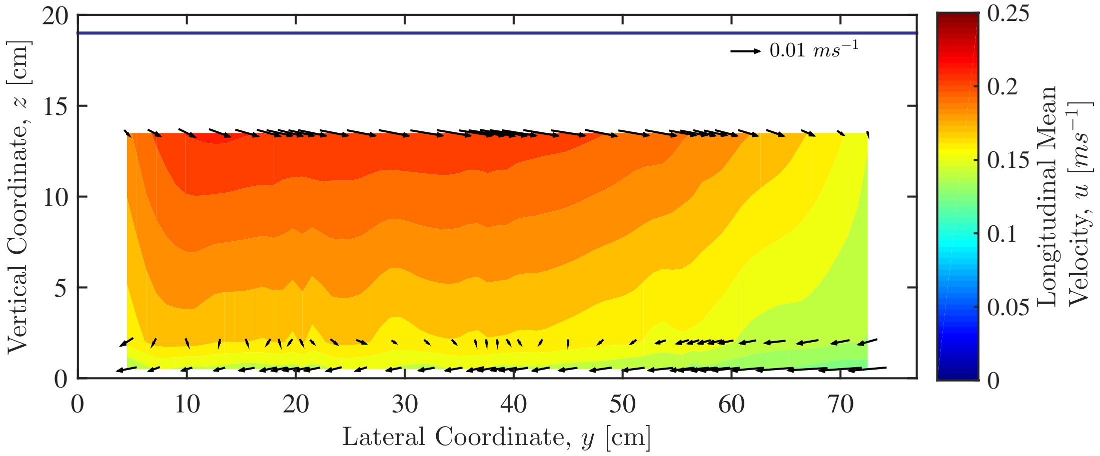

(a) Empty Bed

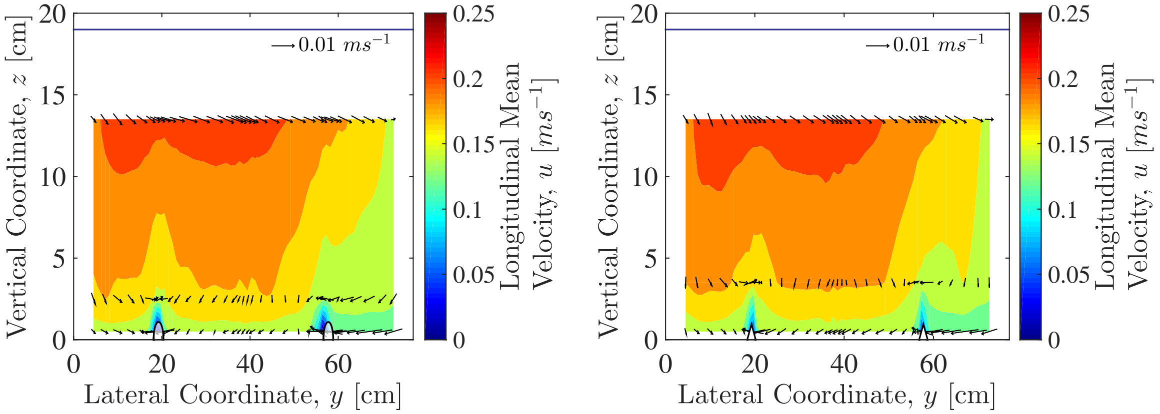

(b) Small Pipe

(c) Small Angle

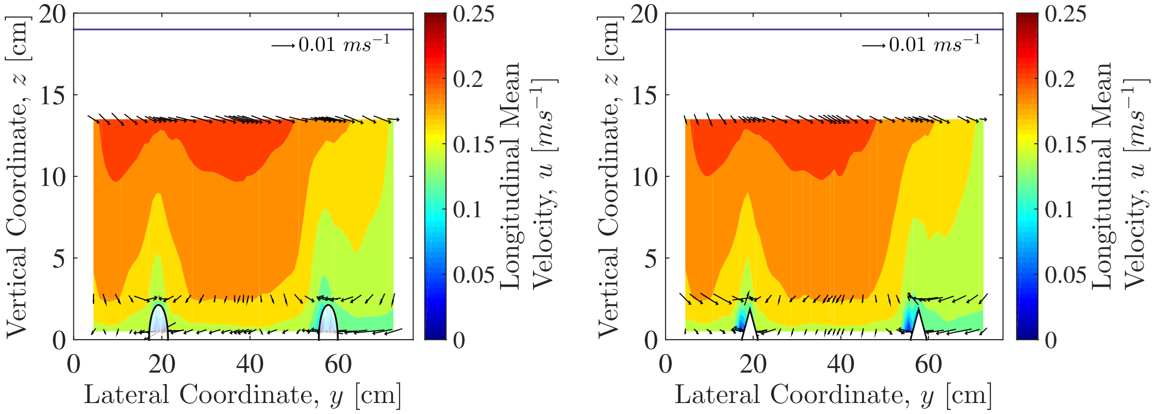

(d) Large Pipe

(e) Large Angle

Figure 3.2: Mean velocities from ADV data at 19 *cm* depth. Colormap indicates the streamwise (longitudinal) velocity, and arrows indicate secondary flows. Arrows additionally indicate measurement locations. Colormap is interpolated between these points.

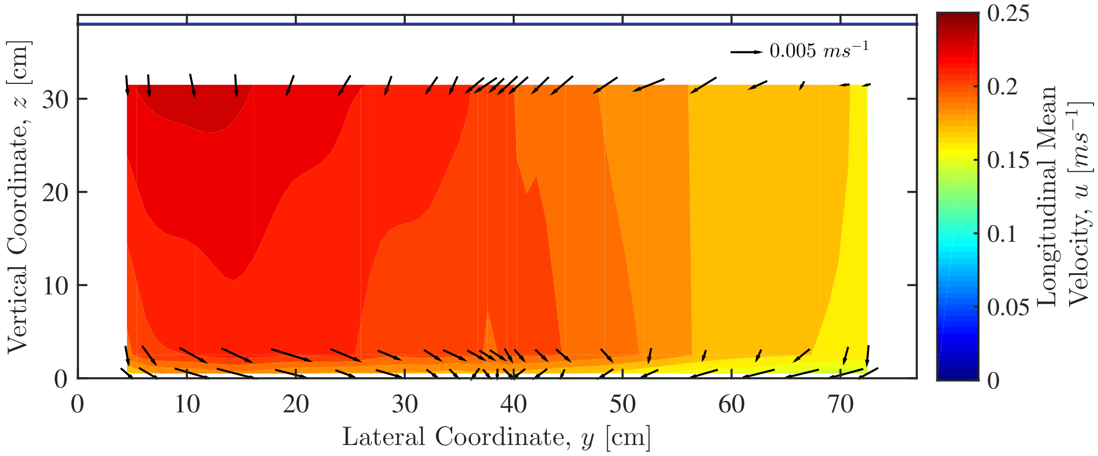

(a) Empty Bed

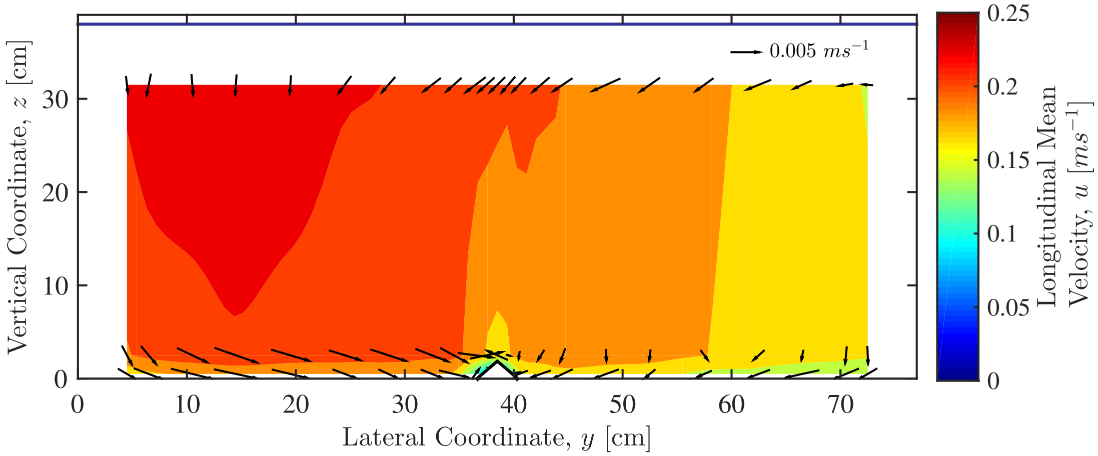

(b) Large Angle

Figure 3.3: Mean velocities from ADV data at 38 *cm* depth. Colormap indicates the streamwise (longitudinal) velocity, and arrows indicate secondary flows. Arrows additionally indicate measurement locations. Colormap is interpolated between these points.

First, it can be observed that near the surface the aforementioned trend holds for the shallow 9.5 *cm* depth case, but for the 19 *cm* depth and 38 *cm* depth no discernible effect from the longitudinal bars can be observed. It appears that there is a mean downward current with lateral velocities that vary by case, and this is true of both the empty bed case and the modified condition. This region is of particular importance to actual reactor applications, as this is the region of maximum light exposure and the region governing the gas transfer. This will be discussed further in Section 3.3.

Second, it is noteworthy to consider the scale of these secondary currents. The maximum upflow magnitude is only about 5% of the nominal velocity, which is consistent with the experiments of Nezu (2005). Table 3.1 summarizes the maximum magnitudes of upwelling velocities for each of the cases. It was found in the 19 *cm* depth case, that the large angle bed modification produced the maximum vertical velocity. Accordingly, both the large angle and large pipe demonstrated the most pronounced change in the structure of the mean secondary velocities. It was determined, therefore, that the large angle case was the most representative of the secondary current motivation, and the large angles were used for all flow depths to represent the modified bed condition.

Table 3.1: Maximum upwelling velocity magnitudes by case.

	Maximum $\overline{w}$ ($cm\ s^{-1}$)		
Case	$h = 9.5\ cm$	$h = 19\ cm$	$h = 38\ cm$
Empty	0.079	-0.15	-0.024
Small Angle	-	0.34	-
Large Angle	0.94	0.58	0.46
Small Pipe	-	0.48	-
Large Pipe	-	0.24	-

3.1.2 Turbulence Statistics

Turbulence statistics provide an additional measure of the activity in the flow that may not contribute to the mean velocities (e.g. periodic behavior). A large suite of turbulence statistics was calculated from velocity time series. In particular, three parameters figure prominently in the V4 (production) and V5 (suppression) terms of vorticity transport equation (see Chapter 1): the Reynolds stress in the secondary plane ($\overline{v'w'}$), the root-mean-square (RMS) of the lateral fluctuations (v'_{rms}), and the RMS of vertical fluctuations (w'_{rms}) (see also presence in Nezu & Nakagawa, 1984). Fields of these three parameters are presented for the empty bed case and the large angle modification for flow depths: $h = 9.5\ cm$ (Figure 3.4), $h = 19\ cm$ (Figure 3.5), and $h = 38\ cm$ (Figure 3.6).

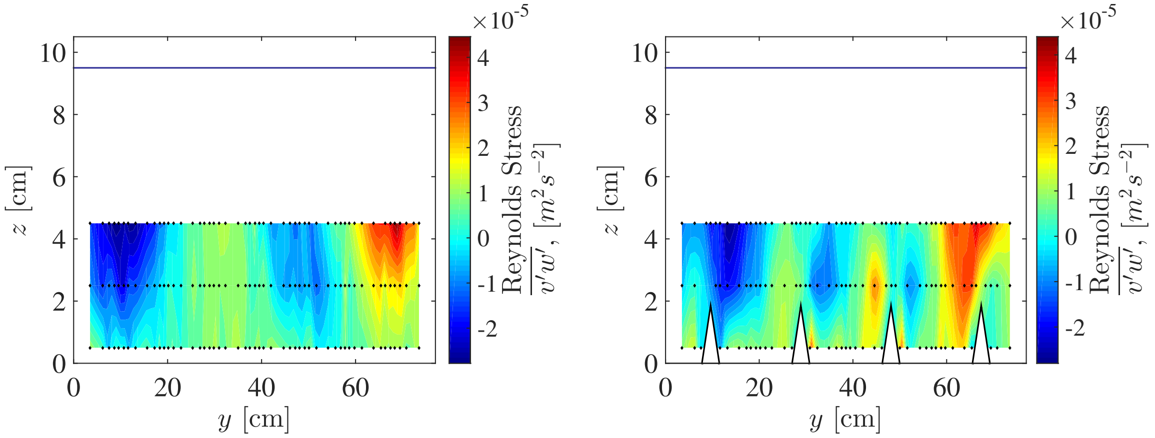

(a) Empty Bed - Reynolds Stress $\overline{v'w'}$ (b) Large Angle - Reynolds Stress $\overline{v'w'}$

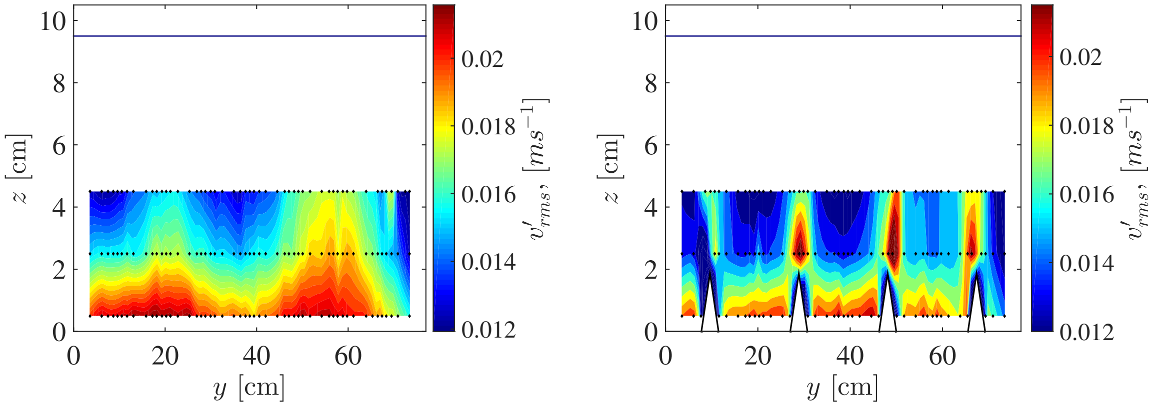

(c) Empty Bed - v'_{rms} (d) Large Angle - v'_{rms}

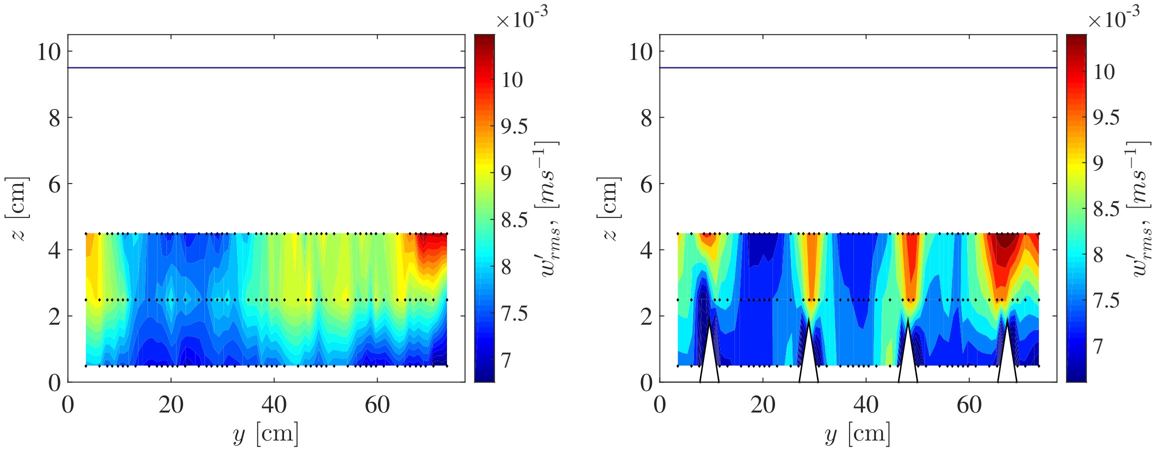

(e) Empty Bed - w'_{rms} (f) Large Angle - w'_{rms}

Figure 3.4: Turbulence statistics from ADV data at 9.5 *cm* depth. Colormap indicates the turbulence parameter, black marks indicate measurement locations. Colormap is interpolated between these points.

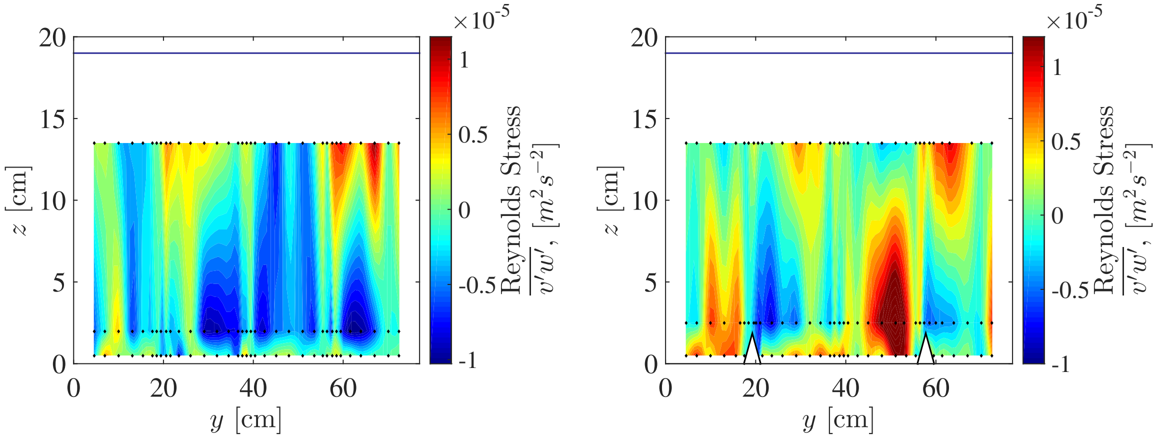

(a) Empty Bed - Reynolds Stress $\overline{v'w'}$ (b) Large Angle - Reynolds Stress $\overline{v'w'}$

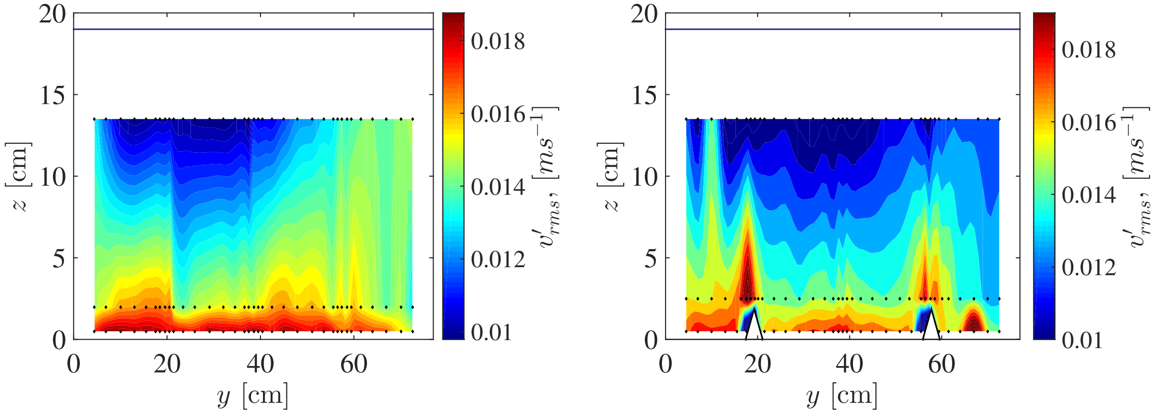

(c) Empty Bed - v'_{rms} (d) Large Angle - v'_{rms}

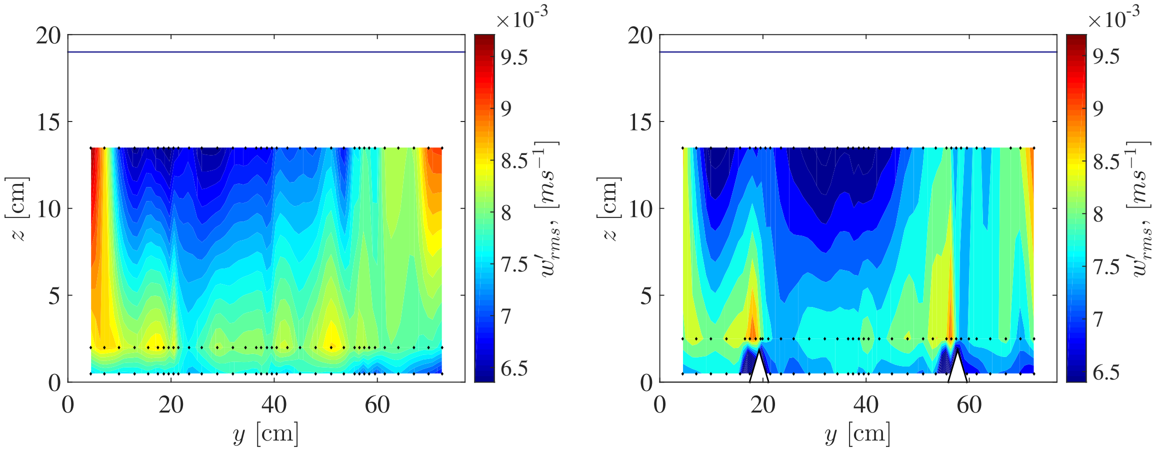

(e) Empty Bed - w'_{rms} (f) Large Angle - w'_{rms}

Figure 3.5: Turbulence statistics from ADV data at 19 *cm* depth. Colormap indicates the turbulence parameter, black marks indicate measurement locations. Colormap is interpolated between these points.

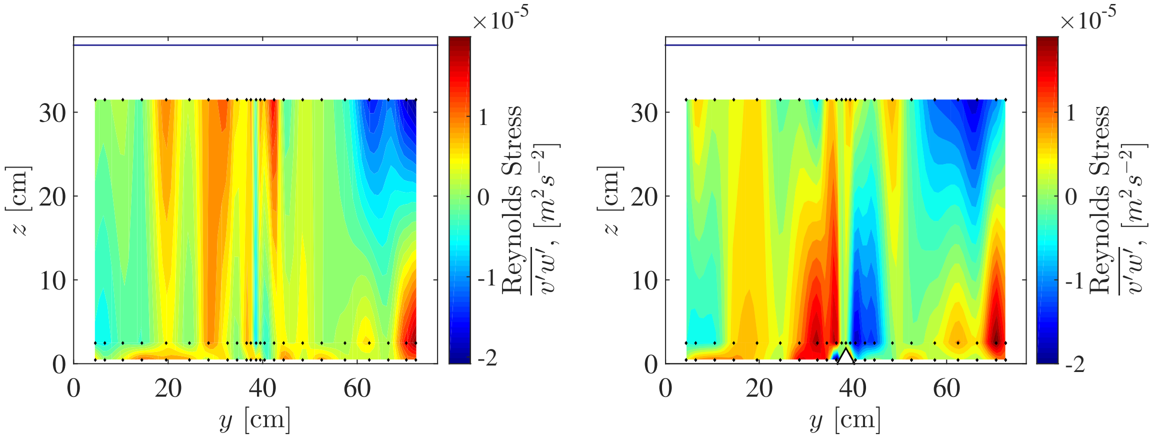

(a) Empty Bed - Reynolds Stress $\overline{v'w'}$ (b) Large Angle - Reynolds Stress $\overline{v'w'}$

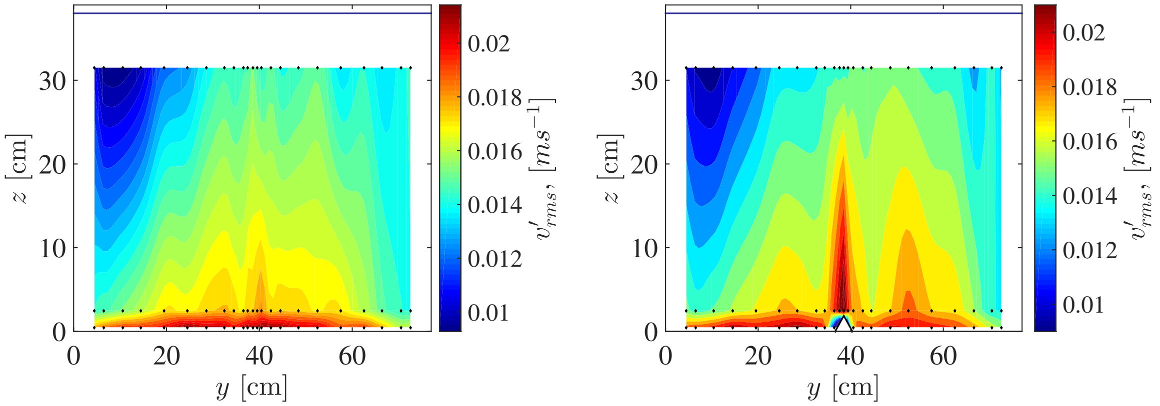

(c) Empty Bed - v'_{rms} (d) Large Angle - v'_{rms}

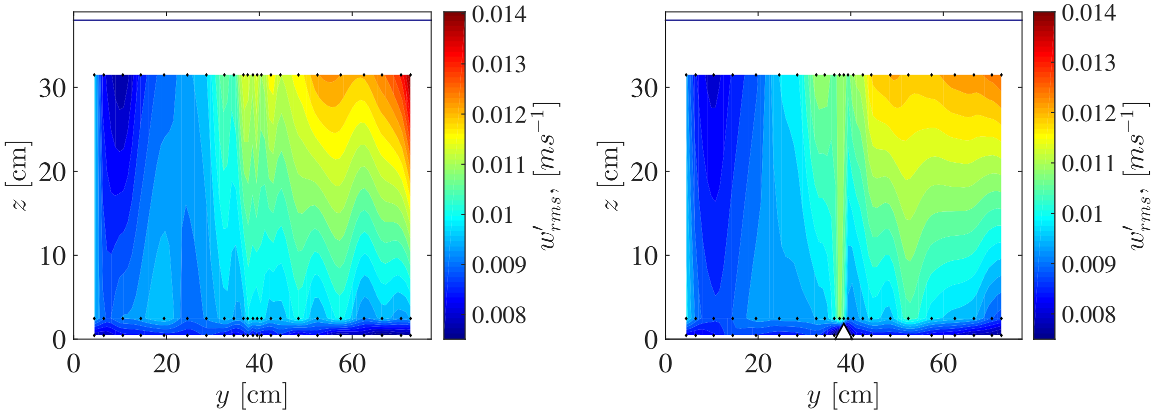

(e) Empty Bed - w'_{rms} (f) Large Angle - w'_{rms}

Figure 3.6: Turbulence statistics from ADV data at 38 *cm* depth. Colormap indicates the turbulence parameter, black marks indicate measurement locations. Colormap is interpolated between these points.

These turbulence fields, like the mean velocity fields, demonstrate enhanced secondary, cellular currents for the case of bed modification. The Reynolds stresses, $\overline{v'w'}$ (top row, Figures 3.4 to 3.6), exhibit an alternating behavior in the presence of the longitudinal ridges that is characteristic of counter-rotations. To the left of the ridges, positive values indicate that lateral and vertical fluctuations are positively correlated (i.e. moving right and up, or left and down). To the right of these ridges, the negative values indicate negative correlation between lateral and vertical fluctuations (i.e. moving left and up, or right and down). This alternating pattern laterally near the bed, as well as alternating positive and negative in the vertical (see $h = 19\ cm$ and $h = 38\ cm$ cases, especially) depicts rotations as shown in Figure 3.7.

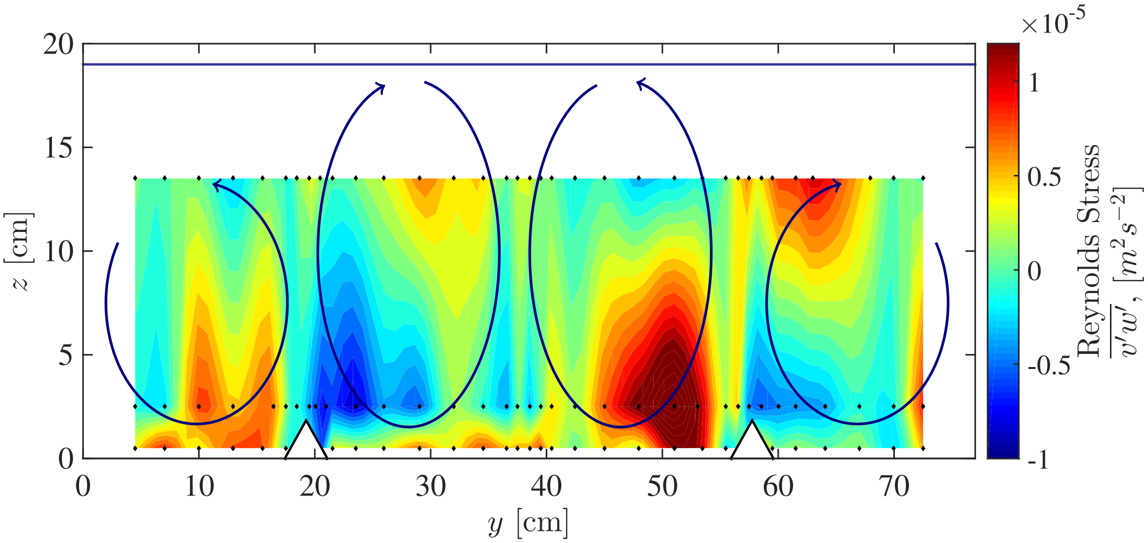

Figure 3.7: Cellular, secondary currents overlaid on Reynolds stress field.

It can be observed that similar patterns are present in the empty bed case (see especially $h = 9.5\ cm$), though they are not as strong or as numerous as the case with the large angle ridges. It is to be expected that these currents would form in straight open channel, however the addition of the bed modifications locks the currents in place and they are strengthened as a result.

The RMS of the lateral velocity fluctuations (middle row, Figures 3.4 to 3.6) are by definition strictly positive, and therefore demonstrate only the magnitude of lateral velocity fluctuations. In the unpopulated bed case, these fluctuations have a strong presence near the bed that diminishes in the upper strata of the flow. This is largely unaltered by the presence of the longitudinal bars, with the exception of fluctuations immediately above the ridges. It is worth noting, values between the top swath and middle swath of measurements are interpolated, and particularly for the larger flow depths, the colormap may not be representative of the actual velocity fluctuations in that region.

The RMS of the vertical fluctuations (bottom row, Figures 3.4 to 3.6) likewise represent a magnitude only. These fields demonstrate that vertical fluctuations are strong above the ridges, as would be expected from cellular, secondary currents, and at least for the $h = 9.5\ cm$ case and the $h = 19\ cm$ case appear to reach the upper edge of the measurement area. No increase in vertical fluctuations is found in the anticipated areas of downwelling.

3.1.3 Power Spectra

The presence of secondary currents has been considered from the perspective of spatial fields of mean velocity and turbulence parameters, but it is also valuable to consider the degree of influence they have in the flow structure, which can be investigated through spectral analysis. Power spectra are calculated from the time series data according to the equation:

$$S(\omega) = \frac{1}{T} \int_0^T \int_0^T \langle u'^*(t) u'(t+\tau) \rangle e^{-i\omega\tau} dt d\tau \tag{3.1}$$

These have been calculated for each of the sampling locations, including the bend ADV sampling, along each of the Cartesian coordinate axes, and representative locations are provided in Appendix B. Figure 3.8 demonstrates representative spectral distributions both in the upstream bend exit ($x = 19\ cm$) and at the measurement section ($x = 638\ cm$). Four recurring frequencies, represented by “spikes” in the spectral signal (red dashed lines in

Figure 3.8), were identified at multiple sampling locations: $f = \{0.59, 1.08, 1.61, 2.10\}\ Hz$. These can serve as indicators of mechanisms that contain significant amounts of energy in the flow.

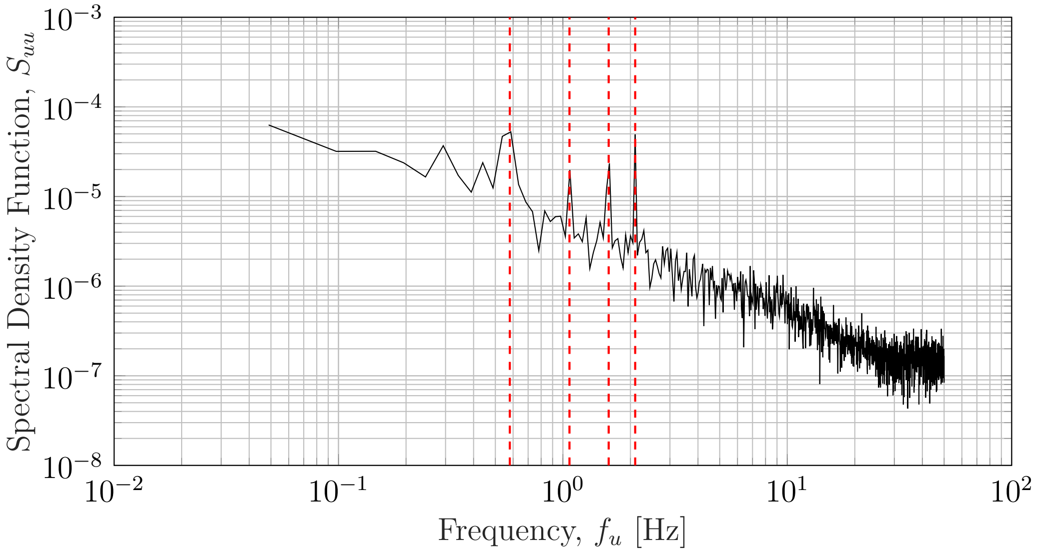

(a) $x = 638\ cm,\ y = 39.5\ cm,\ z = 13.5\ cm$

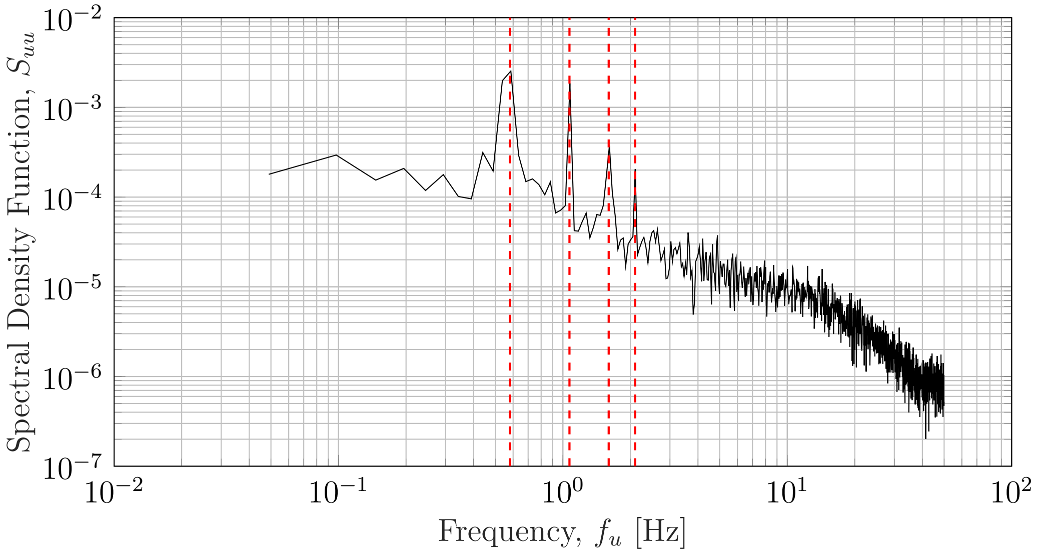

(b) $x = 19\ cm,\ y = 23\ cm,\ z = 13\ cm$

Figure 3.8: Representative power spectra from ADV data for longitudinal velocities at $x = 638\ cm$ and $x = 19\ cm$. The four recurring frequencies (red dashed lines) are evident, and are representative of those found in Appendix B.

3.2 sPIV Results

Because the surface and near surface region is critical to gas transfer and light exposure of algal cells, sPIV measurements were used to elucidate dynamics where ADV measurements were unattainable due to instrument limitations. Like the ADV data, these measurements can be understood through mean velocity fields and power spectra. Additionally, the surface divergence is considered for its influence in the surface divergence gas transfer model.

3.2.1 Mean Velocities

Mean velocity fields as viewed from above (downstream at the top of the plot) are presented for the large angle modification case in Figure 3.9. As discussed in Chapter 2, areas were identified where vector data was insufficient, causing gaps in the field. These can be seen for the lower flow depths ($h = 6.4\ cm$ and $h = 9.5\ cm$), particularly where the velocity magnitude reaches very low values away from the walls. It was evident from the image processing that this was caused by flashing light at the surface, a result of surface waves. This observation will be explored further later in this chapter, as these surface waves are evidence of significant flow structures able to overwhelm secondary currents.

A few observations can be made about these plots. First, the same streamwise velocity bias toward the outer wall (right of the plot) can be seen in the sPIV data as discussed in the ADV data. This is especially visible in the 38 cm depth case, though it is also visible for $h = 19\ cm$ and $h = 9.5\ cm$, as well. Second, it can be observed that there are much more variable lateral fluctuations in the lower flow depths than in the deeper flow depths. For $h = 19\ cm$ and $h = 38\ cm$, where the Froude numbers are very low ($\mathbf{F} = 0.15$ and 0.10), it is likely that the pressure distribution in the downstream bend is forcing fluid toward the outside of the bend. This has less influence in the low flow depth cases ($\mathbf{F} = 0.21$ and 0.25), and therefore these are more representative of the straight section of the reactor. It is notable, as well, for the low flow depths that the time-averaged lateral velocity components can change direction as one moves downstream.

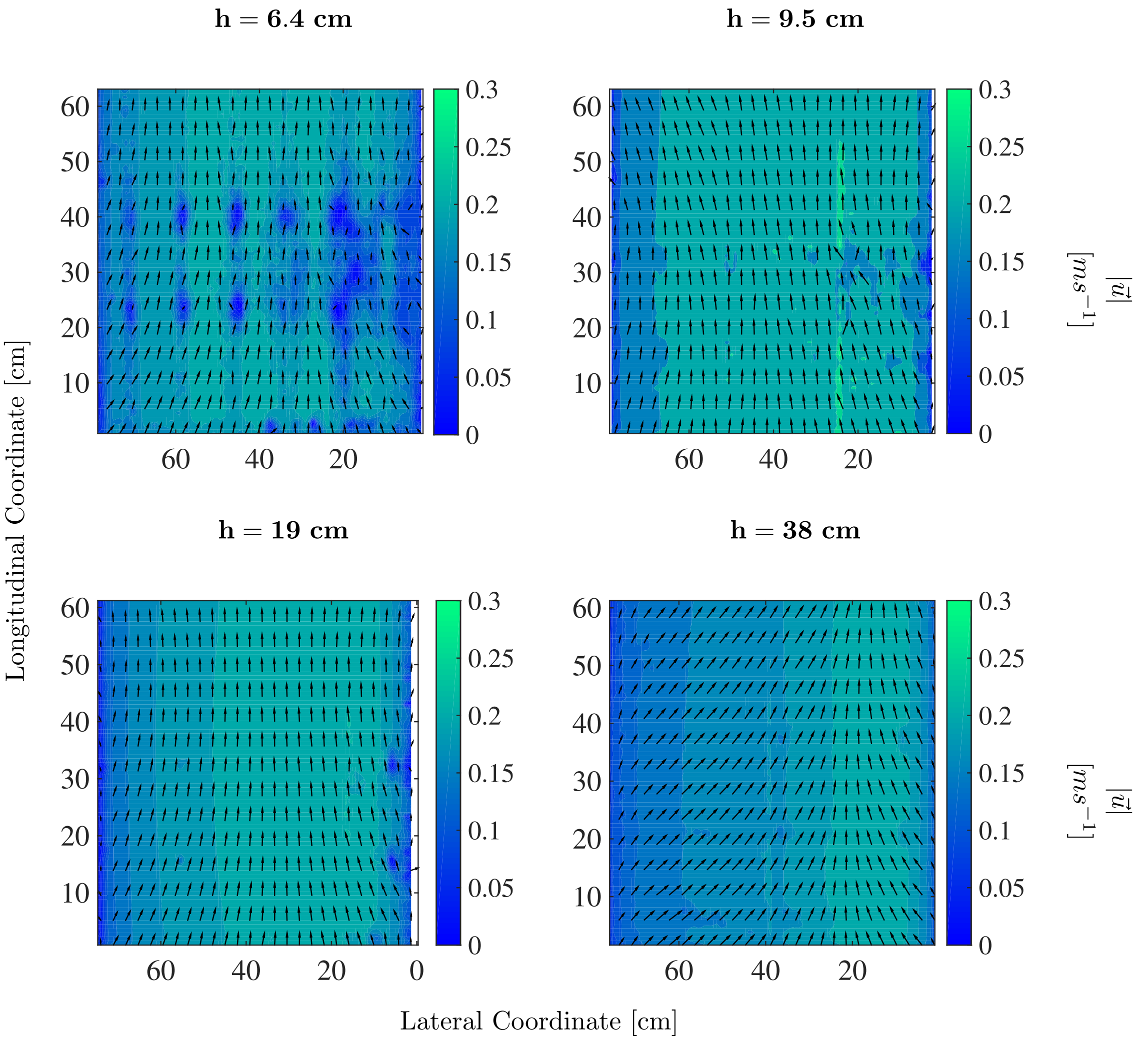

Figure 3.9: Summary of sPIV mean velocity measurements. Colormap indicates mean velocity magnitude, and arrows indicate direction of flow. Lateral coordinates are measured from outside wall ($y = 0$ cm, right), and longitudinal coordinates from upstream ($x = 0$ cm, bottom) to downstream. "Holes" in the velocity field for 6.4 cm and 9.5 cm depths are likely caused by lateral surface waves reflecting incident light.

sPIV data was validated by comparison against the upper swath of ADV measurements. The lateral distribution of mean streamwise velocity is presented in Figure 3.10, and the distribution of mean lateral velocity is presented in Figure 3.11. It is not anticipated that these distributions will be precisely equal as they are influenced by a number of different phenomena in the vertical (e.g. boundary layer development, velocity dip phenomenon), however, they may be compared for general similarity.

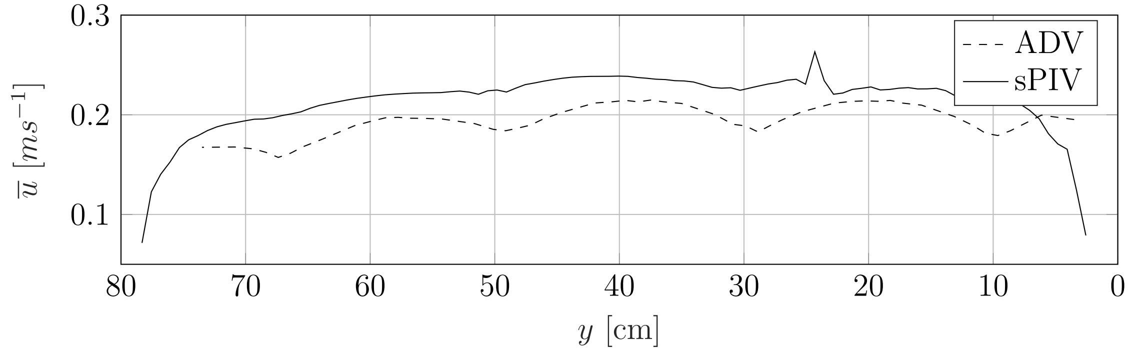

(a) $h = 9.5$ *cm*

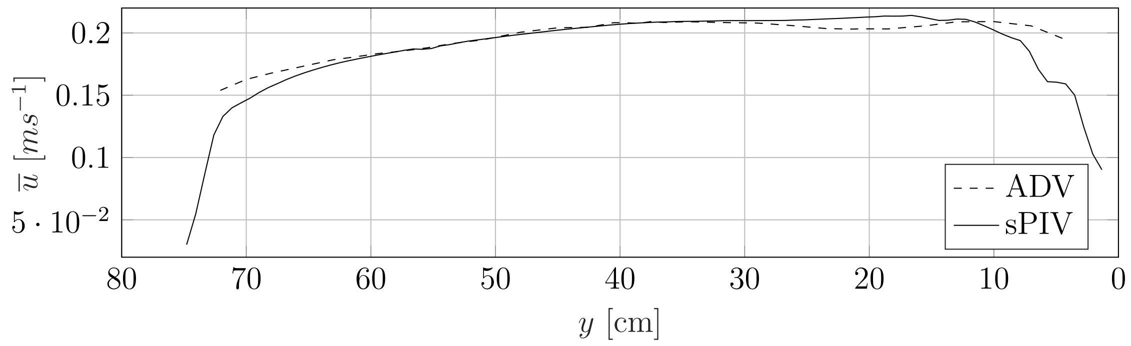

(b) $h = 19$ *cm*

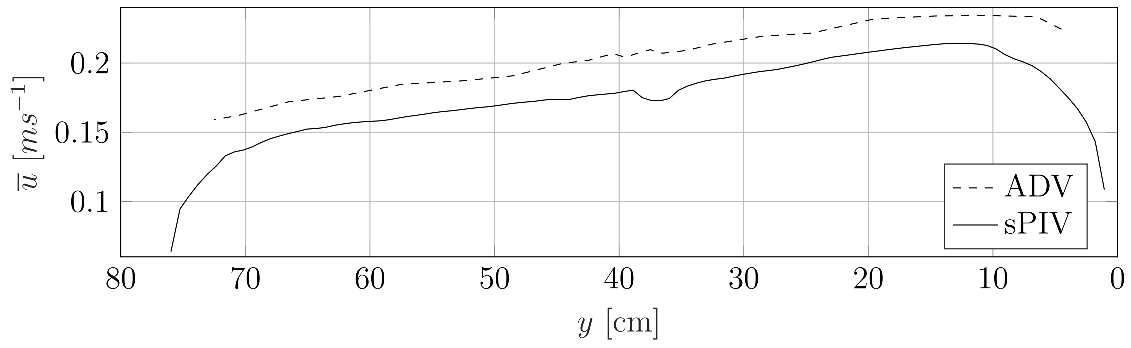

(c) $h = 38$ *cm*

Figure 3.10: Comparison of ADV and sPIV lateral distributions of mean streamwise velocity. ADV measurements were sampled approximately 5 *cm* below the free surface, and sPIV measurements were sampled at the free surface. It can be seen that the distributions follow very similar trends, even the periodic pattern of the 9.5 *cm* depth case, though it is damped in the sPIV data.

The streamwise comparisons follow an expected relationship between the ADV data, approximately 5 cm below the free surface, and the sPIV data. For the 9.5 *cm* depth case, the ADV measurement is located at an elevation less than half of the total flow depth, and therefore the streamwise velocity is lower than that measured at the free surface. Likewise, the bars play a more significant role deeper in the flow, and the local minima are more apparent in the ADV measurements. For the 38 *cm* depth case, the ADV data is relatively close to the surface, but approaching the maximum velocity location as given by the velocity dip phenomenon. The 19 *cm* case, is intermediate to these two, and therefore it approximates the surface velocity fairly well. The streamwise velocity sPIV data, therefore, follows the anticipated relationships to the ADV data and appears to be confirmed.

The lateral velocity comparisons show a little more variability. While the 9.5 *cm* and 38 *cm* depth cases show good agreement between the ADV and sPIV data, with the exception of a few spikes, the 19 *cm* depth case shows significant differences between the two data sets. The cause of these differences was unknown, but plausible explanations could be made that the 19 *cm* depth case is the only case for which one set of measurements was in the boundary layer (ADV) and the other was in the free stream (sPIV). Therefore, the 19 *cm* depth case was monitored for other anomalous phenomena, but was not discarded.

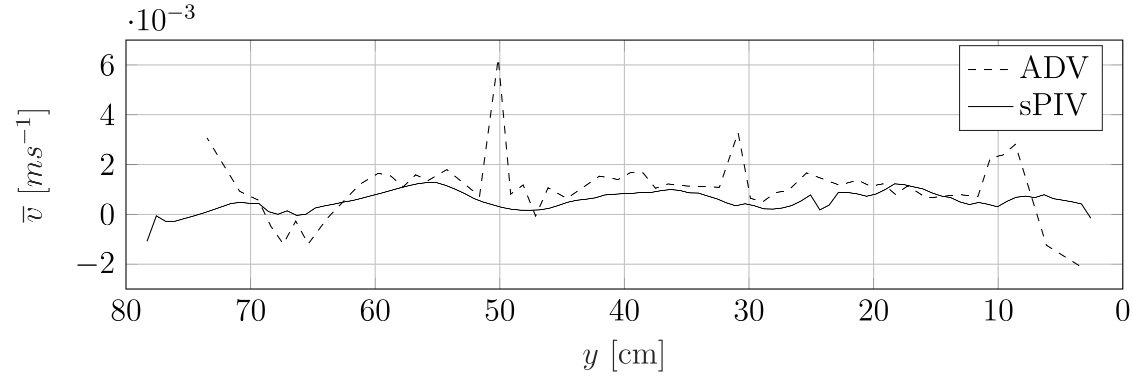

(a) $h = 9.5$ cm

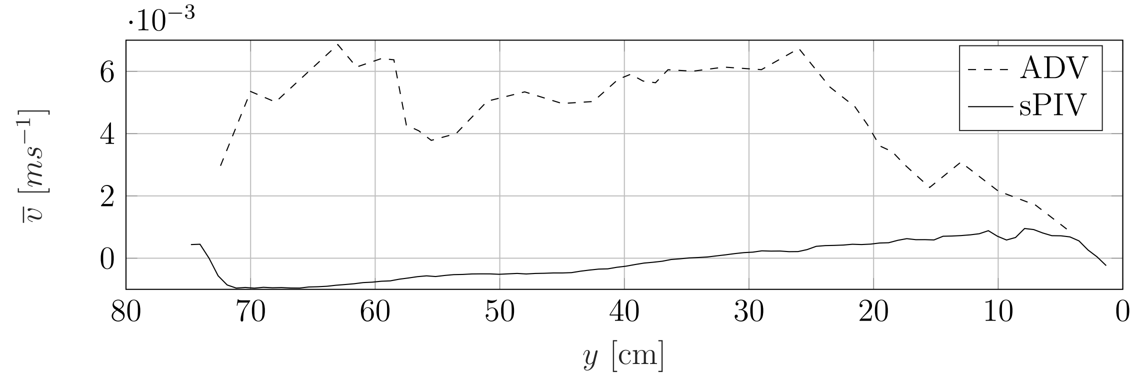

(b) $h = 19$ cm

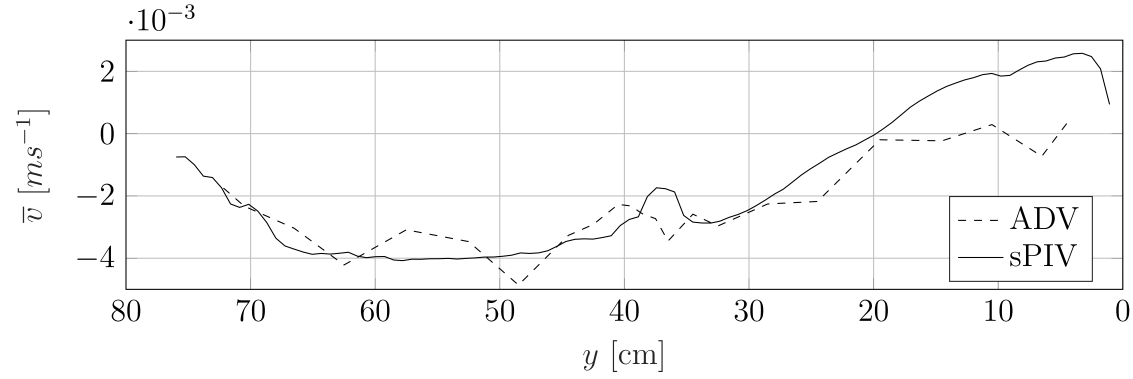

(c) $h = 38$ cm

Figure 3.11: Comparison of ADV and sPIV lateral distributions of mean lateral velocity. The 9.5 cm and 38 cm cases follow similar trends, however the 19 cm case shows significant differences between the two measurement techniques. This could be explained by the difference in the vertical location of the measurements.

Proceeding with the sPIV data, the most significant characteristic of these mean velocity measurements was the difference in mean lateral velocity generated by the longitudinal ridges. It was anticipated that the longitudinal ridges would generate secondary currents that would evidence themselves in alternating diverging and converging currents at the free surface. The lateral velocity fields are summarized for the 6.4 *cm* depth and 9.5 *cm* depth cases in Figure 3.12, and for the 19 *cm* depth and 38 *cm* depth cases in Figure 3.13.

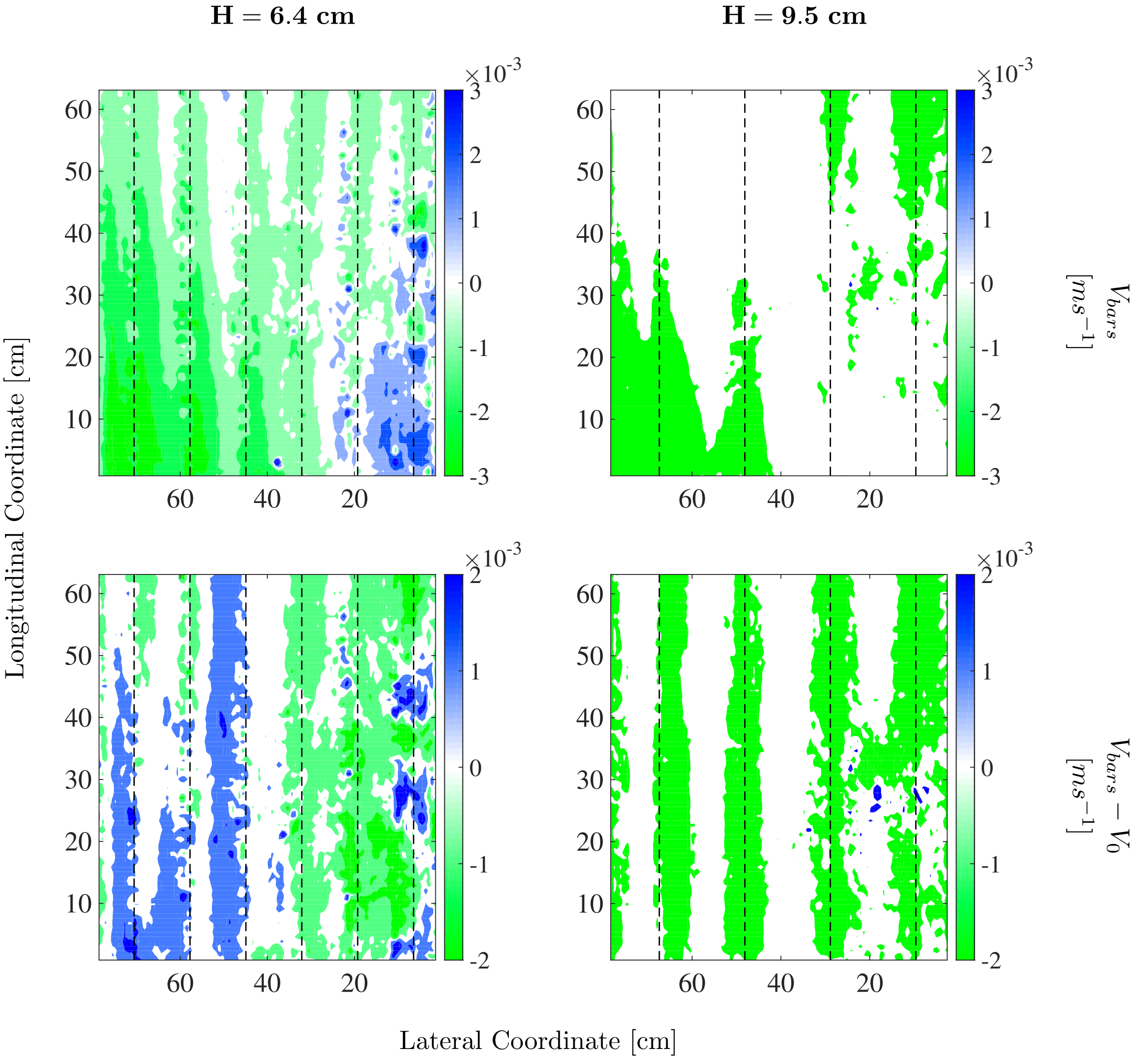

Figure 3.12: sPIV mean lateral velocity measurements, $h = 6.4$ *cm* and $h = 9.5$ *cm* depths. Velocity field as viewed from above, with $y = 0$ *cm* (outer wall) at the right, and local coordinate $x = 0$ *cm* (approximately located at the measurement section) at the bottom. Top row (V_{bars}) is for the large angle bed modification case, with bar locations indicated by dashed lines. Bottom row ($V_{bars} - V_0$) is the change between the empty bed case and the large angle case.

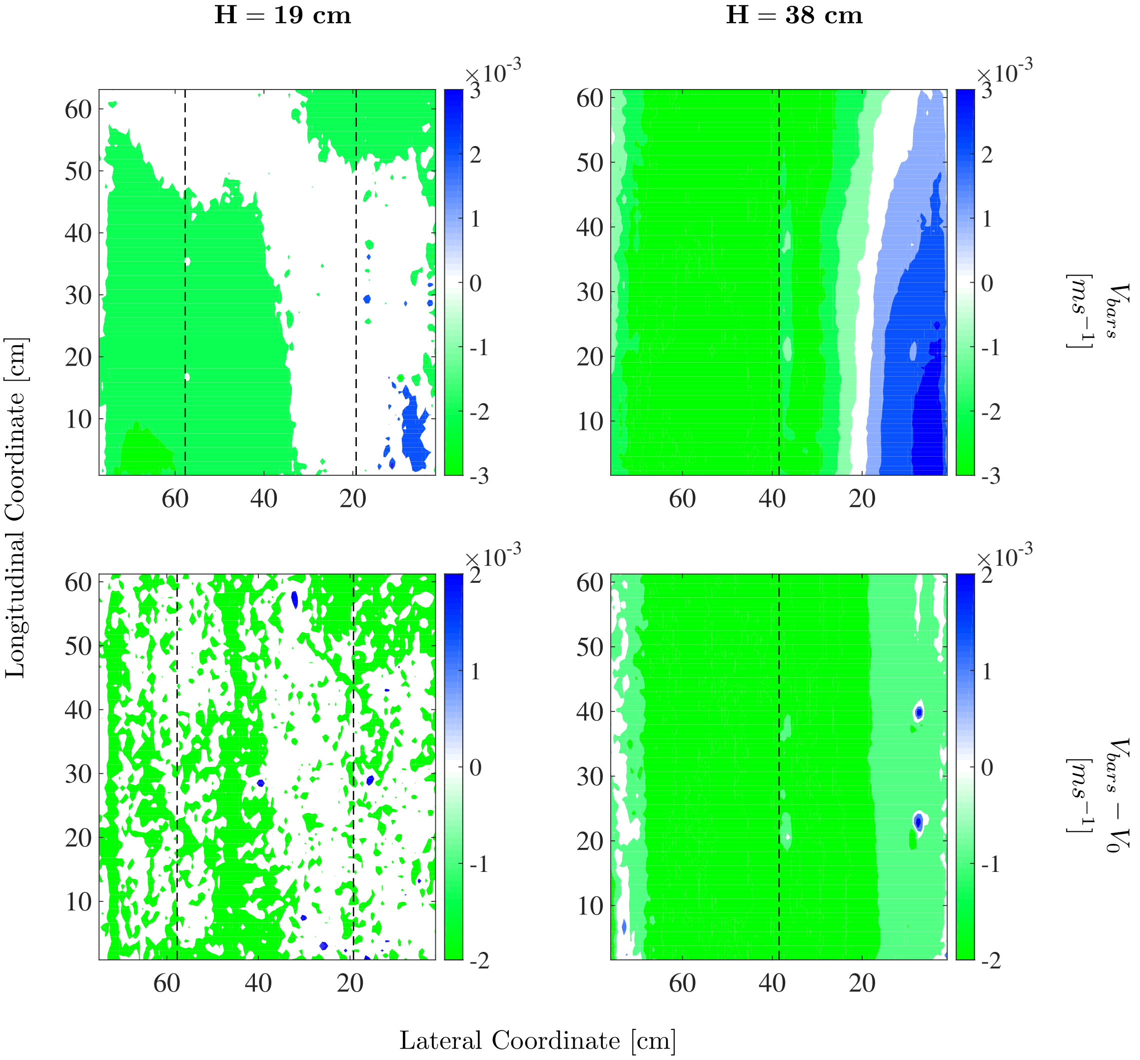

Figure 3.13: sPIV mean lateral velocity measurements, $h = 19$ *cm* and $h = 38$ *cm* depths. Velocity field as viewed from above, with $y = 0$ *cm* (outer wall) at the right, and local coordinate $x = 0$ *cm* (approximately located at the measurement section) at the bottom. Top row (V_{bars}) is for the large angle bed modification case, with bar locations indicated by dashed lines. Bottom row ($V_{bars} - V_0$) is the change between the empty bed case and the large angle case.

The top row of the above two figures gives the absolute lateral velocities for the case of the large angle bed modification, with green indicating negative lateral velocity (to the right) and blue indicating positive lateral velocity (to the left). While there are some alternating patterns that can vaguely be seen in the 6.4 *cm* and 9.5 *cm* cases, they are not especially clear. Thus, the lateral velocities were examined relative to the empty bed case, by subtracting out the mean lateral velocities for the empty bed. This relative velocity field is given in the bottom row of Figures 3.12 and 3.13.

From these relative velocities it can be seen that for the lower flow depths (6.4 *cm* and 9.5 *cm*) there is a strong gradient in the lateral velocities associated with the presence of the longitudinal ridges (dashed lines), however this periodic behavior cannot be found in the deeper flow depths (19 *cm* and 38 *cm*). It appears as if the longitudinal ridges are having no effect on the free surface in the deeper flow depths. This will be significant to the understanding of the secondary current geometry, and will be discussed in Section 3.3.

3.2.2 Power Spectra

Power spectra were calculated in the same way as discussed in the ADV signal processing. Representative plots are given in Figure 3.14 of the longitudinal and lateral velocities for the $h = 19$ *cm* flow depth. The same four frequencies were identified as the dominant spectral modes in the longitudinal velocities, though some are weaker and some are amplified in the lateral component. A more extensive sampling of the sPIV data power spectra is given in Appendix C.

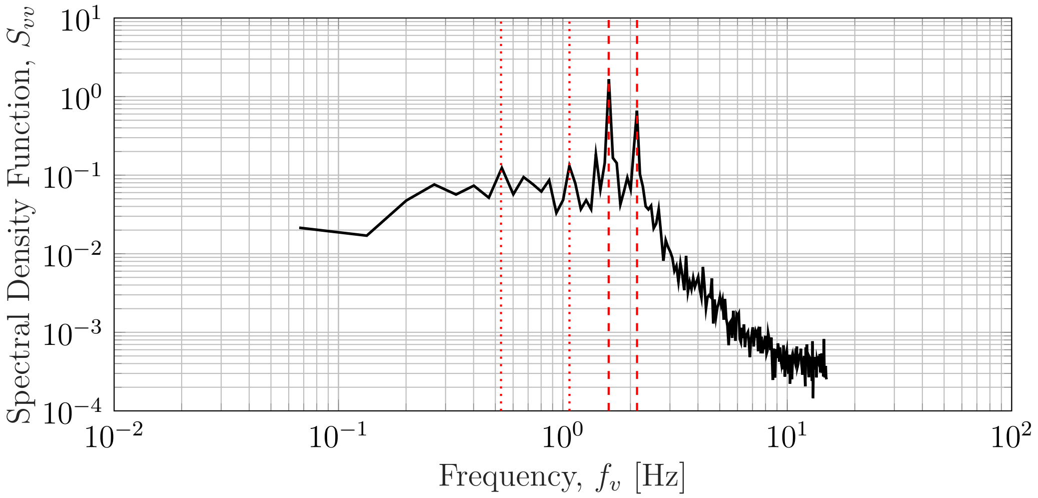

(a) $h = 19\ cm, x \approx 638\ cm, y = 70\ cm$, Lateral Component

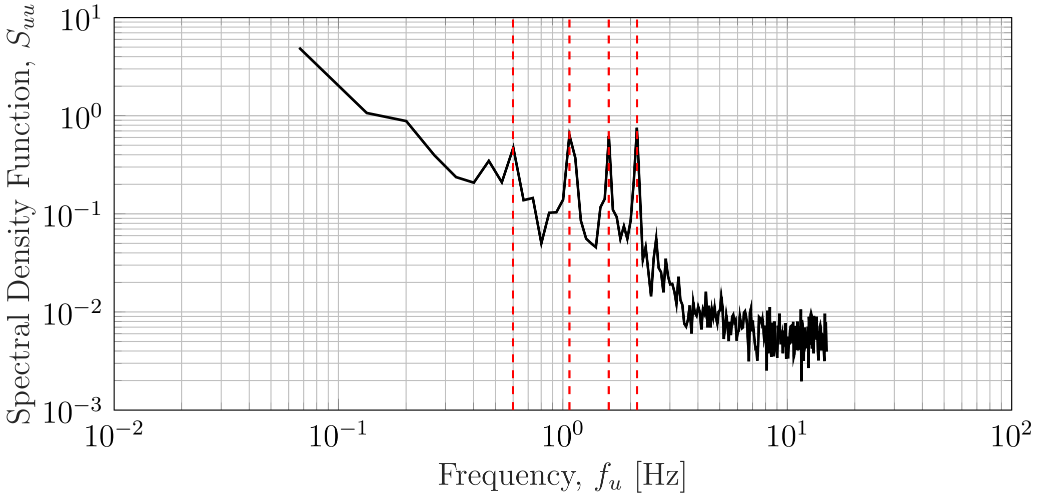

(b) $h = 19\ cm, x \approx 638\ cm, y = 70\ cm$, Streamwise Component

Figure 3.14: Representative power spectra from sPIV data for lateral and longitudinal velocities at the measurement section for the $h = 19\ cm$ flow depth. The four recurring frequencies (red dashed lines) are evident though some are weaker (red dotted lines) and some are amplified in the lateral component. These are representative of the spectra found in Appendix C.

3.2.3 Surface Divergence

Surface divergence is calculated according to:

$$\langle \beta \rangle_{rms} = \left[\left\langle \frac{\partial u'}{\partial x} + \frac{\partial v'}{\partial y} \right\rangle^{2} \right]^{1/2} \tag{3.2}$$

This operation was performed over the measurement domain for the sPIV data, and the resulting field of surface divergence is given in Figure 3.15 for the large angle bed modification case.

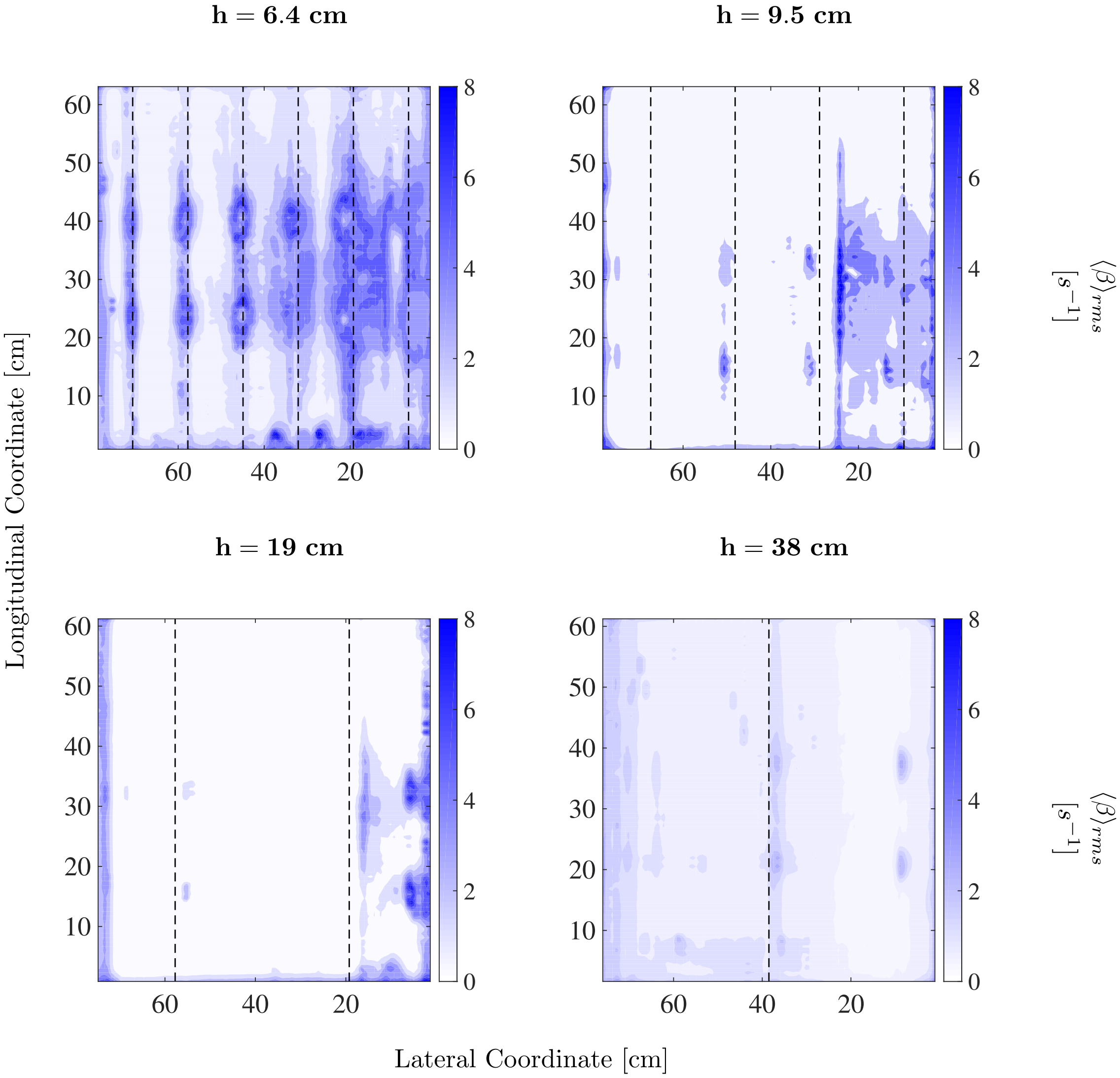

Figure 3.15: sPIV root-mean-square surface divergence for the large angle bed modifications cases. Velocity field as viewed from above, with $y = 0\ cm$ (outer wall) at the right, and local coordinate $x = 0\ cm$ (approximately located at the measurement section) at the bottom. Longitudinal bar locations are indicated by the dashed lines.

The surface divergence is subject to the same data gaps due to the surface waves, which explain some of the "hotspots" of surface divergence in the low flow depth plots. However, even outside of the regions of light reflection it appears that the surface divergence aligns with the longitudinal ridges for the $h = 6.4$ *cm* case, as anticipated from the structure of secondary currents. For the other flow depths, little evidence of surface divergence exists at the longitudinal bars.

3.3 Secondary Currents

Turning again to the first question motivating this study, "Were secondary currents of Prandtl's second kind able to be produced in a full-scale RWT reactor?" The answer is a qualified "yes." It is evident, particularly from the ADV measurements both in mean flow and in turbulence statistics, that the presence of cellular currents in the secondary plane (as identified by Nezu & Nakagawa, 1984; Kinoshita, 1967) were clearly identifiable. Furthermore, the production of these currents is able to be visualized using the generation term of the streamwise vorticity transport equation (see Chapter 1 for derivation):

$$\mathrm{Prod}(\Omega_x) = \frac{\partial^2}{\partial y \partial z}\left(\overline{v'^2} - \overline{w'^2}\right) \tag{3.3}$$

Figure 3.16 presents the field of vorticity generation for the 9.5 *cm* depth case both with and without the longitudinal ridges. It is evident from the figure that the presence of the bars significantly increases the streamwise vorticity production.

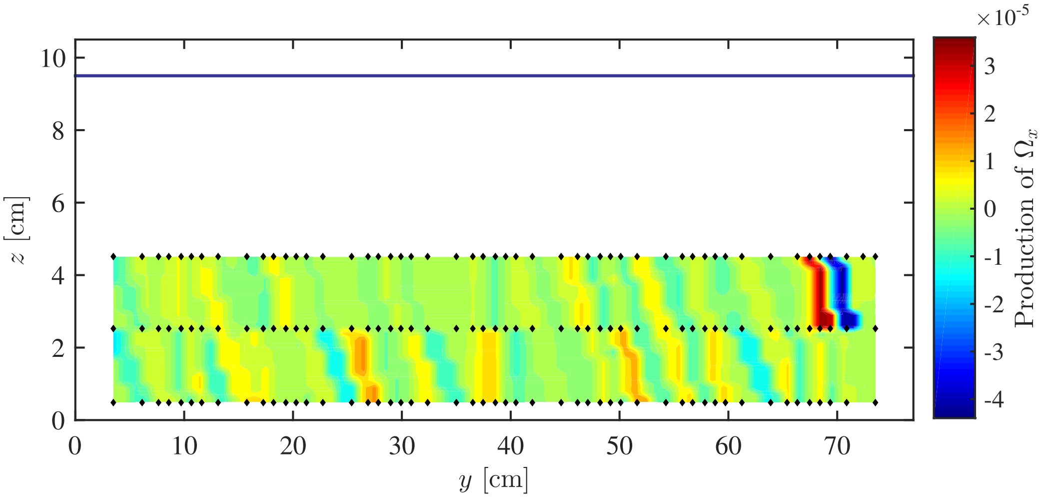

(a) Empty Bed

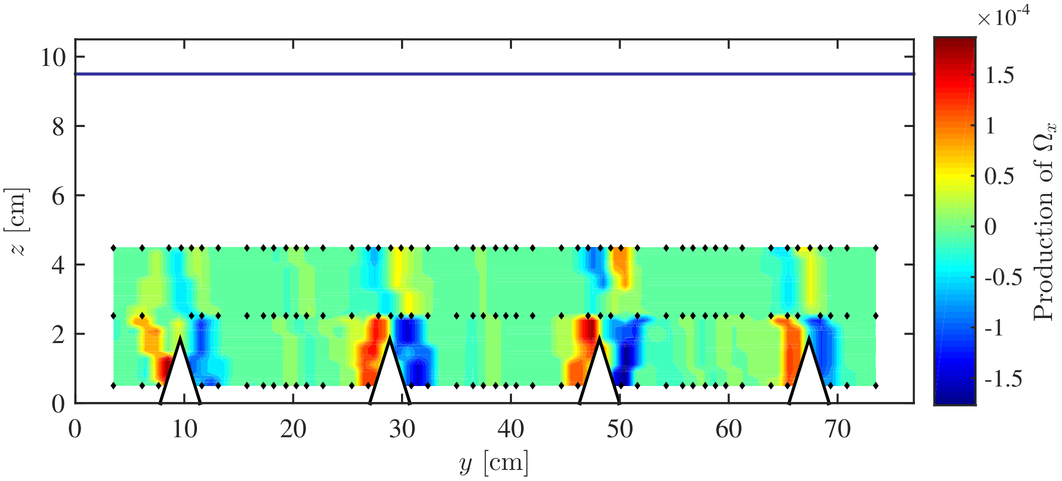

(b) Large Angle

Figure 3.16: Vorticity production color maps. Measurement locations are indicated by black marks. The empty bed case has local hot spots of production near the bed, but this is increased by an order of magnitude with the introduction of the longitudinal bars. Suppression of Ω_x was not able to be calculated because it requires a second derivative in z, which would be meaningless for three measurements in the vertical.

However, these currents were not accompanied by all of the expected, associated phenomena. Near surface measurements were unaffected by the addition of ridges in the deeper flows. Surface divergence only showed up marginally in the case of shallow flows. In both ADV and sPIV data the spatial variations in lateral currents only appeared after subtracting out the background currents. Therefore, further refinement is required to explain the behavior expressed in the experimental data, which can be better explained from boundary layer theory.

3.3.1 Boundary Layer Development

In Chapter 1 it was discussed that the production of turbulence occurs near the bed and scales with the boundary layer thickness. Because these secondary currents are likewise generated near the bed (see Figure 3.16), they too scale with the boundary layer. However, it has been observed that open RWTs undergo significant overturning in the channel bends, and cannot be treated as an infinitely-long, fully-developed flow (see e.g., Figure 2.5). Figure 3.17 reports velocity profiles measured in the upstream bend, and demonstrates how the typical logarithmic velocity profile gets inverted after passing through the channel bend.

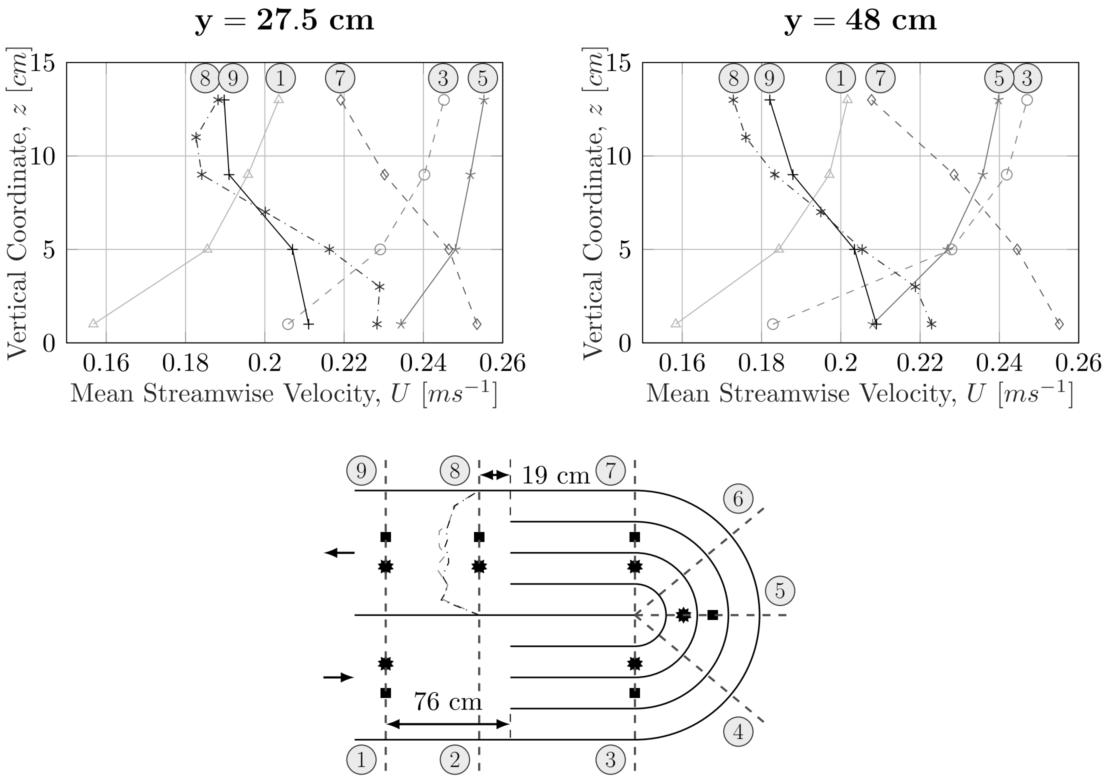

Figure 3.17: Vertical streamwise velocity profiles at the bend, a distance of 27.5 *cm* (squares) and 48 *cm* (stars) from the outer wall for a flow depth of 19 *cm*. The upstream logarithmic boundary layer profiles give way to higher velocities near the bed between transect 5 and transect 7, indicating an overturning current within the bend vanes. Additionally, at section 8 on the schematic lateral transects of mean streamwise velocity are plotted at near bed (gray, dashed line) and near the surface (black, dash-dot line).

Therefore, after undergoing this inversion in the bends, the boundary layer will again develop over a certain length until the boundary layer thickness attains the entire flow depth, or the next channel bend is reached. This development length has been construed for the current RWT application by two methods (as described in Chapter 1), and is summarized in Table 3.2.

Table 3.2: Boundary layer development lengths as determined from Prandtl's 1/7th power law (top portion) and Kirkgöz and Ardiçlioğlu (1997, bottom portion). The ratio of $\mathbf{Re_b}$ to $\mathbf{F}$ in this case are all outside of the experimental range of Kirkgöz and Ardiçlioğlu; the 38 *cm* depth yields non-physical values and was not included. All variables are as previously defined.

Case I.D.	Depth, h (cm)	Nom. Velocity, U (cm s^{-1})	$\mathbf{Re_b} = \frac{Uh}{\nu}$	$\mathbf{Re_x} = \frac{Ux}{\nu}$	δ at x = 6.38m (cm)	Development Length (m)
S2	6.4	20.0	1.28×10^4	1.28×10^6	14.2	3.5
A2, S4, D4	9.5	20.0	1.9×10^4	1.28×10^6	14.2	5.8
S11	19.0	5.0	9.5×10^3	3.19×10^5	18.7	9.7
S10, D8	19.0	10.0	1.9×10^4	6.38×10^5	16.3	11.5
A5, S9, D11	19.0	20.0	3.8×10^4	1.28×10^6	14.2	13.7
A9, S15, D19	38.0	20.0	7.6×10^4	1.28×10^6	14.2	32.5

Case I.D.	Depth, h (cm)	Nom. Velocity, U (cm s^{-1})	$\mathbf{Re_b} = \frac{Uh}{\nu}$	$\mathbf{F} = \frac{U}{\sqrt{gD}}$	Development Length (m)
S2	6.4	20.0	1.28×10^4	0.25	4.5
A2, S4, D4	9.5	20.0	1.9×10^4	0.21	6.3
A5, S9, D11	19.0	20.0	3.8×10^4	0.15	9.5

It can be seen that for the lower flow depths ($h = 6.4$ *cm* and $h = 9.5$ *cm*) the development length is attained before reaching the measurement section by both methods of calculation, and therefore it is expected that the secondary currents generated near the bed would influence the free surface. For the deeper flow depths ($h = 19$ *cm* and $h = 38$ *cm*), however, the boundary layer can require as much as 32.5 *m* to develop, which is much longer than the length of the RWT, itself. As a result, for the 38 *cm* depth, the boundary layer thickness at the measurement section is less than half the total flow depth (14.2 *cm*). This boundary layer development has been plotted with the "calibration" profiles for the 38 *cm* depth in Figure 3.18, which demonstrates that the measured profiles confirm this development length relationship.

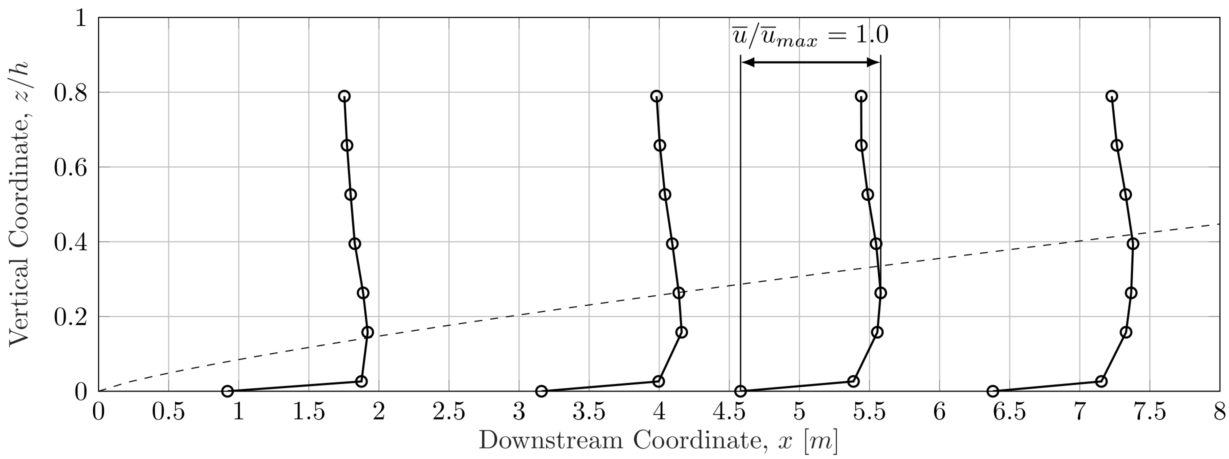

Figure 3.18: Boundary layer development. Non-dimensionalized ($\overline{u}/\overline{u}_{max}$) velocity profile measurements (solid, thick lines) from the flume calibration are plotted with the boundary layer thickness derived from Prandtl's 1/7th power law (dashed line). Measurements and theoretical values shown are for 38 cm depth and free-stream velocity of 20 $cm\ s^{-1}$. It can be seen that for this depth, the boundary layer thickness does not even attain half of the flow depth at downstream distance of 8.0 m.

This lack of development length would adequately explain why the lower flow depths show influence from the bars while the deeper runs lack any discernible influence in near-surface lateral velocity or surface divergence. It implies that if secondary currents are to be used in renewing the surface fluid for gas transfer or in cycling algal cells into and out of the euphotic zone, then long aspect ratios or shallow flow depths will be required in these facilities. Considering the flow depths influence a number of other important factors (e.g. temperature) and are unlikely to change substantially, this confirms the recommendations given by Chisti (2016) that large aspect ratios are desirable in these facilities, on the order of 20 times the width of one cross-section.

3.4 Dominant Mechanisms

This leads to the second question, "If secondary currents are being washed out by other flow structures in the straight portions of the reactor, then what are the dominant mechanisms causing these structures?" It was noticed, for instance, that there were strong lateral currents causing surface waves in the sPIV measurements, and that background lateral currents had to be subtracted out of ADV data to reveal the spatial distribution of the secondary currents.

Figure 3.19 summarizes the process used toward answering this question. First, (upper left) after noticing significant lateral currents overwhelming the secondary currents, the time series of lateral velocities from the sPIV data revealed that there was a strong oscillatory component to the velocity signal with a characteristic period of approximately 0.6 s that was anti-phased with the velocity signal on the opposite side of the cross-section. In order to determine the relative strength of that signal, power spectra (upper right) were used to identify four dominant frequencies in the velocity signal: $f = \{0.59, 1.08, 1.61, 2.10\}$ Hz (see Appendices B and C).

In order to determine if any of these were generated in the straight portion of the reactor, by the bed modifications, the velocity spectra were consulted at the exit of the upstream bend (lower right). It was found that all of the signals noted at the measurement section were present upstream at the bend exit, and therefore the structures of interest for mixing in the straight portion of the reactor were caused by bend dynamics (lower left) or other forcings in the upstream. A phenomenological approach was then employed to identify mechanisms that would produce the dominating frequencies. It is recognized that this does not constitute certain proof that these mechanisms are in fact the direct cause of these four signals, however each has strong evidence to commend itself.

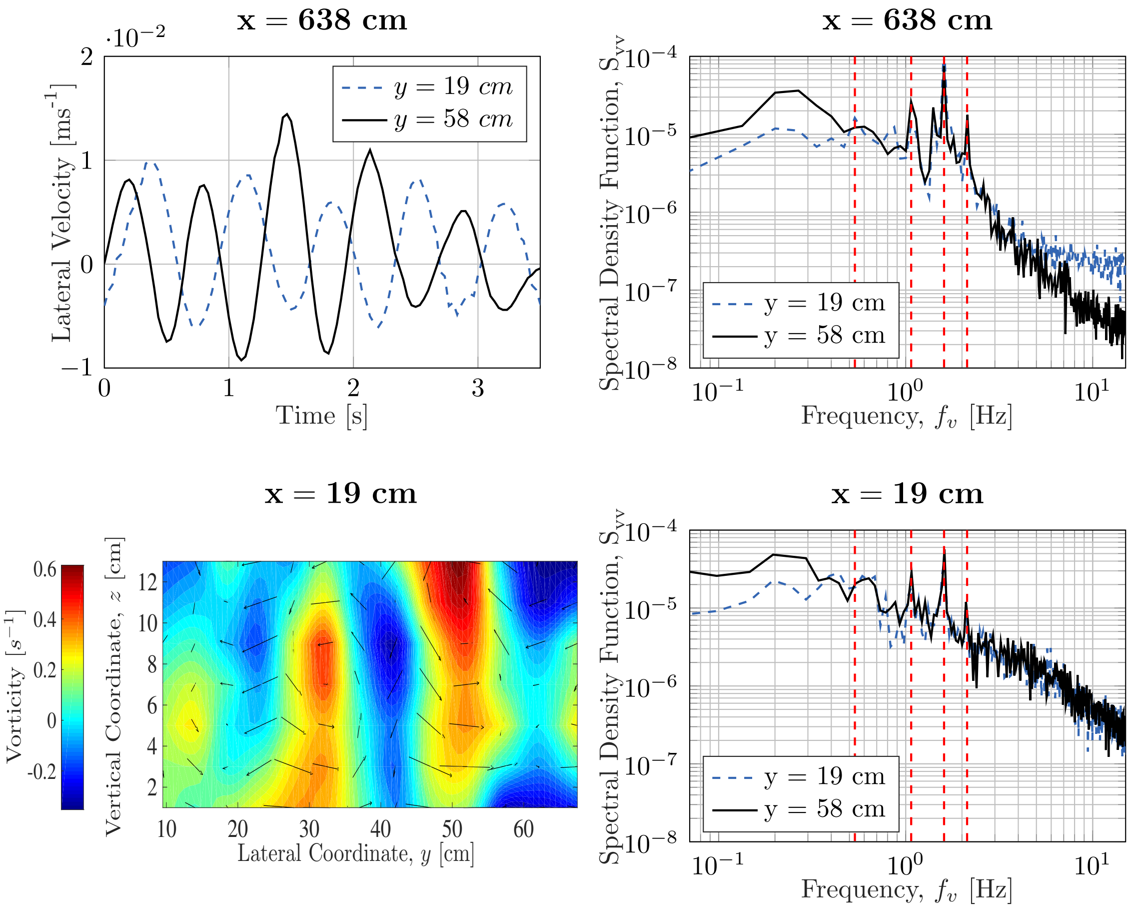

Figure 3.19: Downstream evolution of the power spectral density function. sPIV time series of lateral velocities at the measurement section (upper left) demonstrates there exists a dominant periodicity with a characteristic period of ~ 0.6 s that is anti-phased with the signal at the opposite side of the cross-section. This is confirmed by the peaks in the power spectra of the velocity signal (upper right), and four dominant signals were identified: 0.59, 1.08, 1.61, and 2.10 Hz. All of these signals could likewise be found in the power spectra near the exit from the bend vanes (lower right; spectra were calculated to the Nyquist frequency of 50 Hz, but have been trimmed for similarity to the sPIV data). Vortices caused by bend dynamics (lower left), therefore, among other upstream forcings, are clearly impacting the flow structure at the opposite end of the straight leg.

3.4.1 Paddlewheel

The first frequency, 0.59 Hz, can be readily identified with the energy input from the paddlewheel blades striking the water. The relationship between the inverter frequency and the revolutions per minute of the paddlewheel was determined from the velocity calibration:

$$f_{inverter} = \frac{0.75 f_{paddlewheel}}{60} \qquad \text{[Hz]} \tag{3.4}$$

From this relationship, and the 8 total paddlewheel blades, the frequency of the paddlewheel striking the water can be calculated. This is summarized for several conditions in Table 3.3.

Table 3.3: Paddlewheel frequency summary

Depth (cm)	Nominal Vel. (cm s^{-1})	$f_{inverter}$ (Hz)	$f_{paddlewheel}$ (RPM)	$f_{paddle,water}$ (Hz)	% Error on 0.59 Hz
6.3	20.0	6.6	4.950	0.66	11.8
9.5	20.0	5.8	4.350	0.58	1.7
19.0	20.0	5.1	3.825	0.51	13.6
38.0	20.0	6.3	4.725	0.63	6.8

Considering the power spectra frequency coordinate is subject to resolution error of ±0.03 Hz, these frequencies are remarkably similar to the spike in the power spectra.

What additionally promotes the paddlewheel as the mechanism behind this frequency is the fact that spikes in the power spectra for this frequency are primarily seen in the streamwise velocity component. As the paddlewheel acts evenly across the cross-section and distributed across the vertical profile, the primary axis along which the paddlewheel would oscillate is in the streamwise direction. Finally, this is the lowest frequency identified among the spikes in the velocity spectra, and is thereby most readily identified with the energy input into the system, in this case: the paddlewheel.

3.4.2 Kármán Shedding

The second frequency, $f = 1.08$ Hz, has been identified as the Kármán shedding off of the bend vanes. This signal was not identified in the ADV measurements prior to the exit from the bend vanes (with a notable exception where flow separates at the inner wall), but was especially present immediately downstream of the vanes. Furthermore, the frequency in question was primarily identified in the streamwise and lateral velocity components, as would be expected based on the two-dimensionality of the flow around the bend vanes.

What most commends the mechanism of Kármán shedding off of the vanes, however, is the fact that vortices shed from the bend vanes were visualized with surface tracers and subsequent video allowed for the timing of the vortex shedding. A period of just under $1s$ was determined from the surface tracer analysis, nearly equivalent to the $f = 1.08$ Hz. Figure 3.20 shows the vortices visualized with surface tracer.

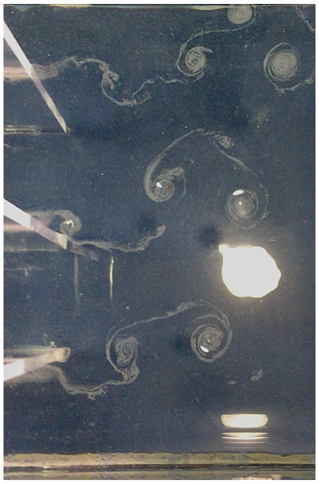

Figure 3.20: Kármán shedding off of the bend vanes

Given that this frequency is associated with shedding off of the bend vanes, the Strouhal number, defined as:

$$\mathbf{St} = \frac{fL}{U} \tag{3.5}$$

is calculated to be 0.11, where f is the shedding frequency, L is the characteristic length scale associated with the obstruction (2 cm), and U is the characteristic velocity, in this case given by the nominal velocity (20 cm s^{-1}). This is fairly consistent with experimental results in the wake of rectangular bluff bodies of similar Reynolds number ($\mathbf{Re} > 10^5$) (Roshko, 1955; Ahlborn et al., 2002; Lee, 1975).

The third frequency, $f = 2.10$ Hz, is almost precisely double this presumed shedding frequency (again subject to the resolution error of ± 0.03 Hz), and in the "near-field" region of the wake contains less energy than the $f = 1.08$ Hz. Therefore, this frequency is considered to be some form of harmonic response to the Kármán shedding.

3.4.3 Bend Vorticity

The last of the four frequencies identified from the power spectra, $f = 1.61$ Hz, can be associated with the vorticity caused by centrifugal forces in the "upstream" bend. In transect 7 of the bend measurements, the most significant spectral mode, aside from the supposed paddlewheel frequency, is this frequency of 1.61 Hz. It is presumed that the dominant mechanism at work generating vorticity in between the bend vanes at transect 7 is the overturning, evidenced by Figure 3.17. Because of the preeminence in spectral space and the supposed dominance of the overturning, the two were paired. Further confirmation would require a more extensive measurement regimen in the upstream bend, which was not performed as part of this study, though it is apparent that strong vorticity does result from the centrifugal forces in the bend (see Figure 3.19, lower left).

3.4.4 Flume Natural Frequency

One additional mechanism, not necessarily associated with generating any of the above frequencies but perhaps amplifying their strength, is the resonance of lateral oscillations with the natural frequency of the flume. This phenomenon has been observed in laboratory studies of vortex shedding behind rigid cylinders (Zima & Ackermann, 2002; Tinoco & Cowen, 2013; Viero et al., 2017), and results in the formation of surface waves. Because surface waves were observed in the sPIV data collection of this study, this mechanism was especially noteworthy.

Resonance occurs when a shedding frequency or some other imposed lateral oscillation nears the natural frequency of the flume, given by the gravity wave dispersion relationship:

$$f_{flume} = \left(\frac{ng}{4\pi B} \tanh\left(\frac{\pi n h}{B}\right) \right)^{1/2} \tag{3.6}$$

where n is the harmonic mode, g is the gravitational acceleration constant, B is the width of the cross-section, and h is the flow depth. Table 3.4 provides the natural frequency of the RWT geometry used in this study under a variety of operational depths.

Table 3.4: Flume natural frequencies under different operational conditions

Flow Depth, h (cm)	Natural Frequency (Hz) Mode 1	 Mode 2
6.4	0.51	0.99
9.5	0.61	1.15
19.0	0.81	1.36
38.0	0.96	1.42

These harmonic responses can act in response to a number of different mechanisms. For instance, at the low flow depths the Mode 1 response nears the paddlewheel frequency, while at the same time the Mode 2 response approaches the presumed vane shedding frequency. At deeper flow depths, however, the Mode 1 response approaches the vane shedding frequency, while the Mode 2 response approaches the presumed bend-induced vorticity frequency. The anti-phased signal that characterizes the surface waves in Figure 3.19 (upper left) is characteristic of a Mode 1 response, and could be amplifying the effects of the paddlewheel.

3.4.5 Quadrant Analysis

Finally, quadrant analysis was performed on ADV data at the presumed mid-cell lateral coordinate near the bed for the $h = 19\ cm$, large angle case (Case I.D. A5), both at transect 8 of the bend measurements ($x = 19\ cm$) and at the measurement section ($x = 638\ cm$). This upstream and downstream sampling was used to determine if the correlations of turbulent events changed along the straight section of the reactor when modified with longitudinal ridges. Figure 3.21 presents the results of this analysis, with grey scatter plots indicating the correlations at $x = 19\ cm$, black scatter plots indicating correlations at $x = 638\ cm$, and the bar graphs to the right summarizing the percentages in each quadrant. Quadrants are numbered with Q1 designating the upper right quadrant (positive-positive correlation) and proceeding counter-clockwise.

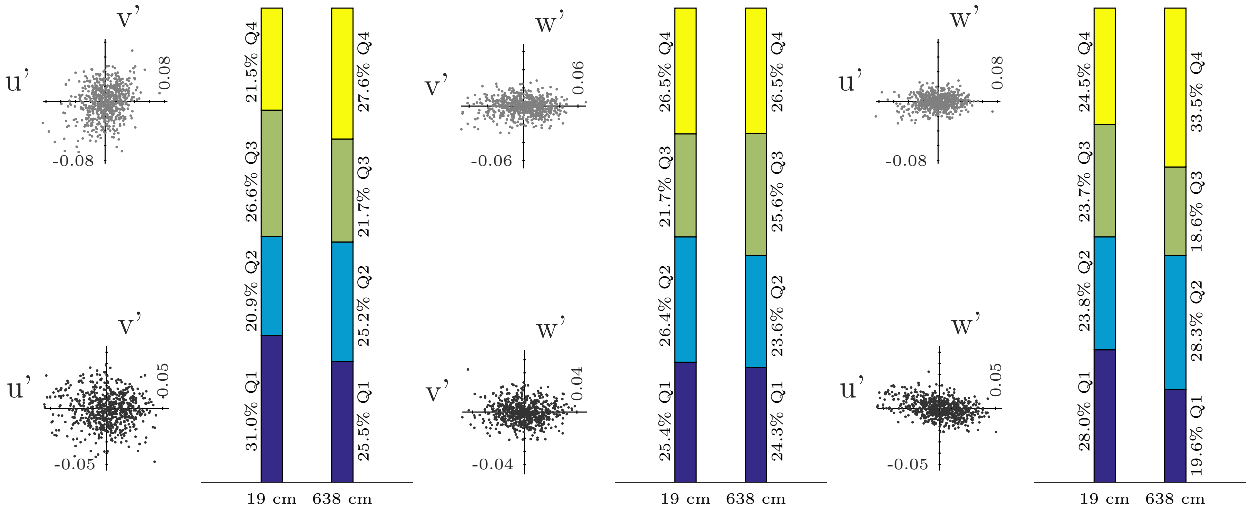

Figure 3.21: Quadrant analysis at upstream and downstream ends of measurement leg. Velocity signal correlations were sampled for $y = 28\ cm,\ z = 3\ cm$ at a location $x = 19\ cm$ (gray) and $x = 638\ cm$ (black) with the large angle bed modifications in place. Percentages in each quadrant are shown in the bar graphs at the right, with Q1 designating the upper right quadrant (positive-positive) and proceeding counter-clockwise. Both $u'v'$ and $u'w'$ show increases downstream in the Q2 and Q4 quadrants (negative correlations), however $v'w'$ shows little variation.

Both $u'v'$ and $u'w'$ showed increases along the measurement leg in Q2 and Q4 correlations (negative-positive and positive-negative), while $v'w'$ showed no substantive change. For $u'w'$, Q2 represents a positive fluctuation in the vertical with a simultaneous negative fluctuation in the streamwise velocity, denoting an updraft or an "ejection." Q4 represents a negative fluctuation in the vertical velocity with a simultaneous positive fluctuation in streamwise velocity, denoting a downdraft or "sweep." Positive correlations in $u'w'$ represent upward interactions (Q1) and downward interactions (Q3). Because of the increase in sweeps and ejections along the measurement leg, it was considered whether bursting phenomena near the bed could be having a significant influence on the flow structures. Nezu (1977) notes that bursting phenomena are a "quasi-cyclic" process which exhibits periodic behavior on average in space and time, but does not demonstrate perfectly periodic behavior at any one place or time. Because the power spectra are ensemble averaged, it was determined that these could contribute to the shape of this function, and should be considered for their effect.

Following Laufer and Narayanan (1971), the bursting period is given by Nezu as $t_B U_{max}/\delta =$ 4.0 to 5.0, where t_B is the bursting period, U_{max} is the maximum streamwise velocity, and δ is the boundary layer thickness. Assuming that the boundary layer thickness extends nearly to the free surface for the 19 *cm* depth case, the bursting frequency is approximately 0.20-0.26 Hz. This is in the "energy-containing eddies" portion of the power spectrum, but no spikes were found there and this was not deemed an overwhelming factor for the secondary currents.

3.4.6 Mechanisms Summary

The picture that emerges from the analysis of these dominant mechanisms can be summarized by Figure 3.22. It is again noted that these mechanisms have not been definitively paired with these frequencies, however there is good phenomenological evidence to believe that the three mechanisms: paddlewheel, vortex shedding, and centrifugal forces are the dominant physical processes involved in mixing the straight portions of the RWT reactor.

As a consequence, it may be observed that secondary currents of Prandtl's second kind are not among the energy containing mechanisms, despite being clearly visualized in the data. If bed modifications are to be used for the purpose of mixing the straight portions of reactors like this experimental facility, it will be necessary to either find ways of minimizing these existing flow structures or working in concert with them to maximize the vertical transport of nutrients and algal cells.

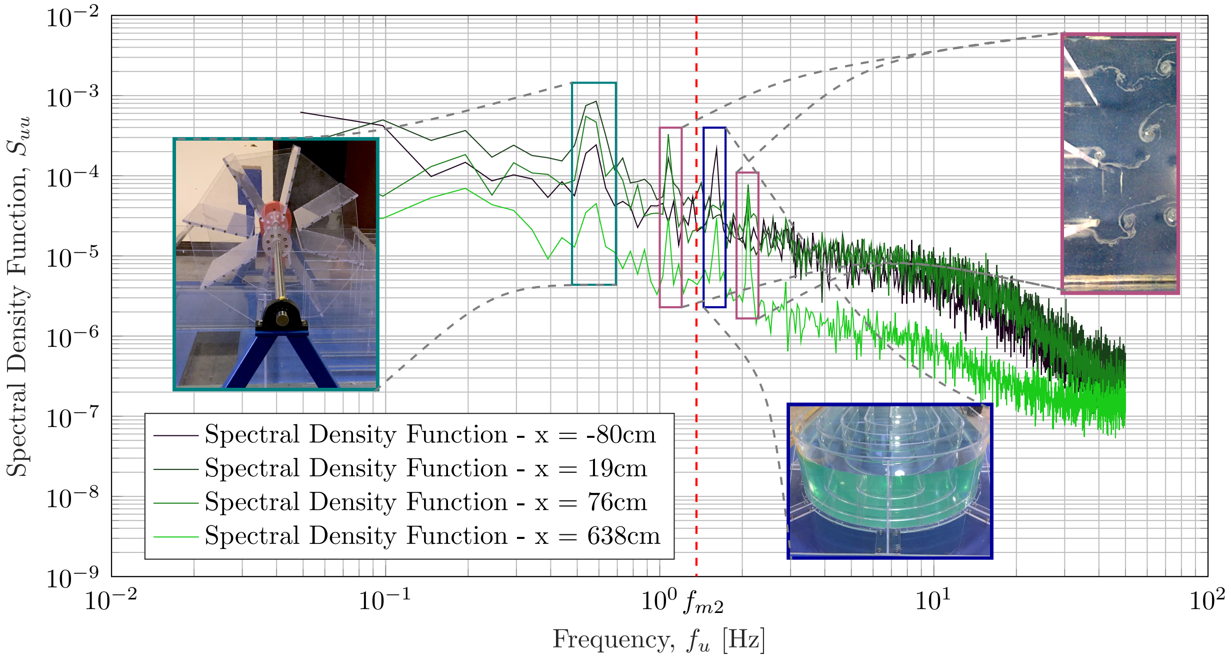

Figure 3.22: Summary of the dominant physical mechanisms as given by the power specta. The periodic effect of the paddlewheel persists at a frequency of 0.5-0.6 Hz. Vortex shedding off of the bend vanes at a frequency of $\sim$ 1.1 Hz yields a Strouhal number of 0.11, consistent with experimental results in wakes of rectangular bluff bodies. This, likewise, produces a harmonic response at $\sim$ 2.1 Hz. Overturning currents in the "upstream" bend caused by centrifugal forces generates a signal of $\sim$ 1.6 Hz. For the 19 cm depth, the mode 2 natural frequency of the flume is calculated to be 1.36 Hz, which could cause amplification of the shedding signal or the overturning signal.

3.5 Conclusions

In summary, the ADV and sPIV results have been presented, and the following observations have been made from the available data:

1. There exists a mean lateral flow that is stronger than the magnitude of the cellular, secondary currents;
2. Secondary flows can be visualized, however, in the mean velocity fields and the turbulence statistics;
3. Secondary flows for the deeper flow depths do not extend all the way to the free surface;
4. This yields little to no effect on the free surface lateral currents for deeper flow depths;
5. Consequently, this yields little to no effect on the surface divergence for deeper flow depths;
6. Several frequencies of interest are identified through signal processing of the velocity measurements; and
7. Good agreement exists between sPIV and ADV measurements, which captures phenomena such as the velocity "dip," and boundary layer development.

From these observations the two motivating questions were addressed. First, the question of whether secondary currents could be induced in a full-scale RWT reactor was addressed with the following conclusions:

1. "Yes," cellular secondary currents can be generated in a full-scale reactor;
2. This can be seen both in the ADV and sPIV mean velocities and turbulence statistics, but also in the production term of streamwise vorticity;
3. These cellular, secondary currents do not have full expression, particularly near the free surface;
4. This is a result of insufficient boundary layer development in the deeper facilities due to overturning at the bends disrupting the boundary layer structure; and

5. Facilities that seek to influence the free surface region with bed modifications may require substantial aspect ratios.

Second, the question of what the dominant physical processes are for mixing in the straight portions of the reactor was raised. The following conclusions were drawn:

1. Dominant frequencies identified from the power spectra at the measurement section are all present at the upstream bend exit, and therefore are not attributable to the bed modifications;
2. The 0.59 Hz frequency can be associated with the energy input of the paddlewheel striking the water;
3. The 1.08 Hz and 2.10 Hz frequencies can be associated with Kármán shedding in the wake of the bend vanes;
4. The 1.61 Hz frequency can be associated with the vorticity caused by centrifugal forces in the upstream bend;
5. Depending on the flow depth and cross-section geometry, these frequencies can be amplified by resonance with the Mode 1 or Mode 2 natural frequencies of the flume; and
6. Other phenomena exist in the flume, like sweeps and ejections seen in the quadrant analysis, however they do not appear as high-energy mechanisms in the power spectra.

It has been observed in Chapter 1 that there have been a growing number of hydrodynamic studies into the peculiarities of these reactor flows. In particular, there have been several studies that seek to make low-cost modifications to existing reactor structure in order to better approximate ideal growing conditions for the microalgae. The results of these experiments have shown that dynamics in the reactor are a complex composite of boundary layer flows, secondary currents, resonance structures, energy input conditions, and shear flows (i.e. bend vane wake). Future studies that would seek to enhance mixing in the straight sections of the flume need to account for the velocity profile, vorticity, and turbulence structure leaving the 180^o bends, as there is a significant amount of energy associated with these flow structures. In particular, generation of secondary currents from bed modifications will require methods of mitigating these other flow structures or working cooperatively with them.

It is further submitted that future studies that would seek to represent these facilities in straight flume, as in the case of Citerone (2016), need to perform the additional step of integrating results back into the larger framework of the open RWT in order to make practicable conclusions. Bend dynamics were found to persist for significant lengths in sufficient energy to overwhelm low-impact mixing strategies.

Finally, it is submitted that in spite of all of the above caveats, bed modifications were able to introduce a measurable influence on the vertical mixing, and could represent a future method for implementing the “flashing light” effect and possibly enhanced gas transfer. This enhanced gas transfer will be the subject of the next chapter.

Chapter 4

Results and Discussion: Gas Transfer

The final component of this study was to observe exchange processes, namely gas transfer at the free surface, in relation to the secondary currents and resulting velocity divergence at the free surface. It was observed in Chapter 3 that secondary currents did form in the straight portions of the reactor, but they were overwhelmed by other energy-containing structures and produced little effect on the surface divergence, particularly for larger flow depths. Therefore, the effects on the gas transfer velocity were anticipated to be minimal. This chapter will explore this impact on gas transfer through the re-aeration curves and calculated transfer velocities, which will then be compared with experimental values from other studies.

4.1 Re-aeration Curves

The re-aeration curves were a direct output from the ODO meter. Figure 4.1 presents the raw time series of DO measurements, in units of $mg\ DO/L$, for the 9.5 cm, 19 cm, and 38 cm flow depths in both the empty bed condition and the large angle condition. For the 9.5 cm depth, 20 $cm\ s^{-1}$ nominal velocity case, two trials were performed. The first, like all other modified bed runs, only included bed modifications along the measurement leg of the flume. The second added longitudinal ridges to both of the straight sections of the reactor to increase the effect of the secondary currents. For comparison purposes, these were performed immediately following two trials of the empty bed condition (denoted Trial 1 and Trial 2 in Figure 4.1). While the two trials tended toward different saturation levels (in $mg\ DO/L$), which is a function of the temperature and barometric pressure, the addition of ridges to the second straight leg showed no substantive change and was not carried forward in the analysis.

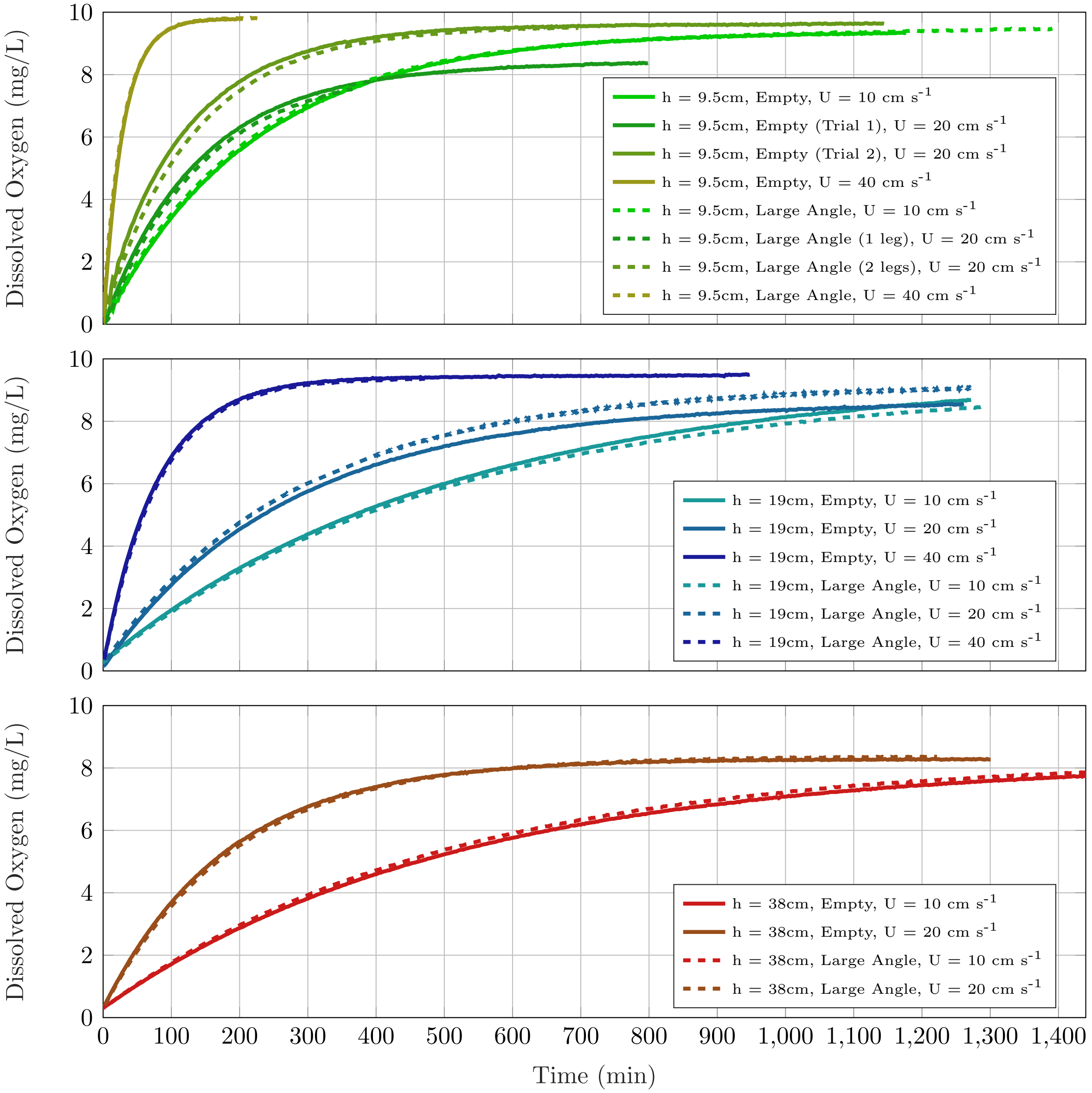

Figure 4.1: Raw re-aeration measurements, for the 9.5 *cm* depth (greens), 19 *cm* depth (blues), and 38 *cm* depth (reds).

It is evident from Figure 4.1 that the raw data required vastly different times to reach a presumed saturation condition (cf. $h = 9.5\ cm$, $U = 40\ cm\ s^{-1}$ and $h = 38\ cm$, $U = 10\ cm\ s^{-1}$), and that the saturation condition in absolute units varied significantly from one run to another. It was therefore deemed necessary to express these re-aeration curves in a normalized, percent-saturation condition. To do so, the experimental data was fitted using least squares regression to an equation of the form:

$$C_{DO} = C_{DO,sat}\Big[1 - \exp\Big\{-\frac{A}{V}\overline{k}t\Big\}\Big] \tag{4.1}$$

where the interfacial area, A ($\sim 16.6\ m^2$), and the volume, V (varied by run), were known. The regression variables, therefore, were the saturation DO concentration, $C_{DO,sat}$, and the average transfer velocity, $\overline{k}$. All of the regression functions had an excellent fit to the experimental data, with $R^2 > 0.99$.

The saturation DO concentration was used to normalize the concentration measurements, and the resulting plots are given in Figure 4.2. While the flow depth (red, blue, green) and the flow velocity (color shades) had a significant impact on the shape of these curves, the bed modifications (dashed lines) showed no consistent or significant deviation from the empty bed cases (solid lines). This was the anticipated response from the sPIV data that showed little impact on the surface divergence in any of these three flow depths.

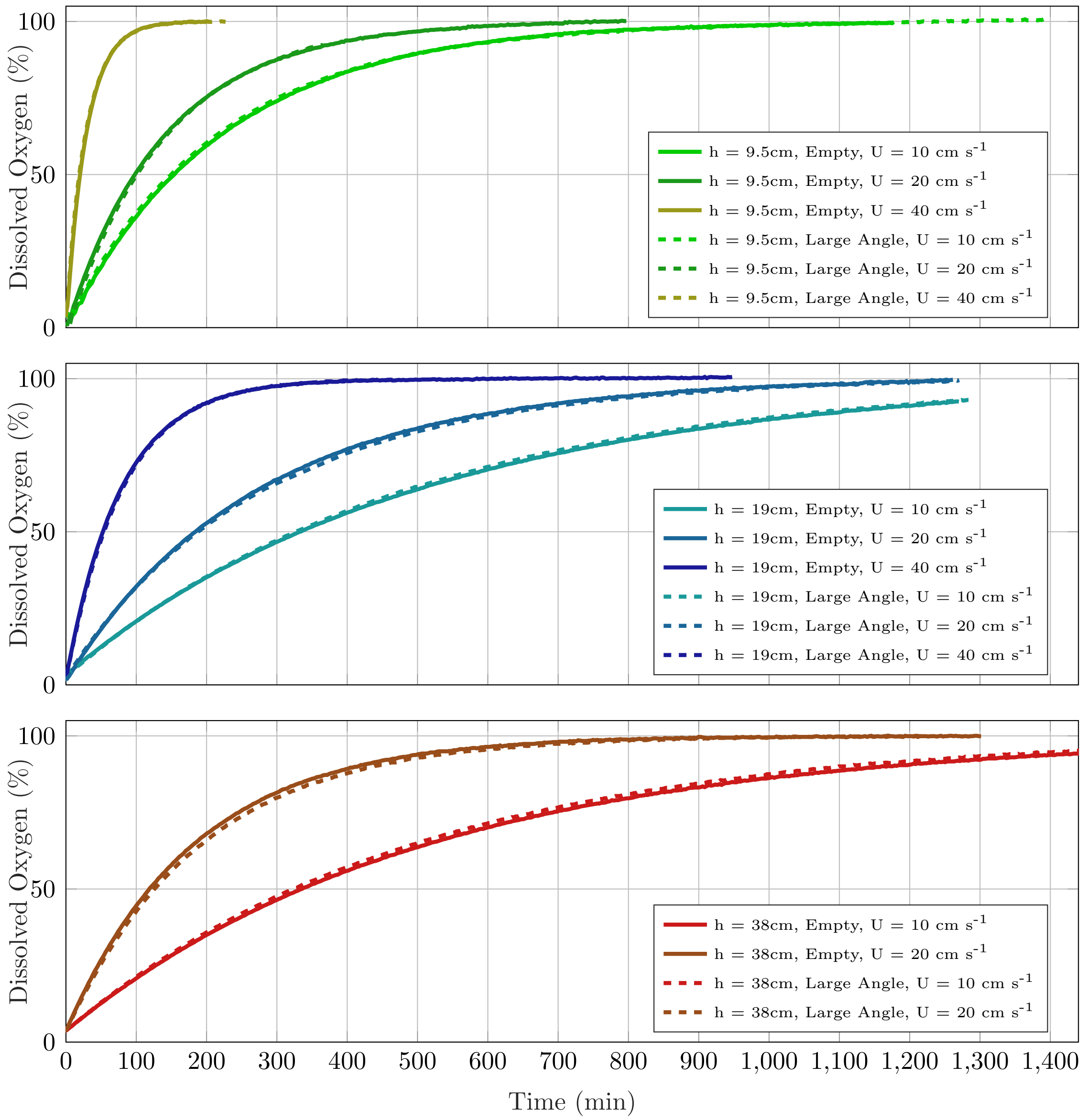

Figure 4.2: Re-aeration curves expressed in percent saturation, for the 9.5 *cm* depth (top), 19 *cm* depth (middle), and 38 *cm* depth (bottom). No consistent benefit was observed in the gas transfer velocity from the modifications of the bed (i.e. comparing solid lines to dashed lines). Experiments were run for a maximum of 21-24 hours, which in some cases was not sufficient to achieve 100% saturation, however all runs followed Equation 4.1 well and could be extrapolated to the saturation condition.

4.2 Transfer Velocities

In addition to the saturation concentration, the regression output the average transfer velocity as one of the regression variables. Average transfer velocities are provided in Table 4.1.

Table 4.1: Transfer velocities by flow depth, lining condition, and nominal velocity.

Depth (cm)	Lining Condition	Nom. Velocity ($cm\ s^{-1}$)	Transfer Velocity ($cm\ hr^{-1}$)
9.5	Empty	10.0	2.56
9.5	Large Angle	10.0	2.58
9.5	Empty	20.0	3.98
9.5	Large Angle	20.0	4.03
9.5	Empty	40.0	19.77
9.5	Large Angle	40.0	19.62
19.0	Empty	10.0	2.23
19.0	Large Angle	10.0	2.29
19.0	Empty	20.0	4.12
19.0	Large Angle	20.0	3.96
19.0	Empty	40.0	14.43
19.0	Large Angle	40.0	14.30
38.0	Empty	10.0	4.39
38.0	Large Angle	10.0	4.60
38.0	Empty	20.0	12.55
38.0	Large Angle	20.0	11.85

These were then plotted against nominal velocity and flow depth in Figures 4.3 and 4.4, respectively, for comparison purposes. The transfer velocity followed a fairly intuitive relationship with the nominal velocity, monotonically increasing for all flow depths with increasing flow velocities. As the nominal velocity increases so does the bulk Reynolds number and associated turbulence, which leads to faster mixing and renewal of the surface diffusive boundary layer. It is noteworthy, as well, that the large angle cases followed the empty bed cases fairly closely as was seen in the re-aeration curves.

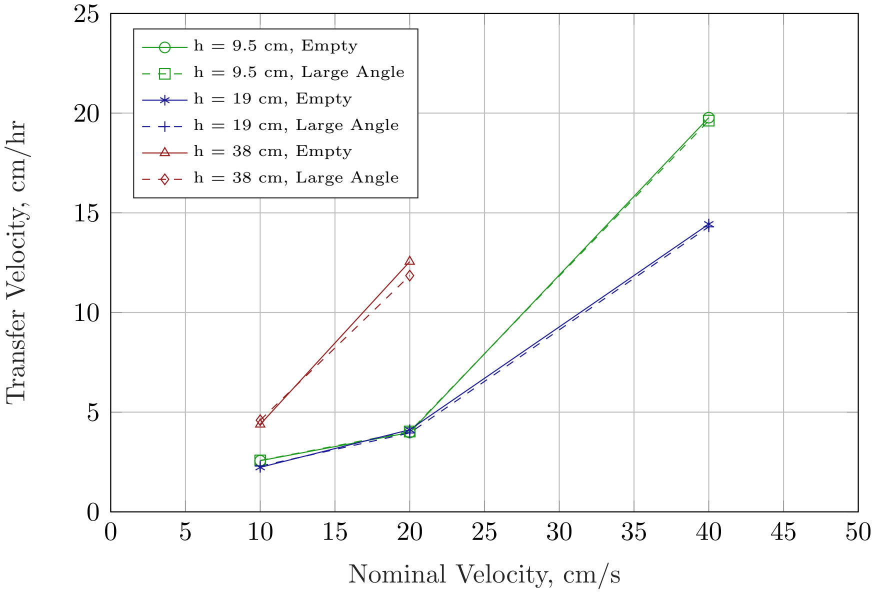

Figure 4.3: Transfer velocities as a function of nominal velocity. In accordance with intuition, the transfer velocity follows a monotonically increasing relationship with the flow velocity for all flow depths. Little difference is seen, however, between the modified bed and empty bed cases.

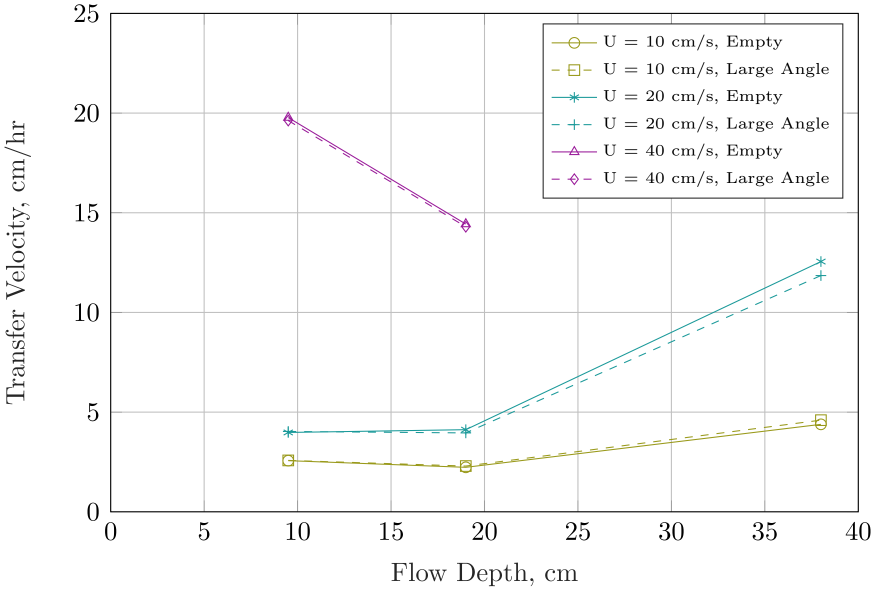

Figure 4.4: Transfer velocities as a function of flow depth. The relationship between the transfer velocity and the flow depth in this set of experiments is complex. A slight decrease is seen from $h = 9.5\ cm$ to $h = 19\ cm$ for nearly all of the flow velocities and lining conditions, with a subsequent increase in moving to $h = 38\ cm$. This varies from the direct proportionality $k \propto h^{1/2}$ found by Sanjou et al. (2017).

The relationship to the flow depth was less intuitive. For nearly all the flow velocity and bed modification conditions, a decrease in transfer velocity was observed from the 9.5 *cm* depth condition to the 19 *cm* depth condition (with the exception of the Empty bed, $U = 20\ cm\ s^{-1}$ case). A subsequent large increase in transfer velocity was then observed from the 19 *cm* depth condition to the 38 *cm* depth condition.

This increasing trend in transfer velocity with depth was observed by Sanjou et al. (2016), and they ascribe it to the fact that the vortices shed from bottom roughness scale with the depth. Presumably, that is to say that there is greater potential to renew the surface with hypoxic parcels of fluid when the characteristic length is greater, though the precise rationale is unspecified. Regardless, the proportionality, $k \propto h^{1/2}$, is confirmed by their experimental results (Sanjou et al., 2016, 2017).

The question remains, why is there a decreasing trend in the present data set between the 9.5 *cm* and 19 *cm* depths? This may be best explained by appealing to the discussion from Chapter 3. It was observed there that a number of dominant mechanisms influence the hydrodynamics of the straight portion of the reactor. Notably, the resonance structures associated with the natural frequency of the flume follow a binary response, amplifying certain frequencies and leaving others unaffected. In the lower flow depths this yielded strong oscillatory lateral currents producing surface waves. It is well documented that the presence of surface waves, at a variety of scales down to capillary waves, yield an increase in the transfer velocity (Coantic, 1986; Zappa et al., 2002), therefore it is hypothesized that the presence of small-scale waves at lower flow depths yielded increased levels of gas transfer. This would be further confirmed by the fact that the largest decrease is observed in the $40\ cm\ s^{-1}$ velocity for which the surface waves were the strongest.

4.3 Comparison to Other Experimental Results

The transfer velocities were then combined with the surface divergence data for comparison with surface divergence model results attained by other experimental studies. The model assumptions are based on molecular diffusion across the interface, for which a diffusivity is required. A molecular diffusivity of $D_z = 1.8 \times 10^{-5}\ cm^2\ s^{-1}$ for dissolved oxygen in water at $20^o\ C$ was adopted (Thibodeaux & Mackay, 2010). The root-mean-square (RMS) of the surface divergence was then averaged over the sPIV sampling domain, and the parameter, $\sqrt{D_z \langle \beta \rangle_{rms}}$, from the surface divergence model was calculated. This was plotted against the measured transfer velocities in Figure 4.5 along with the experimentally determined relationships summarized in Turney and Banerjee (2013, see also Chapter 1), and following the form:

$$\overline{k} = c\sqrt{D_z \langle \beta \rangle_{rms}} \tag{4.2}$$

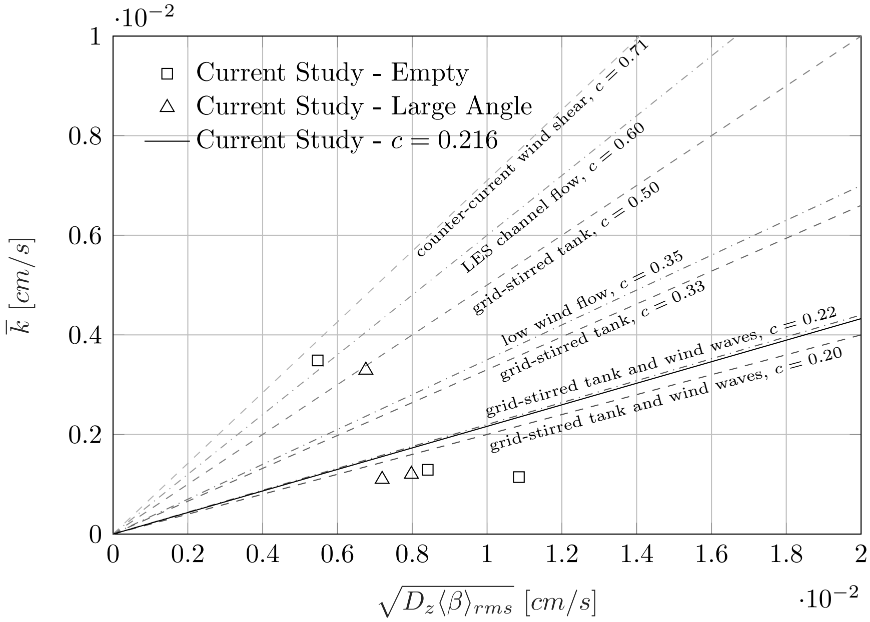

Figure 4.5: Experimental data plotted in the form of the surface divergence model with experimentally determined coefficients from the summary of Turney and Banerjee (2013).

It may first be noted that this method makes one important assumption, namely that the surface divergence characterizing the measurement domain is representative of the entire interfacial area. It is recognized that the paddlewheel will likely be a significant source of dissolved oxygen entrainment and that mixing occurs more in the bends than it does in the straight portions of the reactor. However, the majority of the surface area for the RWT reactor is found in the straight portions, and therefore this assumption will be adopted with the recognition that comparison with other experimental results may confirm or challenge its validity.

Figure 4.5 demonstrates that the 9.5 *cm* and 19 *cm* data are found just outside the envelope of previous experimental relationships, on the low side indicating that the measured transfer velocity was lower than anticipated by the surface divergence measurements and previous relationships. This was similar, however, to the grid-stirred tank with wind waves experiments of Z. Xu et al. (2006) and Law and Khoo (2002), and the linear regression of the data yielded a similar coefficient of 0.216 (with admittedly large scatter). The 38 *cm* depth plotted much higher than the other two cases, which supported the need for a relationship that is based on the flow depth, as proposed by Sanjou et al. (2016, 2017).

Thus, a similar process was performed by incorporating the flow depth, the mean streamwise velocity, and the surface turbulence kinetic energy into the following forms:

$$\overline{k} = c\sqrt{D_z \langle\beta\rangle^2_{rms} \frac{h}{U_s}} \tag{4.3a}$$

$$\overline{k} = c\sqrt{D_z \langle\beta\rangle^2_{rms} \frac{h}{k_s^{1/2}}} \tag{4.3b}$$

The surface turbulence kinetic energy was averaged over a lateral swath of the measurement domain such that it was not impacted by areas of poor vector quality. The surface velocity remained relatively unaffected by the vector density for the cases under consideration, and therefore was averaged over the entire sPIV measurement domain. The resulting relationships using the models of Sanjou et al. are provided in Figures 4.6 and 4.7, for the streamwise velocity formulation (Equation 4.3a) and surface turbulence kinetic energy formulation (Equation 4.3b), respectively.

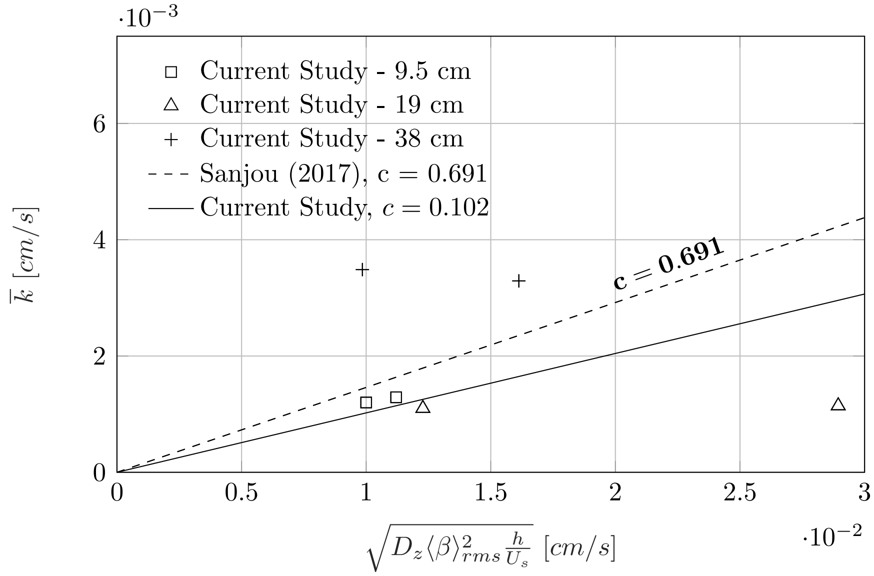

Figure 4.6: Experimental data plotted against the Surface Divergence model of Sanjou et al. (2017) as a function of the depth and mean surface velocity.

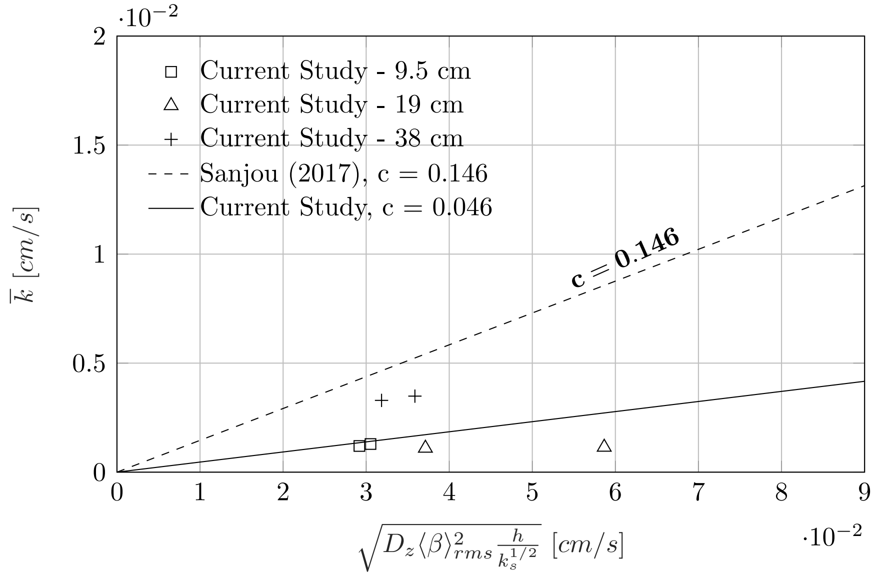

Figure 4.7: Experimental data plotted against the Surface Divergence model of Sanjou et al. (2017) as a function of the depth and mean surface turbulence kinetic energy.

Again, there is a difference of methodology between this experimental work and that of Sanjou et al. In the current study, the dissolved oxygen is measured at one point as a function of time, and again employs the assumption that the measurement domain is characteristic of the entire interface. In the Sanjou et al. (2016, 2017) experiments, the change in dissolved oxygen concentration was measured using two DO probes over a span of 7.0-9.0 m, which resulted in measurements of the change of DO over a particular span. This is more restricted in its domain to the area where surface divergence measurements could be taken, and thus relationships between measured transfer velocity and the surface divergence model do not require the assumption that was made in the present study.

The experimental results in the current study show some deviation about the surface divergence models of Sanjou et al. (2017). In the case of the surface velocity formulation (Figure 4.6), there is still considerable scatter between the 38 cm depth and the lower flow depths. Additionally, least squares regression yields a coefficient significantly smaller than that proposed by Sanjou et al. Likewise, in the case of the surface turbulence kinetic energy formulation (Figure 4.7), all of the points fall below the relationship proposed by Sanjou et al., and the coefficient was only about 30% of that previously proposed.

The precise reason for these discrepancies is not certain, however, it would adequately be explained by the fact that the measurement domain is not in fact representative of the total interface in the RWT reactor. If the bends and the paddlewheel were factored into the k_s, effectively increasing this value, the value on the abscissa would be lowered effectively increasing the slope of the regression line. To fully understand how representative the measurement section is would require additional measurements of the surface velocity fields near the paddlewheel and at the bends, and represents an area of future work. If this is the case, however, it indicates that the primary regions of entrainment of atmospheric mass are located near the paddlewheel and at the bends.

4.4 Conclusions

In summary, the re-aeration curves have been processed using regression techniques and the theoretical form given by Fickian diffusion, and the following observations have been made:

1. The measured re-aeration curves follow Fickian diffusion;
2. No consistent deviation from the unpopulated bed cases was seen in the cases with bed modification, as anticipated by the lack of measurable increase in surface divergence;
3. Transfer velocities showed a monotonically increasing relationship with the nominal velocity, in accordance with the expected increase in turbulence levels;
4. Transfer velocities showed a complex interaction with the flow depth, likely a result of the generation of surface waves at low flow depths;
5. The results showed fair agreement with other experimentally-derived surface divergence models, but demonstrated a strong dependence on the flow depth;
6. This was not entirely captured by the modifications proposed by Sanjou et al. (2016, 2017), and it is thought that discrepancies could be explained by the effects of the paddlewheel and bends; and
7. If this is the case, the entrainment of atmospheric material in the flow is largely driven by the smaller surface areas outside of the straight portions of the reactor.

Thus, it is fairly evident that the addition of bed modifications did not significantly impact the gas transfer across the free surface. This does not imply, however, that the production of strong, secondary currents would not increase the transfer velocity, as it has been demonstrated already that the secondary currents are currently being overwhelmed by other flow structures in the straight portions of the reactor. On the contrary, it is demonstrated that the straight portions of the reactor represent a significant area over which gas transfer across the interface is clearly limited and could be optimized. It is submitted that if efficient introduction of atmospheric carbon is beneficial to the algae development and cost reduction of operating these facilities, then further emphasis and research needs to be devoted to these suboptimal regions like the straight legs of the RWT.

Chapter 5

Final Discussion & Conclusions

In closing, the current chapter will draw together the diverse elements of this study into some final conclusions and suggestions for future work, followed by some final remarks to set the current study in its broader context.

5.1 Final Conclusions

In review, it was concluded in Chapter 3 that secondary currents could be visualized in the straight portions of the RWT reactor in both mean velocity measurements and turbulence statistics, however impacts on the free surface, particularly the velocity divergence, were limited to very low flow depths. It was thereby determined that the bend effects were disrupting the boundary layer flow, and development of the boundary layer thickness required significant lengths for typical operating depths such that vorticity generated near the bed would impact the surface region. It was further demonstrated that there were several other energy-containing flow structures that overpower the secondary currents. These were identified as the effects of the paddlewheel striking the water, the vortex shedding off of the bend vanes, the vorticity induced by centrifugal forces in the bends, and the resonance structures associated with the flume geometry. In light of these complexities, it was recognized that failure to incorporate these elements represents an area of oversight for experiments performed in straight flumes.

In Chapter 4, it was concluded that no consistent effect of the bed modifications and cellular, secondary currents was measurable in the gas transfer velocity. However, the flow depth and culture velocity had significant effects on the transfer velocity. In particular, it was shown that the nominal velocity of the fluid demonstrated a monotonically increasing relationship with the transfer velocity, but that the transfer velocity demonstrated non-linearities with respect to the flow depth. The non-linearities were ascribed to capillary waves that were observed at the free surface of the low flow depth runs. Experimental results demonstrated good agreement with theoretical constructions of the surface divergence model, and confirmed the additional dependence on flow depth as observed by Sanjou et al. (2016, 2017). Models proposed by Sanjou et al. did not accurately represent the current experimental results, but served as an indication that surface exchange processes were concentrated in the paddlewheel region and reactor bends. It was proposed, as a result, that the straight portions of the reactor represent areas of suboptimal gas transfer and should be a focus in future studies that seek to maximize interfacial transfer.

Taken in concert, then, the following conclusions can be drawn:

1. Longitudinal ridges did not increase the gas transfer in the RWT reactor, as in the straight flume experiments of Citerone (2016);
2. However, cellular, secondary currents can be promoted by longitudinal ridges in the straight portions of the reactor; and
3. There are plausible reasons for why these secondary currents aren't fully expressed at the free surface and in the gas transfer, and secondary currents could still represent an effective method of introducing atmospheric carbon into the growth medium if these inhibiting features are overcome.

5.2 Future Work

In light of these conclusions, several areas of future work have been identified. First, it was observed that the paddlewheel pulses, vortex shedding off of the bend vanes, and bend-induced vorticity were overwhelming the secondary currents, and while there exist several studies characterizing the paddlewheel effects (see Ali et al., 2014; Hadiyanto et al., 2013) and the bend dynamics (see Liffman et al., 2013), to the author's knowledge the downstream effects of these mechanisms and of the vortex shedding remain largely unexplored. Further study should be devoted to these phenomena in the application of open RWTs, and how they may be overcome in promoting vertical mixing and streamwise vorticity.

Second, it is proposed that the measurement section be studied in greater lateral and vertical resolution and that additional cross-sections be considered along the measurement leg. It was observed in Chapter 1 that the governing equation for the transport of streamwise vorticity was composed of a generation and a suppression term based on the second derivatives of the Reynold's stresses. Because the vertical resolution of this study consisted of three swaths, the second derivatives in the vertical were meaningless over the measurement domain. Further resolution in the cross-section (both lateral and vertical) could provide insights into local "hot spots" of vorticity generation and suppression. Additionally, the introduction of a second measurement section could provide measurements of streamwise gradients, giving insights into the streamwise development of these structures as well as other terms of the vorticity equation, like the vortex stretching term that characterizes secondary currents of Prandtl's first kind and the primary turbulent stress term.

Third, further work is proposed on characterizing the free surface in the reactor bends and the gas transfer induced by the paddlewheel. It was observed that these could be areas of locally intense gas transfer, and if entrainment of atmospheric material is to be the method of introducing carbon to the growth medium, these regions need to be better understood for their relative importance to the transfer velocity. This would also allow for better comparisons with existing experimental data instead of assuming the straight portions of the reactor as the primary regions of gas transfer.

Finally, it is important that these hydrodynamic considerations be put back into the context of the biological requirements of the microalgae. Therefore, trials with actual growth media and algal cells are required to elucidate some of the externalities to this study (e.g. shear stresses, temperature effects, power inputs). It is proposed that a similar study be performed with a "typical" algal strain in which growth rates can be compared, at fixed intervals, between the unpopulated bed case and the longitudinal ridges case. This will aid in the transition from the experimental realm to the operational facility.

5.3 Final Remarks

In the vein of the final recommendation for future work, it is to be remembered that the present study represents a strictly hydrodynamic approach to evaluating the feasibility of cellular, secondary currents in promoting conditions that are known to benefit the growth of microalgae. In so framing the problem, this opens the study up to a number of externalities that could produce counterintuitive results when applied to the complex interactions that take place between biological and physical processes. This study represents a preliminary evaluation of the feasibility of longitudinal ridges to promote vertical mixing and gas transfer in open RWT reactors.

That said, there is good reason, based on these findings, to say that longitudinal ridges along the bed are capable of promoting cellular, secondary currents and consequent vertical mixing. While increase in gas transfer was not observed in this study, the findings do not preclude the increase in transfer velocity through these mechanisms. Thus, the plausibility of this method in increasing algae growth rates and cost-effectiveness of these facilities remains intact, however it is demonstrated that the problem is, at the same time, more complex than first imagined and will require innovative solutions that interact with the facility as a comprehensive whole and not an array of disparate parts.

References

Ahlborn, B., Seto, M. L., & Noack, B. R. (2002). On drag, strouhal number and vortex-street structure. *Fluid Dynamics Research*, *30*(6), 379–399.

Ali, H., Cheema, T. A., & Park, C. W. (2014). Effect of paddle-wheel pulsating velocity on the hydrodynamic performance of high-rate algal ponds. *Journal of Energy Engineering*, *141*(4), 04014039.

Arenas, E., Palacio, R., Juantorena, A., Fernando, S., & Sebastian, P. (2016). Microalgae as a potential source for biodiesel production: techniques, methods, and other challenges. *International Journal of Energy Research*.

Banerjee, S. (1990). Turbulence structure and transport mechanisms at interfaces. In *Ninth international heat transfer conference* (Vol. 1, p. 395-418).

Banerjee, S., Lakehal, D., & Fulgosi, M. (2004). Surface divergence models for scalar exchange between turbulent streams. *International Journal of Multiphase Flow*, *30*, 963-977.

Banerjee, S., & MacIntyre, S. (2004). The air-water interface: Turbulence and scalar exchange. *Advances in Coastal and Ocean Engineering*, 181-237.

Banerjee, S., Scott, D., & Rhodes, E. (1968). Mass transfer to falling wavy liquid films in turbulent flow. *Industrial & Engineering Chemistry Fundamentals*, *7*(1), 22–27.

Benson, B. B., & Krause, D. (1980). The concentration and isotopic fractionation of gases dissolved in freshwater in equilibrium with the atmosphere. 1. oxygen. *Limnology and Oceanography*, *25*(4), 662–671.

Benson, B. B., & Krause, D. (1984). The concentration and isotopic fractionation of oxygen dissolved in freshwater and seawater in equilibrium with the atmosphere. *Limnology and oceanography*, *29*(3), 620–632.

Blakely, C. D. (2014). Experimental studies of delta wing parameters in open channel raceway determined via validated computational fluid dynamics. *All Graduate Theses and Dissertations. Paper 3291*.

Borowitzka, M. A. (2016). Algal physiology and large-scale outdoor cultures of microalgae. In M. A. Borowitzka, J. Beardall, & J. A. Raven (Eds.), *The physiology of microalgae* (Vol. 6, p. 601-635). Springer.

Chisti, Y. (2007). Biodiesel from microalgae. *Biotechnology advances*, *25*(3), 294–306.

Chisti, Y. (2013). Constraints to commercialization of algal fuels. *Journal of biotechnology*, *167*(3), 201–214.

Chisti, Y. (2016). Large-scale production of algal biomass: Raceway ponds. In F. Bux & Y. Chisti (Eds.), *Algae biotechnology: Products and processes* (p. 21-40). Springer International Publishing Switzerland.

Citerone, V. R. (2016). Enhancing gas transfer at an air-water interface through strengthened secondary flows motivated by algal biofuel production. *MS Thesis, Cornell University.*

Coantic, M. (1986). A model of gas transfer across air-water interfaces with capillary waves. *Journal of Geophysical Research: Oceans*, *91*(C3), 3925–3943.

Coles, D. (1956). The law of the wake in the turbulent boundary layer. *Journal of Fluid Mechanics*, *1*(02), 191–226.

Culbertson, J. K. (1967). Evidence of secondary circulation in an alluvial channel. *US Geological Survey Professional Paper*, D214–D216.

Danckwertz, P. (1951). Significance of liquid-film coefficients in gas absorption. *Industrial & Engineering Chemistry*, *43*(6), 1460–1467.

Demirbas, A. (2008). *Biodiesel: a realistic fuel alternative for diesel engines.* Springer, London. (doi: 10.1007/978-1-84628-995-8)

Demirbas, A. (2010). Use of algae as biofuel sources. *Energy conversion and management*, *51*(12), 2738–2749.

Fortescue, G., & Pearson, J. (1967). On gas absorption into a turbulent liquid. *Chemical Engineering Science*, *22*(9), 1163–1176.

Godfrey, A. H. (2012). An investigation into delta wing vortex generators as a means of increasing algae biofuel raceway vertical mixing including an analysis of the resulting turbulence characteristics. *All Graduate Theses and Dissertations. Paper 1338.*.

Goring, D. G., & Nikora, V. I. (2002). Despiking acoustic doppler velocimeter data. *Journal of Hydraulic Engineering*, *128*(1), 117–126.

Greenwell, H., Laurens, L., Shields, R., Lovitt, R., & Flynn, K. (2009). Placing microalgae on the biofuels priority list: a review of the technological challenges. *Journal of the Royal Society Interface*, rsif20090322.

Grobbelaar, J. U. (1994). Turbulence in mass algal cultures and the role of light/dark fluctuations. *Journal of Applied Phycology*, *6*(3), 331-335.

Guo, M., Song, W., & Buhain, J. (2015). Bioenergy and biofuels: History, status, and perspective. *Renewable and Sustainable Energy Reviews*, *42*, 712-725.

Hadiyanto, H., Elmore, S., Van Gerven, T., & Stankiewicz, A. (2013). Hydrodynamic evaluations in high rate algae pond (hrap) design. *Chemical engineering journal*, *217*, 231–239.

Hanagata, N., Takeuchi, T., Fukuju, Y., Barnes, D. J., & Karube, I. (1992). Tolerance of microalgae to high co2 and high temperature. *Phytochemistry*, *31*(10), 3345-3348.

Herlina, N., & Jirka, G. (2008). Experiments on gas transfer at the air-water interface induced by oscillating grid turbulence. *Journal of Fluid Mechanics*, *594*, 183-208.

Higbie, R. (1935). On the adsorption of a pure gas into a still liquid during short periods of exposure. *Trans. Am. Inst. Chem. Eng.*, *31*, 365-390.

Hreiz, R., Sialve, B., Morchain, J., Escudié, R., Steyer, J.-P., & Guiraud, P. (2014). Experimental and numerical investigation of hydrodynamics in raceway reactors used for algaculture. *Chemical Engineering Journal*, *250*, 230–239.

Hu, Q., Sommerfeld, M., Jarvis, E., Ghirardi, M., Posewitz, M., Seibert, M., & Darzins, A. (2008). Microalgal triacylglycerols as feedstocks for biofuel production: perspectives and advances. *The plant journal*, *54*(4), 621–639.

Kadam, K. L. (1997). Power plant flue gas as a source of co 2 for microalgae cultivation: economic impact of different process options. *Energy Conversion and Management*, *38*, S505–S510.

Karcz, I. (1973). Reflections on the origin of small-scale longitudinal streambed scours. *Fluvial Geomorphology. Allen & Unwin, Binghamton, NY*, 149–173.

Kinoshita, R. (1967). An analysis of the movement of flood waters by aerial photography [japanese]. *Journal of the Japan Society of Photogrammetry*, *6*(1), 1–17.

Kirkgöz, M. S., & Ardiçlioğlu, M. (1997). Velocity profiles of developing and developed open channel flow. *Journal of Hydraulic Engineering*, *123*(12), 1099–1105.

Kok, B. (1953). Experiments on photosynthesis by chlorella in flashing light. *Algal culture: from laboratory to pilot plant*, *600*, 63–75.

Kumar, K., Mishra, S. K., Shrivastav, A., Park, M. S., & Yang, J.-W. (2015). Recent trends in the mass cultivation of algae in raceway ponds. *Renewable and Sustainable Energy Reviews*, *51*, 875–885.

Lamont, J. C., & Scott, D. (1970). An eddy cell model of mass transfer into the surface of a turbulent liquid. *AIChE Journal*, *16*(4), 513–519.

Lance, B. W. (2012). Using stereo particle image velocimetry to quantify and optimize mixing in an algae raceway using delta wings. *All Graduate Theses and Dissertations. Paper 1353*.

Laufer, J., & Narayanan, M. B. (1971). Mean period of the turbulent production mechanism in a boundary layer. *Physics of Fluids (1958-1988)*, *14*(1), 182–183.

Law, C., & Khoo, B. (2002). Transport across a turbulent air-water interface. *AIChE journal*, *48*(9), 1856-1868.

Laws, E., Terry, K., Wickman, J., & Chalup, M. (1983). A simple algal production system designed to utilize the flashing light effect. *Biotechnology and bioengineering*, *25*(10), 2319–2335.

Lee, B. (1975). The effect of turbulence on the surface pressure field of a square prism. *Journal of Fluid Mechanics*, *69*(2), 263–282.

Lewis, W., & Whitman, W. (1924). Principles of gas absorption. *Industrial & Engineering Chemistry*, *16*(12), 1215–1220.

Liao, Q., & Wang, B. (2013). Near surface turbulence and gas exchange across the air-sea interface. *Topics in Oceanography*. (Prof. Enrico Zambianchi (Ed.), In-Tech, DOI: 10.5772/56415. Available from: `http://www.intechopen.com/books/topics-in-oceanography/near-surface-turbulence-and-gas-exchange-across-the-air-sea-interface`)

Liffman, K., Paterson, D. A., Liovic, P., & Bandopadhayay, P. (2013). Comparing the energy efficiency of different high rate algal raceway pond designs using computational fluid dynamics. *Chemical Engineering Research and Design*, *91*(2), 221–226.

Magnaudet, J., & Calmet, I. (2006). Turbulent mass transfer through a flat shear-free surface. *Journal of Fluid Mechanics*, *553*, 155-185.

McCready, M., Vassiliadou, E., & Hanratty, T. (1986). Computer simulation of turbulent mass transfer at a mobile interface. *AIChE Journal*, *32*(7), 1108–1115.

McKenna, S., & McGillis, W. (2004). The role of free-surface turbulence and surfactants in air–water gas transfer. *International Journal of Heat and Mass Transfer*, *47*(3), 539-553.

Mendoza, J., Granados, M., De Godos, I., Acién, F., Molina, E., Banks, C., & Heaven, S. (2013). Fluid-dynamic characterization of real-scale raceway reactors for microalgae production. *Biomass and Bioenergy*, *54*, 267–275.

Mirón, A. S., Garcıa, M. C. C., Gómez, A. C., Camacho, F. G., Grima, E. M., & Chisti, Y. (2003). Shear stress tolerance and biochemical characterization of phaeodactylum tricornutum in quasi steady-state continuous culture in outdoor photobioreactors. *Biochemical Engineering Journal*, *16*(3), 287-297.

Miron, A. S., Gomez, A. C., Camacho, F. G., Grima, E. M., & Chisti, Y. (1999). Comparative evaluation of compact photobioreactors for large-scale monoculture of microalgae. *Journal of Biotechnology*, *70*(1), 249-270.

Nagarajan, S., Chou, S. K., Cao, S., Wu, C., & Zhou, Z. (2013). An updated comprehensive techno-economic analysis of algae biodiesel. *Bioresource technology*, *145*, 150–156.

Nernst, W. (1904). Theory of reaction velocity in heterogenous systems. *Zeit. physikal. Chem*, *47*, 52–55.

Nezu, I. (1977). Turbulent structure in open-channel flows. *Ph. D. thesis, Kyoto University, Japan.*.

Nezu, I. (2005). Open-channel flow turbulence and its research prospect in the 21st century. *Journal of Hydraulic Engineering*, *131*(4), 229–246.

Nezu, I., & Nakagawa, H. (1984). Cellular secondary currents in straight conduit. *Journal of hydraulic engineering*, *110*(2), 173–193.

O'Connor, D. J., & Dobbins, W. E. (1958). Mechanism of reaeration in natural streams. *Transactions of the American Society of Civil Engineers*, *123*(1), 641-666.

Oreskes, N. (2004). The scientific consensus on climate change. *Science*, *306*(5702), 1686–1686.

Perkins, H. (1970). The formation of streamwise vorticity in turbulent flow. *Journal of Fluid Mechanics*, *44*(4), 721–740.

Pope, S. B. (2001). *Turbulent flows.* IOP Publishing.

Prandtl, L. (1904). On fluid motions with very small friction (german). *The International Mathematical Congress. Heidelberg*, 484–491.

Prussi, M., Buffi, M., Casini, D., Chiaramonti, D., Martelli, F., Carnevale, M., … Rodolfi, L. (2014). Experimental and numerical investigations of mixing in raceway ponds for algae cultivation. *biomass and bioenergy*, *67*, 390–400.

Roshko, A. (1955). On the wake and drag of bluff bodies. *Journal of the Aeronautical Sciences*, *22*(2), 124–132.

Rusello, P. J. (2009). A practical primer for pulse coherent instruments. *Nortek technical note No.: TN-027*, *117*.

Sanjou, M., Nezu, I., & Okamoto, T. (2017). Surface velocity divergence model of air/water interfacial gas transfer in open-channel flows. *Physics of Fluids*, *29*(4), 045107.

Sanjou, M., Okamoto, T., & Gotou, S. (2016). The relationship between gas transfer velocity and surface divergence in open-channel with strip roughness. In G. Constantinescu, M. Garcia, & D. Hanes (Eds.), *River flow* (p. 763-768). CRC Press.

Schlichting, H., Gersten, K., Krause, E., & Oertel, H. (1955). *Boundary-layer theory* (Vol. 7). Springer.

Scott, S. A., Davey, M. P., Dennis, J. S., Horst, I., Howe, C. J., Lea-Smith, D. J., & Smith, A. G. (2010). Biodiesel from algae: challenges and prospects. *Current opinion in biotechnology*, *21*(3), 277-286.

Sheehan, J., Dunahay, T., Benemann, J., & Roessler, P. (1998). A look back at the us department of energys aquatic species program: biodiesel from algae. *National Renewable Energy Laboratory*, *328*.

Socolofsky, S. A., & Jirka, G. H. (2005). Special topics in mixing and transport processes in the environment. *Engineering lectures, fifth ed., Coastal and Ocean Engineering Division, Texas A&M University*.

Spolaore, P., Joannis-Cassan, C., Duran, E., & Isambert, A. (2006). Commercial applications of microalgae. *Journal of bioscience and bioengineering*, *101*(2), 87–96.

Stenstrom, M. (2007). Measurement of oxygen transfer in clean water. *Standards ASCE/EWRI*, 2–06.

Stephens, E., Ross, I. L., King, Z., Mussgnug, J. H., Kruse, O., Posten, C., … Hankamer, B. (2010). An economic and technical evaluation of microalgal biofuels. *Nature biotechnology*, *28*(2), 126–128.

Sullivan, J. M., & Swift, E. (2003). Effects of small-scale turbulence on net growth rate and size of ten species of marine dinoflagellates. *Journal of Phycology*, *39*(1), 83–94.

Sutherland, D. L., Turnbull, M. H., & Craggs, R. J. (2014). Increased pond depth improves algal productivity and nutrient removal in wastewater treatement high rate algal ponds. *Water Research*, *53*, 271–281.

Tamburrino, A., & Gulliver, J. S. (2002). Free-surface turbulence and mass transfer in a channel flow. *AIChE Journal*, *48*(12), 2732-2743.

Tennekes, H., & Lumley, J. L. (1972). *A first course in turbulence*. MIT press.

Theofanous, T., Houze, R., & Brumfield, L. (1976). Turbulent mass transfer at free, gas-liquid interfaces, with applications to open-channel, bubble and jet flows. *International Journal of Heat and Mass Transfer*, *19*(6), 613–624.

Thibodeaux, L. J., & Mackay, D. (2010). *Handbook of chemical mass transport in the environment*. CRC Press.

Thielicke, W. (2014). The flapping flight of birds. *Diss. University of Groningen*.

Thielicke, W., & Stamhuis, E. (2014a). Pivlab–time-resolved digital particle image velocimetry tool for matlab, version: 1.41, 2017. *DOI*, *10*, m9.

Thielicke, W., & Stamhuis, E. (2014b). Pivlab–towards user-friendly, affordable and accurate digital particle image velocimetry in matlab. *Journal of Open Research Software*, *2*(1).

Tinoco, R. O., & Cowen, E. A. (2013). The direct and indirect measurement of boundary stress and drag on individual and complex arrays of elements. *Experiments in fluids*, *54*(4), 1509.

Turney, D. E., & Banerjee, S. (2013). Air-water gas transfer and near-surface motions. *Journal of Fluid Mechanics*, *733*, 588.

Turney, D. E., Smith, W. C., & Banerjee, S. (2005). A measure of near-surface fluid motions that predicts air-water gas transfer in a wide range of conditions. *Geophysical research letters*, *32*(4).

U.S. Energy Information Administration. (2017). *Monthly energy review, november 2017.* U.S. Department of Energy, Washington DC.

Van Gerpen, J. (2005). Biodiesel processing and production. *Fuel processing technology*, *86*(10), 1097–1107.

Vaughan, G. (2013). Experimental studies of vertical mixing patterns in open channel flow generated by two delta wings side-by-side. *All Graduate Theses and Dissertations. Paper 1744..*

Viero, D. P., Pradella, I., & Defina, A. (2017). Free surface waves induced by vortex shedding in cylinder arrays. *Journal of Hydraulic Research*, *55*(1), 16–26.

Voleti, R. S. (2012). Experimental studies of vertical mixing in an open channel raceway for algae biofuel production. *All Graduate Theses and Dissertations. Paper 1307..*

Wijffels, R. H., & Barbosa, M. J. (2010). An outlook on microalgal biofuels. *Science*, *329*(5993), 796–799.

Xu, B., Li, P., & Waller, P. (2014). Study of the flow mixing in a novel arid raceway for algae production. *Renewable Energy*, *62*, 249–257.

Xu, Z., Khoo, B., & Carpenter, K. (2006). Mass transfer across the turbulent gas–water interface. *AIChE journal*, *52*(10), 3363-3374.

Zappa, C., Asher, W., Jessup, A., Klinke, J., & Long, S. (2002). Effect of microscale wave breaking on air-water gas transfer. *Gas Transfer at Water Surfaces*, 23–29.

Zima, L., & Ackermann, N. L. (2002). Wave generation in open channels by vortex shedding from channel obstructions. *Journal of Hydraulic Engineering*, *128*(6), 596–603.

Appendix A

ADV Sampling Locations

Table A.1: ADV Sampling Locations for $h = 9.5$ *cm*. All locations at measurement plane, $x = 638$ *cm*.

$\mathbf{z_1}$ (cm)	$\mathbf{z_2}$ (cm)	$\mathbf{z_3}$ (cm)	y (cm)
5.5	7.5	9.5	3.5
5.5	7.5	9.5	6.125
5.5	7.5	9.5	7.625
5.5	7.5	9.5	8.625
5.5	7.5	9.5	9.625
5.5	7.5	9.5	10.625
5.5	7.5	9.5	11.625
5.5	7.5	9.5	13.125
5.5	7.5	9.5	15.75
5.5	7.5	9.5	17.25
5.5	7.5	9.5	18.25
5.5	7.5	9.5	19.25
5.5	7.5	9.5	20.25
5.5	7.5	9.5	21.25
5.5	7.5	9.5	22.75
5.5	7.5	9.5	25.375
5.5	7.5	9.5	26.875
5.5	7.5	9.5	27.875
5.5	7.5	9.5	28.875
5.5	7.5	9.5	29.875
5.5	7.5	9.5	30.875
5.5	7.5	9.5	32.375
5.5	7.5	9.5	35
5.5	7.5	9.5	36.5
5.5	7.5	9.5	37.5
5.5	7.5	9.5	38.5
5.5	7.5	9.5	39.5
5.5	7.5	9.5	40.5
5.5	7.5	9.5	42

Table A.1 Continued: ADV Sampling Locations for $h = 9.5$ *cm*.

$\mathbf{z_1}$ **(cm)**	$\mathbf{z_2}$ **(cm)**	$\mathbf{z_3}$ **(cm)**	**y (cm)**
5.5	7.5	9.5	44.625
5.5	7.5	9.5	46.125
5.5	7.5	9.5	47.125
5.5	7.5	9.5	48.125
5.5	7.5	9.5	49.125
5.5	7.5	9.5	50.125
5.5	7.5	9.5	51.625
5.5	7.5	9.5	54.25
5.5	7.5	9.5	55.75
5.5	7.5	9.5	56.75
5.5	7.5	9.5	57.75
5.5	7.5	9.5	58.75
5.5	7.5	9.5	59.75
5.5	7.5	9.5	61.25
5.5	7.5	9.5	63.875
5.5	7.5	9.5	65.375
5.5	7.5	9.5	66.375
5.5	7.5	9.5	67.375
5.5	7.5	9.5	68.375
5.5	7.5	9.5	69.375
5.5	7.5	9.5	70.875
5.5	7.5	9.5	73.5

Table A.2: ADV Sampling Locations for $h = 19.0$ *cm*. All locations at measurement plane, $x = 638$ *cm*.

$\mathbf{z_1}$ (cm)	$\mathbf{z_2}$ (cm)	$\mathbf{z_3}$ (cm)	y (cm)
5.5	7.5	18.5	4.5
5.5	7.5	18.5	7
5.5	7.5	18.5	10
5.5	7.5	18.5	13
5.5	7.5	18.5	15.5
5.5	7.5	18.5	17.5
5.5	7.5	18.5	18.5
5.5	7.5	18.5	19.5
5.5	7.5	18.5	20.5
5.5	7.5	18.5	21.5
5.5	7.5	18.5	23.5
5.5	7.5	18.5	26
5.5	7.5	18.5	29
5.5	7.5	18.5	32
5.5	7.5	18.5	34.5
5.5	7.5	18.5	36.5
5.5	7.5	18.5	37.5
5.5	7.5	18.5	38.5
5.5	7.5	18.5	39.5
5.5	7.5	18.5	40.5
5.5	7.5	18.5	42.5
5.5	7.5	18.5	45
5.5	7.5	18.5	48
5.5	7.5	18.5	51
5.5	7.5	18.5	53.5
5.5	7.5	18.5	55.5
5.5	7.5	18.5	56.5
5.5	7.5	18.5	57.5
5.5	7.5	18.5	58.5
5.5	7.5	18.5	59.5
5.5	7.5	18.5	61.5
5.5	7.5	18.5	64
5.5	7.5	18.5	67
5.5	7.5	18.5	70
5.5	7.5	18.5	72.5

Table A.3: ADV Sampling Locations for $h = 38.0$ *cm*. All locations at measurement plane, $x = 638$ *cm*.

$\mathbf{z_1}$ **(cm)**	$\mathbf{z_2}$ **(cm)**	$\mathbf{z_3}$ **(cm)**	**y (cm)**
5.5	7.5	36.5	4.5
5.5	7.5	36.5	6.5
5.5	7.5	36.5	10.5
5.5	7.5	36.5	14.5
5.5	7.5	36.5	19.5
5.5	7.5	36.5	24.5
5.5	7.5	36.5	28.5
5.5	7.5	36.5	32.5
5.5	7.5	36.5	34.5
5.5	7.5	36.5	36.5
5.5	7.5	36.5	37.5
5.5	7.5	36.5	38.5
5.5	7.5	36.5	39.5
5.5	7.5	36.5	40.5
5.5	7.5	36.5	42.5
5.5	7.5	36.5	44.5
5.5	7.5	36.5	48.5
5.5	7.5	36.5	52.5
5.5	7.5	36.5	57.5
5.5	7.5	36.5	62.5
5.5	7.5	36.5	66.5
5.5	7.5	36.5	70.5
5.5	7.5	36.5	72.5

Table A.4: ADV Sampling Locations for bend section 8, located at $x = 19$ cm.

$\mathbf{z_1}$ (cm)	$\mathbf{z_2}$ (cm)	$\mathbf{z_3}$ (cm)	$\mathbf{z_4}$ (cm)	$\mathbf{z_5}$ (cm)	$\mathbf{z_6}$ (cm)	$\mathbf{z_7}$ (cm)	**y** (cm)
1	3	5	7	9	11	13	9.4
1	3	5	7	9	11	13	14
1	3	5	7	9	11	13	18.6
1	3	5	7	9	11	13	23.2
1	3	5	7	9	11	13	27.8
1	3	5	7	9	11	13	32.4
1	3	5	7	9	11	13	37
1	3	5	7	9	11	13	42
1	3	5	7	9	11	13	47
1	3	5	7	9	11	13	52
1	3	5	7	9	11	13	57
1	3	5	7	9	11	13	62
1	3	5	7	9	11	13	67.5

Table A.5: ADV Sampling Locations for all other bend sections; x-coordinates vary.

$\mathbf{z_1}$ (cm)	$\mathbf{z_2}$ (cm)	$\mathbf{z_3}$ (cm)	$\mathbf{z_4}$ (cm)	**y** (cm)
1	5	9	13	9.4
1	5	9	13	27.8
1	5	9	13	47
1	5	9	13	67.5

Appendix B

ADV Power Spectra

The following are the power spectra from the ADV measurements. Locations and depth conditions (where applicable) are listed, and all cases are for a nominal velocity of 20 $cm\ s^{-1}$.

B.1 Bend Section 7 ($x = -80\ cm$)

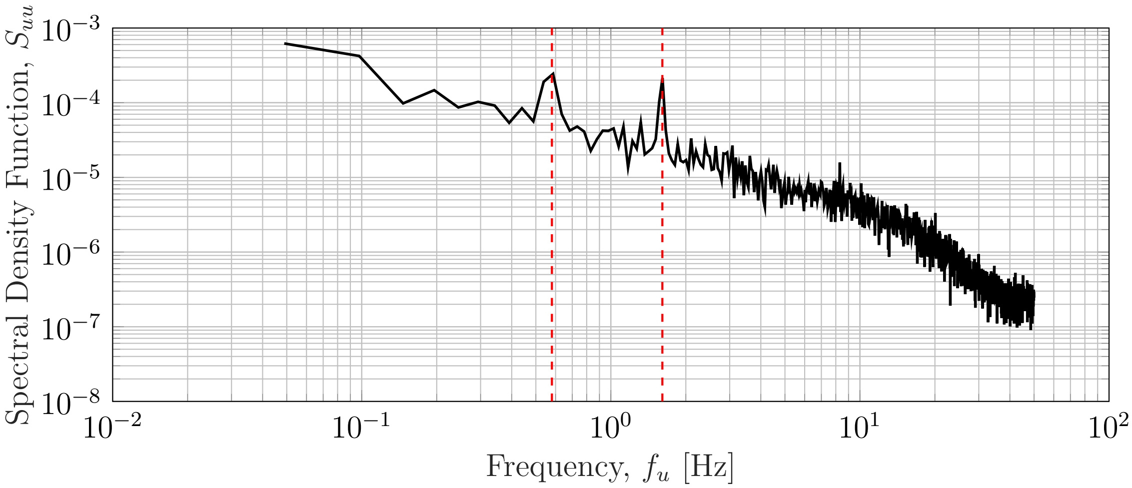

Figure B.1: Power spectra - longitudinal velocity at $x = -80\ cm,\ y = 28\ cm,\ z = 13\ cm$

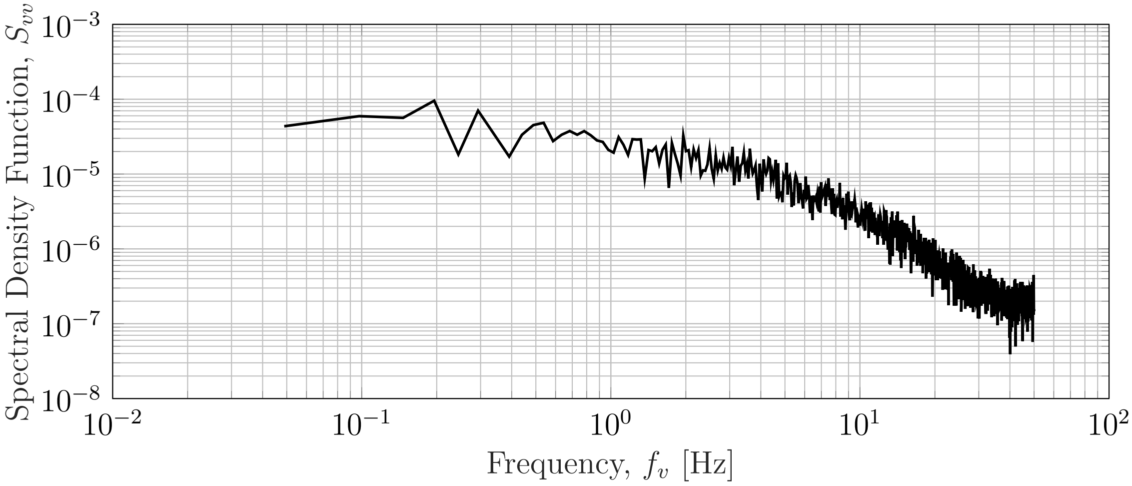

Figure B.2: Power spectra - lateral velocity at $x = -80\ cm,\ y = 28\ cm,\ z = 13\ cm$

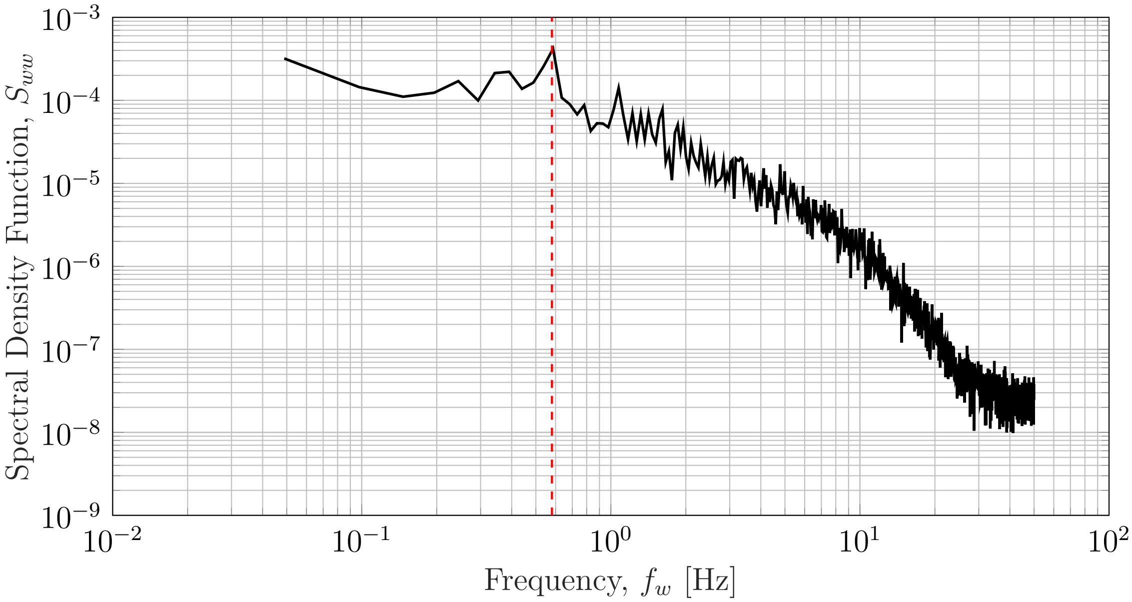

Figure B.3: Power spectra - vertical velocity at $x = -80\ cm,\ y = 47\ cm,\ z = 13\ cm$

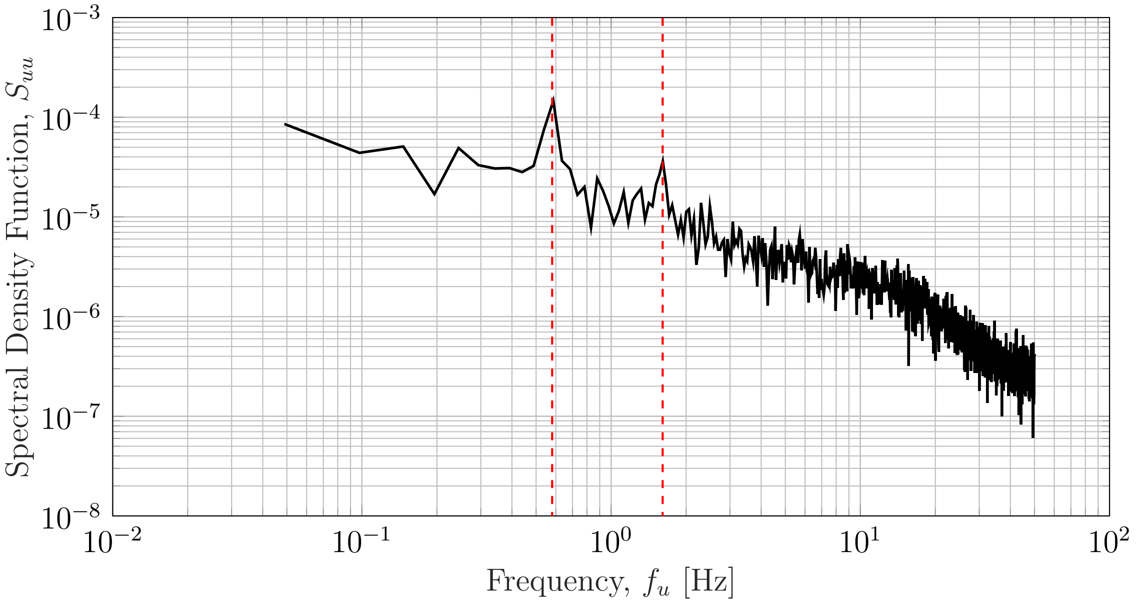

Figure B.4: Power spectra - longitudinal velocity at $x = -80\ cm,\ y = 28\ cm,\ z = 5\ cm$

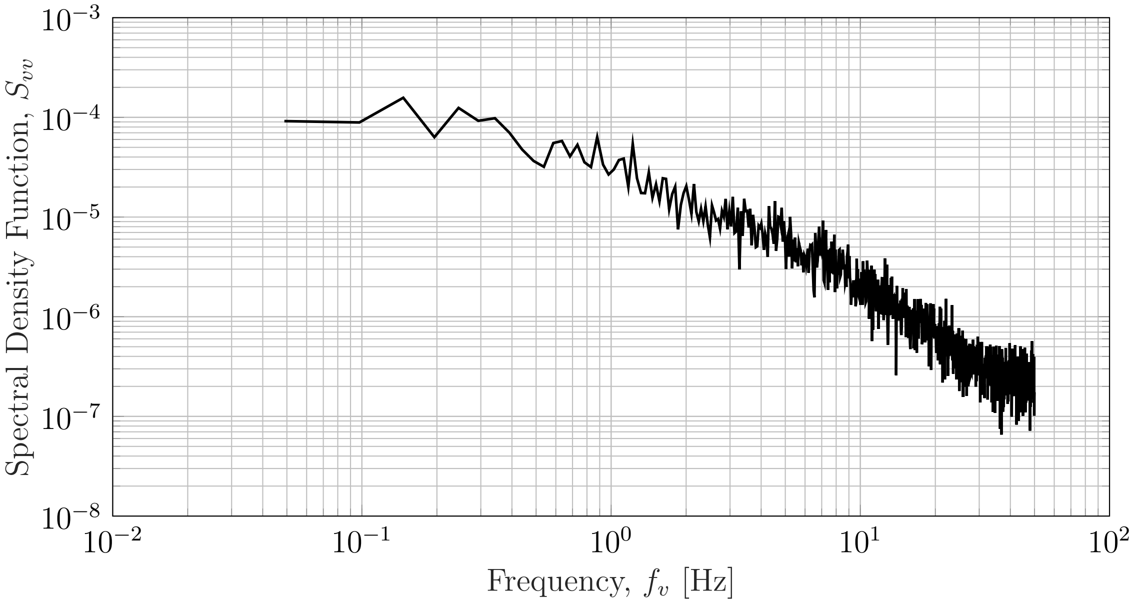

Figure B.5: Power spectra - lateral velocity at $x = -80\ cm,\ y = 28\ cm,\ z = 5\ cm$

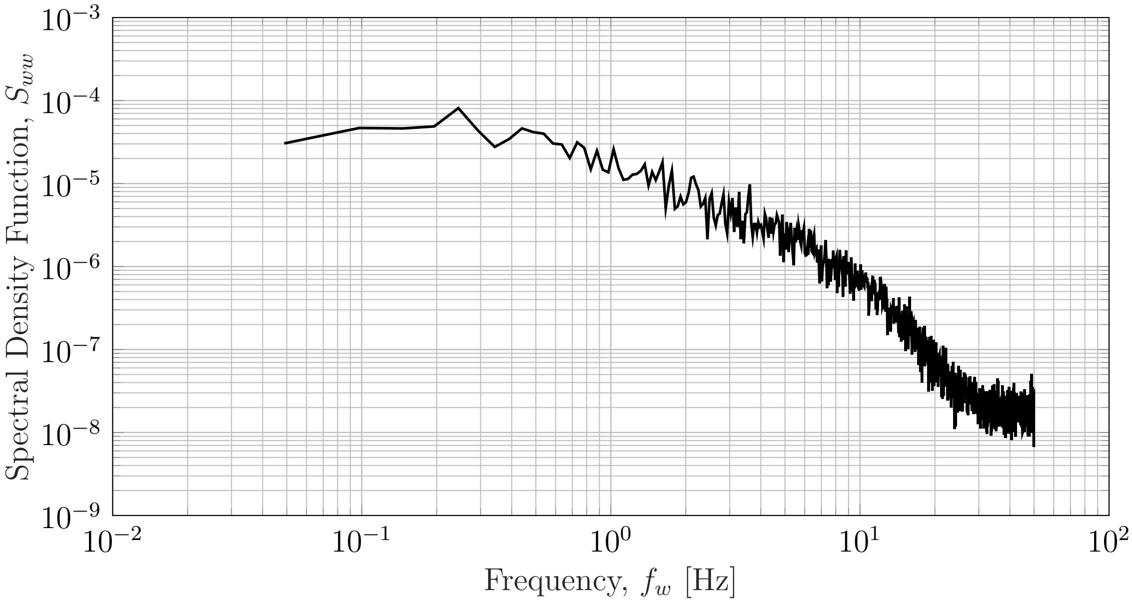

Figure B.6: Power spectra - vertical velocity at $x = -80\ cm,\ y = 28\ cm,\ z = 5\ cm$

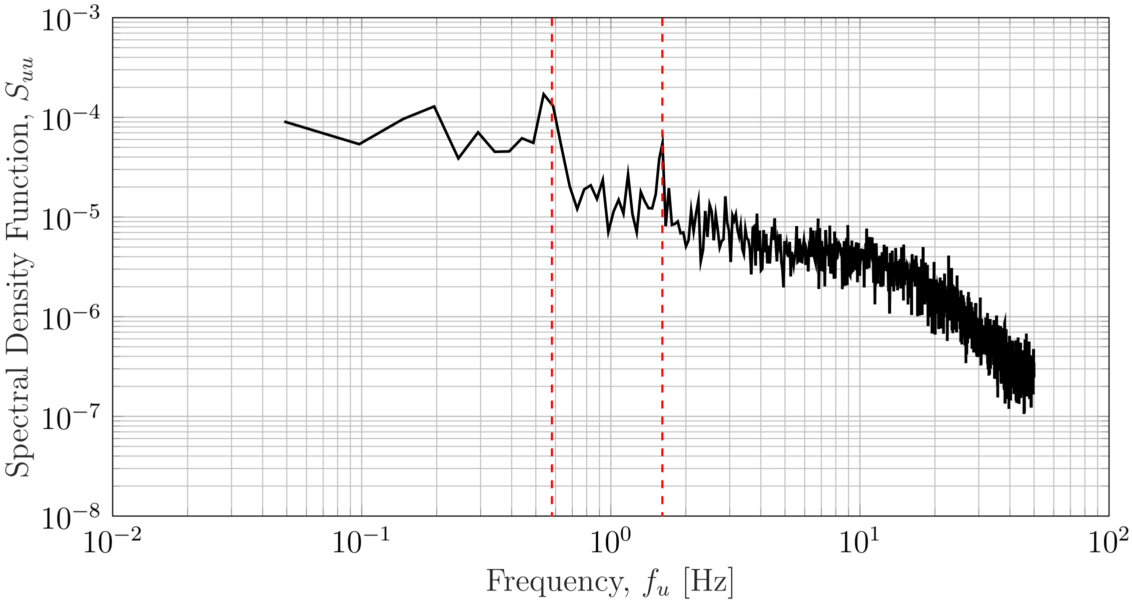

Figure B.7: Power spectra - longitudinal velocity at $x = -80\ cm,\ y = 28\ cm,\ z = 1\ cm$

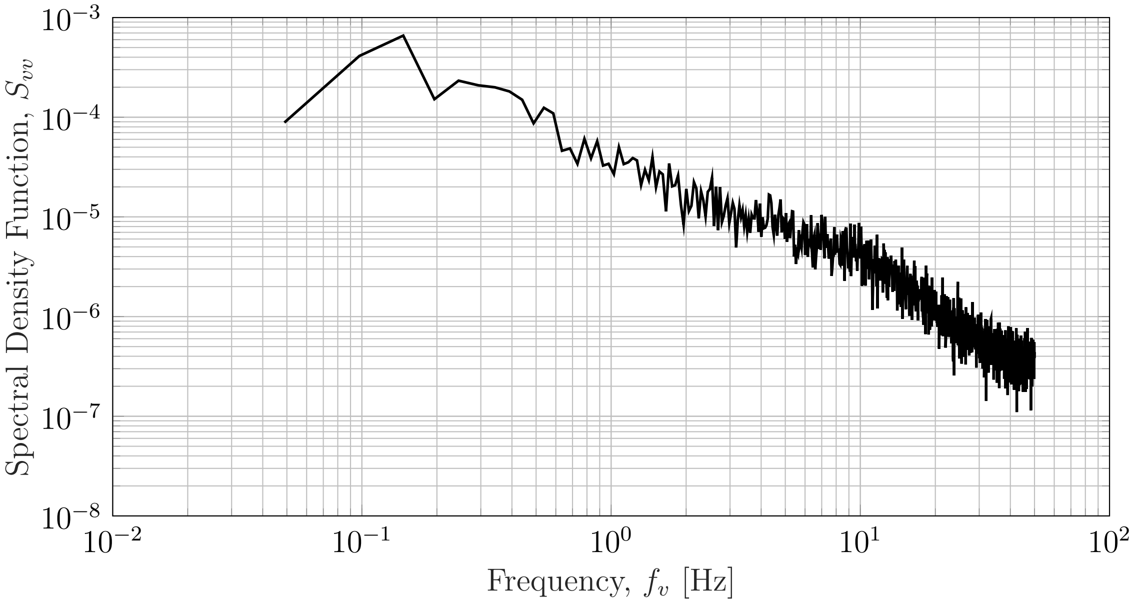

Figure B.8: Power spectra - lateral velocity at $x = -80\ cm,\ y = 28\ cm,\ z = 1\ cm$

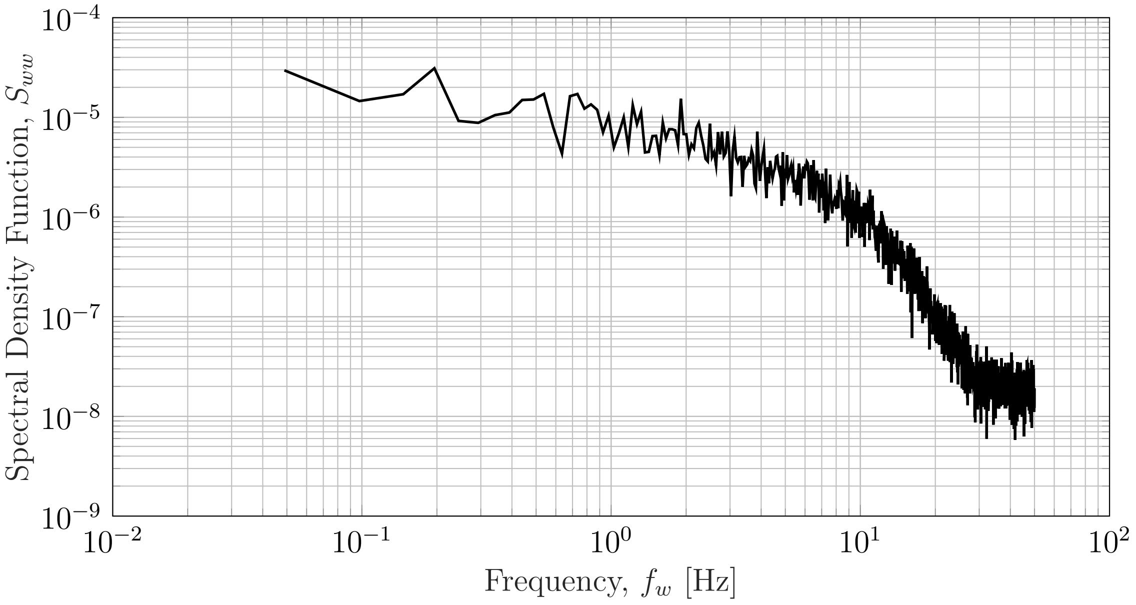

Figure B.9: Power spectra - vertical velocity at $x = -80\ cm,\ y = 28\ cm,\ z = 1\ cm$

B.2 Bend Section 8 ($x = 19\ cm$)

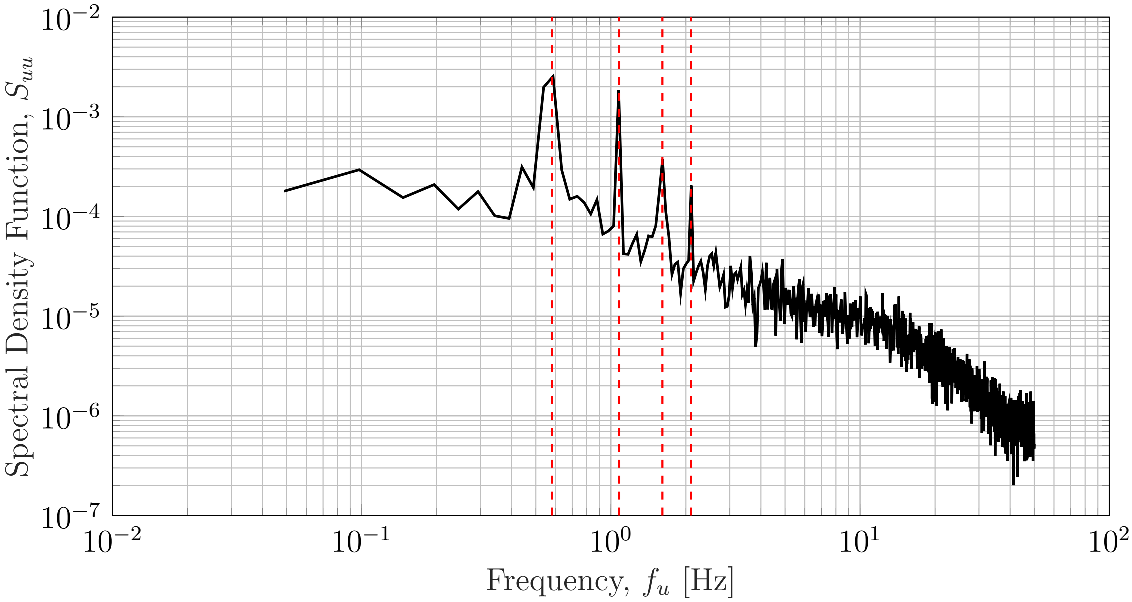

Figure B.10: Power spectra - longitudinal velocity at $x = 19\ cm,\ y = 23\ cm,\ z = 13\ cm$

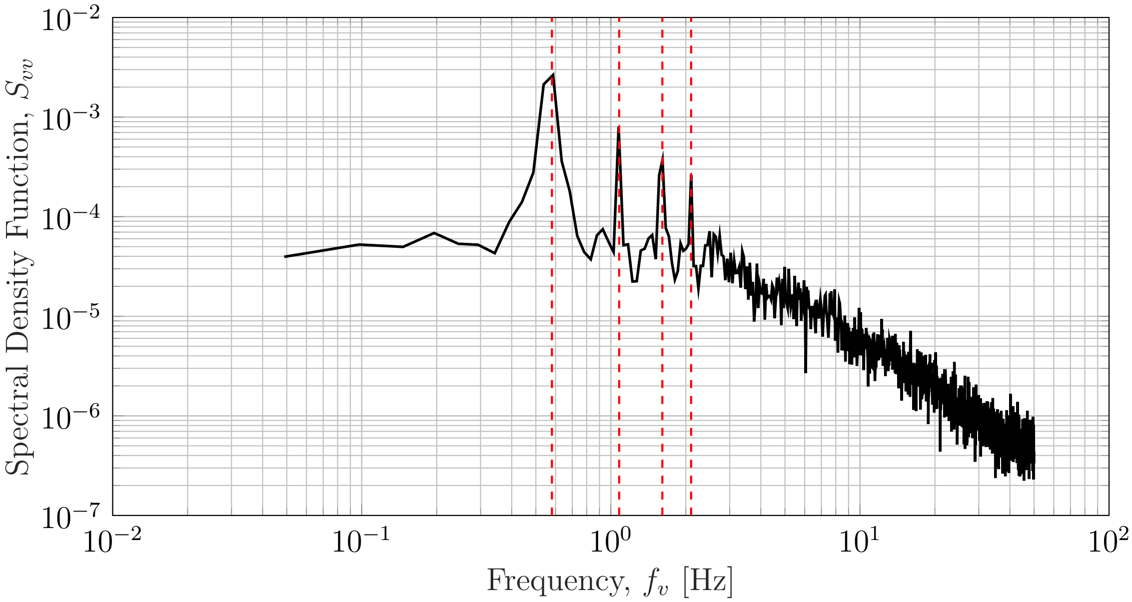

Figure B.11: Power spectra - lateral velocity at $x = 19\ cm,\ y = 23\ cm,\ z = 13\ cm$

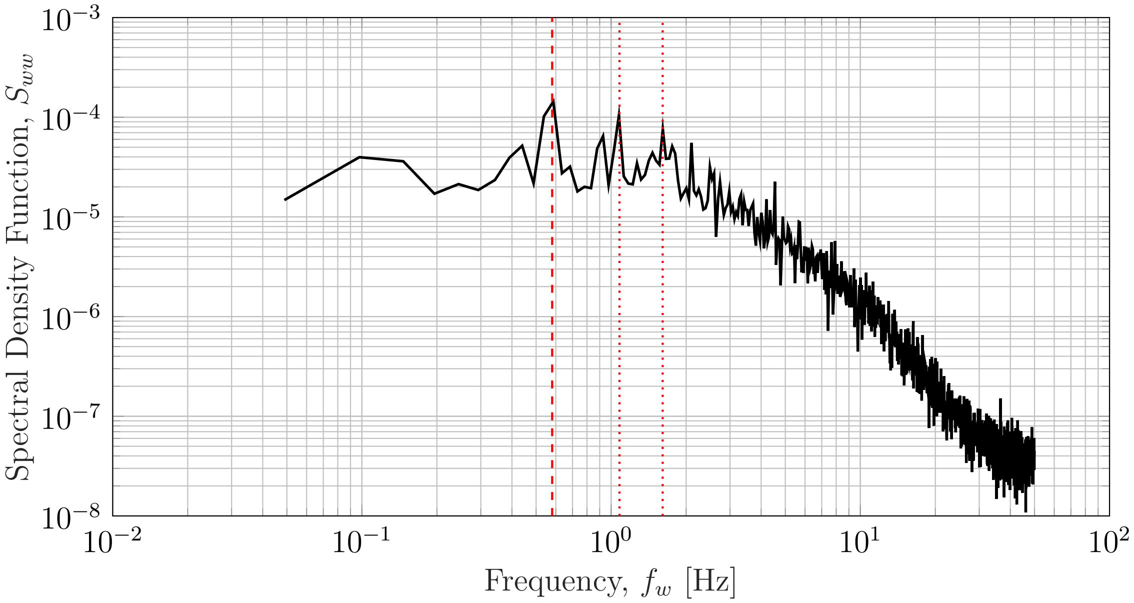

Figure B.12: Power spectra - vertical velocity at $x = 19\ cm,\ y = 23\ cm,\ z = 13\ cm$

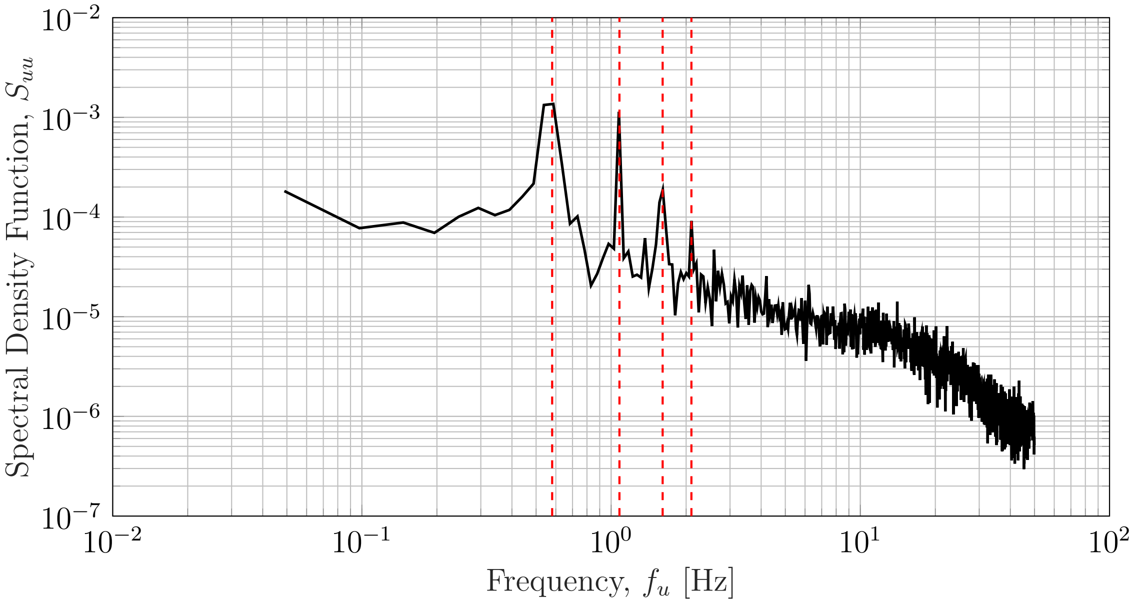

Figure B.13: Power spectra - longitudinal velocity at $x = 19\ cm,\ y = 23\ cm,\ z = 5\ cm$

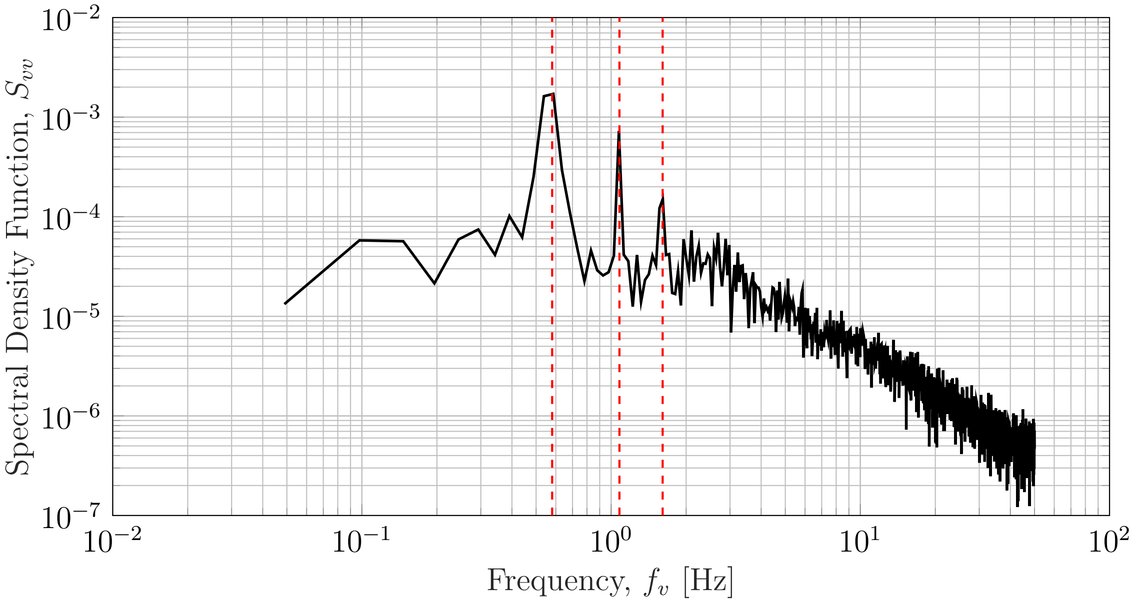

Figure B.14: Power spectra - lateral velocity at $x = 19\ cm,\ y = 23\ cm,\ z = 5\ cm$

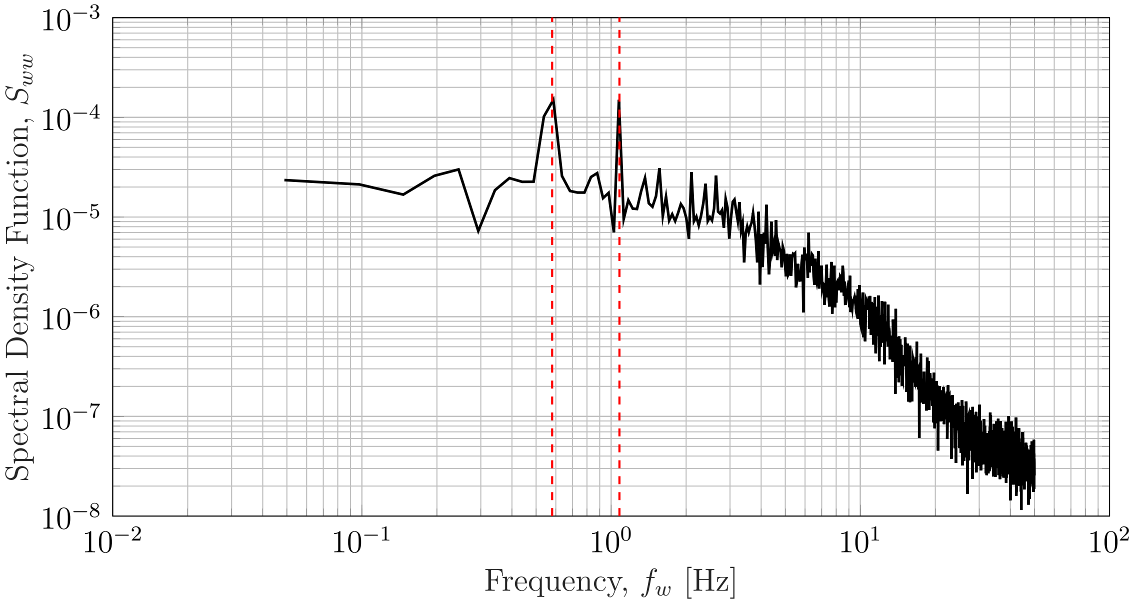

Figure B.15: Power spectra - vertical velocity at $x = 19\ cm,\ y = 23\ cm,\ z = 5\ cm$

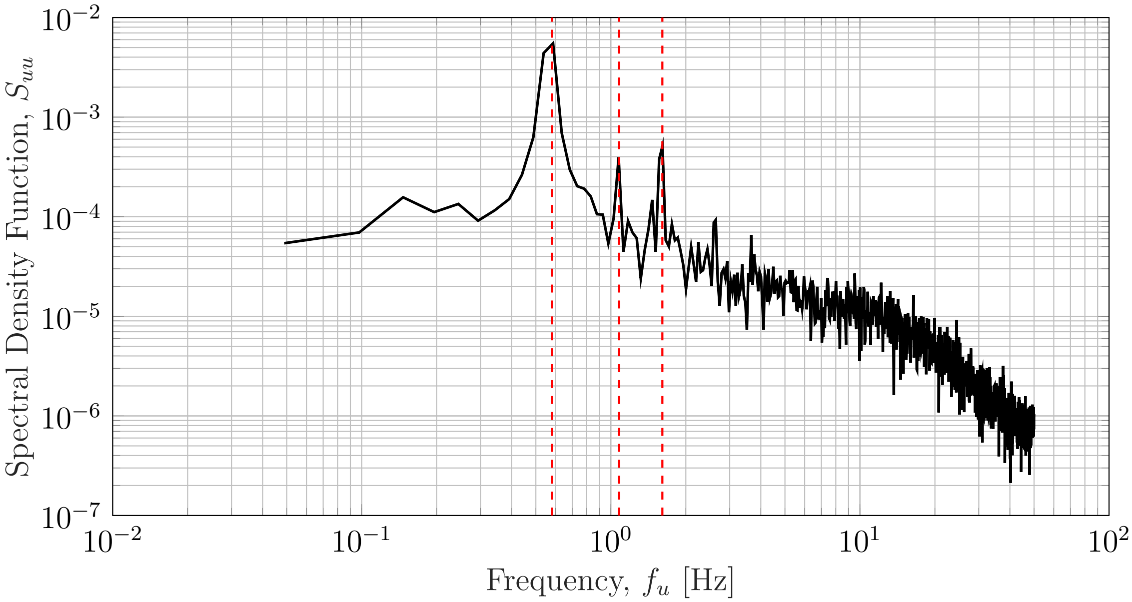

Figure B.16: Power spectra - longitudinal velocity at $x = 19\ cm,\ y = 23\ cm,\ z = 1\ cm$

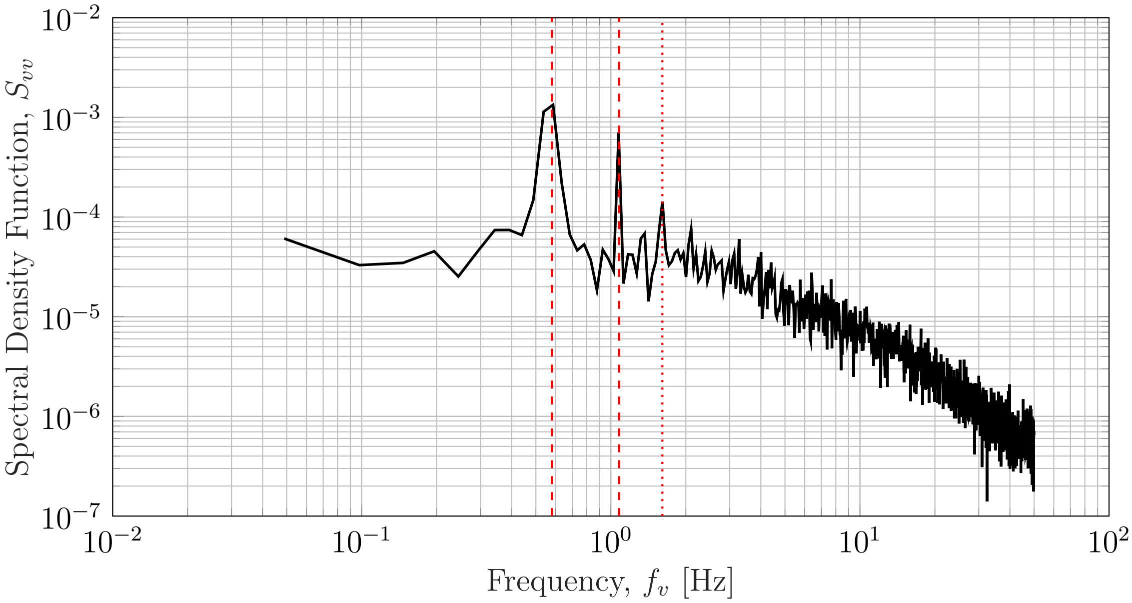

Figure B.17: Power spectra - lateral velocity at $x = 19\ cm,\ y = 23\ cm,\ z = 1\ cm$

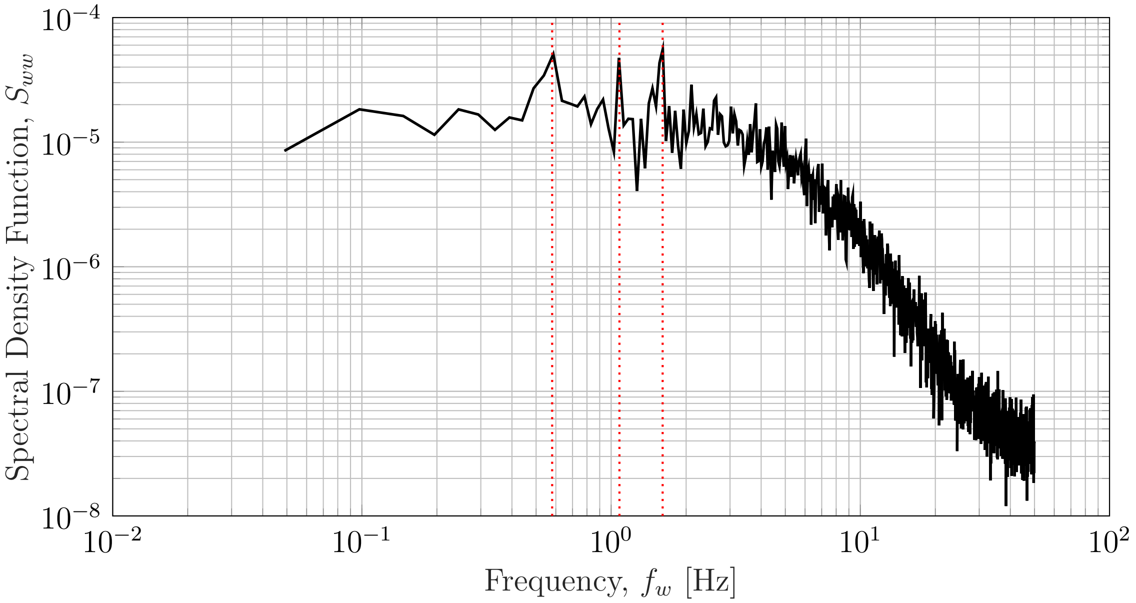

Figure B.18: Power spectra - vertical velocity at $x = 19\ cm,\ y = 23\ cm,\ z = 1\ cm$

B.3 Bend Section 9 ($x = 76\ cm$)

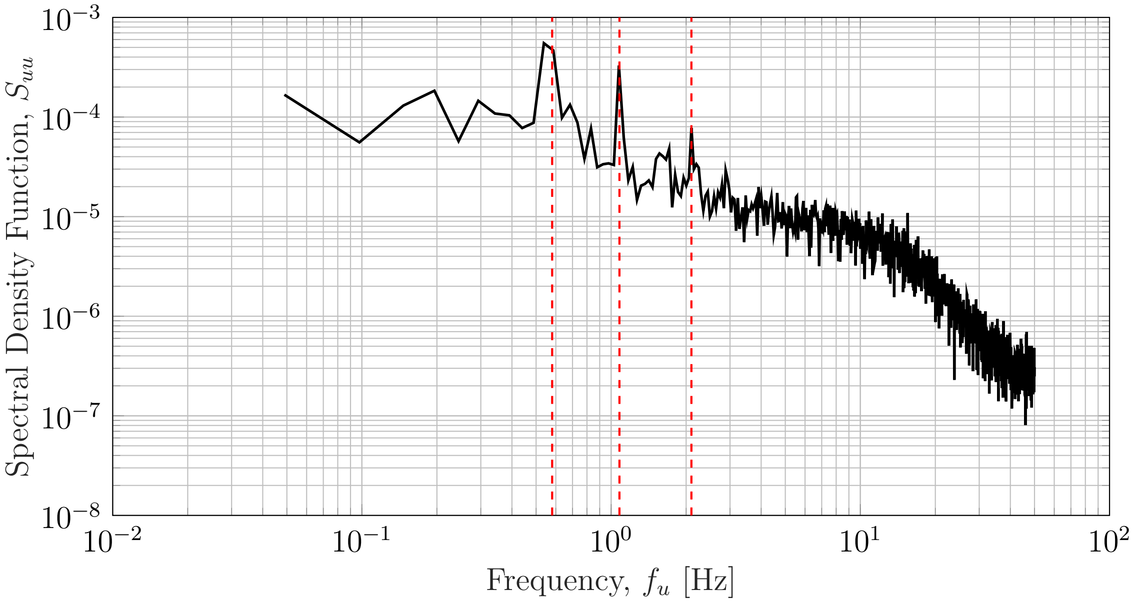

Figure B.19: Power spectra - longitudinal velocity at $x = 76\ cm,\ y = 28\ cm,\ z = 13\ cm$

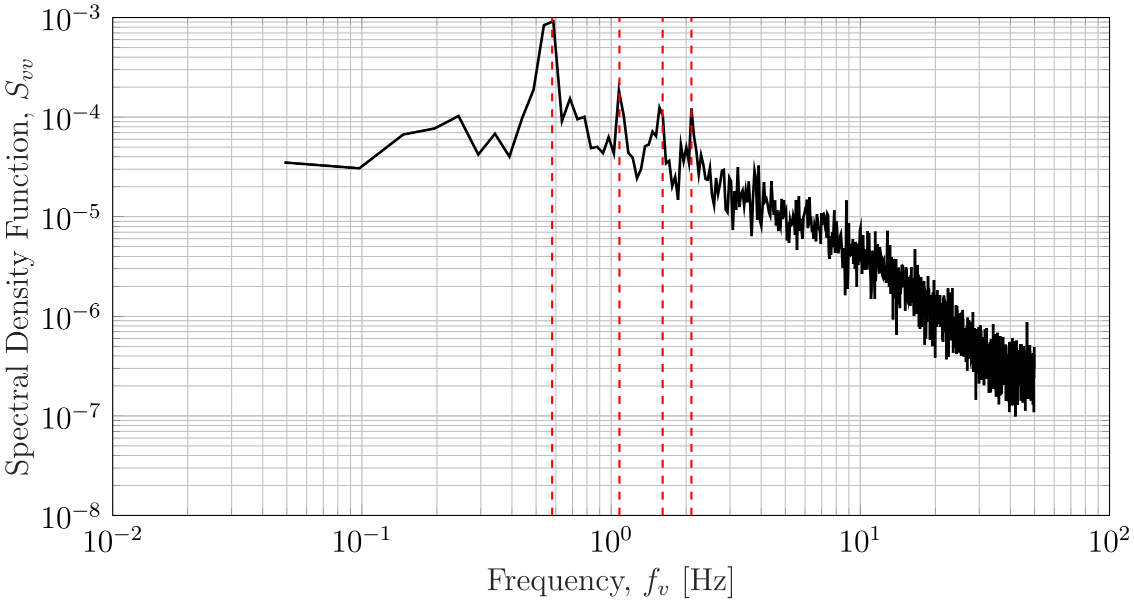

Figure B.20: Power spectra - lateral velocity at $x = 76\ cm,\ y = 28\ cm,\ z = 13\ cm$

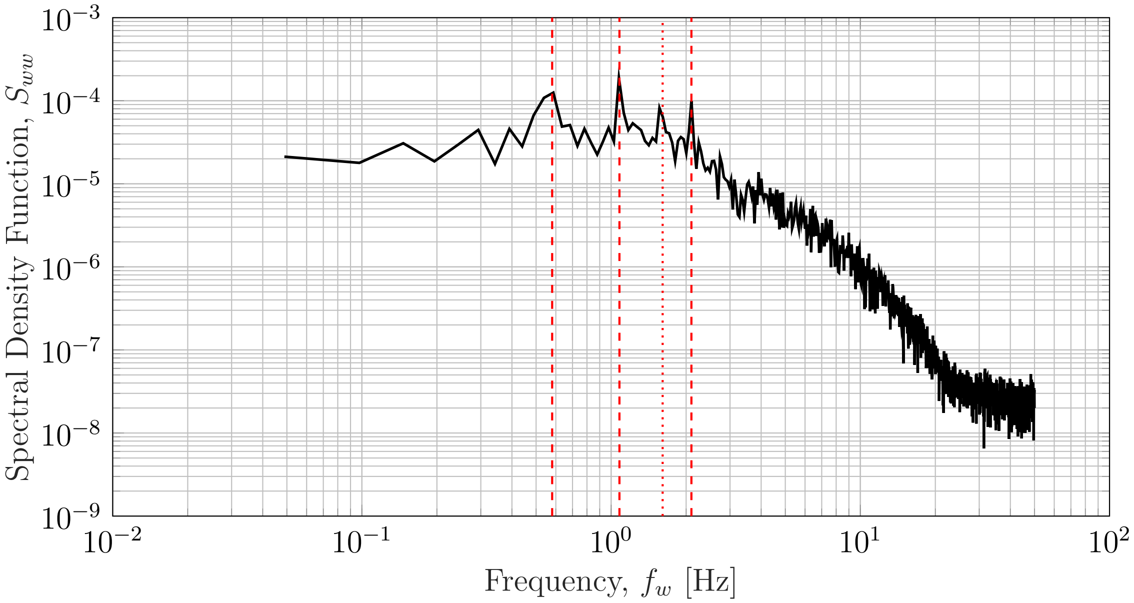

Figure B.21: Power spectra - vertical velocity at $x = 76\ cm,\ y = 28\ cm,\ z = 13\ cm$

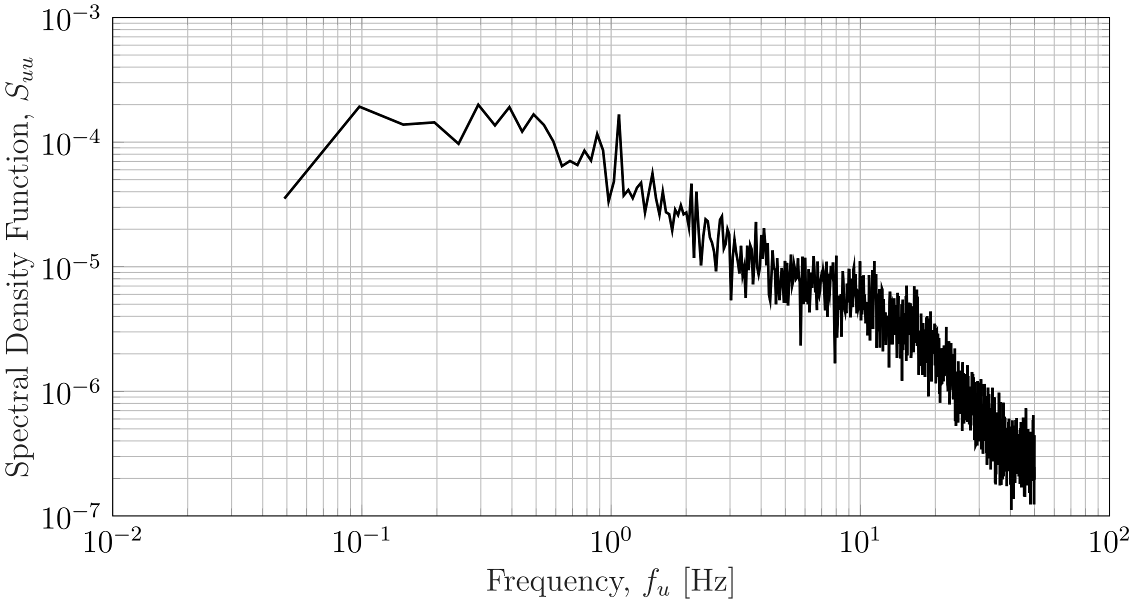

Figure B.22: Power spectra - longitudinal velocity at $x = 76\ cm,\ y = 28\ cm,\ z = 5\ cm$

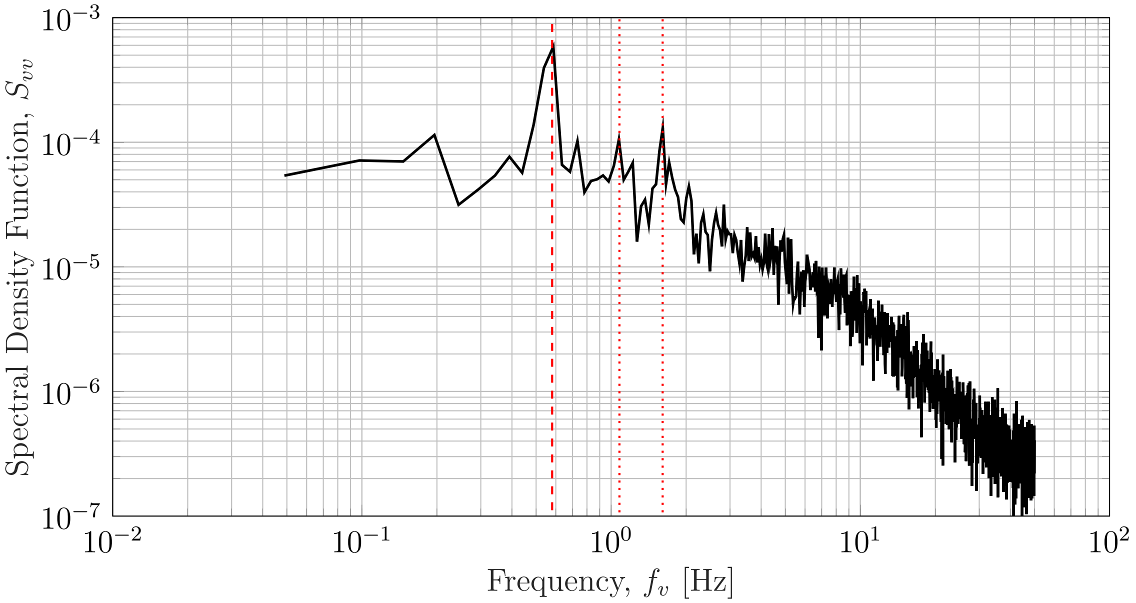

Figure B.23: Power spectra - lateral velocity at $x = 76\ cm,\ y = 28\ cm,\ z = 5\ cm$

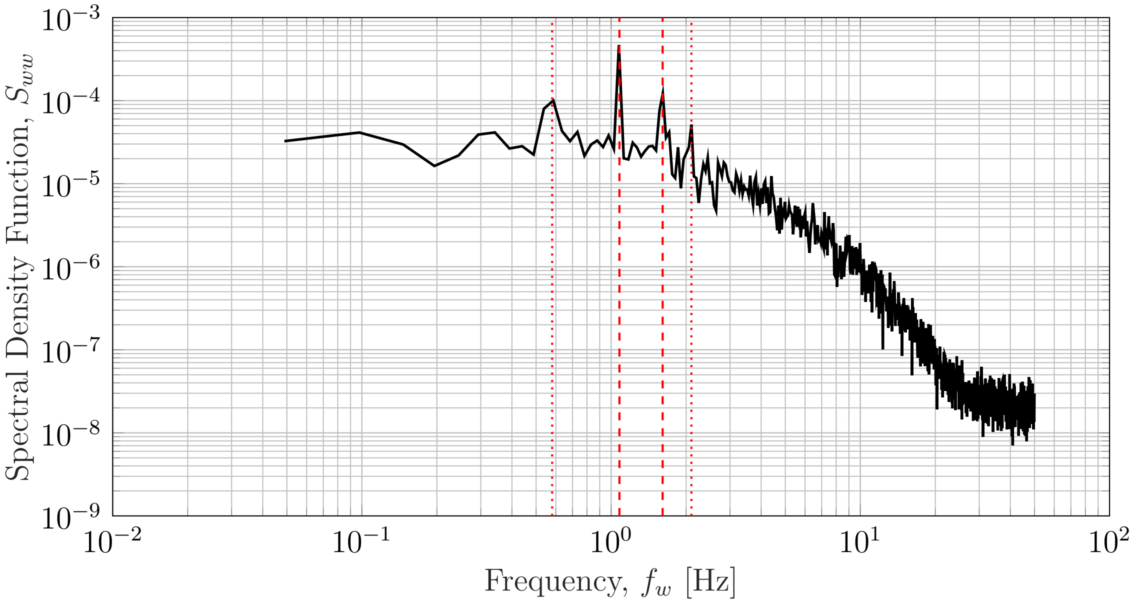

Figure B.24: Power spectra - vertical velocity at $x = 76\ cm,\ y = 28\ cm,\ z = 5\ cm$

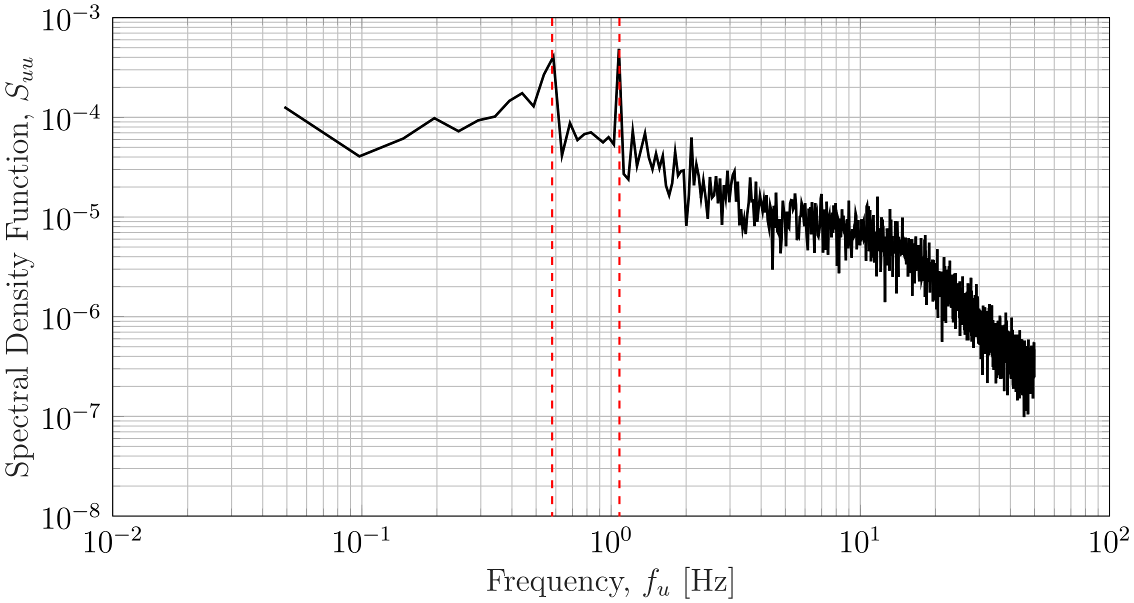

Figure B.25: Power spectra - longitudinal velocity at $x = 76\ cm,\ y = 28\ cm,\ z = 1\ cm$

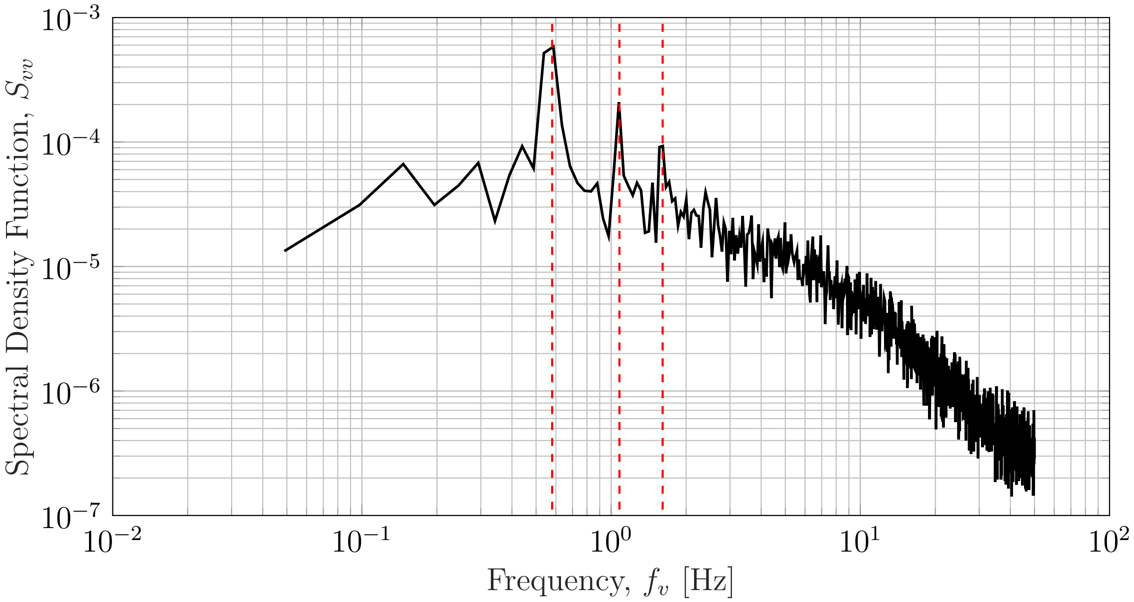

Figure B.26: Power spectra - lateral velocity at $x = 76\ cm,\ y = 28\ cm,\ z = 1\ cm$

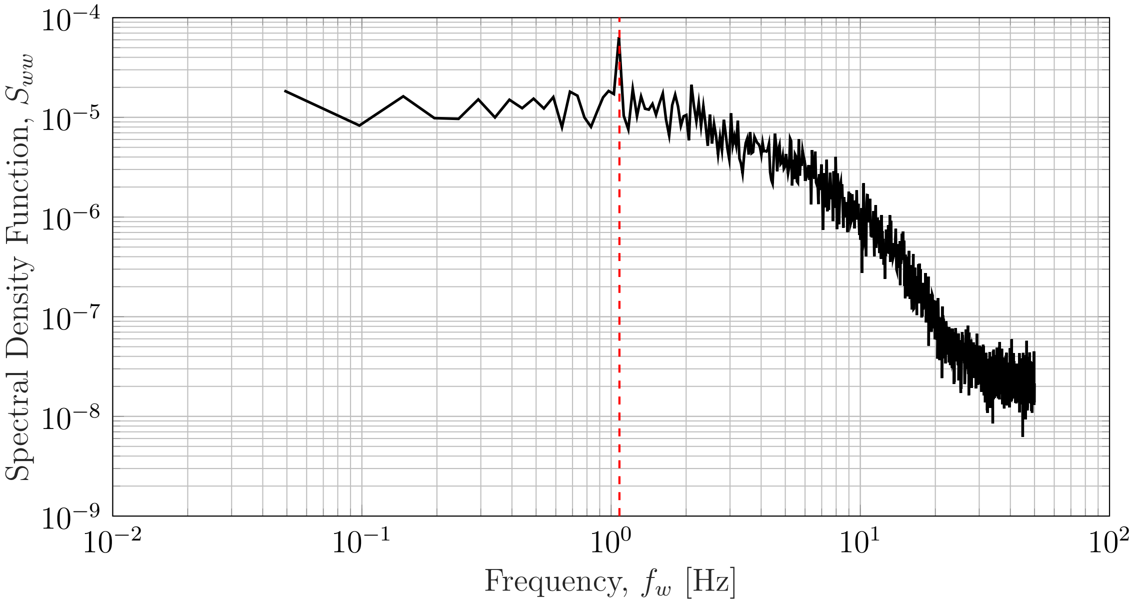

Figure B.27: Power spectra - vertical velocity at $x = 76\ cm,\ y = 28\ cm,\ z = 1\ cm$

B.4 Measurement Section ($x = 638\ cm$, $h = 19\ cm$)

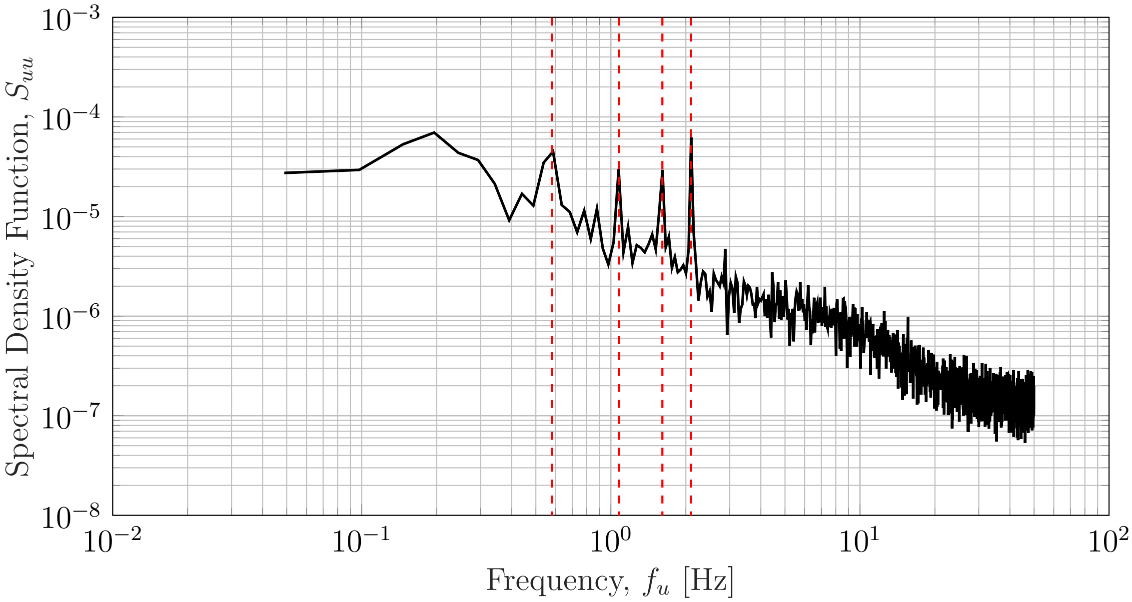

Figure B.28: Power spectra - longitudinal velocity at $h = 19\ cm,\ x = 638\ cm,\ y = 29\ cm,\ z = 13.5\ cm$

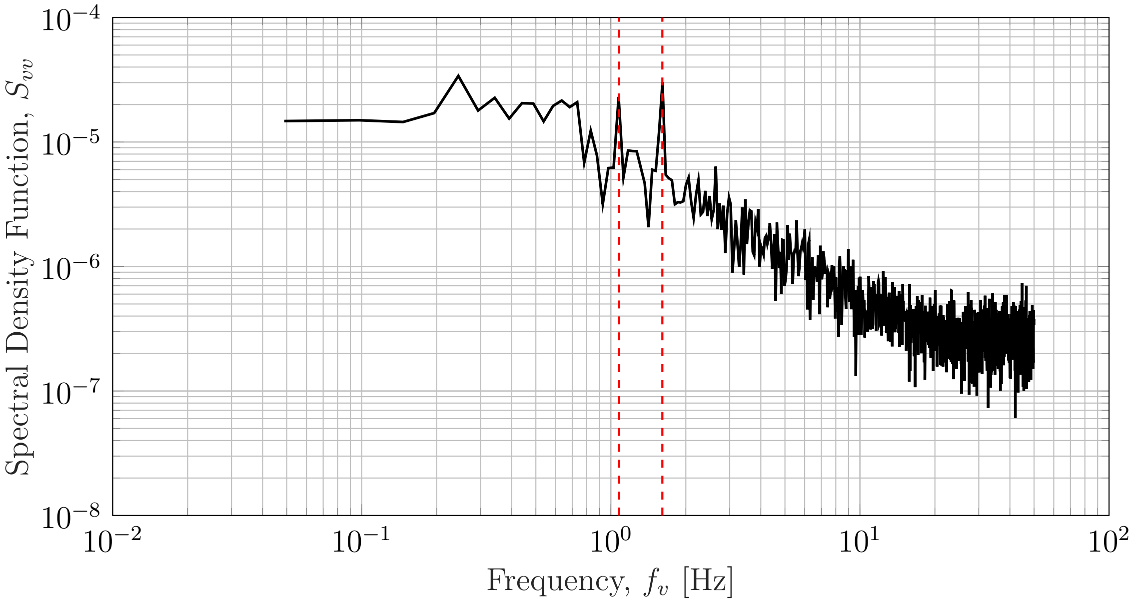

Figure B.29: Power spectra - lateral velocity at $h = 19\ cm,\ x = 638\ cm,\ y = 29\ cm,\ z = 13.5\ cm$

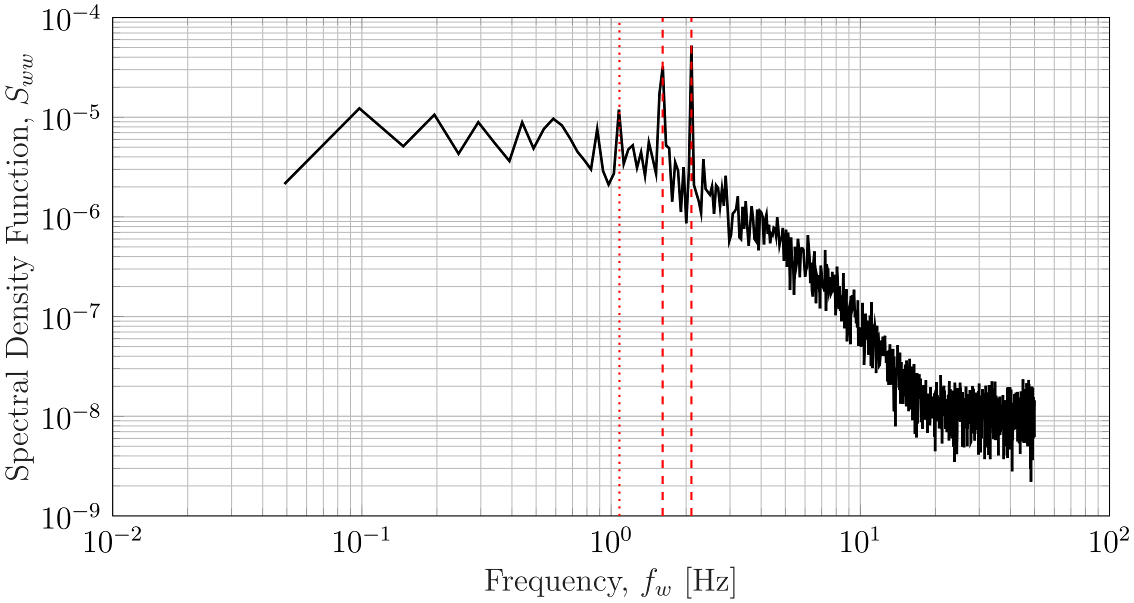

Figure B.30: Power spectra - vertical velocity at $h = 19\ cm,\ x = 638\ cm,\ y = 29\ cm,\ z = 13.5\ cm$

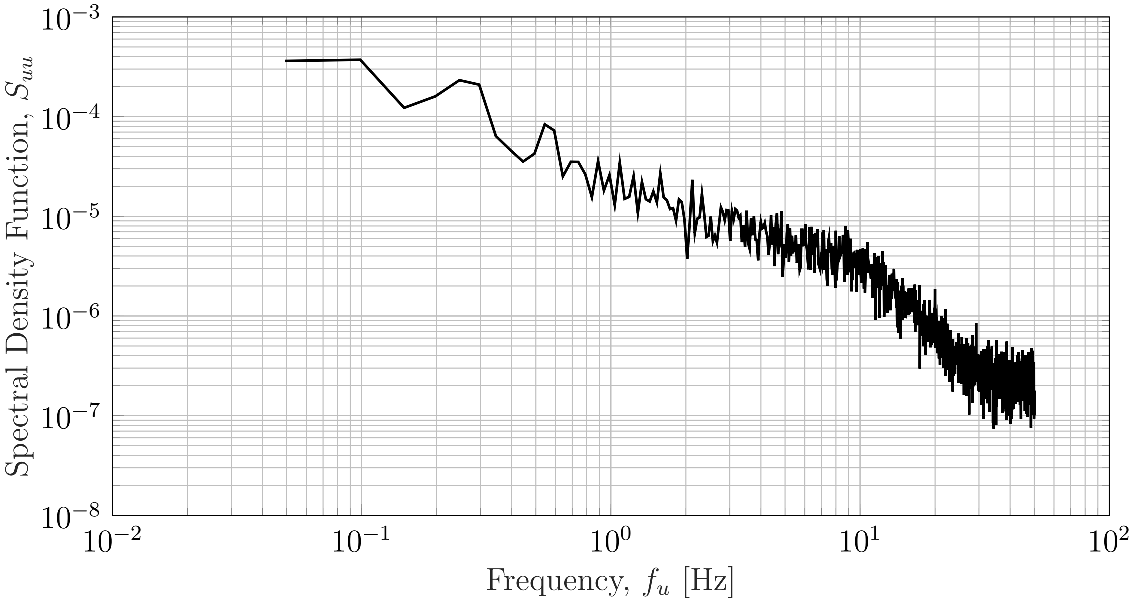

Figure B.31: Power spectra - longitudinal velocity at $h = 19\ cm,\ x = 638\ cm,\ y = 29\ cm,\ z = 7.5\ cm$

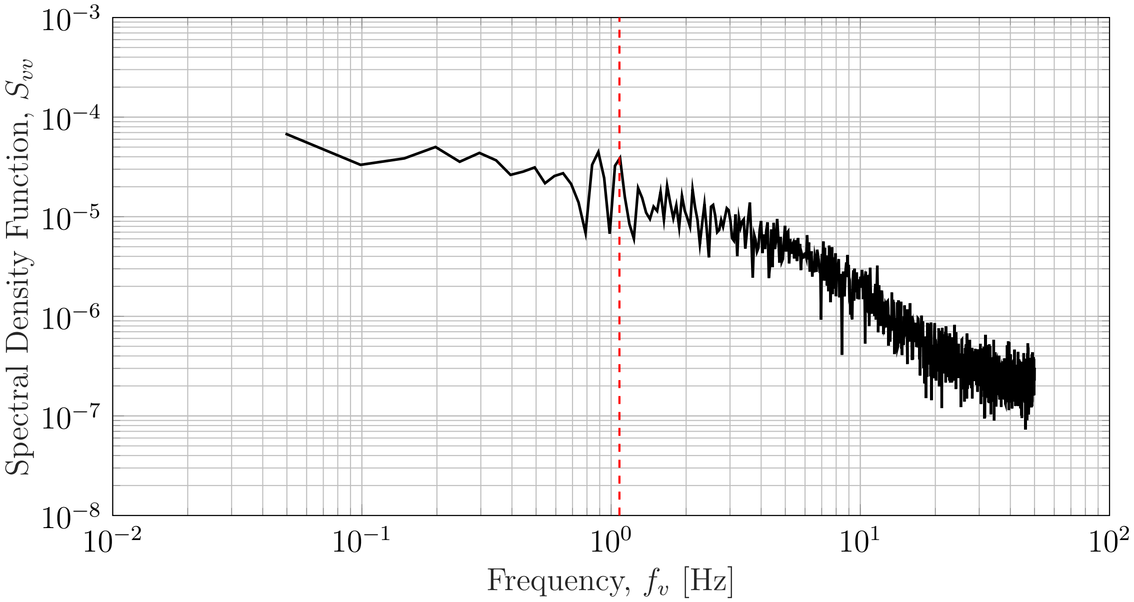

Figure B.32: Power spectra - lateral velocity at $h = 19\ cm,\ x = 638\ cm,\ y = 29\ cm,\ z = 7.5\ cm$

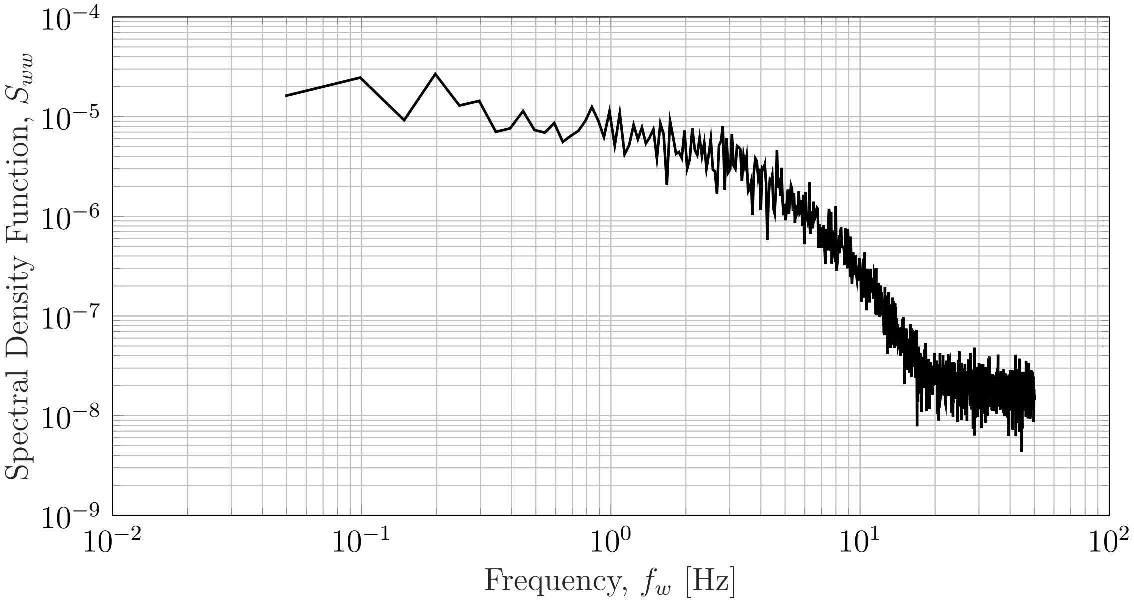

Figure B.33: Power spectra - vertical velocity at $h = 19\ cm,\ x = 638\ cm,\ y = 29\ cm,\ z = 7.5\ cm$

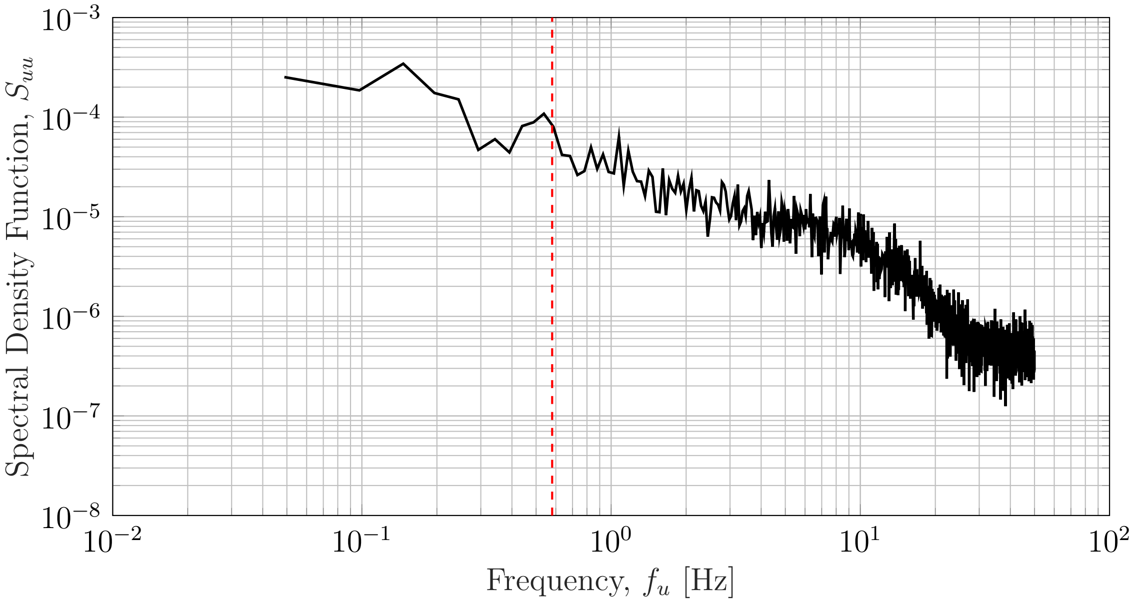

Figure B.34: Power spectra - longitudinal velocity at $h = 19\ cm,\ x = 638\ cm,\ y = 29\ cm,\ z = 0.5\ cm$

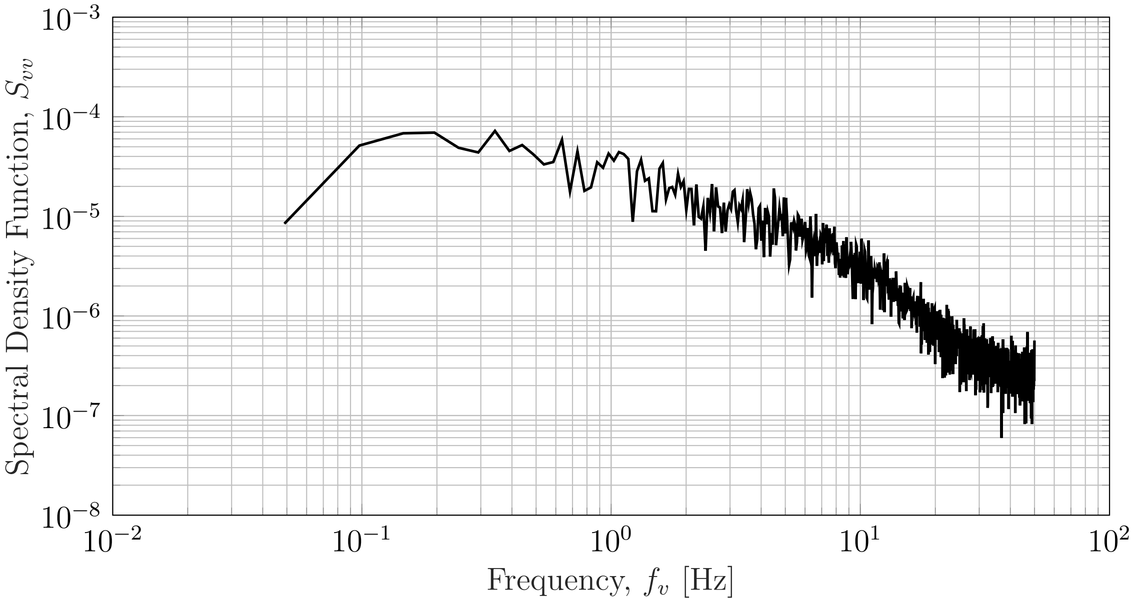

Figure B.35: Power spectra - lateral velocity at $h = 19\ cm,\ x = 638\ cm,\ y = 29\ cm,\ z = 0.5\ cm$

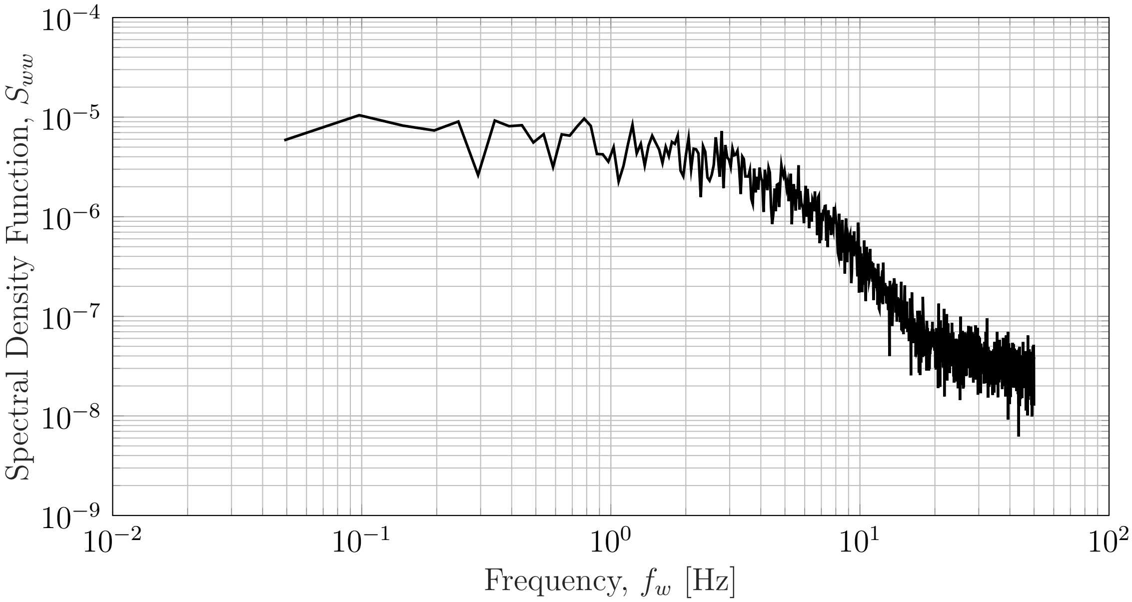

Figure B.36: Power spectra - vertical velocity at $h = 19\ cm,\ x = 638\ cm,\ y = 29\ cm,\ z = 0.5\ cm$

B.5 Measurement Section ($x = 638\ cm,\ h = 9.5\ cm$)

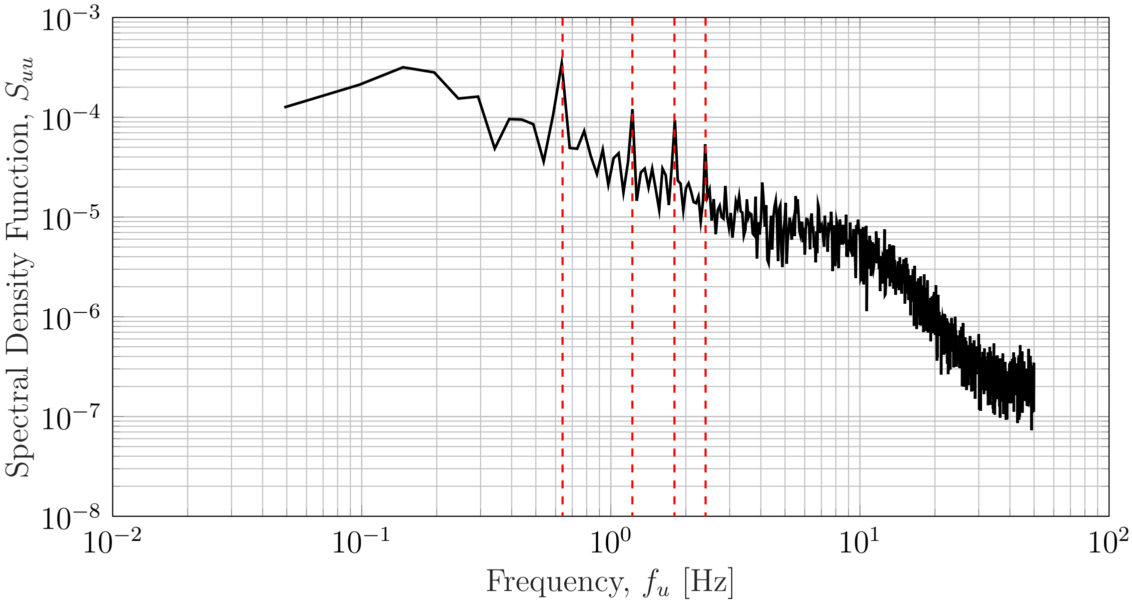

Figure B.37: Power spectra - longitudinal velocity at $h = 9.5\ cm,\ x = 638\ cm,\ y = 29\ cm,\ z = 13.5\ cm$

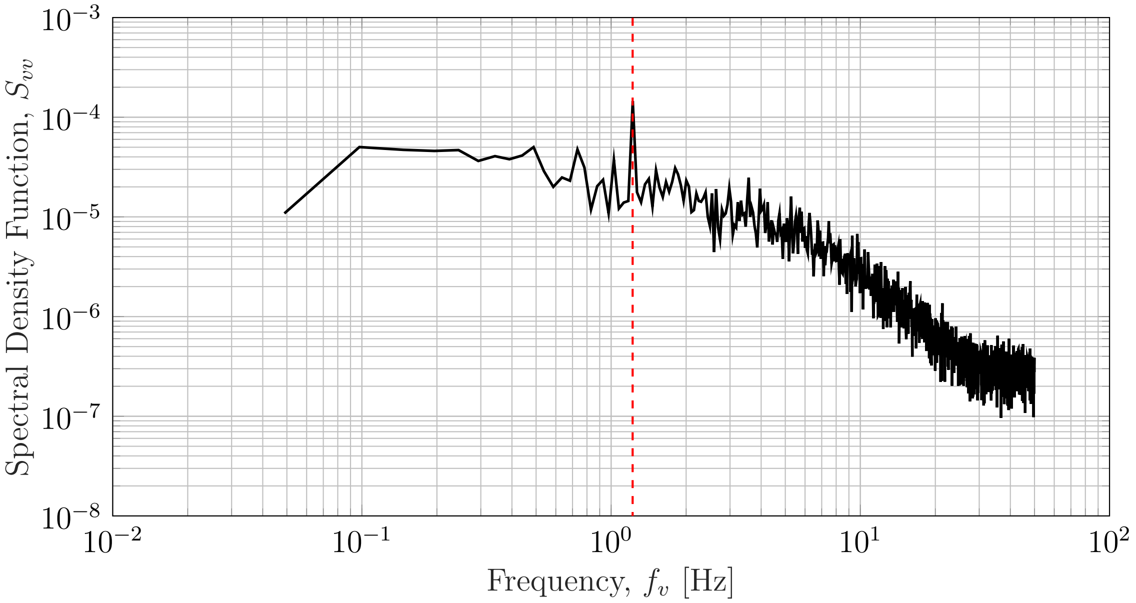

Figure B.38: Power spectra - lateral velocity at $h = 9.5\ cm,\ x = 638\ cm,\ y = 29\ cm,\ z = 13.5\ cm$

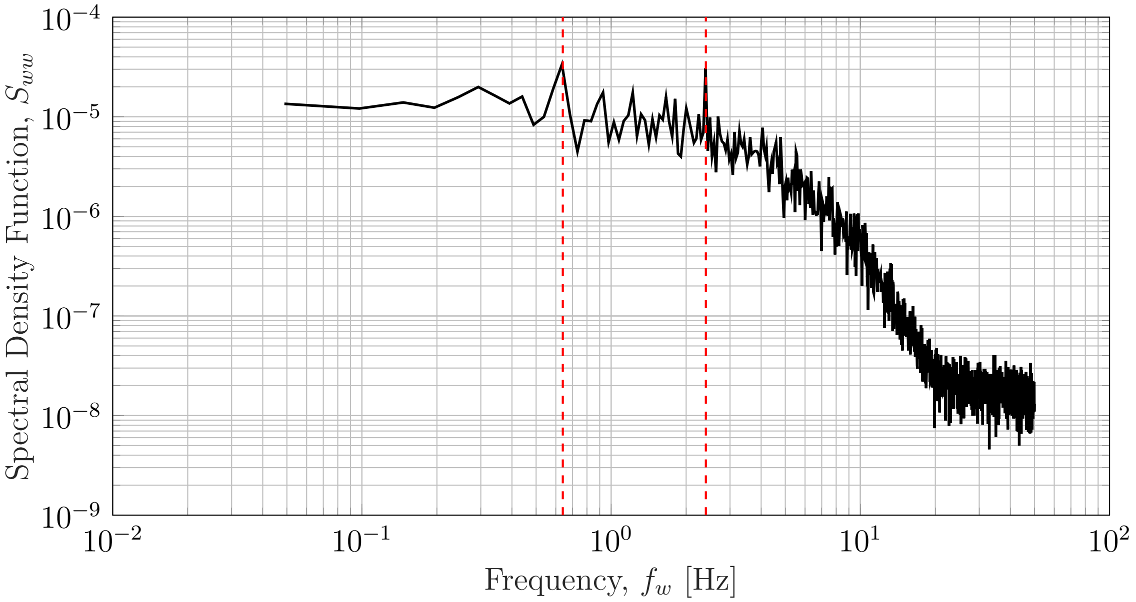

Figure B.39: Power spectra - vertical velocity at $h = 9.5\ cm,\ x = 638\ cm,\ y = 29\ cm,\ z = 13.5\ cm$

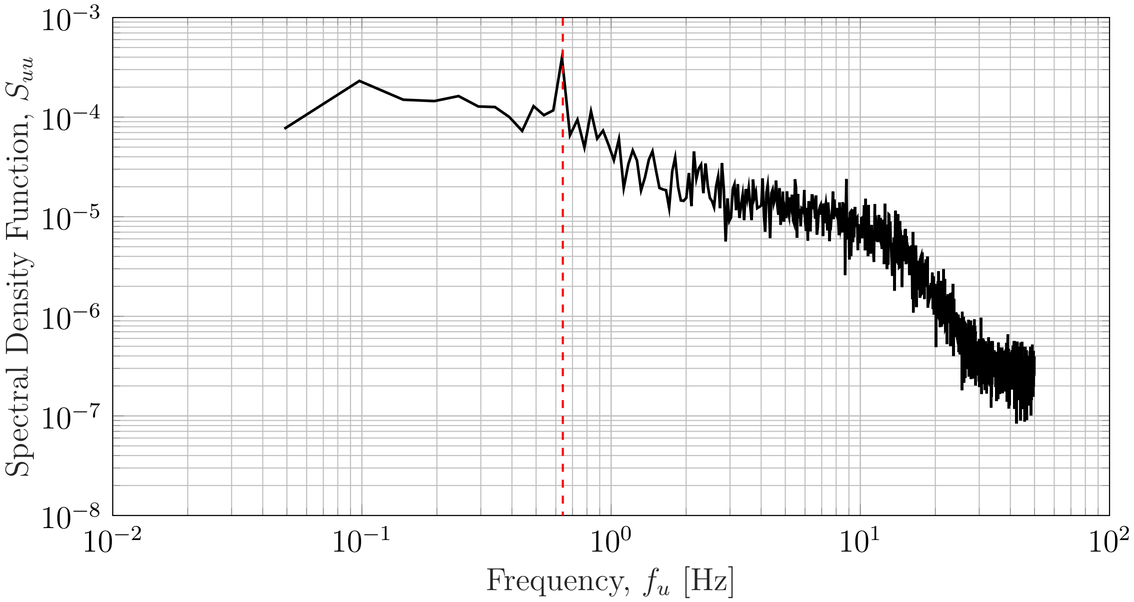

Figure B.40: Power spectra - longitudinal velocity at $h = 9.5\ cm,\ x = 638\ cm,\ y = 29\ cm,\ z = 7.5\ cm$

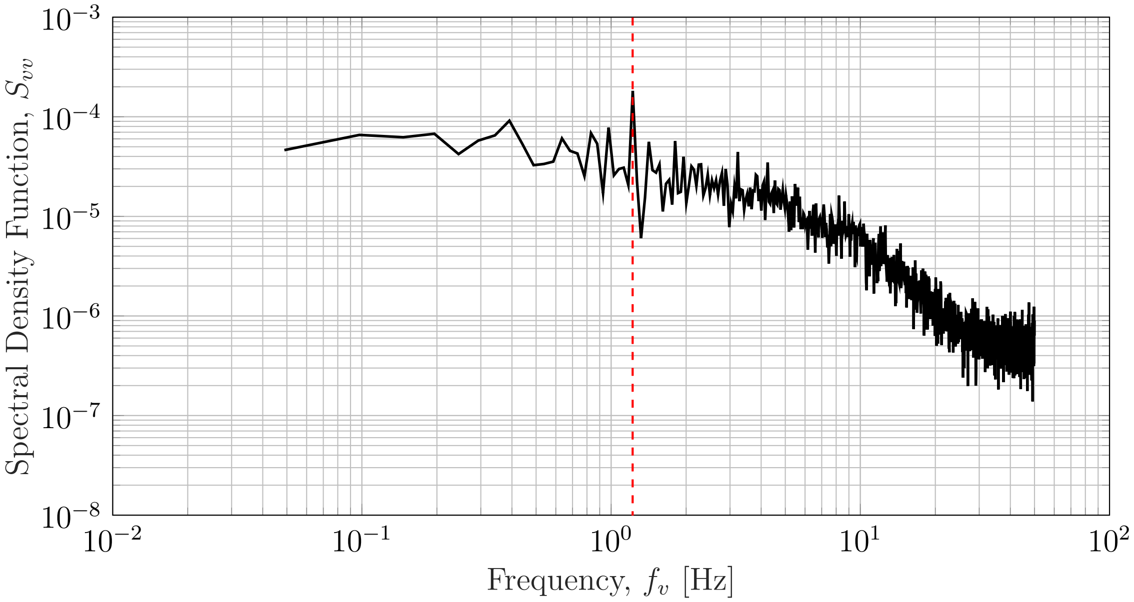

Figure B.41: Power spectra - lateral velocity at $h = 9.5\ cm,\ x = 638\ cm,\ y = 29\ cm,\ z = 7.5\ cm$

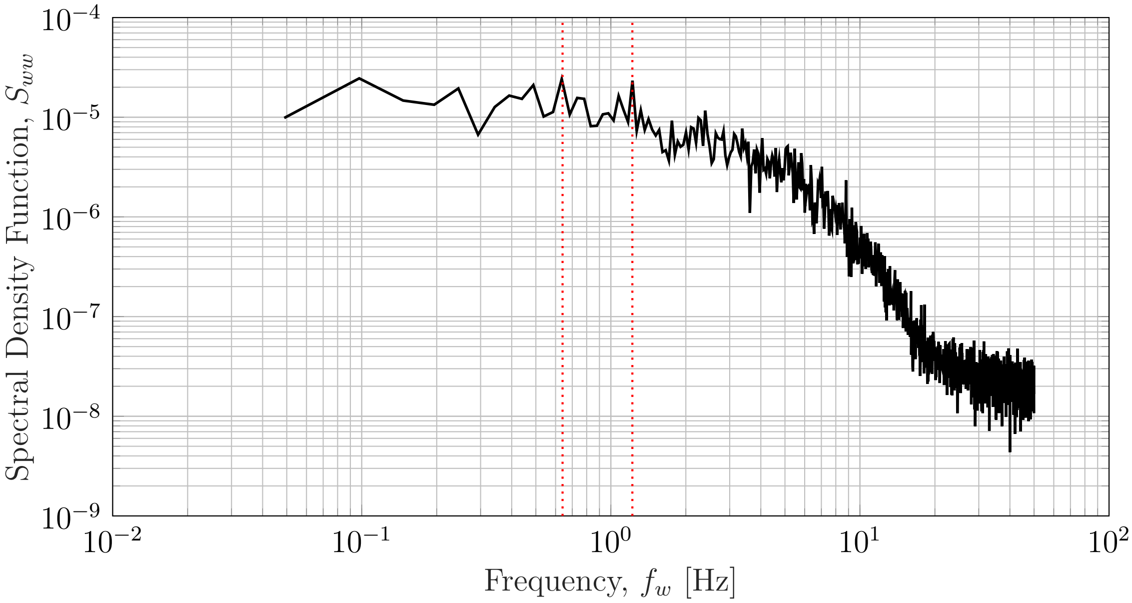

Figure B.42: Power spectra - vertical velocity at $h = 9.5\ cm,\ x = 638\ cm,\ y = 29\ cm,\ z = 7.5\ cm$

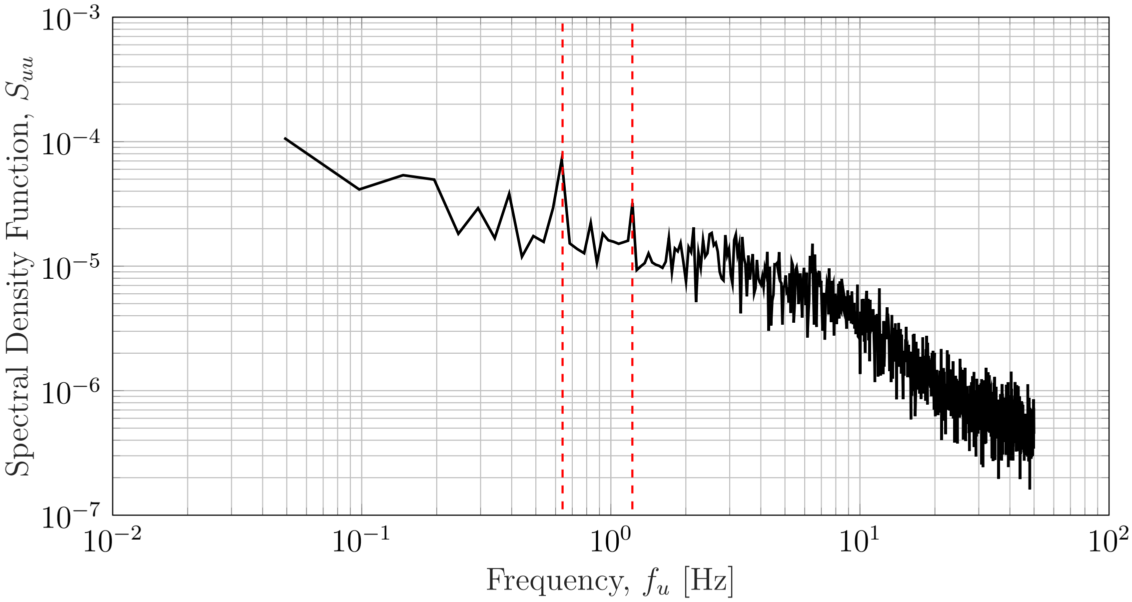

Figure B.43: Power spectra - longitudinal velocity at $h = 9.5\ cm,\ x = 638\ cm,\ y = 29\ cm,\ z = 0.5\ cm$

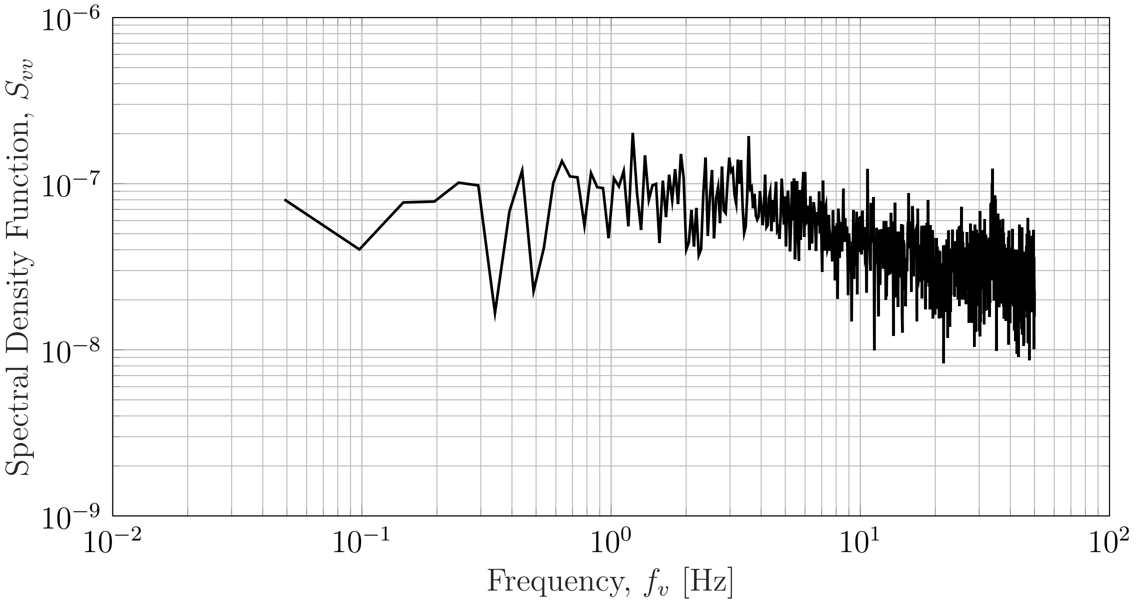

Figure B.44: Power spectra - lateral velocity at $h = 9.5\ cm,\ x = 638\ cm,\ y = 29\ cm,\ z = 0.5\ cm$

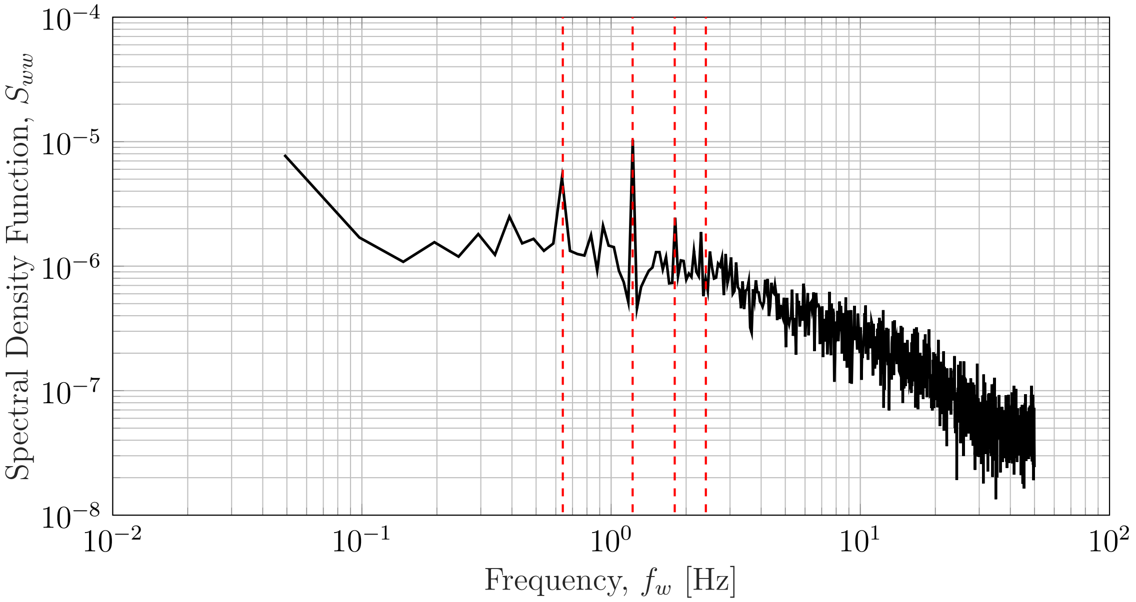

Figure B.45: Power spectra - vertical velocity at $h = 9.5\ cm,\ x = 638\ cm,\ y = 29\ cm,\ z = 0.5\ cm$

B.6 Measurement Section ($x = 638\ cm$, $h = 38\ cm$)

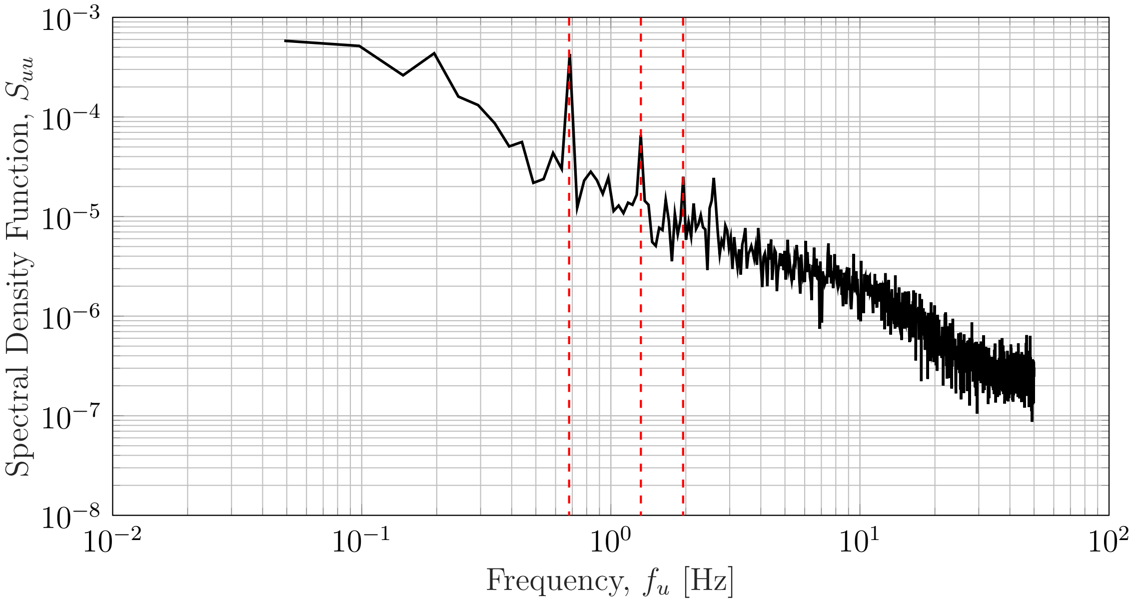

Figure B.46: Power spectra - longitudinal velocity at $h = 38\ cm,\ x = 638\ cm,\ y = 48.5\ cm,\ z = 13.5\ cm$

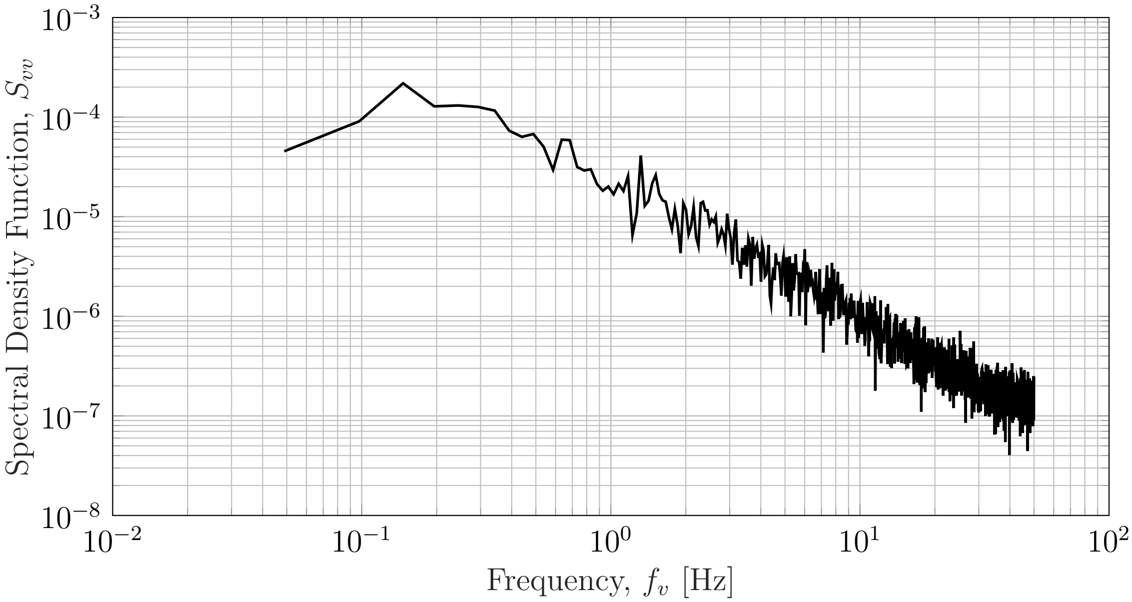

Figure B.47: Power spectra - lateral velocity at $h = 38\ cm,\ x = 638\ cm,\ y = 48.5\ cm,\ z = 13.5\ cm$

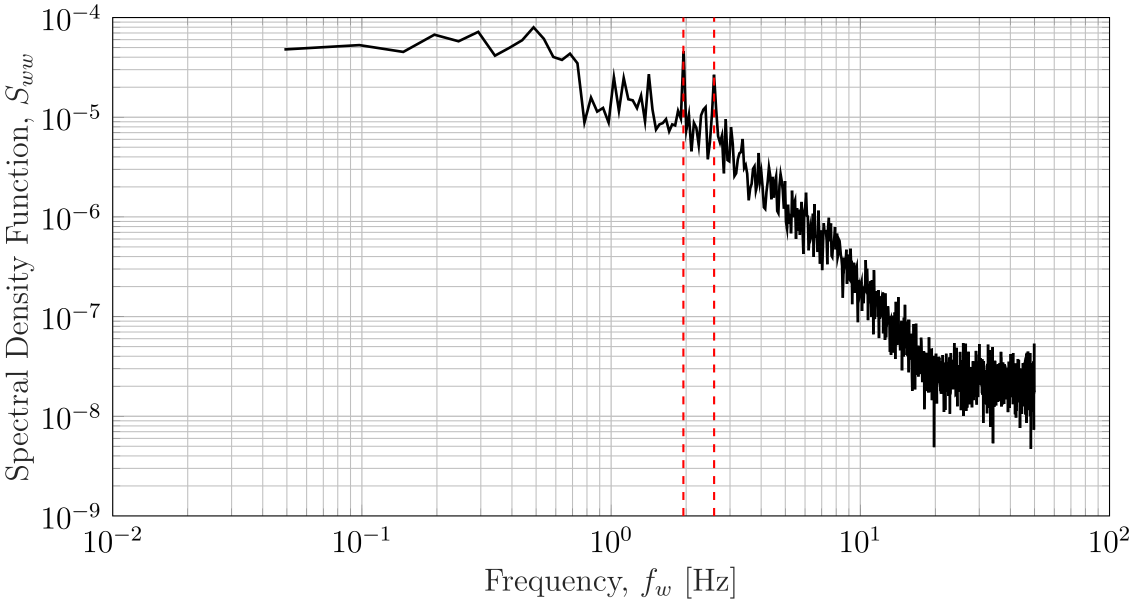

Figure B.48: Power spectra - vertical velocity at $h = 38\ cm,\ x = 638\ cm,\ y = 48.5\ cm,\ z = 13.5\ cm$

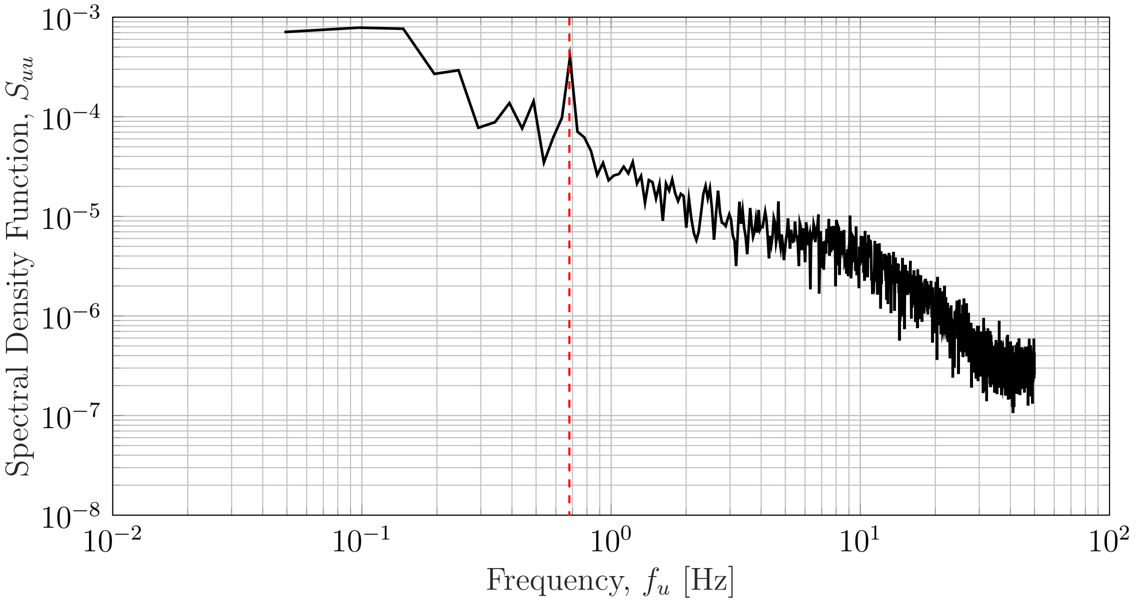

Figure B.49: Power spectra - longitudinal velocity at $h = 38\ cm,\ x = 638\ cm,\ y = 48.5\ cm,\ z = 7.5\ cm$

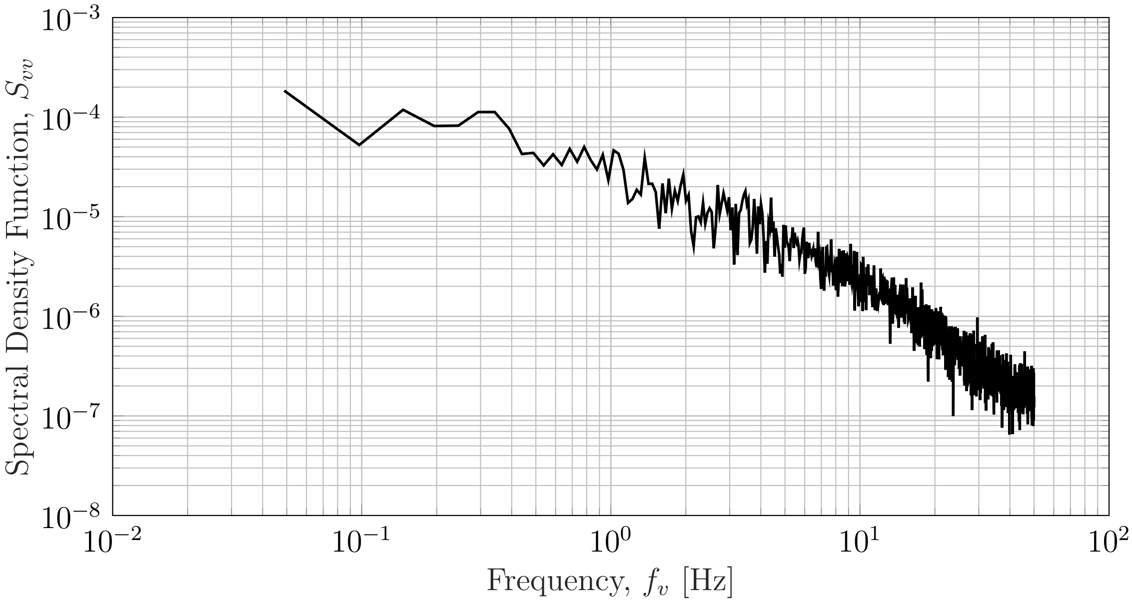

Figure B.50: Power spectra - lateral velocity at $h = 38\ cm,\ x = 638\ cm,\ y = 48.5\ cm,\ z = 7.5\ cm$

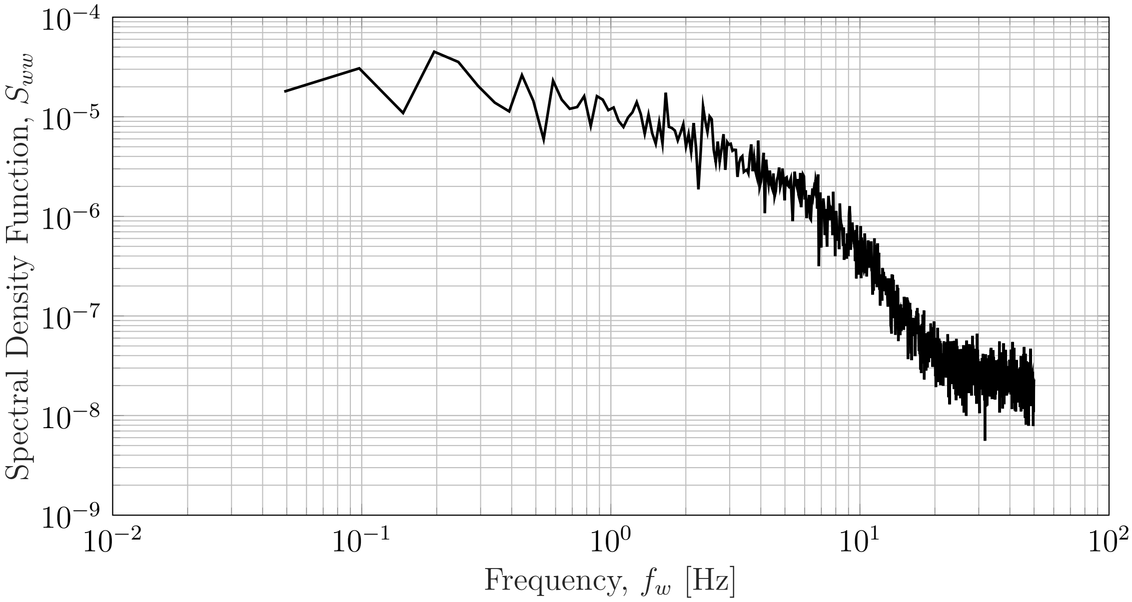

Figure B.51: Power spectra - vertical velocity at $h = 38\ cm,\ x = 638\ cm,\ y = 48.5\ cm,\ z = 7.5\ cm$

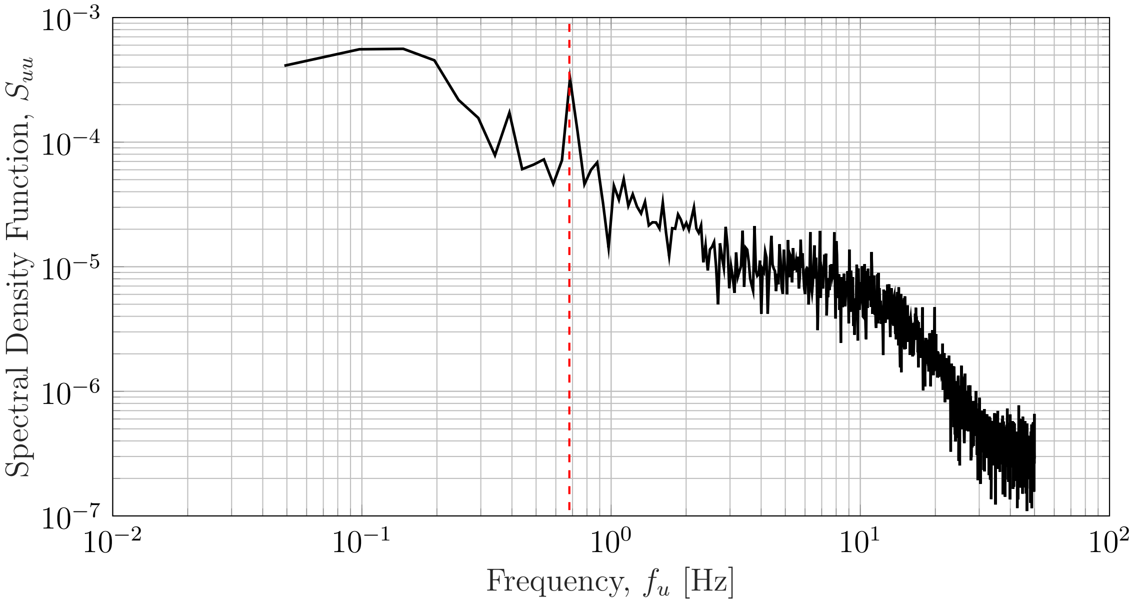

Figure B.52: Power spectra - longitudinal velocity at $h = 38\ cm,\ x = 638\ cm,\ y = 48.5\ cm,\ z = 0.5\ cm$

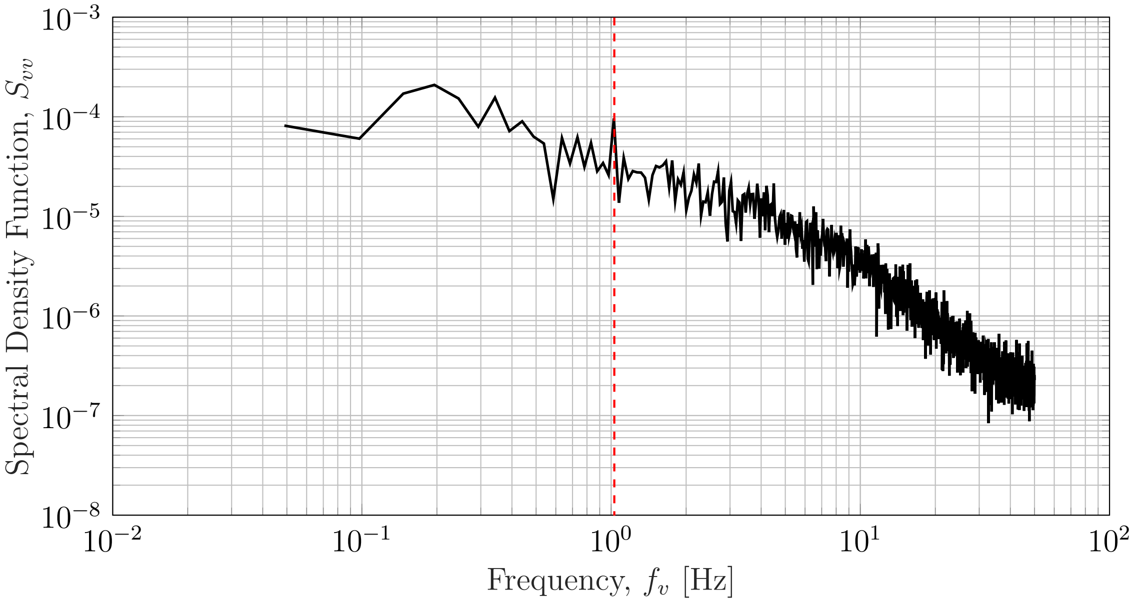

Figure B.53: Power spectra - lateral velocity at $h = 38\ cm,\ x = 638\ cm,\ y = 48.5\ cm,\ z = 0.5\ cm$

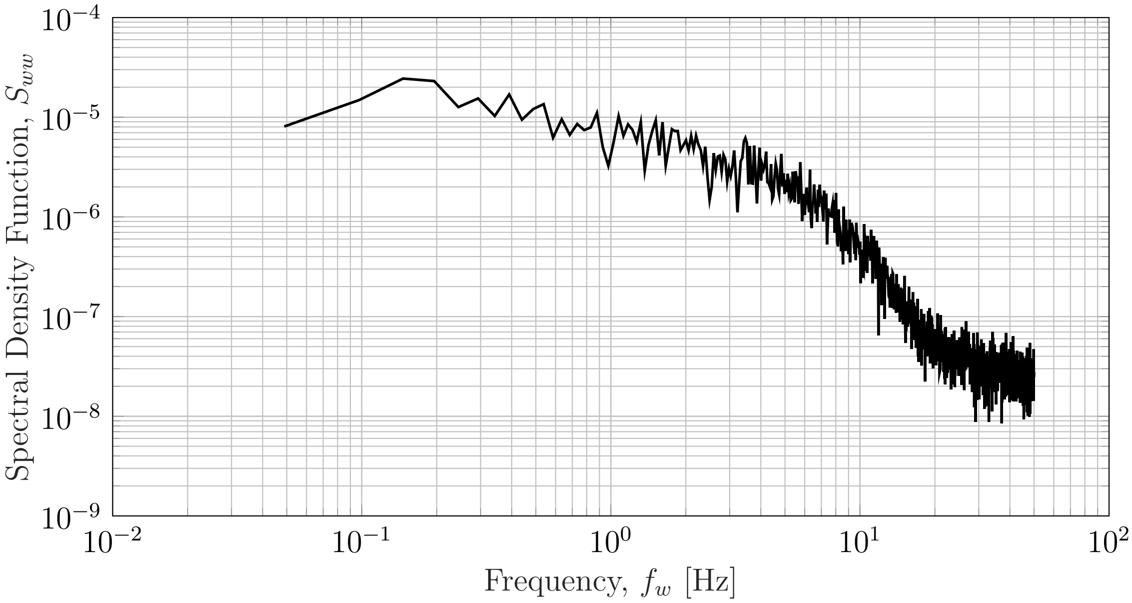

Figure B.54: Power spectra - vertical velocity at $h = 38\ cm,\ x = 638\ cm,\ y = 48.5\ cm,\ z = 0.5\ cm$

Appendix C

sPIV Power Spectra

The following are the power spectra from the sPIV measurements. Locations and depth conditions are listed, and all cases are for a nominal velocity of 20 $cm\ s^{-1}$.

C.1 Measurement Section ($x \approx 638\ cm,\ h = 6.4\ cm$)

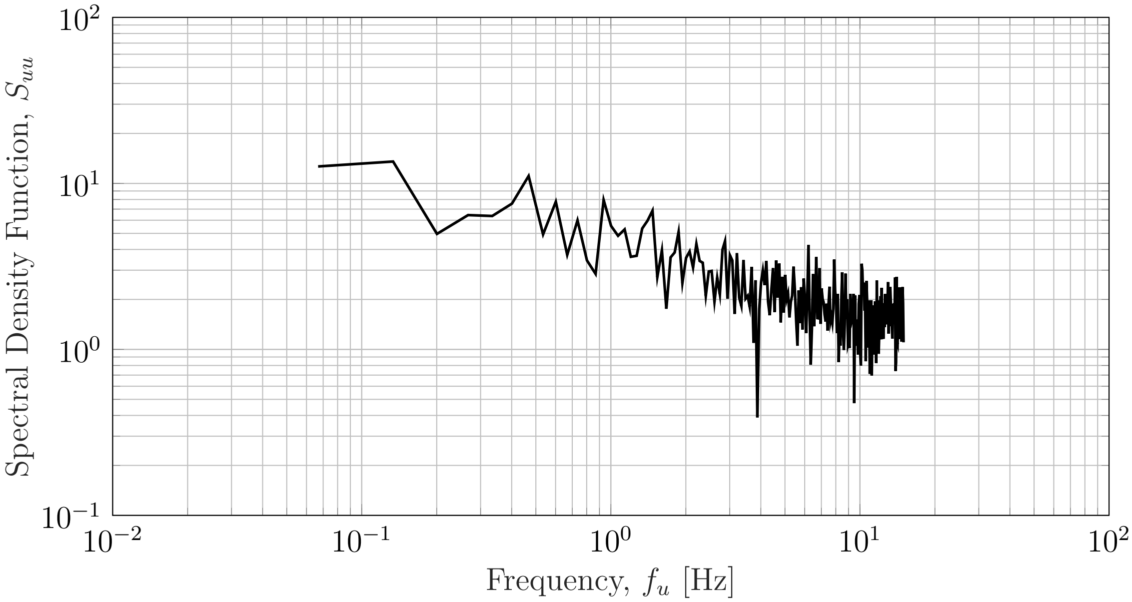

Figure C.1: Power spectra - longitudinal velocity at $x \approx 638\ cm,\ y = 19.25\ cm,\ z = 6.4\ cm$

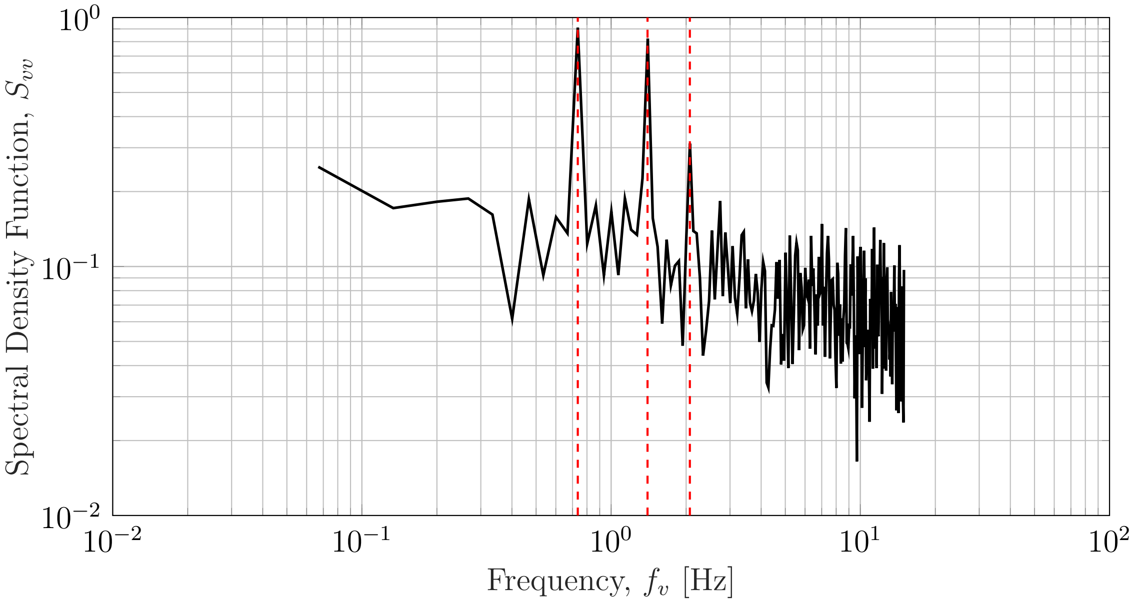

Figure C.2: Power spectra - lateral velocity at $x \approx 638\ cm,\ y = 19.25\ cm,\ z = 6.4\ cm$

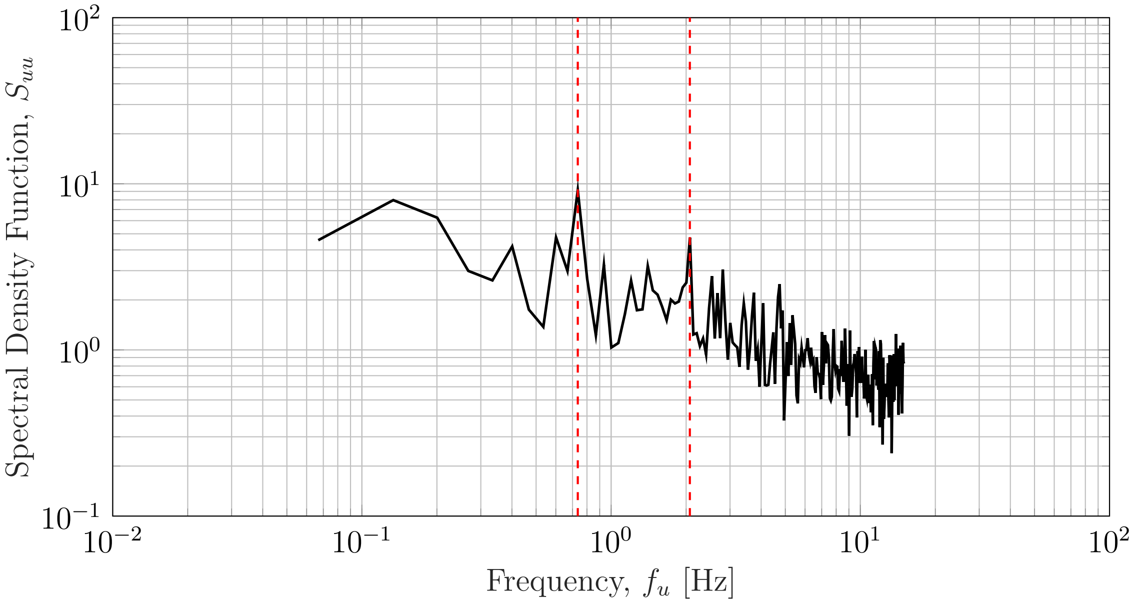

Figure C.3: Power spectra - longitudinal velocity at $x \approx 638\ cm,\ y = 22.5\ cm,\ z = 6.4\ cm$

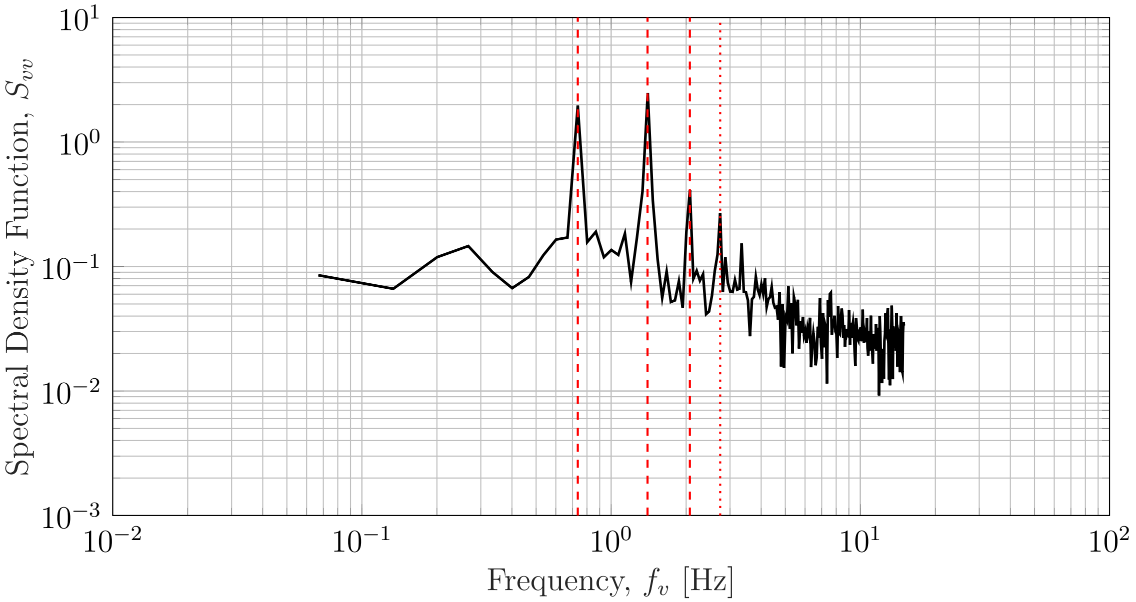

Figure C.4: Power spectra - lateral velocity at $x \approx 638\ cm,\ y = 22.5\ cm,\ z = 6.4\ cm$

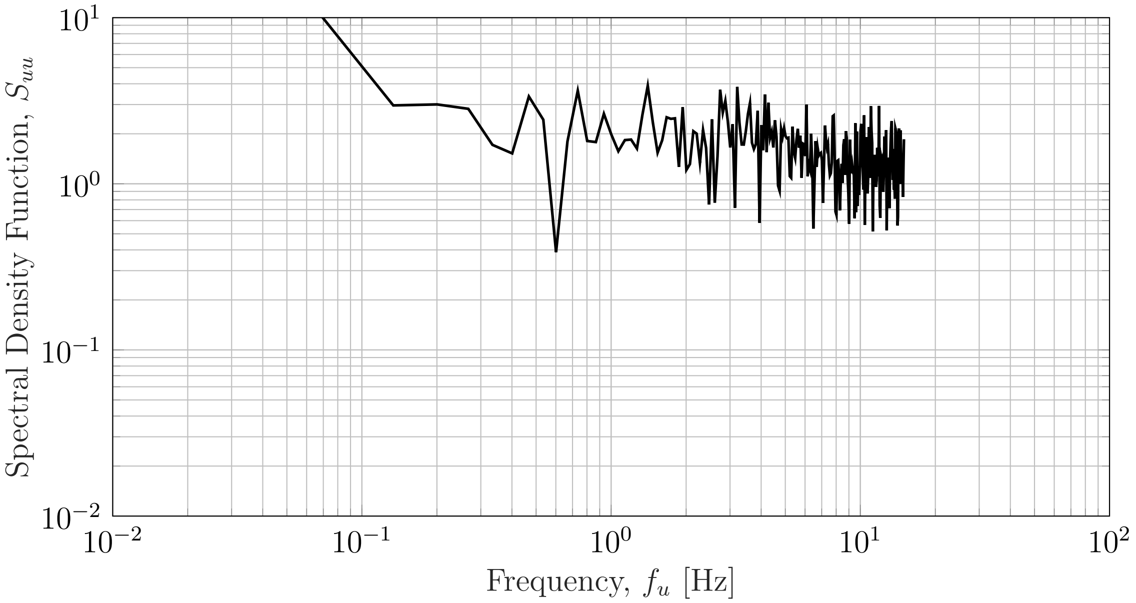

Figure C.5: Power spectra - longitudinal velocity at $x \approx 638\ cm,\ y = 25.7\ cm,\ z = 6.4\ cm$

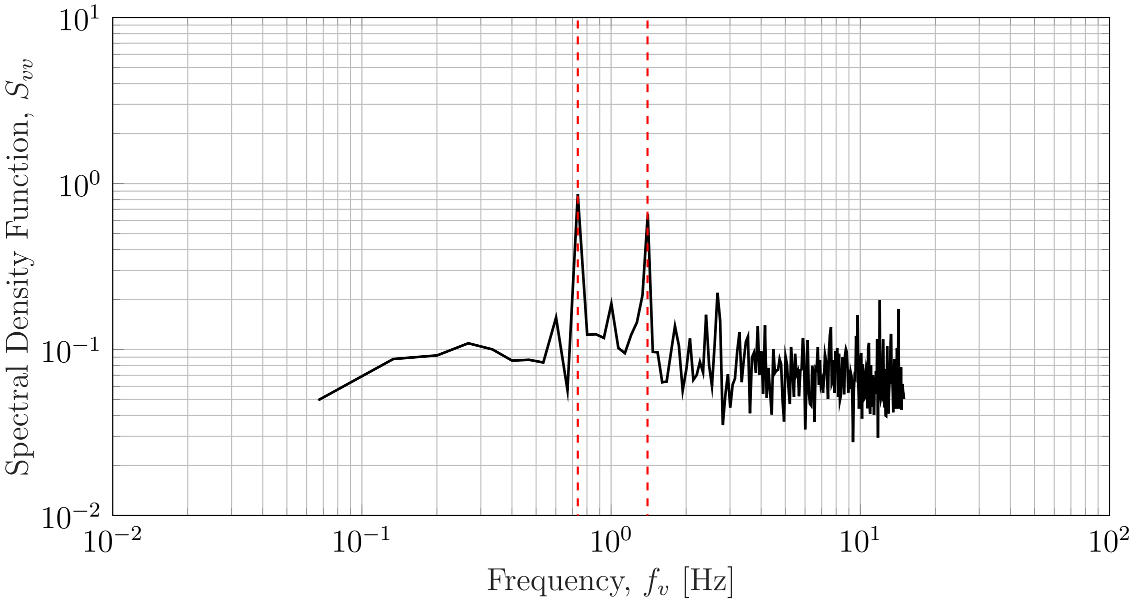

Figure C.6: Power spectra - lateral velocity at $x \approx 638\ cm,\ y = 25.7\ cm,\ z = 6.4\ cm$

C.2 Measurement Section ($x \approx 638\ cm,\ h = 9.5\ cm$)

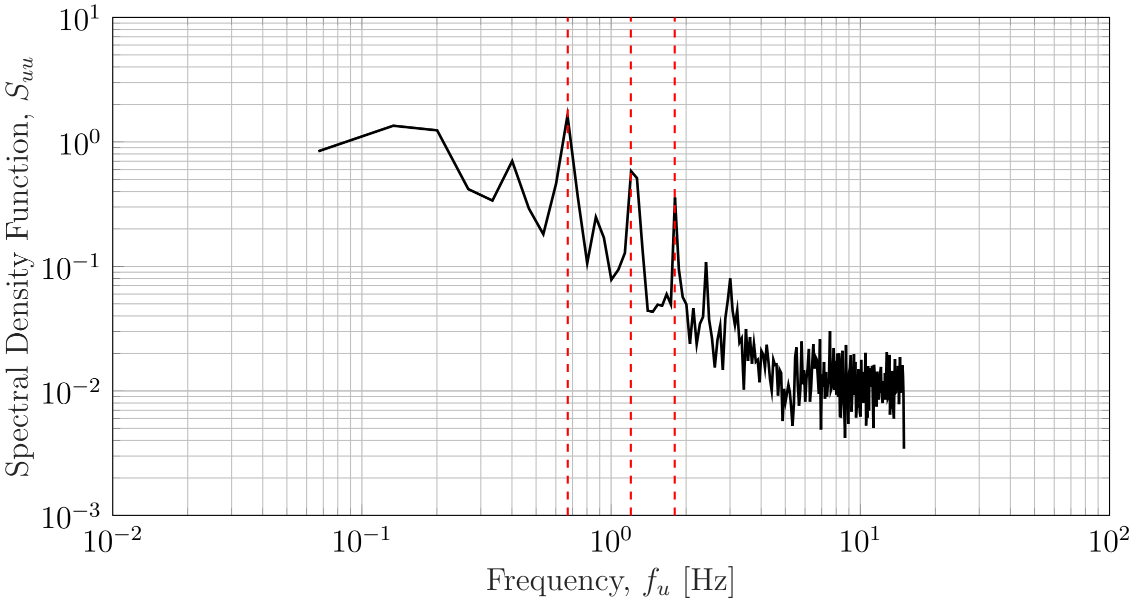

Figure C.7: Power spectra - longitudinal velocity at $x \approx 638\ cm,\ y = 49.8\ cm,\ z = 9.5\ cm$

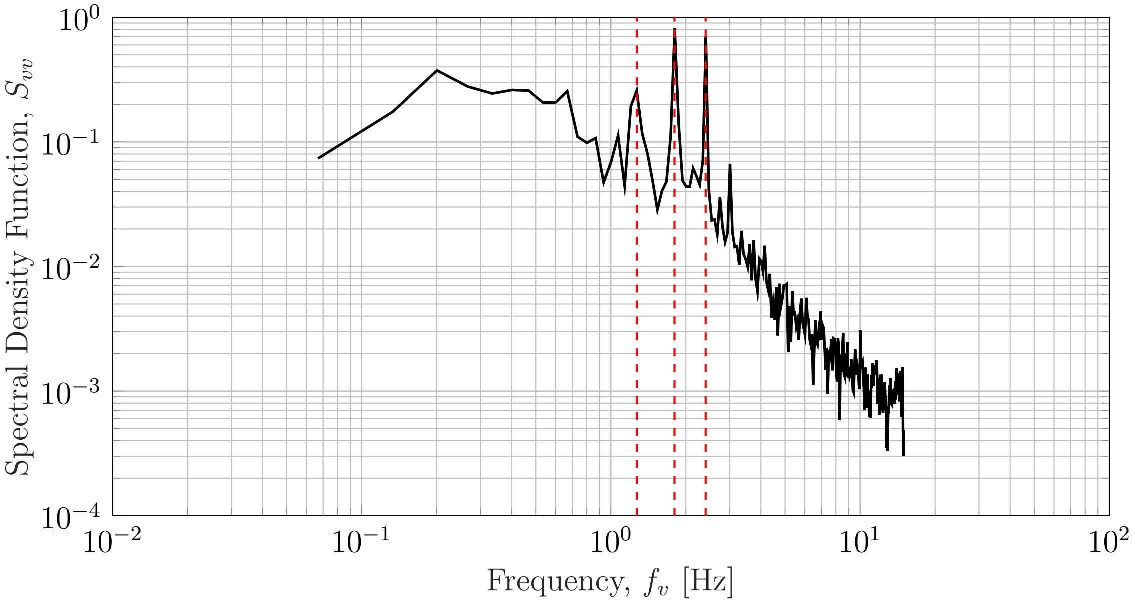

Figure C.8: Power spectra - lateral velocity at $x \approx 638\ cm,\ y = 49.8\ cm,\ z = 9.5\ cm$

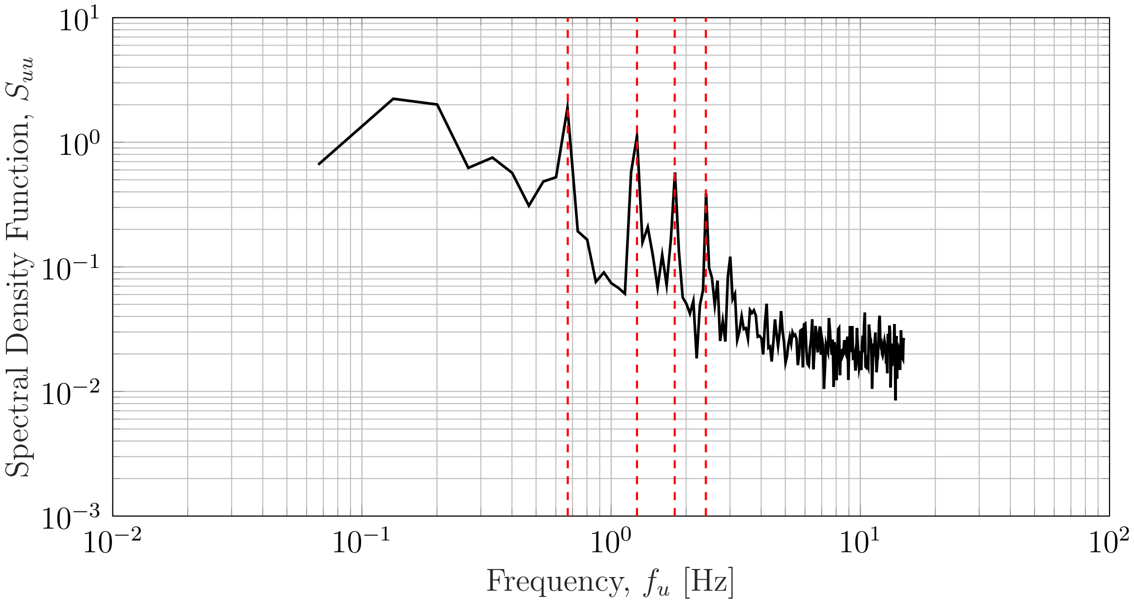

Figure C.9: Power spectra - longitudinal velocity at $x \approx 638\ cm,\ y = 44.5\ cm,\ z = 9.5\ cm$

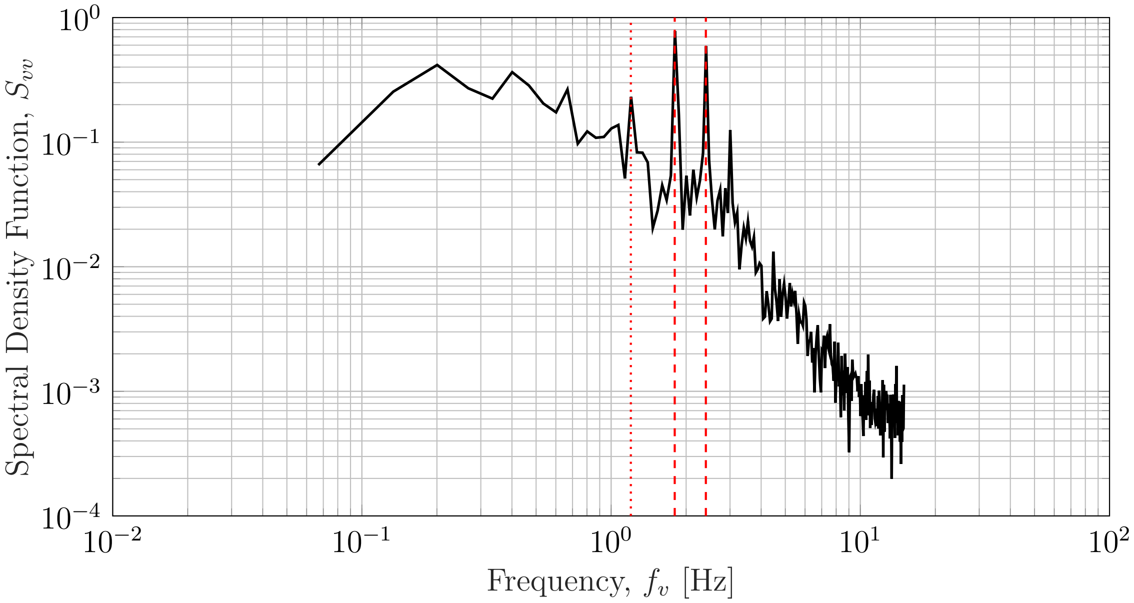

Figure C.10: Power spectra - lateral velocity at $x \approx 638\ cm,\ y = 44.5\ cm,\ z = 9.5\ cm$

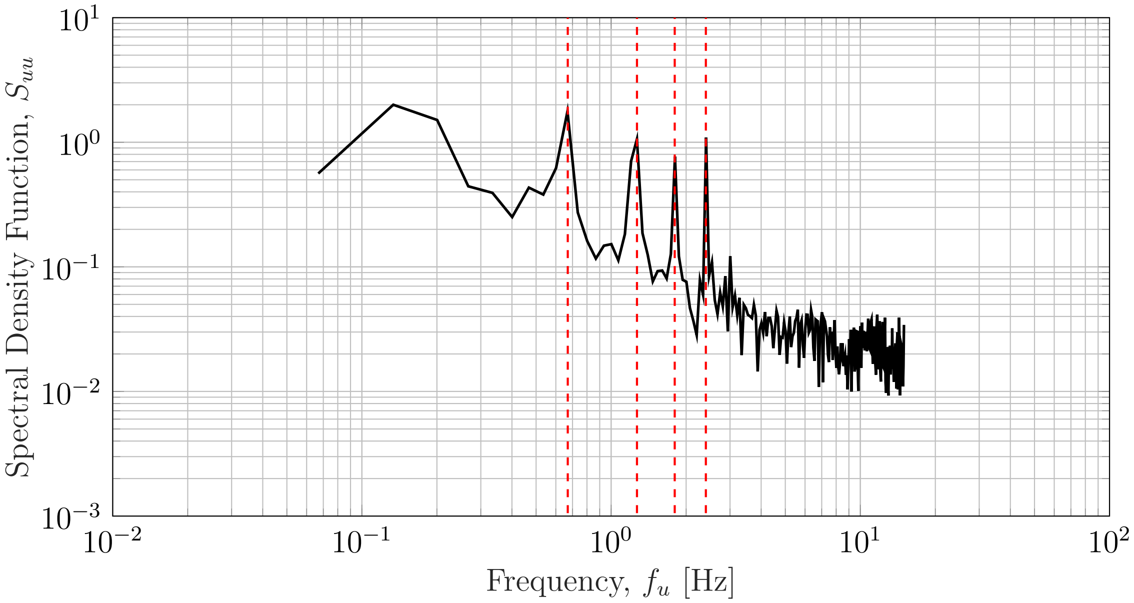

Figure C.11: Power spectra - longitudinal velocity at $x \approx 638\ cm,\ y = 40.0\ cm,\ z = 9.5\ cm$

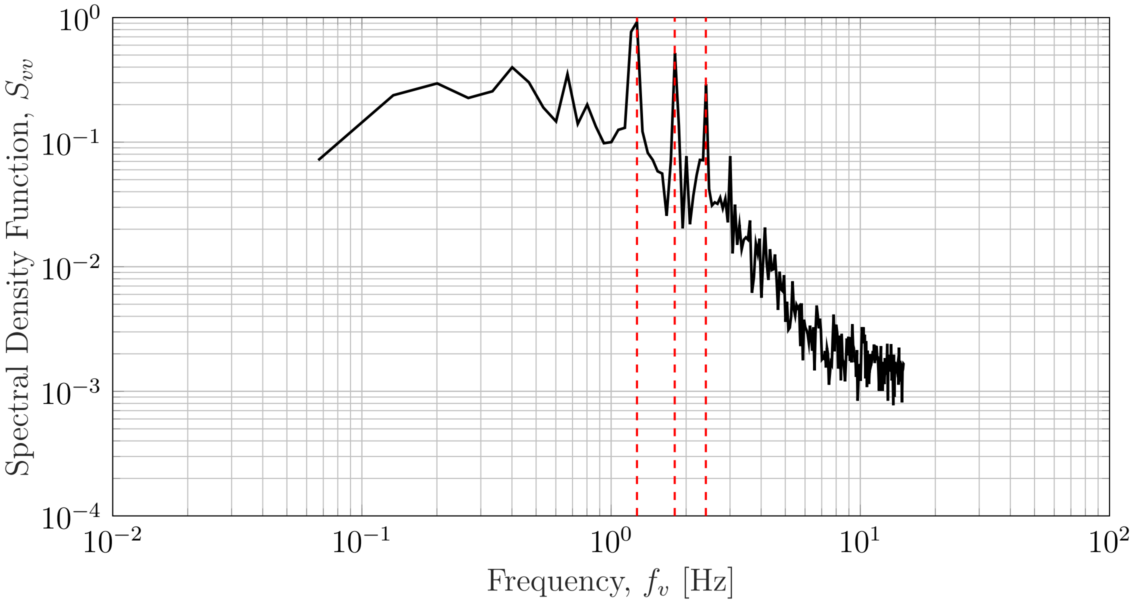

Figure C.12: Power spectra - lateral velocity at $x \approx 638\ cm,\ y = 40.0\ cm,\ z = 9.5\ cm$

C.3 Measurement Section ($x \approx 638\ cm,\ h = 19\ cm$)

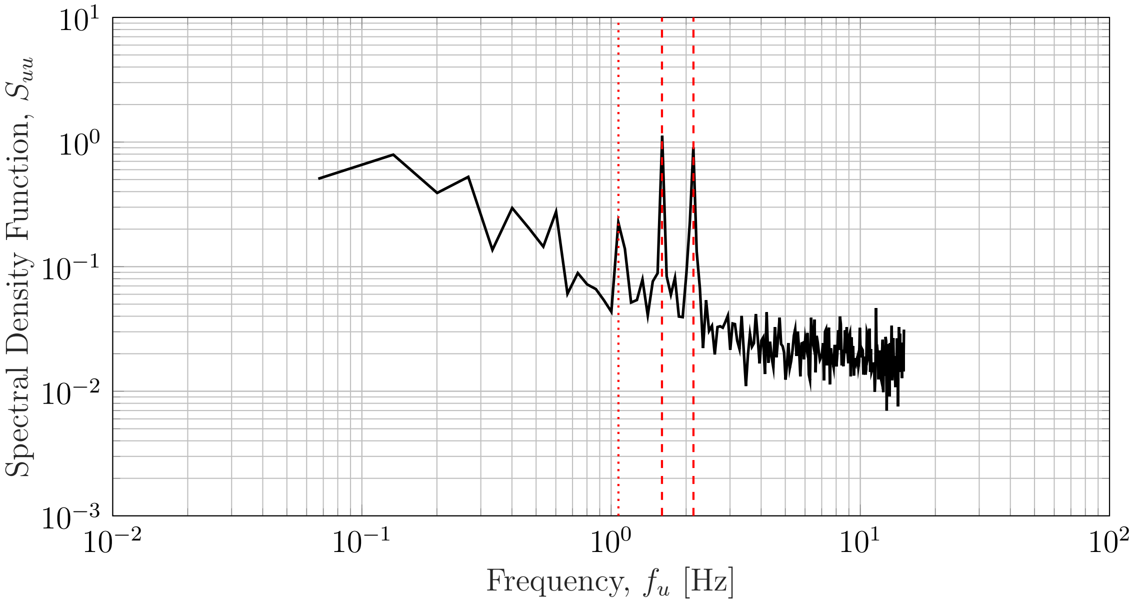

Figure C.13: Power spectra - longitudinal velocity at $x \approx 638\ cm,\ y = 19.25\ cm,\ z = 19\ cm$

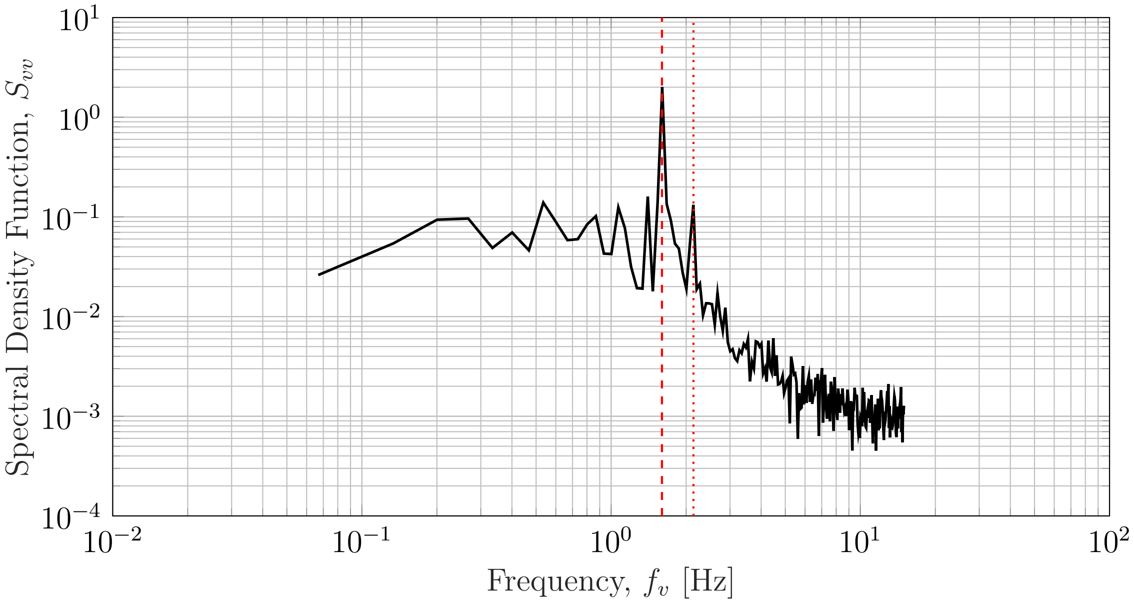

Figure C.14: Power spectra - lateral velocity at $x \approx 638\ cm,\ y = 19.25\ cm,\ z = 19\ cm$

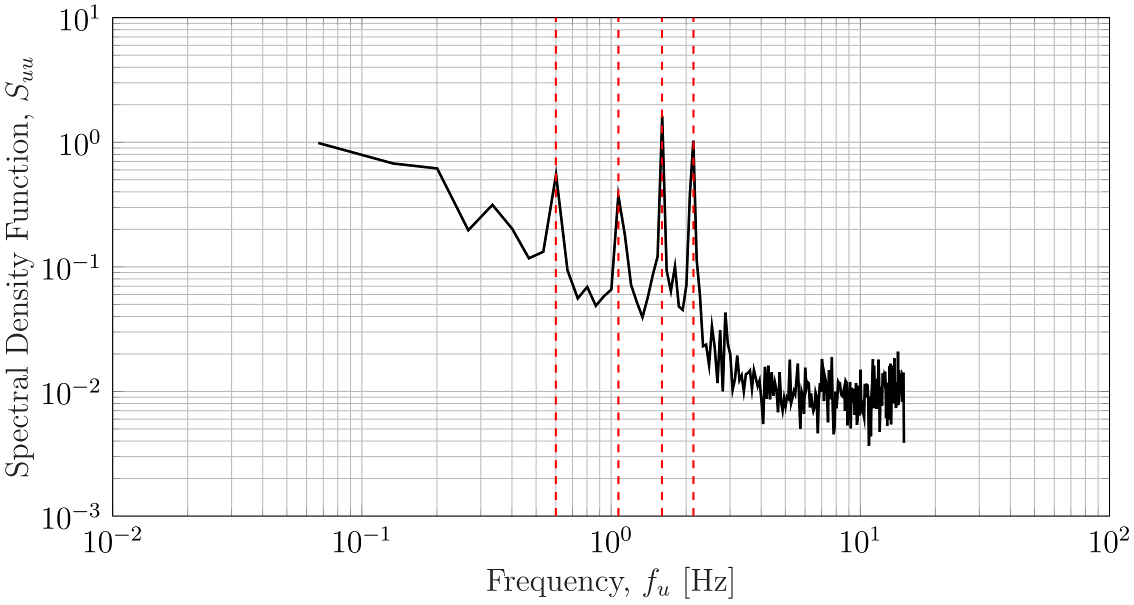

Figure C.15: Power spectra - longitudinal velocity at $x \approx 638\ cm,\ y = 28.9\ cm,\ z = 19\ cm$

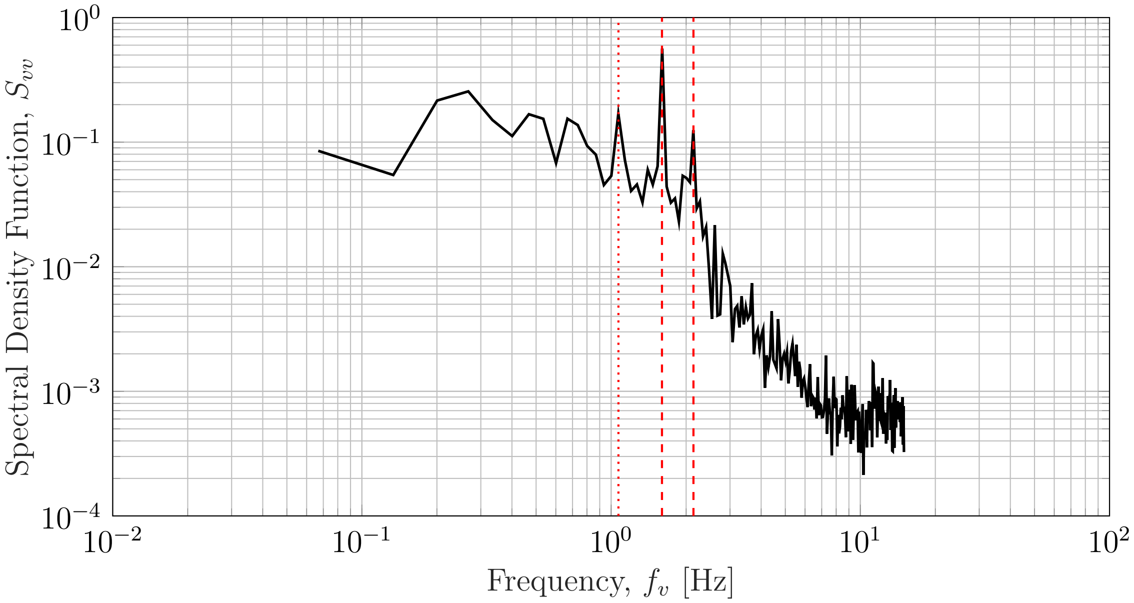

Figure C.16: Power spectra - lateral velocity at $x \approx 638\ cm,\ y = 28.9\ cm,\ z = 19\ cm$

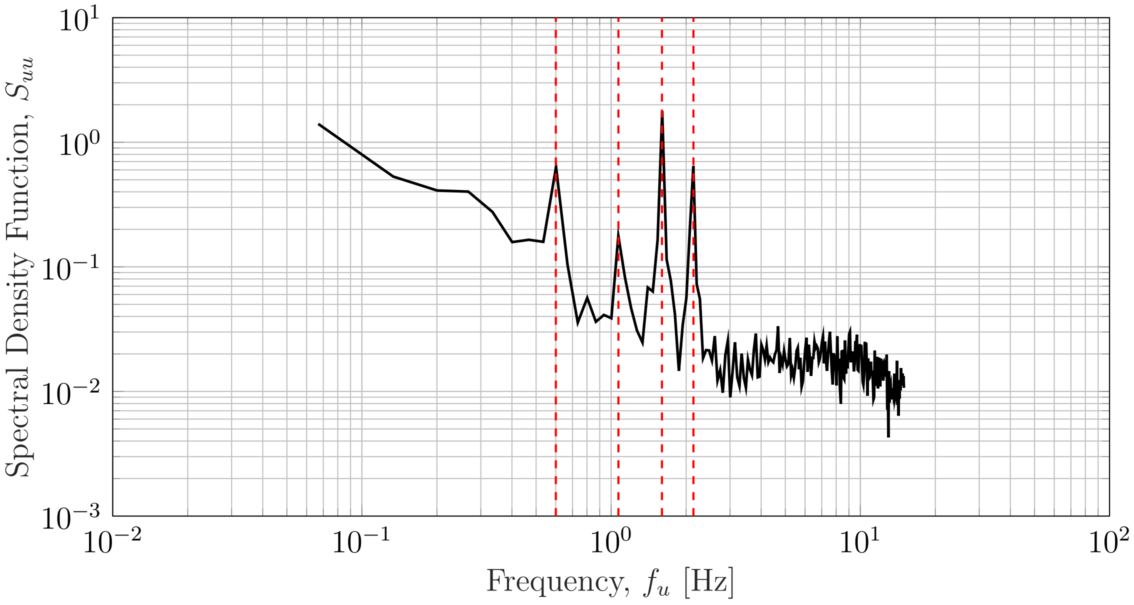

Figure C.17: Power spectra - longitudinal velocity at $x \approx 638\ cm,\ y = 38.5\ cm,\ z = 19\ cm$

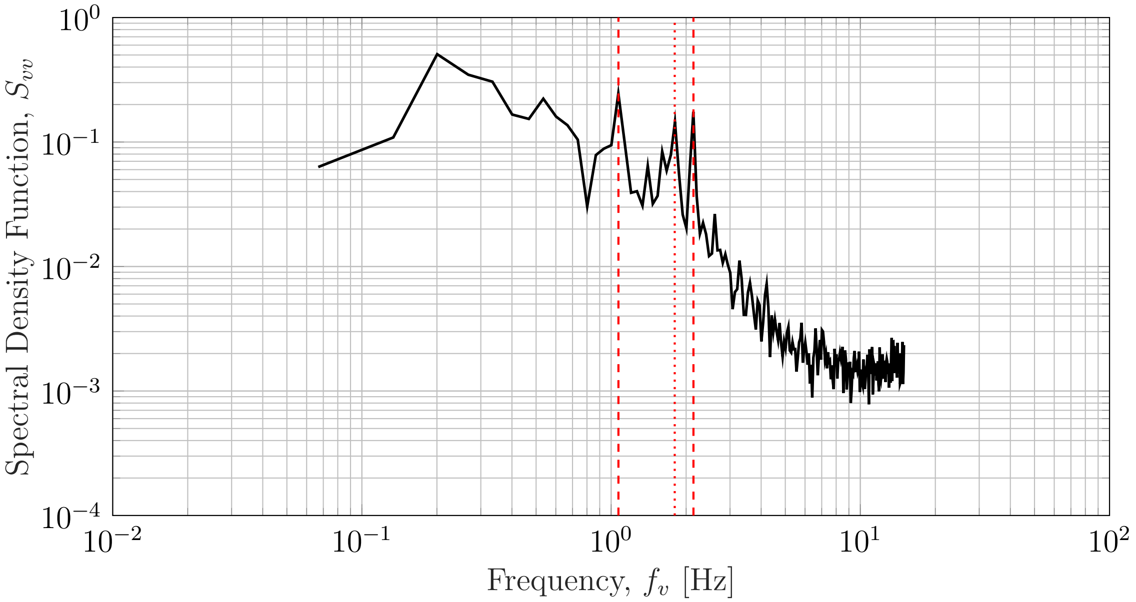

Figure C.18: Power spectra - lateral velocity at $x \approx 638\ cm,\ y = 38.5\ cm,\ z = 19\ cm$

C.4 Measurement Section ($x \approx 638\ cm,\ h = 38\ cm$)

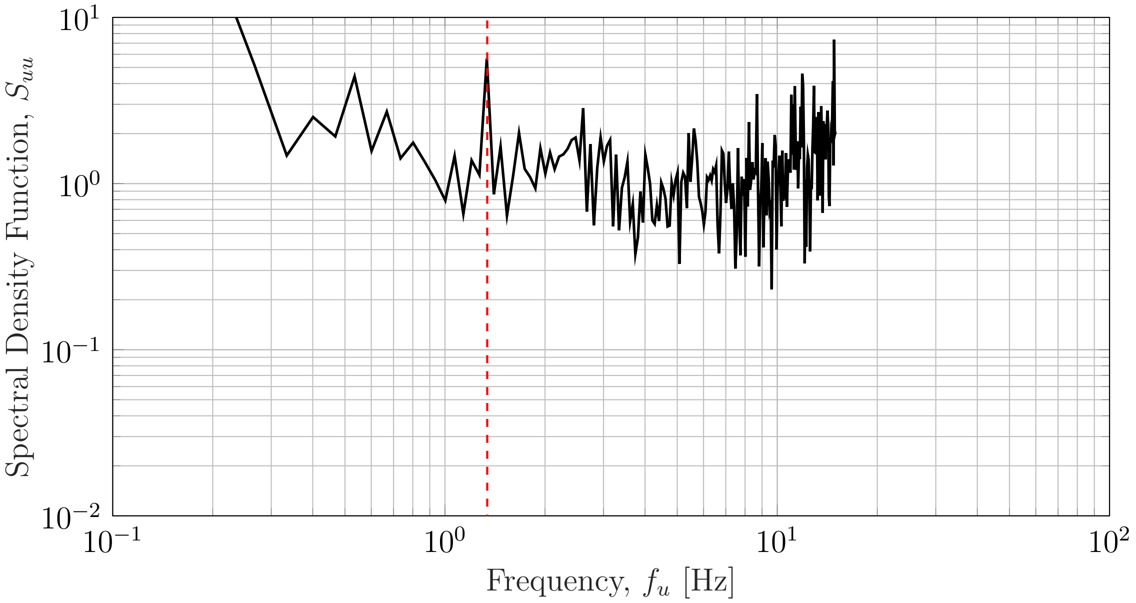

Figure C.19: Power spectra - longitudinal velocity at $x \approx 638\ cm,\ y = 19.25\ cm,\ z = 38\ cm$

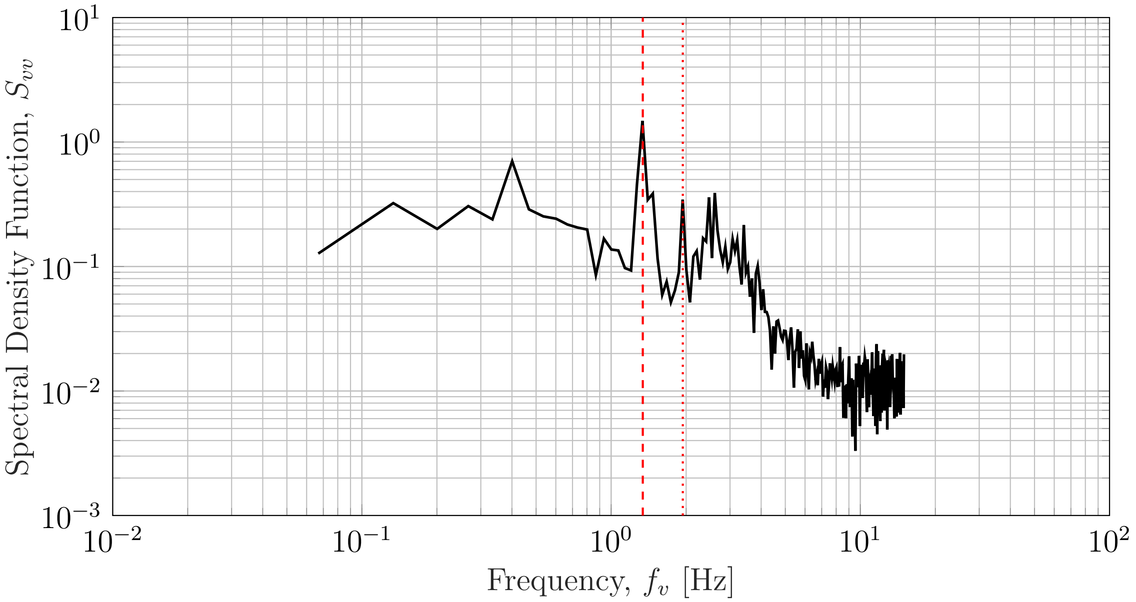

Figure C.20: Power spectra - lateral velocity at $x \approx 638\ cm,\ y = 19.25\ cm,\ z = 38\ cm$

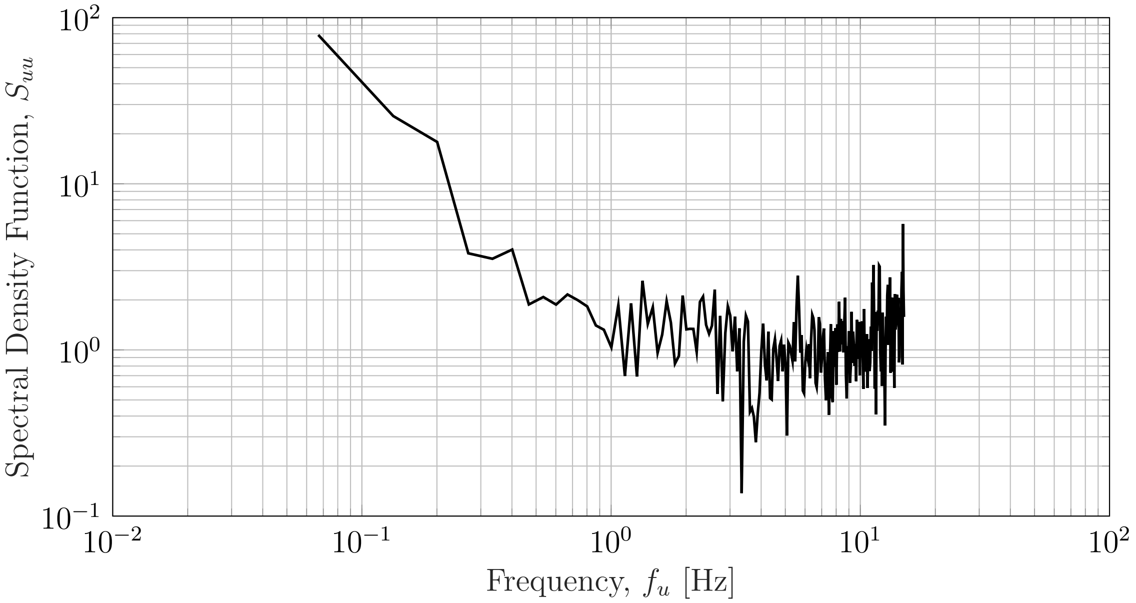

Figure C.21: Power spectra - longitudinal velocity at $x \approx 638\ cm,\ y = 38.5\ cm,\ z = 38\ cm$

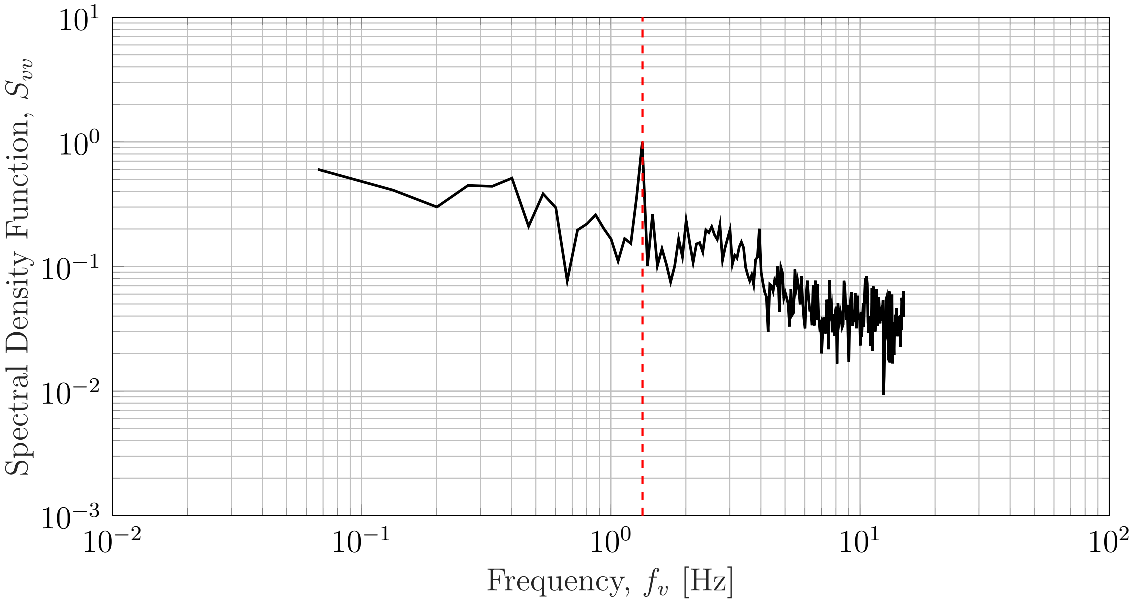

Figure C.22: Power spectra - lateral velocity at $x \approx 638\ cm,\ y = 38.5\ cm,\ z = 38\ cm$